

MICROCOPY RESOLUTION TEST CHART
NATIONAL BUREAU OF STANDARDS-1963-A

11

AD-A161 202

DYNAMICS OF HIGH TEMPERATURE PLASMAS
Report No. SAIC-85/1846
October 1, 1985

DTIC FILE COPY

DTIC
ELECTE
NOV 18 1985
S E D

This document has been approved
for public release and sale; its
distribution is unlimited.

Science Applications International Corporation

85 10 10 044

11.

DYNAMICS OF HIGH TEMPERATURE PLASMAS

Report No. SAIC-85/1846

October 1, 1985

SAIC
10/1/85
E



Science Applications International Corporation

Post Office Box 1303, 1710 Goodridge Drive, McLean, Virginia 22102, (703) 821-4300

FINAL REPORT

Report No. SAIC-85/1846

DYNAMICS OF HIGH TEMPERATURE PLASMAS

N00014-83-C-2138

SEPTEMBER 1985

Submitted by:

DR. ELLIS HYMAN

SCIENCE APPLICATIONS INTERNATIONAL CORPORATION

1710 GOODRIDGE DRIVE

MCLEAN, VA 22170

Contributing Authors:

D. Dialetis, J. Finn, H. Freund, A. Mondelli,

E. Ott, C. Pellegrini, R. Sudan

Submitted to:

DR. GLENN JOYCE

PLASMA THEORY BRANCH - CODE 4790

PLASMA PHYSICS DIVISION

NAVAL RESEARCH LABORATORY

Accession For	
NTIS GRA&I	<input checked="" type="checkbox"/>
DTIC TAB	<input type="checkbox"/>
Unannounced	<input type="checkbox"/>
Justification	<i>per</i>
By	
Distribution/	
Availability Codes	
Dist	Avail and/or Special
<i>A-1</i>	

TABLE OF CONTENTS

<u>SECTION</u>	<u>PAGE</u>
I. INTRODUCTION	1
II. ENVELOPE MODEL FOR BEAM TRANSPORT AND FOCUSING IN AN INDUCTION LINAC	2
III. HIGH-CURRENT ACCELERATORS (A)	18
IV. FREE-ELECTRON LASER STUDIES	21
V. HIGH CURRENT ACCELERATORS (B)	25
VI. LASER BEAT WAVE PARTICLE ACCELERATION	27
VII. ORBITRON MASER DESIGN	30
VIII. ELECTRON BEAM STABILITY IN THE MODIFIED BETATRON	32
IX. RELATIVISTIC ELECTRON BEAM DIODE DESIGN	35
X. FREE ELECTRON LASER APPLICATION TO XUV PRODUCTION AND PARTICLE ACCELERATION	37
APPENDIX A	A-1
APPENDIX B	B-1
APPENDIX C	C-1
APPENDIX D	D-1
APPENDIX E	E-1
APPENDIX F	F-1
APPENDIX G	G-1
APPENDIX H	H-1
APPENDIX I	I-1

TABLE OF CONTENTS (continued)

	<u>PAGE</u>
APPENDIX J	J-1
APPENDIX K	K-1
APPENDIX L	L-1
APPENDIX M	M-1
APPENDIX N	N-1
APPENDIX O	O-1

I. INTRODUCTION

This final report for the Science Applications International Corporation (SAIC) contract "Dynamics of High Temperature Plasmas", contract number N00014-83-C-2138, covers the technical period 15 March 1983 to 1 August 1985. We present the results of studies in several topics of importance for the understanding of high temperature plasmas, performed in support of programs of the Plasma Theory Branch (CODE 4790) of the Plasma Physics Division at the Naval Research Laboratory (NRL).

In the following sections we describe briefly the tasks performed. Details are included in the various Appendices to this report. The topics discussed include: II. Envelope Model for Beam Transport and Focusing in An Induction Linac, III. High Current Accelerators (A), IV. Free-Electron Laser Studies, V. High Current Accelerators (B), VI. Laser Beat Wave Particle Acceleration, VII. Orbitron Maser Design, VIII. Electron Beam Stability in the Modified Betatron, IX. Relativistic Electron Beam Diode Design, and X. Free Electron Laser Applications to XUV Production and Particle Acceleration.

II. ENVELOPE MODEL FOR BEAM TRANSPORT AND FOCUSING
IN AN INDUCTION LINAC

The NBS induction linear accelerator produces an electron beam of energy 800 keV ($\gamma=2.5$), beam current $I_b=800$ A, beam radius $r_b=0.5$ cm, and beam pulsewidth $\tau_b=2$ μ s. Experiments at NRL have used this beam to drive a free-electron laser, where the wiggler field is $B_w=0.1-1.0$ kG, the straight section is $L_w=60$ cm, the wiggler wavelength is $\lambda_w=3$ cm, and the solenoidal focusing field is $B_s=1-5$ kG. With these parameters, peak output power ≈ 60 MW is possible with a theoretical efficiency $\approx 10\%$, at an output wavelength of $\lambda=3-4$ mm ($\lambda=\lambda_w/2\gamma^2$).

To realize these goals, it is necessary to transport the electron beam through the induction linac and match it to the FEL wiggler. Figure 1 shown a schematic drawing of the induction linac, showing the graded diode region, the locations of the seven focusing coils, the two accelerating gaps, and the iron cores of the induction modules. Figure 2 illustrates the FEL configuration with its solenoidal focusing and wiggler fields. The last (seventh) focusing coil of the induction linac is also shown on the figure, as well as a plot of the wiggler field on-axis. Three different approaches to the transport problem have been utilized:

THIS DOC
Reproduced from
best available copy.

- o SLAC Gun code -- S. Slinker,
- o Numerical Simulation -- Austin Research Associates (ARA),
- o Beam Envelope Calculations -- this report

The beam envelope equation may be expressed as

$$R'' + \Omega^2 R - U/R - \epsilon_n^2/R^3 = 0,$$

where

$$\Omega^2 = \gamma'^2(2+\gamma^2)/(4\beta^4\gamma^4) + \Omega_{0z}^2/(4\beta^2\gamma^2c^2)$$

$$U = 2\beta v/\gamma^2$$

$$\beta v = I_b [\text{kA}]/17$$

$$\epsilon_n = \beta\gamma\epsilon = 0.2(I_b [\text{kA}])^{1/2}$$

$$R = (\beta\gamma)^{1/2} r_b$$

$$\gamma' = d\gamma/dz = -|e|E_z(z)/mc^2$$

$$\Omega_{0z} = |e|B_z(z)/mc^2$$

This equation will apply under the assumption that the canonical angular momentum (P_θ) of the electrons is zero, the transverse density and current density of the beam are uniform, the beam and fields are axisymmetric ($\partial/\partial\theta = 0$), the axial fields are independent of r , and the radial fields are linear in r . In addition, the paraxial approximation, $|v_z| \gg |v_\perp|$, is used for the beam. The radial fields are

expressed as

$$E_r = -(r/2)E_z' + \{\text{self-fields}\}$$

$$B_r = -(r/2)B_z'$$

When the fields have no z dependence, as inside a long solenoid, the equilibrium envelope equation, $R'' = 0$, may be solved for the equilibrium beam radius,

$$r_{b,eq} = (1/\gamma\beta)(U/2\Omega^2) \left\{ 1 + [1 + 4\Omega^2\epsilon_n^2/U^2]^{1/2} \right\}$$

Small oscillations of the beam radius about this equilibrium can occur with the frequency, ω , given by

$$\omega^2 = \Omega^2 + U/R_{eq}^2 + 3\epsilon_n^2/R_{eq}^4$$

Given a solution of the envelope equation, it is possible to generate "sub-envelopes", which correspond to nested beam ellipses in phase space, ie. to ellipses with x' and x scaled in the same ratio as in the original ellipse. For these ellipses, I/ϵ will be invariant, since $I \sim x^2$ and $\epsilon \sim xx'$ and $x \sim x'$. The sub-envelope solutions can be used to determine the acceptance of any aperture in the beam-line.

If the beam is adiabatically compressed by a longitudinal magnetic field, its envelope will follow a flux surface, given by $r^2 B_z = \text{constant}$. Unfortunately, the field

coils of the induction linac do not readily lend themselves to this simple solution.

The accelerating gaps of the induction linac are modeled as sections of pipe of length L and radius a with a gap (of width d) located at $L/2$. The axial electric field is assumed to vanish at $z=0$ and $z=L$, as well as along the pipe wall. In the gap the E_z field at $r=a$ is assumed to be uniform, E_0 . The E_z field may then be expressed as

$$E_z = \sum_{n=1}^{\infty} A_n(r) \sin(k_n z) ,$$

where $k_n = n\pi/L$,

$$A_n(a) = (2E_0 d/L) [\sin(k_n d/2)/(k_n d/2)] \sin(n\pi/2) ,$$

and

$$A_n(r) = A_n(a) I_0(k_n r)/I_0(k_n a)$$

The on-axis field due to each field coil is calculated from a simple prescription. Let the coil have inner radius r_1 , outer radius r_2 , length $2l$, and be centered at z_0 . The field at the center of such a coil is given by

$$B_z(z_0) = NIF(\alpha, \beta)/[2r_1\beta(\alpha-1)] ,$$

$$F(\alpha, \beta) = (4\pi\beta/10) \ln \left\{ [1 + \sqrt{1 + \beta^2}] / [1 + \sqrt{1 + \beta^2}] \right\} ,$$

where $\alpha=r_2/r_1$, $\beta=l/r_1$, N is the number of turns (assumed

uniformly wound), and I is the current per turn in Amperes. Since the on-axis field at the center of a uniform coil must be due to equal contributions from each half of the coil, the on-axis field at the end of a coil is just half the field at the center of an identically-constructed coil with twice the length. The field at any on-axis location, z , may then be found by a superposition of end fields of coils having positive and negative current, as shown in Figure 3, to obtain

$$B_z(z) = NI[F(\alpha, \beta + \tilde{z}) + F(\alpha, \beta - \tilde{z})] / [4r_1 \beta (\alpha - 1)] ,$$

where $\tilde{z} = |z - z_0| / r_1$. Figure 4 shows the field due to each of the seven coils in the induction linac. The solid line is the experimentally measured field strength on axis, while the dots are the calculated field. The agreement is very good, except for coil #4, which is located close to the induction cores, and is therefore more sensitive to the magnetization of the cores.

To correct for the magnetization of the cores, the magnetic field on axis was measured with no coils energized, after running the field coils for some time. The resulting residual B_z profile on-axis is shown in Figure 5. This field has been digitized and is used as a correction for the magnetic field in the envelope equations.

Figure 6 shows the complete on-axis field profile used

in the code, including a nominally 2 kG solenoid in the wiggler region. Each field coil in the model is treated as a module so that once the fields have been calculated, it becomes a simple matter to redo the calculation with particular coils shifted along the axis.

The solution of the envelope equation for this field profile is shown in Figure 7. The axial locations of the field coils is shown at the top of the figure. For this run a 400 keV beam was injected and a single gap was energized with 300 kV, at the position marked by "G". The wall of the guide tube is also shown on the figure. (Note that the scales of the R and Z axes distort the shape of the wall). The envelope solution is also plotted, and displays some rather violent oscillations before entering the wiggler region. These results used $r'=0$ as the initial condition at the anode plane.

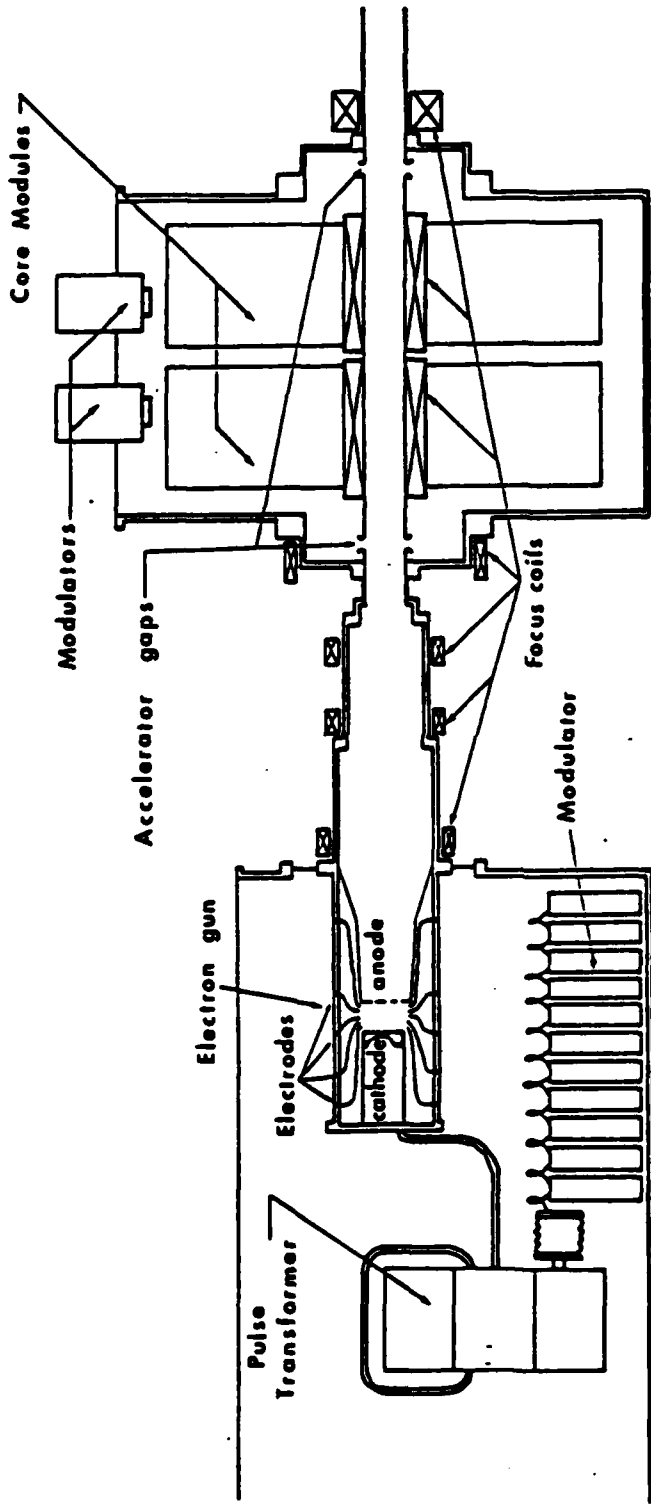
The ARA simulations have been used to model the diode region, and to obtain the entrance angle, r' , for initializing the envelope equations. The envelope in this case (shown in Figure 8) displays oscillations which qualitatively agree with those in the simulation. The outer beam envelope hits the wall near the first gap, where the ARA simulation calculates a scrape-off of 135 A of the 718 A beam current.

It is also possible to initialize a matched beam in the

wiggler solenoid, and to propagate the envelope backward, from right to left, as shown in Figure 9 for a beam with $\epsilon_n = 0.260$ rad-cm and $r_{eq} = 0.704$ cm in the wiggler solenoid. In this case, the code determines the radial location and angle at which the beam arrives at the anode plane. Since the beam angle at the anode is difficult to control experimentally, however, this approach proved of little benefit.

The experimental parameters and measurements used in this model were supplied by R. Lucey, often after making measurements specifically for this purpose. The code was transferred to the FEL experimenters (Lucey and Pasour) who used it as a tool in adjusting the focusing system to guide the beam to their FEL.¹

INDUCTION LINAC



V = 0.8 MV
I = 0.8 kA

$\tau = 2.0 \mu s$
 $\frac{\Delta V}{V} = 3\%$
N = 10^{16} particles

Figure 1. Induction Linac

FREE ELECTRON LASER EXPERIMENT

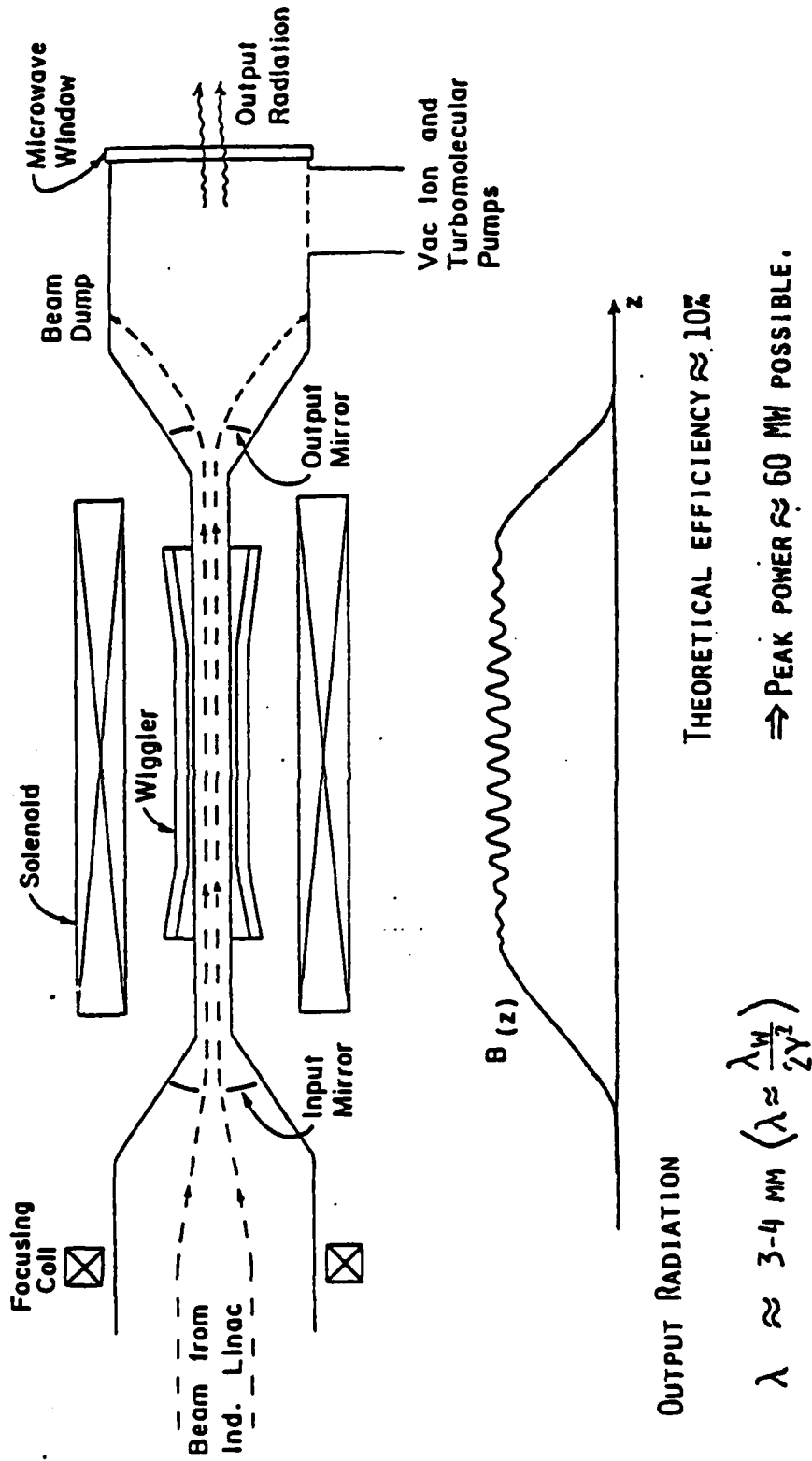


Figure 2. Free-Electron Laser Experiment

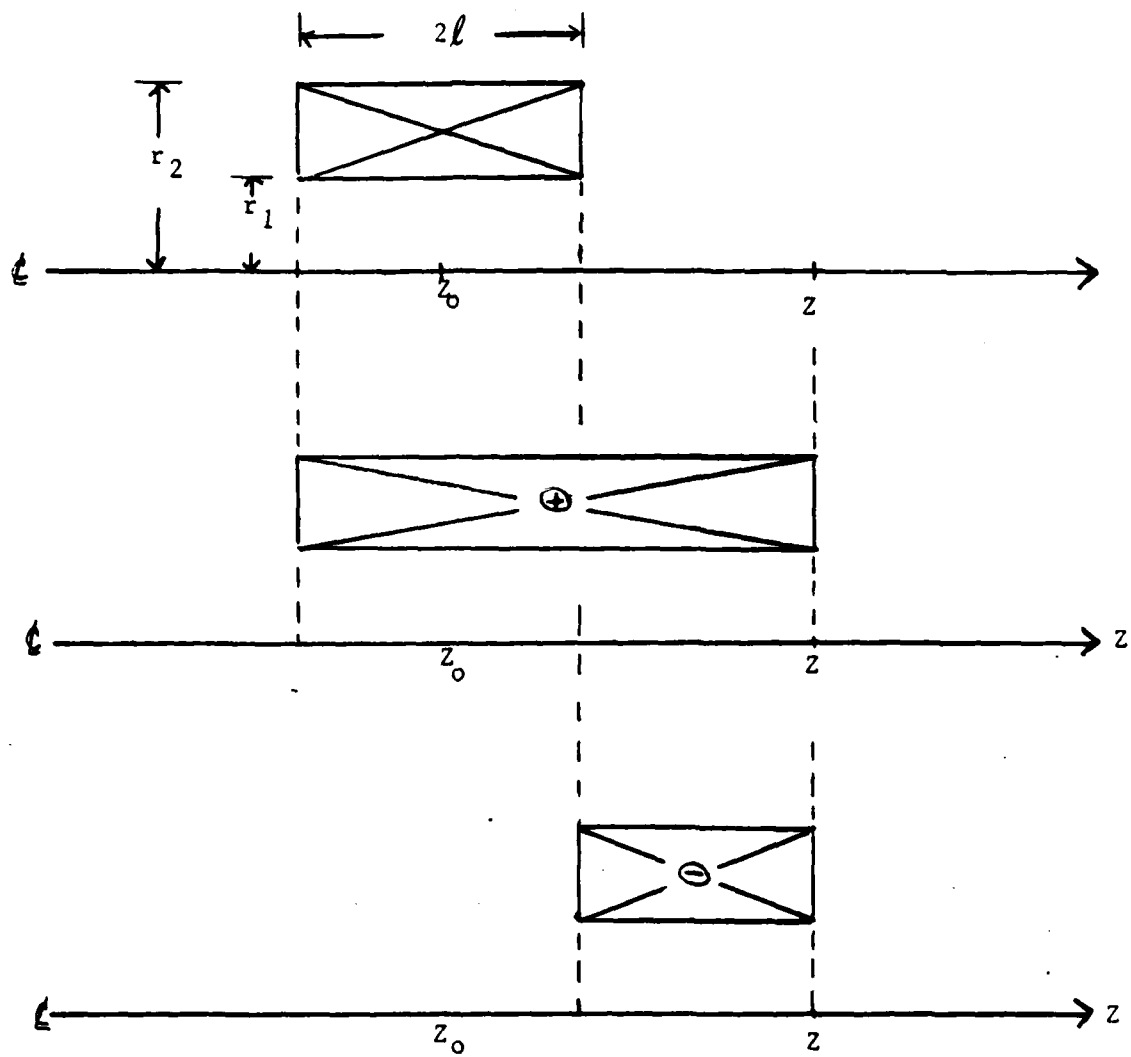


Figure 3. On-Axis Magnetic Field Model

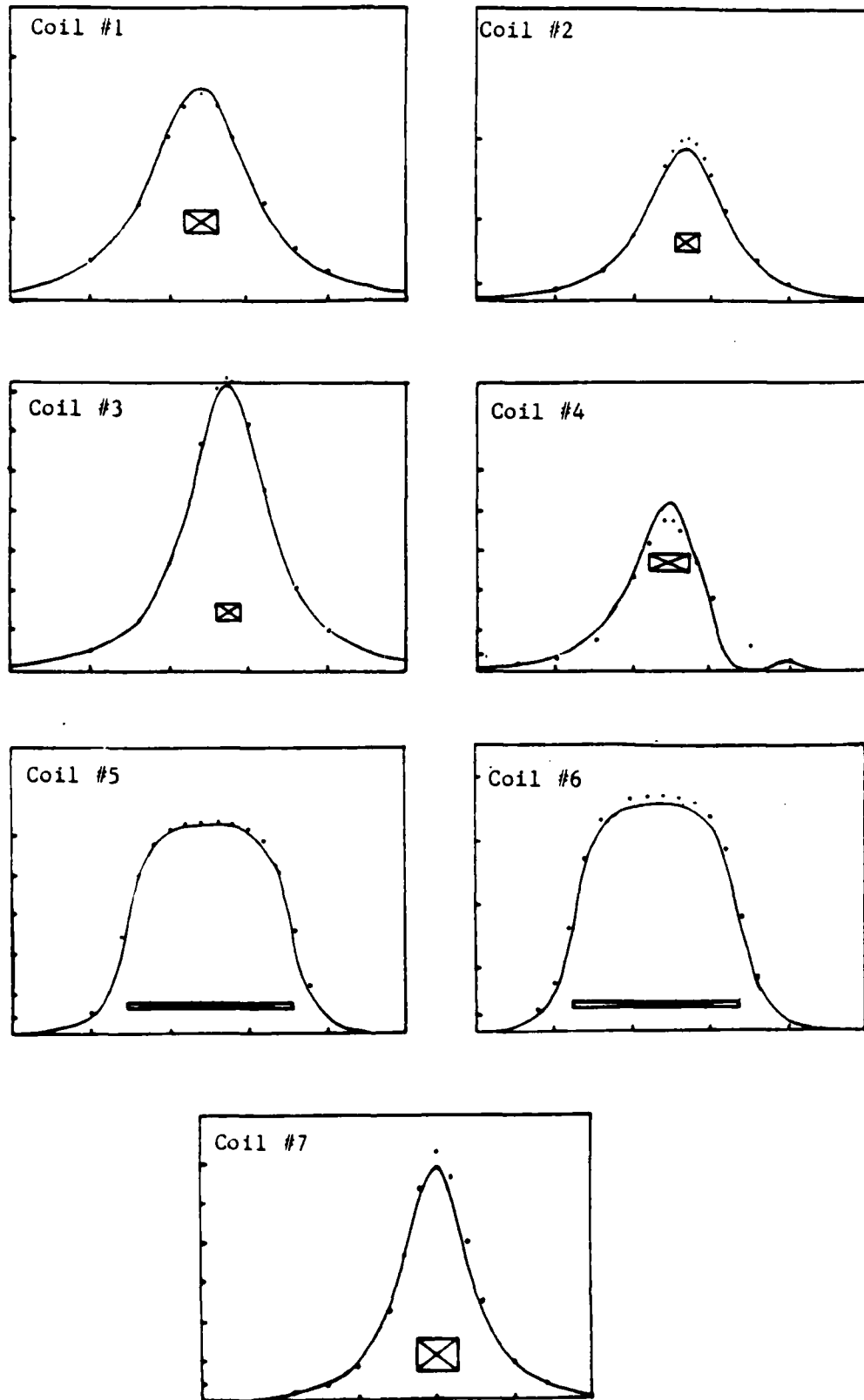


Figure 4. On-Axis Magnetic Field Profile for Each of the Induction Linac Focusing Coils

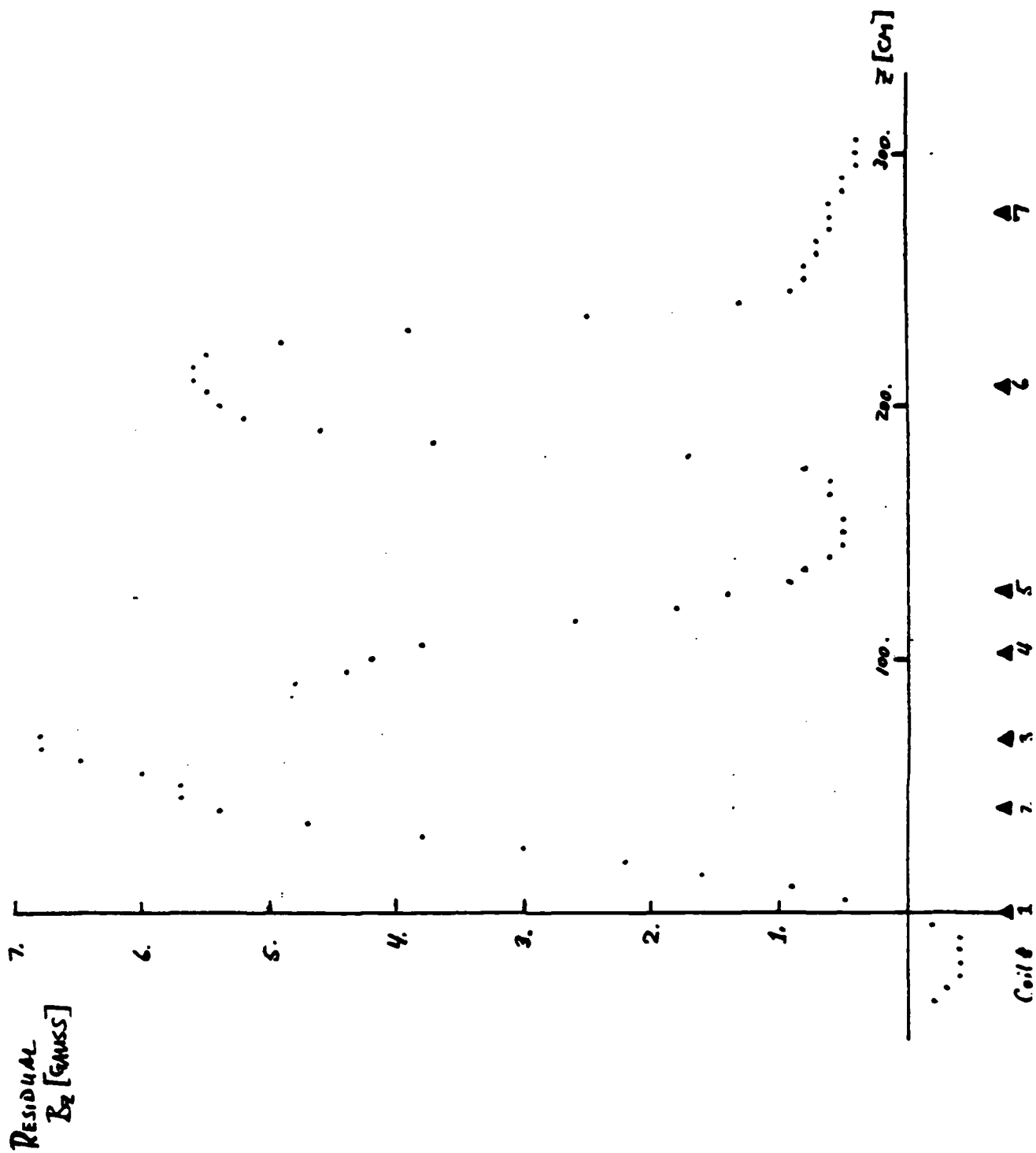


Figure 5. Residual On-Axis Magnetic Field

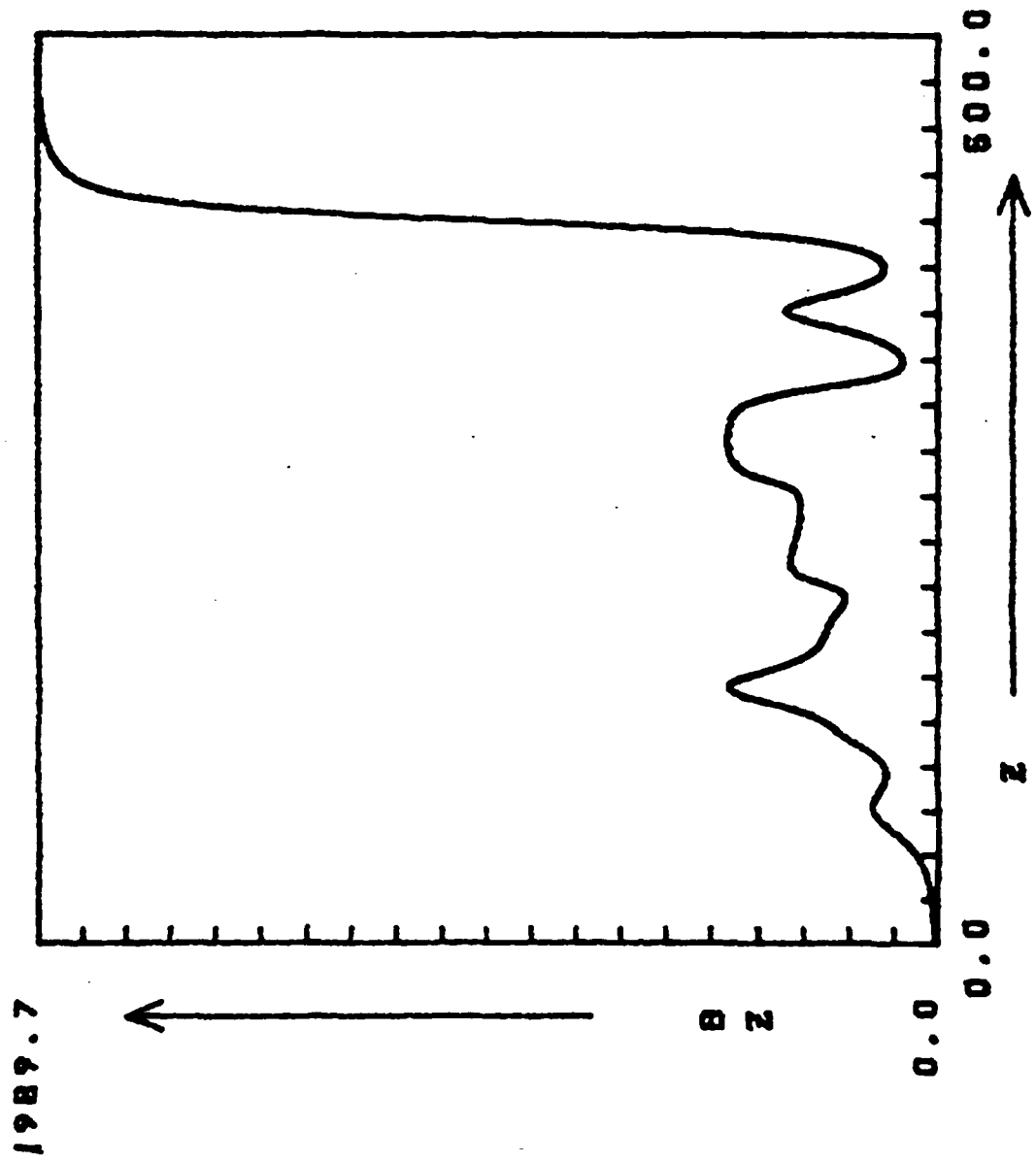


Figure 6. On-Axis Magnetic Field Profile for the Complete System

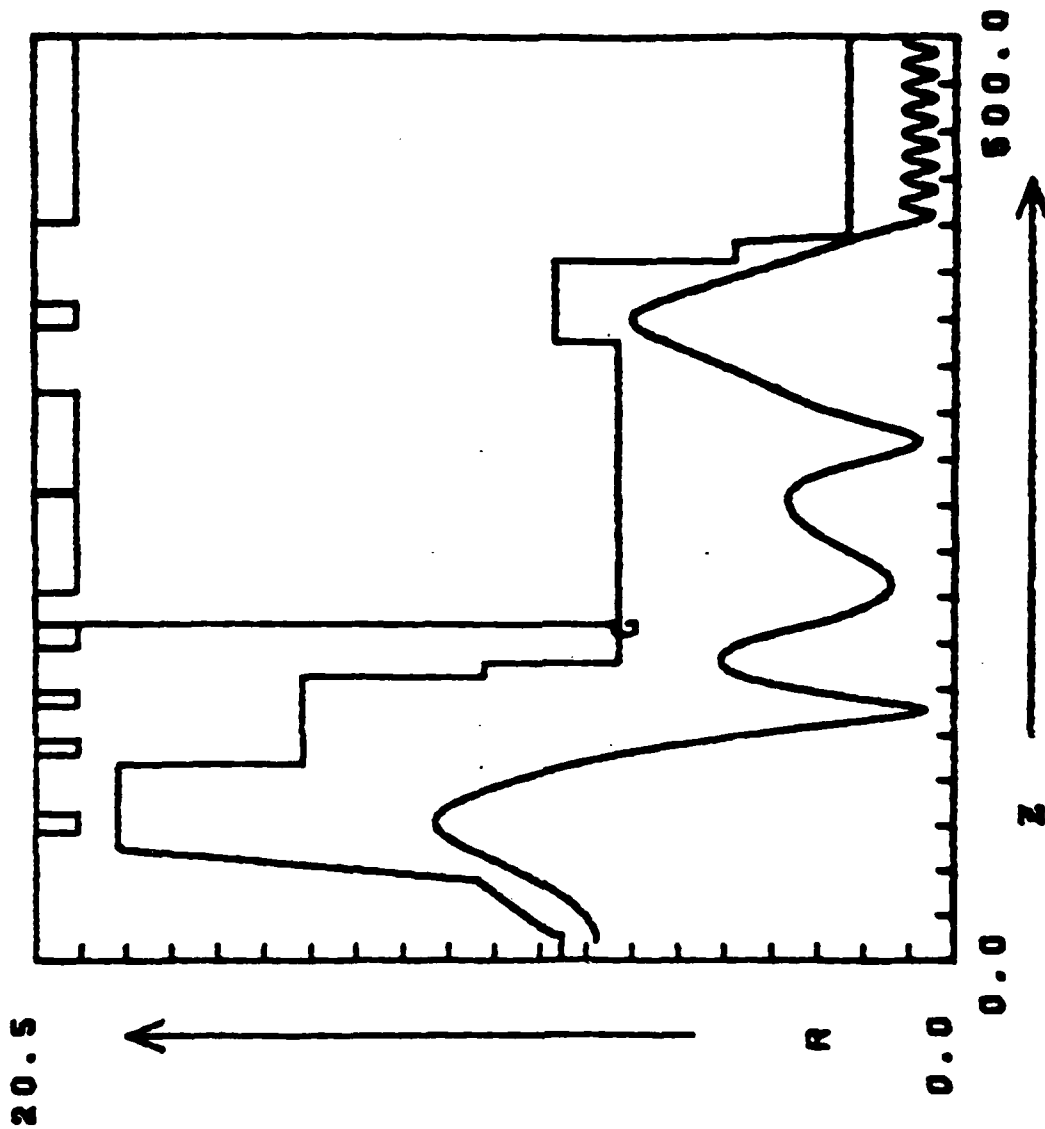


Figure 7. Envelope Solution for $R'=0$ At the Anode

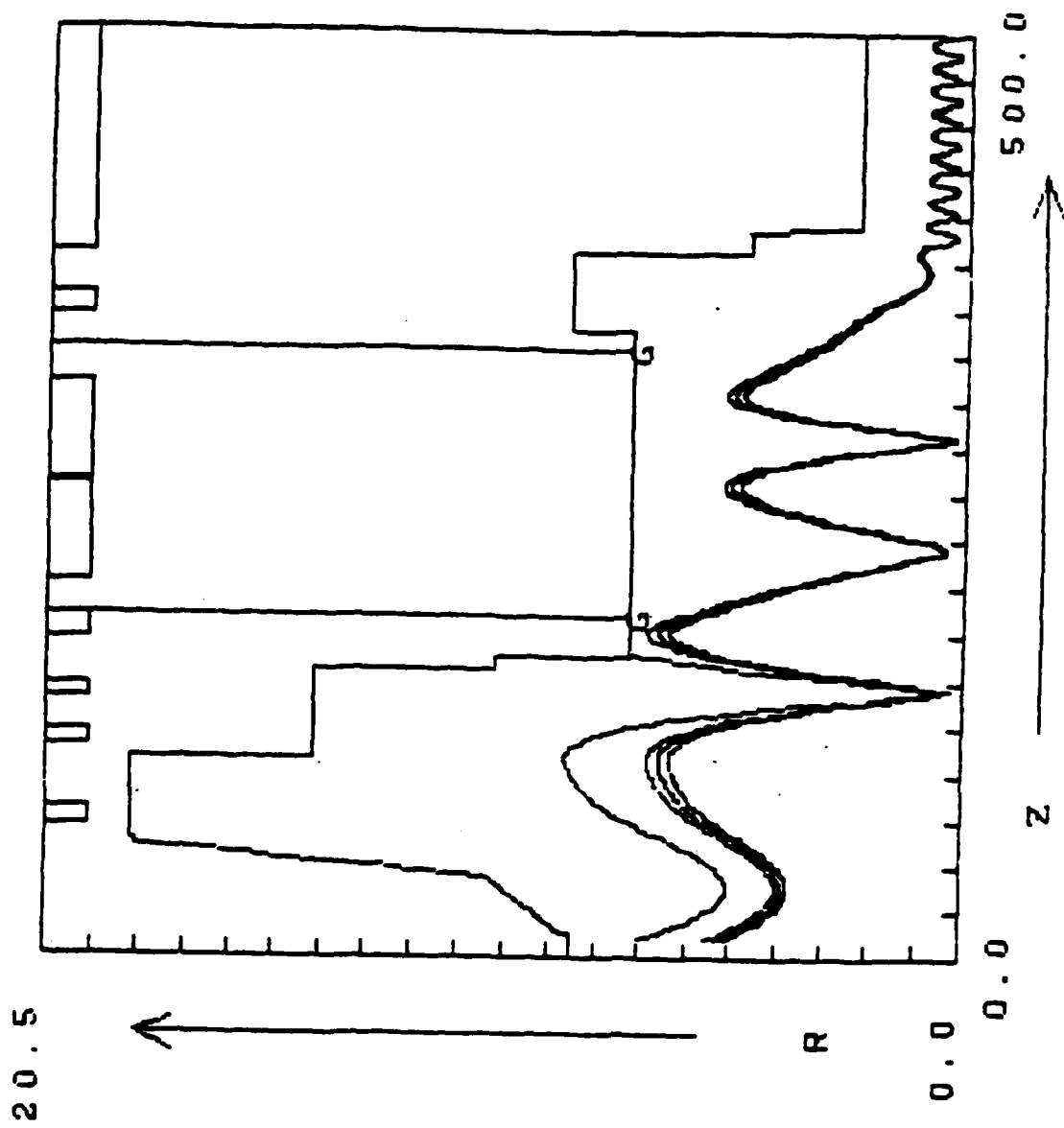


Figure 8. Envelope Solution for R' At the Anode
Determined from ARA Simulations

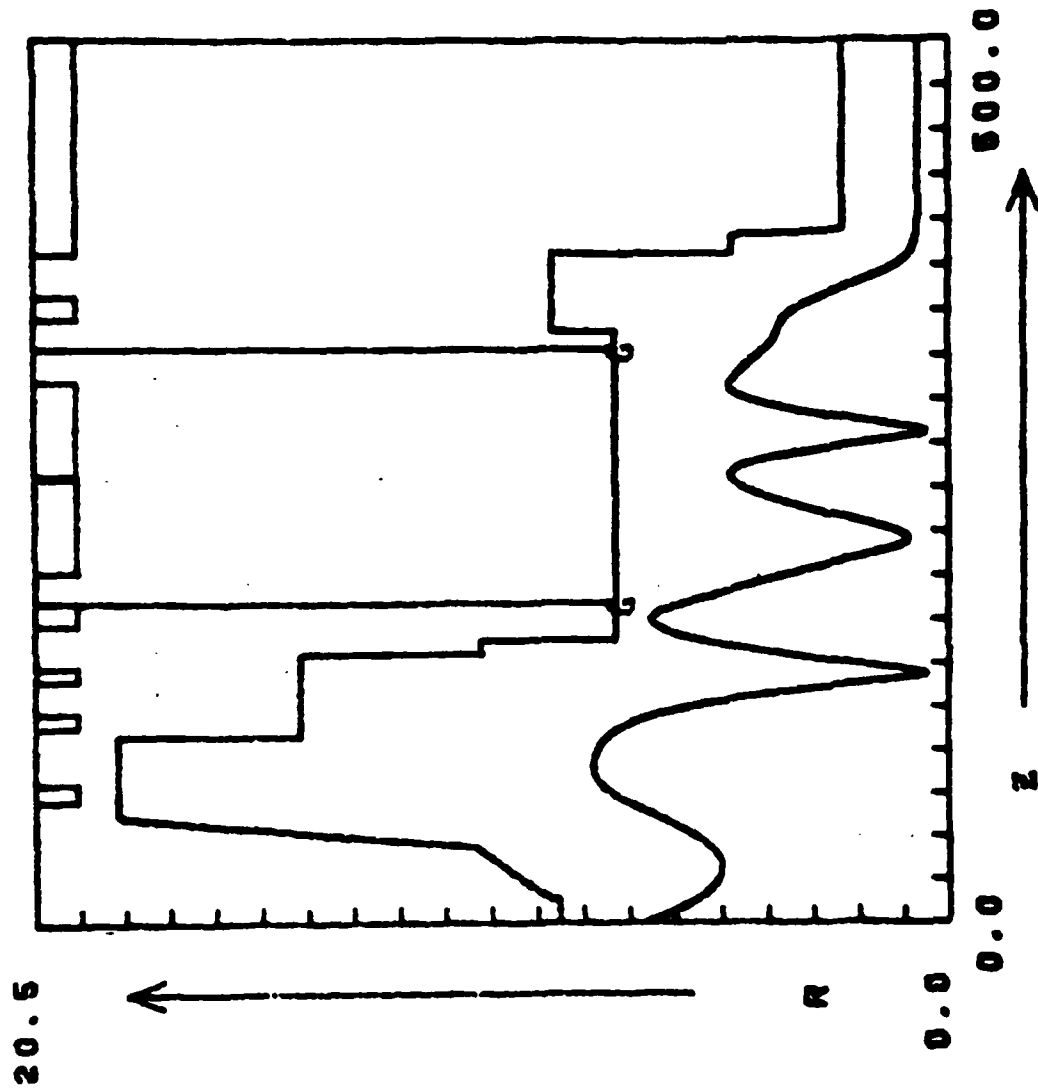


Figure 9. Envelope Solution Calculated Backward From the Matched-Beam Solution In the Wiggler Solenoid

III. HIGH-CURRENT ACCELERATORS (A)

The NRL Advanced Accelerator Project has embarked on the task of developing a compact, high-current (~10 kA) accelerator. The first effort in this direction is the modified betatron accelerator, which is a conventional betatron focusing system, augmented by a toroidal magnetic field to control the self-forces of an intense electron beam. In parallel with the mainline program on the modified betatron, NRL has supported a modest effort to explore other configurations, such as the racetrack induction accelerator², the stellatron³, and the bumpy-torus betatron⁴. These alternative approaches have in common the use of strong-focusing fields to increase the tolerance of the accelerator to mismatch between the vertical magnetic field and the electron energy. In the language of accelerator designers, the strong focusing increases the "momentum compaction" of the accelerator, where the momentum compaction is the ratio of momentum mismatch to beam displacement. We describe this property of the strong-focused accelerator in terms of the tolerance "bandwidth", which is the relative energy (or momentum) mismatch which can be tolerated before a beam initialized on the accelerator reference orbit will hit the inner wall of the vacuum vessel. For weak-focused accelerators, such as

the betatron or the modified betatron, the bandwidth is approximately

$$\Delta\gamma/\gamma_0 = a/(4r_0)$$

where a/r_0 is the inverse aspect ratio of the torus. For $a/r_0 \sim 0.1$, the bandwidth is approximately 2.5%. The strong-focused accelerators, on the other hand, can readily achieve bandwidth in excess of 50%. Although it is possible to use this property of strong-focused accelerators to design fixed-field focusing systems operating at very large mismatch ($\geq 1000\%$)⁵, such devices will be limited to modest beam energy and relatively poor beam quality. The addition of strong focusing fields to a betatron configuration will enhance the bandwidth of that accelerator while operating near a matched field condition. The enhanced bandwidth, in turn, relaxes costly requirements on field uniformity, injector ripple and shot-to-shot reproducibility.

Recognizing these potential advantages of strong-focused betatrons, two types of strong-focusing fields have been investigated in some detail, with research papers reprinted as appendices to this final report. The first configuration is the $l=2$ stellarator field, which is a rotating quadrupole field, analogous to alternate-gradient strong-focusing configurations used in most high-energy synchrotrons. The second configuration is a bumpy-torus field, which is an $l=0$

stellarator configuration. Both of these configurations provide an alternating transverse magnetic gradient at the beam reference orbit; the alternating transverse gradient is the defining characteristic of a strong-focused accelerator. All other l -number stellarator fields are weak-focusing.

The research papers in Appendices A and B demonstrate the single-particle orbit stability of these configurations and show that enhanced bandwidth ($\geq 50\%$) can be obtained for reasonable focusing field strength. They are titled, respectively, "High current Betatron with Stellarator Fields", C. W. Roberson, A.A. Mondelli, and D. Chernin, Phys. Rev. Lett. 50, 507 (1983) and "A Bumpy-Torus Betatron", D. Chernin, A Mondelli, and C. Roberson, Phys. Fluids 27, 2378 (1984).

IV. FREE-ELECTRON LASER STUDIES

Analysis of the Free Electron Laser (FEL) has proceeded on a number of levels and included analyses both of the linear gain and nonlinear efficiency in both one and three-dimensions. The fundamental configuration analyzed describes the propagation of a relativistic electron beam through a combined helical wiggler and axial guide magnetic field. Of particular interest is the effect of the axial guide magnetic field on the FEL interaction, since this is the configuration relevant to the experimental program at the Naval Research Laboratory. This work has been described in Appendices C ("Design and Operation of Collective Millimeter-Wave Free-Electron Laser, J. Quantum Elect. QE-19, 346 (1983)) and D ("Study of Gain, Bandwidth, and Tunability of a Millimeter-Wave Free-Electron Laser Operating in the Collective Regime", Phys. Fluids 26, 2683 (1983)).

Previous analysis of the linear growth rate of the FEL in one-dimension showed substantial enhancements possible due to a resonant interaction in the presence of an axial guide field. This occurred when the Larmor period due to the axial magnetic field approached the wiggler period. In view of this result, a one-dimensional particle simulation code was developed to study the nonlinear aspects of the

interaction with the goal of determining saturated power levels for an FEL amplifier. Results of the nonlinear analysis showed substantial enhancements to be possible in the presence of an axial guide field. For the model parameters chosen, efficiency enhancements of greater than 100% over the zero-guide field limit were found. Details of this work are included in Appendix E of this report titled "Nonlinear Analysis of Free-Electron Amplifiers with Axial Guide Fields", Phys. Rev. A 27, 1977 (1983).

An anomalous effect on the electrostatic beam space-charge has also been demonstrated in the presence of an axial guide field. In the collective Raman regime the FEL interaction proceeds by an induced scattering of the wiggler field (which appears as an electromagnetic wave in the electron beam frame) and a slow space-charge wave to produce the output radiation. This is a three-wave scattering process. In the absence of an axial guide field, the beam space-charge waves are stable. However, it has been shown that the presence of a strong axial guide magnetic field can drive the electrostatic space-charge modes unstable due to a negative-mass type of effect. This can have profound consequences for the FEL interaction, and experimental observations (see Appendix C) show peak output powers precisely in the unstable space-charge wave regime. This work is given in detail in Appendix F, titled "Unstable

Electrostatic Beam Modes in Free-Electron Laser Systems", Phys. Rev. A 28, 1835 (1983).

Having completed the analysis of both the linear and nonlinear phases of the FEL interaction in one-dimension in the presence of an axial guide field, attention turned to the inclusion of three-dimensional effects on the interaction. To this end, analyses of the linear gain were conducted during the contract period for a configuration which consists of the propagation of a relativistic electron beam through a loss-free cylindrical waveguide in the presence of helical wiggler and axial guide magnetic fields. The analysis was performed in both the low-gain Compton and high-gain collective regimes, and included the effect of the overlap of the electron beam and the waveguide modes (i.e., the filling factor) in a self-consistent manner. As in the one-dimensional case, substantial enhancements in the linear gain were found to result from the presence of the axial guide field. The low-gain Compton regime is documented in Appendix G, "Three-Dimensional Theory of Free-Electron Lasers with an Axial Guide Field", J. Quantum Elec. QE-19, 322 (1983). The high-gain collective regime is found in Appendix H, "Three-Dimensional Theory of the Free-Electron Laser in the Collective Regime", Phys. Rev. A 28, 3438 (1983).

Finally, an important application of the theory,

developed during the contract period, was to the design and interpretation of experimental results obtained by the FEL amplifier experiment in Code 4740 at the Naval Research Laboratory. This work is described in more detail in the previously referenced Appendices C and D.

V. HIGH CURRENT ACCELERATORS (B)

High energy accelerators that can produce high current electron beams are rapidly becoming an active area of research. Among the various schemes of acceleration, induction accelerators are the most promising. They are inherently low impedance devices and are thus suited to drive high current beams. Induction accelerators are divided into linear and cyclic. In both cyclic and linear devices, the acceleration process is based on the inductive electric field produced by a time varying magnetic field. In the linear accelerators, the total change in flux occurs in one transit time, typically in less than 100 nsec, while in cyclic accelerators the same change occurs over several thousand revolutions in a typical time of one msec.

As a consequence of the slow acceleration, the accelerated beam must be confined by the focusing magnetic field over long periods of time and, thus, field errors, instabilities and radiation losses pose limitations on the cyclic accelerators. These limitations can be substantially relaxed if the acceleration could occur rapidly as in the linear accelerators. A device has been proposed that combines the rapid acceleration of the linear accelerators and the compactness in size of the cyclic accelerators. It has been named REBA-TRON (Rapid Electron Beam Accelerator).

An extensive numerical and analytical investigation has been carried out on the beam dynamics of the rebatron accelerator. The acceleration occurs by a localized, high gradient electric field produced by convoluted parallel transmission lines, and beam confinement is achieved by a strong focusing torsatron magnetic field. The study indicates that both the bandwidth and the maximum electron beam current that can be confined by this device is remarkably high. Details can be found in Appendix I, "Rapid Electron Beam Accelerators (REBA-TRONS)", NRL Memorandum Report 5503.

VI. LASER BEAT WAVE PARTICLE ACCELERATION

The acceleration of charged particles to high energy by "collective" fields in a plasma or in non-neutral particle rings has been pursued vigorously for some time. The promise of the delivery of high power ($\geq 10^{14}$ watts) by modern lasers is a great inducement to generate schemes which could avail this power for accelerating bursts of particles to energies in the TeV range and beyond. It is also becoming apparent that the very successful schemes of particle acceleration in current use may not be able to push particle energy much above the TEV level without an enormous amplification in cost. Thus the combination of a need for superhigh energies and the availability of high powered lasers spawned a recent LANL workshop on "Laser Acceleration"

One of the concepts presented at the workshop was a proposal by Tajima and Dawson. Two plane laser waves with frequencies ω_1 and ω_2 , well in excess of the electron plasma frequency, ω_p , beat with each other to produce a plasma wave of frequency $\omega_1 - \omega_2 = \omega_p$ and wavelength $k_1 - k_2 = k_p$. It is assumed that the amplitude of the beat wave saturates only by accelerating and trapping a sizeable fraction of the plasma electrons. Elementary estimates yield a saturated amplitude, as measured in the laboratory frame, to be $E_p =$

$(mc/e)\omega_p$ or $E_p^2/4\pi = n_e m_e c^2$, where n_e is the ambient electron density. This very substantial electric field (10^8 v/cm for $n_e \approx 10 \text{ cm}^{-3}$) can be employed for accelerating ions or electrons and the proposal contains optimistic scenarios by which a phased sequence of acceleration (up to 10^5) could get proton energy to 10^{14} eV.

Unfortunately a plasma supports an uncomfortably large number of collective modes and although a particular sequence of interaction between some modes may be postulated for some process, in general, it is necessary to show that the sum of all other possible interactions is not significant for the success of that particular process. In what follows we outline the following possible limitations imposed on the Tajima-Dawson scheme. They include

- (1) The finite transverse dimensions of the laser-plasma interaction region, finite coherence time and finite correlation length of the laser beams.
- (2) The inhomogeneity of the plasma density.
- (3) The effect of the magnetic field caused by current created by the accelerated electrons.
- (4) The depletion of the beat wave energy through other channels, typically through the parametric pumping of short wavelength electron and ion fluctuations.

- (5) The generation of ion sound caused by electron drifts.
- (6) The scattering of laser waves on such ion sound waves, the so-called Brillouin scattering.
- (7) The actual requirements on phasing for ion acceleration.

What emerges from this analysis is that although the interactions postulated by Tajima and Dawson do occur the bulk of laser wave energy will be transferred to heating the plasma with concomitant drop in the efficiency of electron acceleration. We make no comment on techniques for ion acceleration by beat waves because the development of this aspect of the proposal has not proceeded beyond the stage of elementary wishful thinking. As a first step in the investigation of the above issues we have published two papers, "Excitation of the Plasma Waves in the Laser Beat Wave Accelerator," Appl. Phys. Lett. 45, 375 (1984) and "Dynamics of Space-Charge Waves in the Laser Beat Wave Accelerator", Phys. Fluids 28, 1974 (1985). These papers are reproduced in this report as Appendix J and Appendix K respectively.

VII. ORBITRON MASER DESIGN

In this work we have developed a device concept based on the orbitron mechanism, originally seen experimentally by Alexeff. We have also carried out extensive linear theory analysis to obtain growth lengths for amplifier configurations and thresholds for start oscillation for oscillators. Our device concept, the orbitron maser, is similar to an electron cyclotron maser that uses axis encircling electron orbits. However, an orbitron employs an electric field to radially confine the electrons, instead of a magnetic field. The device has a coaxial cylindrical geometry with the inner conductor held at a positive potential with respect to the outer conductor, as shown in Figure 10. The advantage of such a device is that, like the gyrotron, it can produce very short wavelength waves (e.g. $\lambda \sim 1\text{mm}$ or less) but it does not require a large magnetic field. Thus the device can potentially be much cheaper and more compact. A paper based on this work is in preparation with W. Manheimer and J. Burk.

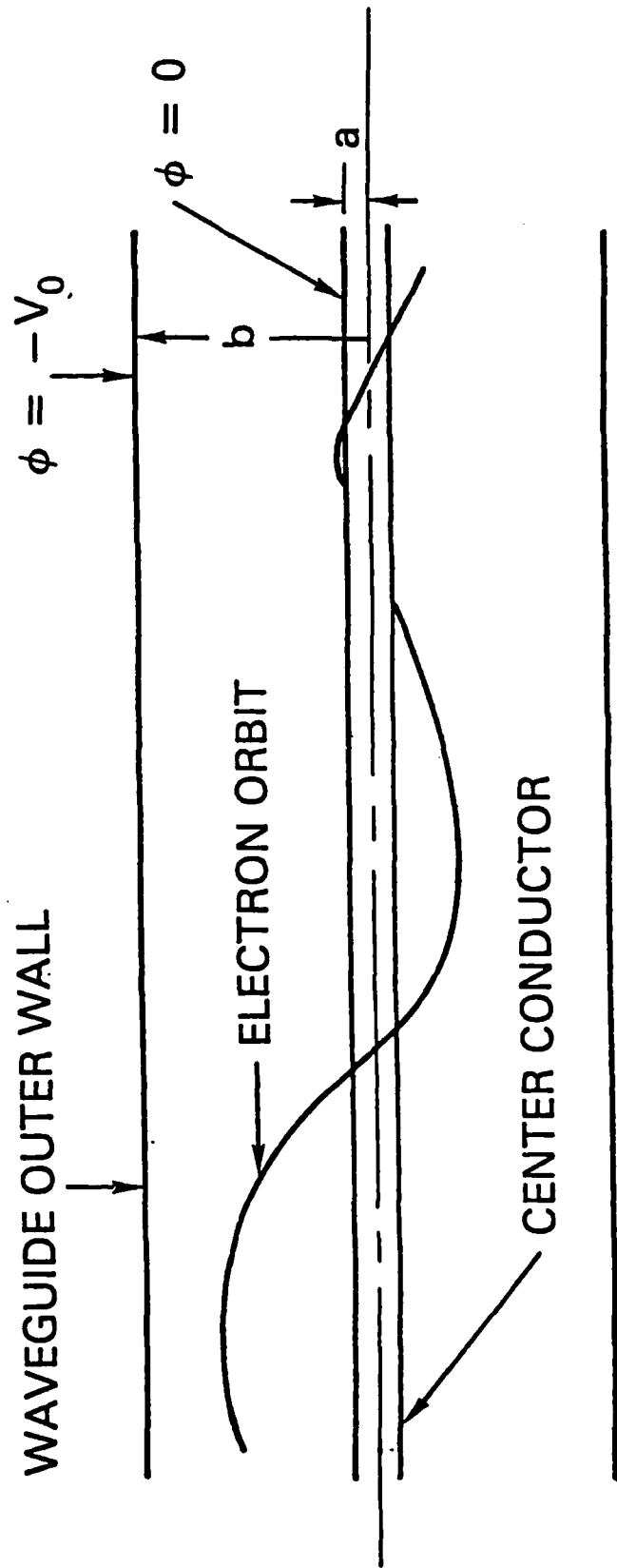


FIGURE 10. The Orbitron Maser Configuration

VIII. ELECTRON BEAM STABILITY IN THE MODIFIED BETATRON

In the modified betatron application, previous work⁷ has shown that $m \geq 2$ resistive wall modes can be very dangerous (m = poloidal mode number). However, that analysis was for zero Larmor radius particles. The question arises as to whether finite Larmor radius (FLR) effects will stabilize these modes. In order to gain insight on the general question of FLR effects on modes of this type we have done a treatment, not of the cylindrical geometry resistive wall mode, but rather of a simpler more analytically tractable problem: namely, FLR effects on diocotron modes in slab geometry. The indication of the results of this analysis is that FLR effects are ineffective in achieving stabilization of such modes. The basic problem considered was that of the diocotron instability of an electron layer in which the typical electron is allowed to have a Larmor radius of the order of the layer thickness. The principal results of the analysis are:

- (1) An integral equation eigenvalue problem for the Fourier transform of the electrostatic potential is formulated.
- (2) An exact analytical solution to the full problem is given for a special case which,

however, is general enough to encompass the full range of ratios of Larmor radius to layer thickness and of Larmor radius to wavelength. We believe that the results obtained for this special case are representative of what happens in general.

- (3) Using the results of the analytical solution we find the following: (a) Finite Larmor radius does not stabilize a beam wherein the guiding centers are localized (i.e., $\Delta = 0$, where Δ is the half-thickness of the guiding center spread), and instability persists at all wavelengths, although the growth rates are reduced. (b) Beams of fixed thickness $\delta = 2(\Delta + \rho)$ (where ρ is the Larmor radius) are destabilized by increasing the relative fraction $2\rho/\delta$ of beam thickness due to gyroradius. (c) For a beam of fixed guiding center spread Δ , increasing ρ is stabilizing, in that the growth rates are reduced and the range of unstable wavenumber becomes smaller.
- (4) A necessary and sufficient condition for instability in the form of an energy principle is derived for the case of a general symmetric distribution of guiding centers that decreases

monotonically away from the center of the layer.

- (5) As in the case of zero Larmor radius, the diocotron instability occurs only if the component of the propagation direction along the magnetic field is less than a certain small critical value.

The paper resulting from this study is titled "Finite Larmor Radius Diocotron Instability", Phys. Fluids 28, 941 (1985) and is included here as Appendix L.

IX RELATIVISTIC ELECTRON BEAM DIODE DESIGN

In collaboration with Drs. A. Fliflet and W. Manheimer we have developed several one dimensional methods to aid in the design of diodes for the production of high current relativistic electron beams for gyrotron applications. These methods are (i) relativistic slab model with or without self B_y , (ii) non-relativistic conical model without self B_ϕ , (iii) superrelativistic conical model with or without self B_ϕ . These methods, together with electrode synthesis, were used to obtain approximate designs for two diodes. The diodes produce 1 MV beams with 2 kA in a field around 2 kg, to be magnetically compressed to form a 1 GW beam for a 35 GHz gyrotron oscillator. The Hermansfeldt code was used to refine the design to produce a beam with these parameters and a relatively flat $\alpha = p_\perp/p_\parallel$ profile. These results are summarized in the enclosed manuscript "One Dimensional Models for Relativistic Electron Beam Design" to be submitted for publication. This paper is included here as Appendix M.

We have begun a collaboration with Drs. W. Manheimer and S. McDonald to study the eigenmodes of slotted vacuum gyrotron cavities. The purpose of this study is to find a cavity design that allows only one mode, i.e., has a high Q for that mode and rather low Q for all others. We have

begun to develop a numerical code to solve the Helmholtz equation in cylindrical geometry for TE or TM modes for arbitrarily shaped (open or closed) cross section. The computational method is based on a boundary-layer integral formulation of the wave equation; this has the advantage that only the boundary needs to be discretized (a one-dimensional set, as opposed to the two-dimensional interior discretized by standard finite-difference schemes). Furthermore, outgoing wave boundary conditions are automatically included in the free-space Green's function used in the boundary integral formulation. We have also proved that the response in such a cavity to an arbitrary beam interaction can be represented in terms of these damped eigenfunctions. To date, the code has been tested for the interior and the exterior of a circle and good agreement was found. The code has been modified to treat walls that consist of segments of elliptic cylinders displaced by an arbitrary amount and with a gap of arbitrary size. Preliminary runs have been performed to determine the Q of several TE modes that occur in the same frequency range, namely the $(m,n) = (1,4)$, $(3,3)$, and $(6,2)$ modes.

X FREE ELECTRON LASER APPLICATIONS TO XUV
PRODUCTION AND PARTICLE ACCELERATION

During this period we have performed studies of the theory of Free Electron Lasers (FEL) and their applications to the production of XUV electromagnetic radiation and particle acceleration to high energy. In the following we describe the work done on each of these three subjects. These works are clearly interrelated, and results obtained in one area can often be useful in the other.

The research on FEL's has made remarkable progress during the last few years. Very exciting results have been obtained both theoretically and experimentally. Good agreement exists between the theory and the experiments performed up to now. The technology needed for FEL development is also making rapid progress. All this leads us to explore new areas of applications, such as FEL's operating at short wavelength, in the XUV region of the spectrum, where commercial lasers are not presently available and few experimental systems have been operated, at only a few wavelengths and with very low power.

We have studied the scaling laws for operation of an FEL in the XUV region and they compare favorably with those of other possible laser systems. The main requirements for operation of an FEL in the XUV region are: small electron

beam emittance, small energy spread, and large current for a large FEL gain.

The electron beam emittance must be smaller or on the order of the wavelength that one wants to produce. Analyzing the beam emittance produced by present day accelerators, one comes to the conclusion that the only accelerator that one can use for wavelengths shorter than 100nm is a storage ring. This has led us to the study of electron storage rings⁸ and the emittance limitations in this system. The first results obtained show that it is possible to design rings optimized for FEL's applications, with an emittance small enough to reach FEL operation at about 10nm.

It is important to notice that the same minimum emittance requirement is also needed for the next generation of synchrotron radiation sources, and for the linear colliders which are now being studied to push the high energy physics frontier in the TeV region.

To analyse the large gain regime of an FEL we have used the theory developed recently by Bonifacio, Pellegrini and Narducci, Optics Communications 50, 373 (1984) entitled, "Collective Instabilities and High-Gain Regime in a Free Electron Laser", and included here as Appendix N. These results allow us to express both the gain parameter and the condition on the beam energy spread using only one quantity,

ρ , related to the relativistic beam plasma frequency and the radiation wavelength. A calculation of this quantity, based on the use of a 750 MeV storage ring to provide the electron beam, shows that one can expect gains larger than 100% per pass in a storage ring based FEL oscillator, down to wavelengths of about 10nm.

One problem in the successful operation of such an oscillator is posed by the optical cavity mirrors, which must have a reflectivity not smaller than 50% per reflection and be capable of withstanding strong incoherent synchrotron radiation produced by the undulator without a reflectivity degradation. We have proposed and studied a possible alternative to the oscillator, the operation of an FEL in the Self Amplified Spontaneous Emission mode. These results are given in detail in Appendix O entitled "Free Electron Lasers for the XUV Spectral Region" and have been published in Nucl. Instr. and Meth. A237, 159 (1985). This mode requires the use of a long undulator, with a few hundred periods, based in a storage ring bypass. Its main advantages are the absence of optical elements and the possibility of obtaining large peak power, on the order of several MW, in the 10 to 100 nm region.

As discussed in the previous section we have reformulated the FEL theory in a form well suited to the discussion of high gain experiments. This formulation has

allowed us to introduce a single parameter that must be optimized in the design of the storage ring driving the FEL and has thus allowed a better ring design. We have also started the analysis of other theoretical problems important in defining the characteristics of the radiation produced in the SASE mode, such as the laser startup from noise and the coherence properties of the radiation produced. The work on these problems is still in an initial stage and will require further study.

The FEL can also be used to accelerate particles⁹. When used in this mode we call it the Inverse Free Electron Laser (IFEL). The question of whether the IFEL can be used to accelerate electrons in the hundred GeV region has been recently studied (^{9,10}) and it has been shown that this is possible using a laser waveguide to propagate and keep focused a high power laser beam. We have done studies on the characteristics of this waveguide and the possible tolerances on imperfections and construction errors. The results show that the waveguide needs to be built to quality optical standards and that if this can be done one can propagate a high power laser beam in the guide over a distance of the order of kilometers with negligible losses. The work on this problem is continuing, in particular to study the region where the laser beam enters the guide.

Work has also continued to study the dynamics of the

particles in the IFEL, with particular attention to the problem of optimum undulator design to maximize the acceleration rate and of emittance scaling with energy. Optimum undulator design leads to an accelerator rate on the order of 250 MeV/m, up to an energy of about 300 GeV. At higher energy the synchrotron radiation losses produced by the wiggling particle motion in the undulator, reduces the acceleration rate to lower values. The emittance scaling with energy offers interesting possibilities for producing high energy-low emittance beams by proper undulator design. This opens the possibility of using the IFEL as an injector for a TeV, high luminosity electron-positron collider system.

We can summarize the previous discussion, by listing the main topics on which we have worked, in the three areas of FEL theory, FEL operation in the XUV region, and IFEL accelerator concepts.

- (a) FEL theory: high gain regime, collective FEL instability, non linear saturation regime, radiation self-focusing and diffraction effects, FEL start-up from noise, coherence properties of the radiation.
- (b) FEL in the XUV region: scaling laws, Self Amplified Spontaneous Emission operation mode, storage ring for XUV-FEL, limitations on storage ring emittance

and energy spread, design of storage rings for FEL's, effect of multiple Touschek scattering on storage ring emittance.

- (c) IFEL: scaling laws for acceleration rate, system design for maximum acceleration rate, laser waveguide design, laser waveguide error tolerances, longitudinal emittance scaling laws.

REFERENCES

1. J. A. Pasour, R. F. Lucey, and C. A. Kapetanacos, Phys. Rev. Lett. 53, 1728 (1984); C. W. Roberson, J. A. Pasour, F. Mako, R. Lucey, and P. Sprangle, "A Free-Electron Laser Driven by a Long-Pulse Induction Linac", NRL Memo Report 5013 (1983).
2. A. A. Mondelli and C. W. Roberson, Part. Accel. 15, 221 (1984).
3. C. W. Roberson, A. Mondelli, and D. Chernin, Phys. Rev. Lett. 50, 507 (1983).
4. D. Chernin, A. Mondelli, and C. Roberson, Phys. Fluids 27, 2378 (1984).
5. C. A. Kapetanacos, P. Sprangle, S. J. Marsh, D. Dialetis, C. Agritellis, and A. Prakash, "Rapid Electron Beam Accelerators (REBATRONS)", NRL Memo Report 5503 (1985).
6. H. P. Freund, P. Sprangle, D. Dillenburg, E. H. da Jornada, R. S. Schneider, and B. Liberman, Phys. Rev. A 26, 2004 (1982).

7. R. G. Kleva, E. Ott, and P. Sprangle, *Phys. Fluids* 26, 2689 (1983).
8. J. Bisognano, C. Pellegrini, et al., Feasibility Study of a Storage ring for a High Power XUV Free Electron Laser, submitted to *Particle Accelerators*.
9. C. Pellegrini, et al., in *Laser Accelerators*, P. Channel, ed., Amer. Inst. of Physics, 91 (1982).
10. C. Pellegrini, P. Sprangle and W. Zakowicz, in *Proc. of the XII Intern. Conf. on High Energy Accelerators*, Batavia, Illinois, (1983).

APPENDIX A

HIGH-CURRENT BETATRON WITH STELLARATOR FIELDS

High-Current Betatron with Stellarator Fields

C. W. Roberson

Office of Naval Research, Arlington, Virginia 22217

and

A. Mondelli

Science Applications, Inc., McLean, Virginia 22102

and

D. Chernin

Berkeley Research Associates, Springfield, Virginia 22150

(Received 2 November 1982)

By adding an $l=2$ stellarator field to a betatron accelerator, a new configuration is obtained which is capable of accelerating multikiloamp beams and which will tolerate a large (more than 50%) mismatch between the particle energy and the vertical magnetic field. The additional field is a twisted quadrupole which acts as a strong-focusing system. This device has been analyzed both analytically and numerically.

PACS numbers: 52.75.D1, 29.20.Fj

Conventional betatrons^{1,2} are current limited at injection. Recently, efforts have been made to extend the current-carrying capability of the betatron. For example, the plasma betatron³ employs a toroidal magnetic field in the direction of the particle orbit to contain the plasma. Current interest is focused on high-current nonneutral electron acceleration in modified betatrons.⁴⁻⁶

By adding a stellarator field to a cyclic accelerator, a strong-focusing system⁷ is obtained which can sustain high currents and large mismatch between particle energy and vertical field. The energy bandwidth relaxes the design requirements for the injector and the magnetic field system. Unlike fixed-field alternating-gradient betatrons,⁸ the stellarator-betatron (or stellatron) includes a strong toroidal field to confine very high currents. Figure 1 shows a sketch of the stellatron configuration.

We have quantitatively studied the stellatron configuration. Our studies have consisted of numerical and single-particle orbit calculations, as well as analytical linearized orbit theory, including the beam self-fields.

We may study the behavior of an intense electron beam in the stellatron quantitatively by considering small departures from a "reference orbit," a circle located at the null point in the quadrupole field, at $r=r_0$, $z=0$. Here and below we use a cylindrical (r, θ, z) coordinate system with origin at the center of the torus's major cross section. Quantities evaluated at the reference orbit will carry a subscript 0 below; departures from this orbit will carry a subscript 1.

The twisted quadrupole field, of period $2\pi/m$, then is written as

$$B_z \cong kB_s(-r_1 \sin m\theta + z_1 \cos m\theta), \quad (1)$$

$$B_s \cong kB_s(r_1 \cos m\theta + z_1 \sin m\theta), \quad B_\theta \cong B_{\theta 0},$$

where $k, B_s, B_{\theta 0}$ are constants, and the betatron field is

$$B_r \cong -nB_{\theta 0}z_1/r_0, \quad B_z \cong B_{\theta 0}[1 - n(r_1/r_0)], \quad (2)$$

where $B_{\theta 0}$ is the vertical field at the reference orbit and n is the usual field index.

We consider the motion of an electron located within a beam whose center is located at $r=r_0 + \Delta r$, $z=\Delta z$; the electron's position is $r=r_0 + \Delta r + \delta r \cong r_0 + r_1$, $z=\Delta z + \delta z \cong z_1$. Using a cylindrical approximation for the beam self-fields, we

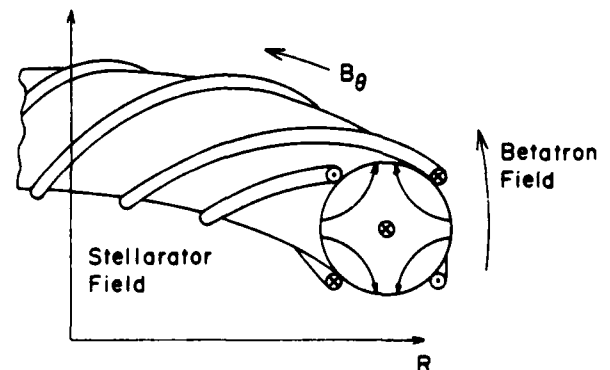


FIG. 1. Stellatron configuration.

find

$$\ddot{r}_1 + \Omega_{e0}^2(1 - n + \mu \cos m\theta)r_1 - \frac{1}{2} \frac{\omega_b^2}{\gamma_0^2} \left(\delta r + \frac{r_b^2}{a^2} \Delta r \right) = \frac{\gamma_1 c^2}{\gamma_0 r_0} - (\mu \Omega_{e0}^2 \sin m\theta)z_1 + \Omega_{e0} \dot{z}_1, \quad (3a)$$

$$\ddot{z}_1 + \Omega_{e0}^2(n - \mu \cos m\theta)z_1 - \frac{1}{2} \frac{\omega_b^2}{\gamma_0^2} \left(\delta z + \frac{r_b^2}{a^2} \Delta z \right) = -(\mu \Omega_{e0}^2 \sin m\theta)r_1 - \Omega_{e0} \dot{r}_1, \quad (3b)$$

$$\dot{\theta}_1 = - (r_1/r_0)\Omega_{e0}, \quad (3c)$$

where $\Omega_{e0} = eB_{e0}/m\gamma_0 c$, γ_0 is the relativistic factor for the reference orbit, $\omega_b^2 = 4\pi n_0 e^2/m\gamma_0$, n_0 is the beam number density, r_b is the minor radius of the beam, a is the minor radius of the (perfectly conducting) chamber, and $\mu = kr_0 B_s/B_{e0}$.

By performing a formal ensemble average of (3a)–(3c) one may find equations governing single-particle motion and that of the beam centroid. Details will be published elsewhere. By changing the independent variable from t to θ , and making the transformation $\xi = (r_1 + iZ_1)/r_0 = \psi \exp(im\theta/2)$, one obtains an equation for ψ which may be solved in the special case, $n = \frac{1}{2}$, with the following results.

Particle motion is oscillatory (under certain conditions; see below) about a center located at

$$\frac{\delta r}{r_0} = \frac{\Delta - \langle \Delta \rangle}{\bar{n}_b + \mu^2(m^2 + mb - \bar{n}_b)^{-1}}, \quad (4)$$

where $\bar{n}_b = \frac{1}{2} - n_s$, $n_s = \omega_b^2/2\gamma_0^2\Omega_{e0}^2$, $b = B_{\theta 0}/B_{e0}$, $\Delta = \gamma_1/\beta_0^2\gamma_0$, and angular brackets denote an ensemble average. There are five characteristic oscillation frequencies, $m\Omega_{e0}$ and $(m/2 \pm \nu_{\pm})\Omega_{e0}$, where

$$\nu_{\pm}^2 = \hat{n} + \frac{1}{4}\hat{m}^2 \pm (\hat{n}\hat{m}^2 + \mu^2)^{1/2} \quad (5)$$

with $\hat{n} = \bar{n}_b + \frac{1}{4}b^2$, $\hat{m} = m + b$. These frequencies are real when the system is located within the regions of the plane of Fig. 2 marked "stable." We remark that for low-current beams ($n_0 \rightarrow 0$) the stability condition reduces to

$$|\frac{1}{2}m^2 + mb - 1| > |2\mu|. \quad (6)$$

The "most" stable configuration results when the field lines are twisted clockwise ($m > 0$) when viewed in the direction of $B_{\theta}\hat{\theta}$, i.e., in the same sense as electron gyration about B_{θ} .

Similarly, the motion of the beam center is itself oscillatory about a center located at

$$\frac{\Delta r}{r_0} = \frac{\langle \Delta \rangle}{\bar{n}_b + \mu^2(m^2 + mb - \bar{n}_b)^{-1}}, \quad (7)$$

where $\bar{n}_b = \frac{1}{2} - (r_b^2/a^2)n_s$, with characteristic frequencies as in (5), under the replacement $n_s \rightarrow (r_b^2/a^2)n_s$.

Two important features of the solution are worth

pointing out. First, stable motion is possible throughout an injection-acceleration cycle. This has been checked for many possible time histories. A typical trajectory in the stability plane is shown in Fig. 2. The unstable region on the left of the diagram would not be entered in this case even if the acceleration were continued; " u " never changes sign in this case.

The second important feature of the solution pertains to the energy bandwidth of this machine. We note that the radial shift (7) of the orbit of a mismatched beam is, as expected, much smaller than that in a weak focusing ($\mu = 0$) device. (μ can easily exceed 100–200 in designs we have considered.) The stelleron's large energy bandwidth has very helpful consequences for injector and magnetic field design tolerances.

The introduction of fixed toroidal and helical fields to the betatron causes the betatron wavelengths to depend on energy, resulting in resonant instabilities driven by field errors during acceleration. If the toroidal field is sufficiently large, the betatron wavelengths will be insensitive to beam current. Such instabilities may be avoided by holding all the fields in constant ratio during acceleration. Alternatively, the effect of the

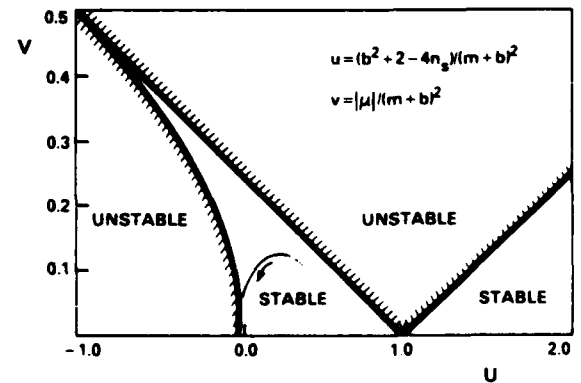


FIG. 2. Stelleron stability plane ($n = \frac{1}{2}$). The dotted line is the trajectory of an experiment with $I = 10$ kA, $B_{\theta 0} = 5$ kG, $\epsilon_s = 2\mu/m = 1$, $m = 20$, $r_0 = 1$ m, while B_{e0} is raised from 118 to 1700 G, corresponding to an increase in energy from ~ 3.5 to 50 MeV.

instabilities may be minimized if the energy gain per revolution is large enough to pass rapidly through each resonance.

A single-particle code, which integrates the relativistic equations of motion for an electron in an applied magnetic field, has been utilized to study certain nonlinear aspects of the stellatron configuration. Unlike the analytical analysis of the preceding paragraphs, this analysis does not employ a paraxial approximation for the electron motion and does not use an expansion in the particle displacement from a reference orbit. Also, the applied field in this analysis includes toroidal corrections to first order in the inverse aspect ratio.

The total magnetic field utilized by the code may be expressed as $\vec{B} = \vec{B}_b + \vec{B}_s$, where \vec{B}_b is the conventional betatron field, given by Eq. (2), and \vec{B}_s is the stellarator field, given by $\vec{B}_s = \nabla\Phi_s$, in terms of the magnetic scalar potential, Φ_s , which may be expressed as $\Phi_s^{(0)} + \Phi_s^{(1)}$, where

$$\Phi_s^{(0)}(\rho, \varphi, s) = B_{\theta 0} \{ s + (\epsilon_1/\alpha) I_1(x) \sin[l(\varphi - \alpha s)] \}.$$

Here, $x = l\rho$, $\alpha = 2\pi/L$, L is the helix pitch length, and I_1 represents the modified Bessel function. The coordinates (ρ, φ, s) form a local cylindrical system centered on the minor axis, where $s = R_0\theta$ is distance measured along the minor axis for toroidal angle θ , and (ρ, φ) are polar coordinates in the plane transverse to the

minor axis at s . The toroidal correction, $\Phi_s^{(1)}$, is given to first order in the inverse aspect ratio by Danilkin.⁹ All calculations have been performed for $l=2$. The variables μ and m , which describe the helical field in the previous analytical analysis, are given by $\mu = \epsilon mb/2$ and $m = 2\alpha R_0$ for $l=2$.

This model has been utilized to investigate the single-particle bandwidth of the stellatron. As ϵ_1 increases, the allowed mismatch in the stellatron becomes too large to be correctly modeled by the linearized theory. Figure 3 shows the results from both models for bandwidth versus ϵ_1 . These calculations assume a torus having a 1-m

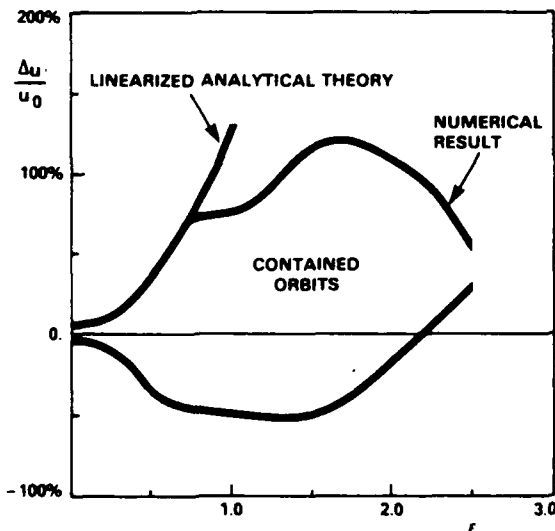


FIG. 3. Stellatron single-particle bandwidth. The bandwidth $\Delta u/u_0$, where $u = \gamma\beta$, is plotted against $\epsilon_1 \cong 2\mu/mb$. The accelerator is matched at $\gamma = 7$ with $B_{x0} = 118$ G, and $B_{\theta 0} = 1$ kG.

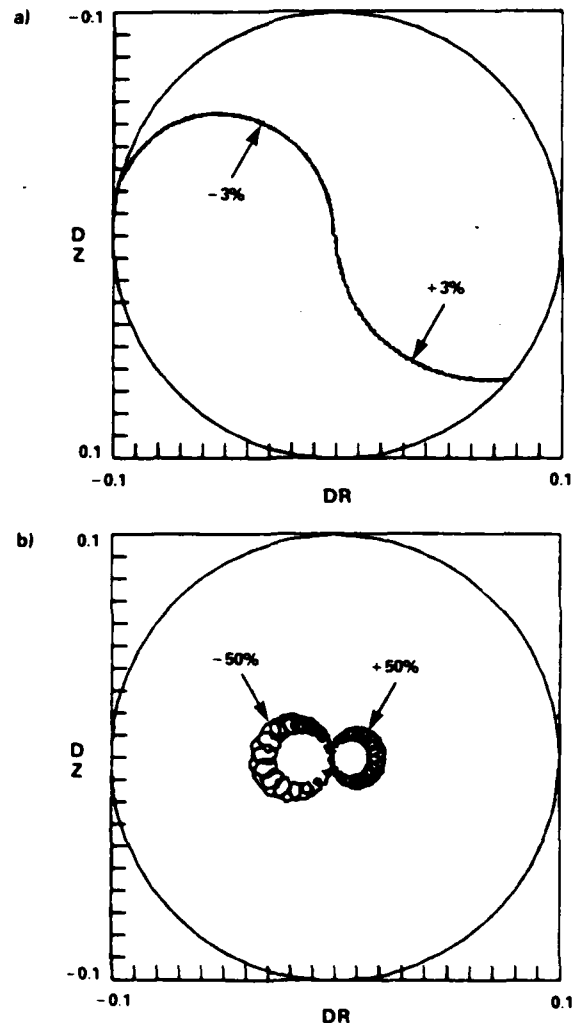


FIG. 4. Single-particle orbits. (a) Without the helical field components ($\epsilon_1 \cong 0$), $\Delta u/u_0 = \pm 3\%$; (b) stellatron orbit with $\epsilon_1 = \frac{1}{2}$, $\Delta u/u_0 = \pm 50\%$.

major radius and a 10-cm minor radius. A test electron is launched tangent to the minor axis with relativistic momentum $u = \gamma\beta$, which differs from the matched momentum, u_0 , by varying amounts, Δu . The figure shows $\Delta u/u_0$ against ϵ_1 , and represents the maximum $|\Delta u/u_0|$ for which the test orbit remained confined in the device. Mismatch in excess of 50% can be tolerated for these parameters.

Figure 4(b) shows typical stelleron orbits, projected on the minor cross section, for $B_{\theta 0} = 5$ kG, $\epsilon_1 = \frac{1}{2}$ for $\pm 50\%$ mismatch. The betatron field is again 118 G with $n = \frac{1}{2}$. Without the helical field contribution, Fig. 4(a) shows that as little as $\pm 3\%$ mismatch is not tolerable.

The superposition of twisted quadrupole, toroidal, and conventional betatron magnetic fields appears to offer significant practical advantages for the confinement and acceleration of large electron currents (tens of kiloamperes) to moderate energies (hundreds of megaelectronvolts). Foremost among these advantages is the greatly improved energy bandwidth over that of a weak-focusing device. The large bandwidth of the stelleron relaxes the requirements for monoenergetic injection, for a uniform (within a few percent) magnetic field configuration, and for a rigid mechanical design. Injection should not be any more difficult than for other high-current accelerator concepts, and is facilitated by the externally applied rotational transform of the stelleron field. The orbits should remain stable

from injection up to the highest energies achievable by conventional inductive acceleration.

It is a pleasure to acknowledge numerous discussions with members of the Naval Research Laboratory Special Focus Program "Advanced Accelerators." This work was supported by the Naval Research Laboratory.

¹D. W. Kerst, *Phys. Rev.* **58**, 841 (1940).

²D. W. Kerst, G. D. Adams, H. W. Koch, and C. S. Robinson, *Phys. Rev.* **78**, 297 (1950).

³L. A. Ferrari and K. C. Rogers, *Phys. Fluids* **10**, 1319 (1967).

⁴P. Sprangle and C. A. Kapetanacos, *J. Appl. Phys.* **49**, 1 (1978).

⁵N. Rostoker, *Comments Plasma Phys. Controlled Fusion* **6**, 91 (1980).

⁶P. Sprangle, C. A. Kapetanacos, and S. J. Marsh, in *Proceedings of the International Topical Conference on High-Power Electron and Ion Beam Research and Technology*, Palaiseau, France, 1981 (unpublished), p. 803.

⁷A. A. Mondelli and C. W. Roberson, *NRL Memorandum Report No. 5008*, 1982 (unpublished).

⁸K. R. Symon, D. W. Kerst, L. W. Jones, L. J. Laslett, and K. M. Terwilliger, *Phys. Rev.* **103**, 1837 (1956).

⁹I. S. Danilkin, in *Stellarators. Proceedings of the P. N. Lebedev Physics Institute*, edited by D. V. Skobel'tsyn (Consultants Bureau, New York, 1974), Vol. 65, p. 61ff.

APPENDIX B

A BUMPY-TORUS BETATRON - C1

A bumpy-torus betatron

D. Chernin^{a)}

Berkeley Research Associates, Springfield, Virginia 22150

A. Mondelli

Science Applications, Inc., McLean, Virginia 22102

C. Roberson

Office of Naval Research, Arlington, Virginia 22217

(Received 30 August 1983; accepted 11 June 1984)

The combination of a bumpy-torus field and a conventional betatron field leads to an interesting strongly focused, high-current accelerator configuration. The question of orbital stability of a test particle in such a device is discussed and it is shown that the alternating gradient focusing in this accelerator can easily lead to greater than 20% bandwidth in allowed mismatch between the vertical magnetic field and the average beam particle energy.

Conventional betatrons¹ are current-limited due to the defocusing effects of space charge at injection. In recent years there have been several renewed attempts at overcoming this (rather severe) space-charge limit. Specifically, there have been high-current conventional betatrons proposed² which employ high-energy injectors as well as so-called modified betatrons^{3,4} which employ a toroidal magnetic field to prevent space-charge blowup of the beam. In both of these cases, however, a mismatch between the injection energy and vertical field of a few percent or so will cause the beam to hit the wall, a matter of some concern in a high-current device. The maximum allowed error in the vertical field is typically on the order of a few gauss in designs which have been considered. Recently, it was shown⁵ that the combination of an $l = 2$ stellarator field and ordinary weak focusing betatron field results in a strong focusing high-current betatron or, "stellatron," with a large energy bandwidth. Such a configuration has the advantages of relaxing the vertical field and injector tolerances. In addition, the strong focusing introduces a threshold for the negative mass instability, so that this instability does not operate at injection (though other fast growing resistive or kink modes may occur below the negative mass threshold). In this brief communication we report analytical and numerical results on the bandwidth and stability of an alternative strong focusing scheme, namely, a combination "bumpy torus" and betatron field, corresponding to the $l = 0$ stellatron.

The bumpy-torus betatron field consists of a superposition of an $l = 0$ stellarator field and the field of a conventional betatron. Near the minor axis at $r = r_0, z = 0$, this field has the form

$$\begin{aligned} B_r &= -nyB_{z0} + \frac{1}{2}\delta B_\theta mx \sin m\theta, \\ B_\theta &= B_{\theta 0} [1 + (\delta B_\theta / B_{\theta 0}) \cos m\theta], \\ B_z &= B_{z0}(1 - nx) + \frac{1}{2}\delta B_\theta my \sin m\theta, \end{aligned} \quad (1)$$

where $x \equiv (r - r_0)/r_0, y \equiv z/r_0, \theta$ is the azimuthal angle, n is the vertical field index, and m is the number of bumpy-torus field periods around the torus. $B_{z0}, B_{\theta 0}$, and δB_θ are constants.

Treating the self-fields of the beam by a simple cylindrical model, we find the equation of motion for a test particle

within the beam is, in the paraxial approximation, for $n = \frac{1}{2}$,

$$\begin{aligned} \frac{d^2\psi}{d\theta_m^2} + \frac{1}{m^2} [2 - 4n_z + b^2(1 + \epsilon \cos 2\theta_m)^2] \psi \\ = \frac{4}{m^2} \frac{\delta P}{P_0} \exp[(ib/2m)(2\theta_m + \epsilon \sin 2\theta_m)], \end{aligned} \quad (2)$$

where

$$\theta_m \equiv m\theta/2,$$

$$\psi \equiv (x + iy) \exp[(ib/2m)(2\theta_m + \epsilon \sin 2\theta_m)],$$

$$b \equiv B_{\theta 0}/B_{z0}, \quad \epsilon \equiv \delta B_\theta/B_{\theta 0}.$$

Here P_0 is the momentum of a particle which would circulate on the minor axis, δP is the "momentum error," $n_z \equiv \omega_b^2/(2\gamma_0^2 \Omega_{z0}^2)$ where ω_b, Ω_{z0} are the beam plasma frequency and the vertical field cyclotron frequency, respectively, and $\gamma_0 \equiv [1 + (P_0/mc)^2]^{1/2}$. We are interested both in the solution to the homogeneous part of (2), which will give orbital stability criteria, as well as in the solution to the inhomogeneous problem which will give the momentum compaction of the machine.

The quantity n_z , appearing in Eq. (2) describes the (net defocusing) effect of the self-electric and magnetic forces of the beam. Since it depends on beam density and therefore on the beam minor radius, n_z will in general vary with azimuthal angle θ around the device in a manner governed by the standard beam envelope equation. Consequently, when the beam envelope is stable, we expect n_z to behave as $n_z(\theta) \approx n_{z0} + n_{z1} \cos m\theta + \dots$ but we shall assume here, for simplicity, that $\epsilon b \gg n_{z1}$ so that, in (2), n_z may be adequately approximated by its average value.

Equation (2) is a Hill equation, which has characteristic bands of stability, as shown in Fig. 1. The boundaries of the stable regions have been obtained numerically, using standard methods.⁶ The shaded regions in the figure are unstable portions of the plane, ϵ vs b/m , for the case $n_z = 30$ and $m = 30$. The intersections of the unstable regions with the abscissa are given by

$$(b^2 + 2 - 4n_z)/m^2 = q^2, \quad \text{where } q = 0, 1, 2, \dots,$$

which is the condition that the transverse rotation frequency of a particle within the beam is an integer multiple of the "focusing frequency," $m\Omega_{z0}$ —a condition which allows res-

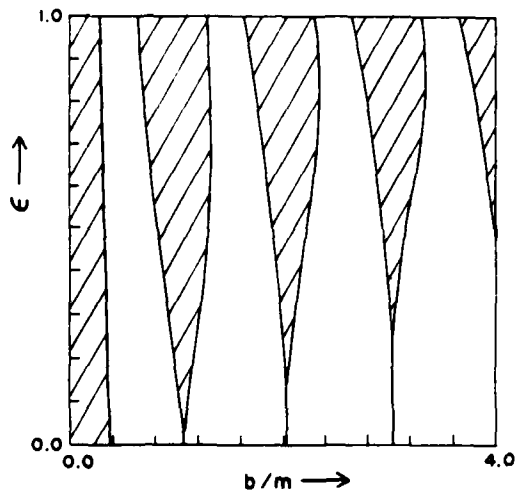


FIG. 1. Stability plane for the bumpy-torus betatron, for the case $n_s = m = 30$. The shaded regions are unstable for particle motion.

onant transfer of energy from the longitudinal to transverse degrees of freedom and, consequently, exponential growth of the betatron oscillation amplitude.

As B_z is increased during acceleration, one typically would not wish to increase B_θ simultaneously since this would require significant additional energy storage. The result is that the operating point of the accelerator will move right to left in Fig. 1. Consequently, the accelerator should be run in the left-most stable band to avoid crossing unstable bands. These considerations require $m > b$ at injection and force the use of a large number of field periods in the design of the focusing system. The left-most unstable band, corresponding to $q = 0$, is due to beam space-charge and rapidly disappears during acceleration since the self-field index n_s is proportional to γ_0^{-3} , where γ_0 is the relativistic factor. The left-most stable band, therefore, becomes broader during acceleration; the first stable band is at its most narrow at injection, when γ_0 is smallest.

We next consider the important question of containment of particles whose average momentum is not matched

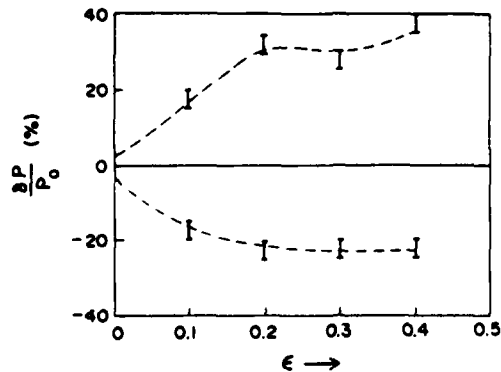


FIG. 2. Single particle bandwidth. Data points indicate the maximum value of momentum mismatch tolerated by the device versus the bump size ϵ for particles initialized on the minor axis, for the specific case $B_{\theta 0} = 118$ G, $B_{z 0} = 2$ kG, $r_0 = 100$ cm, $m = 30$.

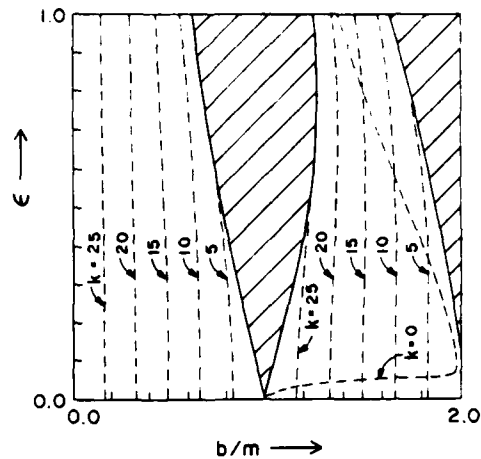


FIG. 3. Stability plane for bumpy-torus betatron with the single particle resonance lines $k = 0, 5, 10, 15, 20, 25$, indicated for the case $n_s = 0$, $m = 30$.

to the vertical betatron field, i.e., the question of the momentum compaction of this configuration. In order to address this question we have examined numerically the behavior of single particle orbits, neglecting beam self-fields but employing the full Bessel function representation of the $l = 0$ focusing field. Figure 2 shows the allowed mismatch, $\delta P/P_0$, plotted against $\epsilon \equiv \delta B_\theta/B_\theta$ for $B_{\theta 0} = 2$ kG, $B_{z 0} = 118$ G, $n = \frac{1}{2}$, $r_0 = 100$ cm, and $m = 30$. This plot is generated numerically by launching particles on the minor axis in the toroidal direction with various amounts of mismatch. The figure shows the largest mismatch for which the calculated orbits are contained in a 10 cm minor radius chamber. Containment of particles with a mismatch of $\pm 20\%$ is obtained for $\epsilon \approx 0.2$. We stress that the momentum compaction of this configuration is due to the alternating gradient field of the "bumps," though the phase shift per period is dominated by the average value of the toroidal field. Using Eq. (2), with $n_s = 0$, a perturbative calculation valid for small values of ϵ , of the momentum compaction factor, gives

$$\frac{\delta r/r_0}{\delta P/P_0} = 2 \left[1 - \left(\frac{\epsilon m b}{2} \right)^2 \frac{1}{m^2 - b^2} \right], \quad (3)$$

which holds only for $m > b$. One sees in (3) the helpful effect of a bumpy torus field.

In conventional betatrons, resonances are automatically avoided by increasing the particle momentum and the vertical magnetic field in synchronism. The introduction of nonsynchronous fields (a fixed toroidal field, for example) makes the betatron wavelengths energy dependent, which can lead to the crossing of resonances driven by field errors during acceleration. As in all strong focusing devices, the occurrence of orbital resonances plays an important role in the operation of the bumpy-torus betatron. Using the Floquet solutions to (2) (for $n_s = 0$) it is possible to obtain a condition for the integer resonances, when space-charge effects may be neglected:

$$\psi_l(\pi) = \cos \{ \pi [(b + 2k)/m] \}, \quad (4)$$

where $\psi_l(\theta_m)$ is the solution to (2) with $\delta P \equiv 0$ satisfying

$\psi_1(0) = 1$, $\psi_1'(0) = 0$ and where k is an integer, the Fourier component number of the dipole field error. Equation (4) provides the basis for a numerical calculation of contours in the stability plane on which (4) is satisfied for a given k ; an example is given in Fig. 3.

If all the fields cannot be made synchronous with the particle energy, the effects of orbital resonances might be minimized by making the energy gain per pass large. Other possibilities for coping with resonance crossings are currently under investigation.

In conclusion, we find the spatially alternating transverse magnetic field gradient associated with a bumpy torus leads to a potentially interesting strongly focused accelerator configuration which is seen to have a region of stable orbits, and to have a significant bandwidth in allowed mismatch between the vertical magnetic field and the particle momentum.

ACKNOWLEDGMENTS

We wish to acknowledge discussions with members of the Advanced Accelerator Project at the Naval Research Laboratory.

This work was supported by the Naval Research Laboratory.

¹Present address: Science Applications, Inc., McLean, Virginia 22102.

¹See, e.g., D. W. Kerst, in *Handbuch der Physik*, edited by S. Flügge (Springer, Berlin, 1959), Vol. XLIV, p. 13.

²E. P. Lee, A. Faltens, L. J. Laslett, and L. Smith, Proc. 1983 Particle Accelerator Conference, IEEE Trans. Nucl. Sci. NS-30, 2504 (1983).

³P. Sprangle and C. A. Kapetanacos, J. Appl. Phys. 49, 1 (1978).

⁴N. Rostoker, Comm. Plasma Phys. 6, 91 (1980).

⁵C. Roberson, A. Mondelli, and D. Chernin, Phys. Rev. Lett. 50, 507 (1983).

⁶W. Magnus and S. Winkler, *Hill's Equation* (Dover, New York, 1979).

APPENDIX C

DESIGN AND OPERATION OF A COLLECTIVE
MILLIMETER-WAVE FREE-ELECTRON LASER

Design and Operation of a Collective Millimeter-Wave Free-Electron Laser

ROBERT H. JACKSON, STEVEN H. GOLD, ROBERT K. PARKER, HENRY P. FREUND, PHILIP C. EFTHIMION, VICTOR L. GRANATSTEIN, MELVIN HERNDON, A. K. KINKEAD, JOHN E. KOSAKOWSKI, AND THOMAS J. T. KWAN

Abstract—A new free-electron laser experiment has been designed at NRL to operate at millimeter wavelengths using a collective beam-wave interaction. Critical features of the experiment include an apertured diode which provides a low-emittance electron beam, a wiggler magnet with adiabatic entrance and exit, and an operational domain centered around the wiggler-guide field gyroresonance. With the experiment configured as a superradiant amplifier, the effects of the gyroresonance on

beam dynamics and the beam-wave interaction have been studied. Measurements indicate a peak power production of 35 MW at 4 mm with an electronic efficiency of 2.5 percent. Aspects of the experimental design are discussed, and the results of a parametric study of the power dependence on the fields are presented. Detailed calculations (both analytic and computational) have been performed to analyze the linear and nonlinear effects in the experiment. The results of these calculations are shown to be in good agreement with laboratory measurements.

Manuscript received July 7, 1982; revised October 1, 1982. This work was supported by the U.S. Naval Air Systems Command Under Contract WF32-389-592, and by the U.S. Air Force Office of Scientific Research under contract to North Carolina State University.

R. H. Jackson was with North Carolina State University, Raleigh, NC 27650. He is now with the Mission Research Corporation, Alexandria, VA 22312.

S. H. Gold, R. K. Parker, H. P. Freund, P. C. Efthimion, V. L. Granatstein, A. K. Kinkead, and J. E. Kosakowski are with the Naval Research Laboratory, Washington, DC 20375.

M. Herndon was with the Naval Research Laboratory, Washington, DC 20375. He is now deceased.

T.J.T. Kwan is with Los Alamos National Laboratory, Los Alamos, NM 87545.

I. INTRODUCTION

THE free-electron laser has become the subject of intensive research because of its potential as an efficient, high-power source of continuously tunable coherent radiation. Essentially, the free-electron laser is a linear fast-wave device in which a signal wave is amplified at the expense of the axial kinetic energy of a codirectional relativistic electron beam through interaction with the periodic transverse field of a "wiggler" or pump magnet. The output wavelength is related to the wiggler period

by the approximate relationship $\lambda_o \approx \lambda_w/2\gamma^2$, where λ_o and λ_w are, respectively, the output wavelength and wiggler period and γ is the relativistic mass factor. This frequency upshift provides an obvious advantage for high-frequency power production.

Within the range of available electron beam and wiggler technologies, free-electron lasers can be designed such that the beam-wave interaction can be dominated by either single particle or collective effects. If the Debye length of the electron beam is less than the wavelength, collective effects dominate and the resultant three-wave parametric interaction is described as stimulated Raman scattering. This relationship leads to a requirement for a high electron density and a small spread in the axial velocity distribution of the electron beam. More specifically, the axial velocity spread must be much less than $\lambda_w\omega_p(\gamma-1)/4\pi\gamma\gamma_z^3$, where ω_p is the invariant plasma frequency, $\gamma = (1-\beta^2)^{-1/2}$, $\beta = v/c$, $\gamma_z \equiv (1-\beta_z^2)^{-1/2}$, $\beta_z = v_z/c$, c is the speed of light. In practical terms, this constraint means that considerable care must be taken to control the beam emittance if intense beam experiments conducted at millimeter and submillimeter wavelengths are to exhibit wave-wave scattering.

When collective effects are dominant, positive gain is achieved when the pump-shifted, negative-energy, space-charge wave is synchronous with an appropriate waveguide mode. The primary advantage of wave-wave scattering is that it offers significantly higher gain and intrinsic electronic efficiency than can be obtained with wave-particle (Compton) scattering. The higher gain of the collective interaction is sufficient to make amplifier operation practical. Calculations based on an idealized model [1] indicate that electronic efficiencies in excess of 10 percent and power exponentiation lengths of several centimeters are achievable at millimeter wavelengths.

Critical performance features predicted for the collective interaction have not been demonstrated in previous experiments. Although exceptionally high peak powers have been reported, the corresponding gains and efficiencies have been comparatively low. In an early stimulated scattering experiment conducted at NRL [2], a superradiant output of 1 MW at 0.4 mm was generated with an approximate efficiency of 10^{-3} percent using an electromagnetic pump wave. A subsequent oscillator experiment [3] with a magnetostatic pump produced a comparable peak power at the same frequency with an efficiency of 3×10^{-3} percent. In other experiments, peak powers of 8 MW at 1.5 mm and 20 MW at 11 mm with corresponding efficiencies of 0.2 percent and 0.3 percent have been reported [4], [5].

Recent computational analysis of the electron flow in the cold-cathode diodes typically used in these experiments has indicated that poor beam quality likely had a strong influence on observed performance [6]. Recognition of the constraints on beam quality led to the assembly of a new experimental configuration designed to study the Raman interaction at millimeter wavelengths [7]. With this apparatus, the combined effects of the axial guide and helical wiggler magnetic fields on the electron dynamics and the beam-wave interaction have been studied in initial experiments. These effects are of interest because a significant gain enhancement can be obtained near the gyroresonance which occurs when the electron transit

time through a wiggler period corresponds to one cyclotron period.

II. EXPERIMENTAL APPARATUS

A. Experimental Configuration

For these studies, the VEBA pulse-line accelerator was modified [8] and interaction parameters were selected to ensure a collective interaction. Computational analysis produced an injection diode design [9] which provided significantly improved beam quality. As shown in Fig. 1, the diode was formed by locating a cylindrical graphite cathode with hemispherical tip at a distance of 1 cm from a shaped graphite anode. A 6 mm diameter aperture in the anode plate was used to collimate the injected beam. Electrode contours were derived computationally to provide radial force balance for near-axis electron trajectories. With this design, the axial velocity spread of the beam injected through the aperture was reduced to less than 0.1 percent, which corresponds to a normalized beam emittance of 30π mrad · cm.

The pump wave was a right-hand circularly polarized magnetostatic field produced by a 63 cm long bifilar helix of 3 cm periodicity. The bifilar helix consisted of two coils of copper magnet wire with four layers per coil wound on a grooved nylon form. To prevent perturbation of the beam, a gradual transition into the wiggler field was necessary. A 21 cm transition region was provided by flaring the radius of the helical windings along a circular arc while keeping the period of the windings constant. The windings were joined at the end of the flare by wrapping alternate layers in opposite directions around the nylon form. This counter-winding reduced the magnetic field perturbation caused by the termination of the windings. The measured and calculated [10] fields in the taper are shown in Fig. 2. With the exception of field values near gyroresonance, the adiabaticity condition was well satisfied by the transition field as discussed in the section on theory. In addition, a 15 cm adiabatic exit from the wiggler was provided to reduce possible RF noise production resulting from unnecessary perturbation of the beam.

The initial experiments were conducted with the device configured as a superradiant, or noise, amplifier. With 1.35 MV applied to the diode, a 1.5 kA electron beam of 60 ns duration was extracted through the anode aperture and propagated through a tapered-wall transition into a cylindrical stainless steel waveguide of 1.1 cm inner diameter. The axial magnetic field was held constant from behind the cathode to beyond the interaction space and was variable up to 20 kG. The wiggler field was variable from 0.1 to 4 kG. With this selection of parameters, the beam axial velocity spread had to be much less than 0.5 percent for collective effects to dominate the interaction.

To provide temporal isolation from reflected signals, the radiation diagnostics were separated from the interaction space by a 5 m length of waveguide. The principal radiation diagnostic was a Laser Precision KT 1540S pyroelectric detector which provided a time dependent measure of radiated power. Absolute integrated power measurements were made using a pyramidal millimeter-wave calorimeter [11] constructed at the labora-

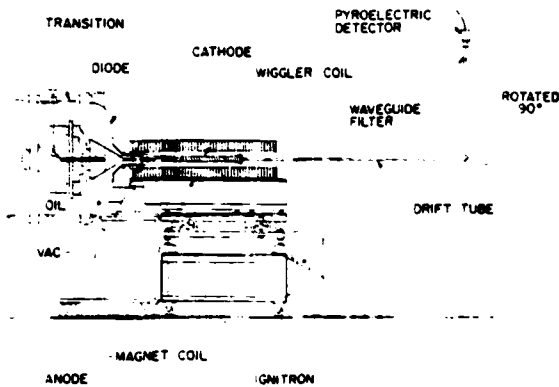


Fig. 1. Experimental setup for superradiant millimeter-wave Raman free-electron laser.

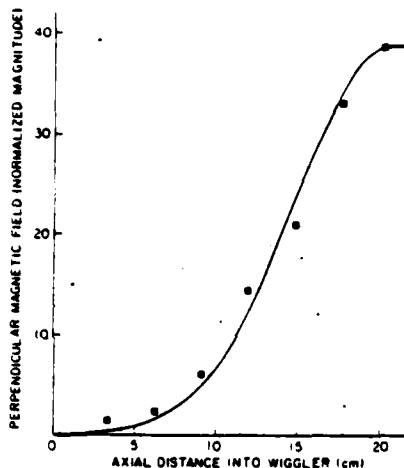


Fig. 2. The on-axis wiggler field profile in the 21 cm adiabatic entrance of the bifilar helix. The solid curve is based on the equations in [10], and the squares are the normalized measurements.

tory. Spectral information was obtained by sequentially placing a series of high-pass filters in front of the detector. The high-pass filters were cutoff waveguides of two mechanical designs, both fabricated from aluminum cylinders. The filter designs used either a single axially located hole with tapered entrance and exit or symmetrical arrays of constant diameter holes.

For these experiments, the beam-wave interaction parameters were chosen such that the pump-shifted negative-energy space-charge wave would couple with the fundamental TE_{11} mode of the cylindrical waveguide. An overlay of the uncoupled beam and waveguide dispersion curves shows that two intersections with the forward wave are possible. Primary interest is centered on the upper intersection, which produces a large relativistic upshift. In the limit $\beta_1 = 0$ ($\beta_1 = v_1/c$), this intersection occurs at about 180 GHz, while the lower intersection is about 20 GHz. The effect of increasing the wiggler field is to increase β_1 while simultaneously decreasing the axial velocity β_2 . This shifts the upper intersection to lower frequencies (and the lower intersection upwards), until coupling is lost at ≈ 60 GHz for $\beta_1 \approx 0.34$. To block the transmission of any low-frequency power not associated with the upper intersection, a 5 mm (60 GHz) high-pass filter was inserted near the detector.

B. Diode Design

Theory places severe constraints on the quality of an electron beam for collective processes to dominate the beam-wave interaction. Computational analysis of the foil-less diodes used in previous experiments has shown that the beams taken as a whole did not satisfy the theoretical quality requirement, although in some cases layers within a beam were cold enough to permit marginal collective interaction [6]. Furthermore, the analysis indicated that there are inherent problems in obtaining high-quality beams in foil-less diode geometries. Two alternative designs were considered: injection through an anode foil and a collector anode with a beam extraction aperture. The use of an anode foil was considered to be unattractive because of consequent beam scattering in the foil, the necessity for replacement of foils after every shot, and resultant beam pinching in the diode. Analytic and computational analysis of the apertured diode indicated that this approach could provide the required beam quality.

The apertured diode was designed using a modified version [11] of the SLAC Electron Optics Code [12]. The objective was to produce paraxial electron flow in the diode near the axis by shaping the electrode surfaces to provide a radial electric field to balance the pinching effects of the beam self B_θ field. Since the cathodic electric fields were too high to control the emitting surface, it was necessary to collect the excess current (≈ 90 percent) and allow only the cold, near-axis portion of the beam to propagate into the interaction region. The final diode design, along with the computed electron trajectories, is shown in Fig. 3. In this design the cathode was a graphite cylinder with a hemispherical tip. To keep the emitting surface small and the diode impedance high, the cathode tip had a radius of curvature of 2.5 cm on the face and 0.5 cm on the edge. The anode was a graphite disk with a 10° conical depression and a 6 mm diameter aperture on axis. The aperture was extended 15 cm into the interaction region with a gradual taper to the 11 mm diameter of the cylindrical waveguide. Because the 1 cm diode gap was sensitive to voltage prepulse [13], a dielectric surface-flashover switch [11] was installed in the cathode shank. The switch eliminated prepulse problems and, in addition, sharpened the voltage rise time. The reduced rise time enhanced the formation of a homogeneous, uniformly expanding cathode plasma, and thereby acted to preserve the basic diode geometry. The importance of eliminating prepulse problems was illustrated by two experimental observations. First, when a prepulse current occurred, the beam noise (no wiggler) in W -band jumped by more than an order of magnitude. Secondly, with the wiggler field, power output was greatly reduced when even small prepulse currents occurred. These observations indicate a reduced beam quality when the cathode plasma formation is not rapid and uniform.

The calculated trajectories shown in Fig. 3 represent the electron flow expected for a guide field of 10 kG and an applied voltage of 1.5 MV. The "grid" in the figure is a computational device used to give a physically meaningful boundary condition to the electron emission from the cathode shank while avoiding the problems of resolving the crossed-field flow. The net effect of the applied and self-generated fields is to produce an elec-

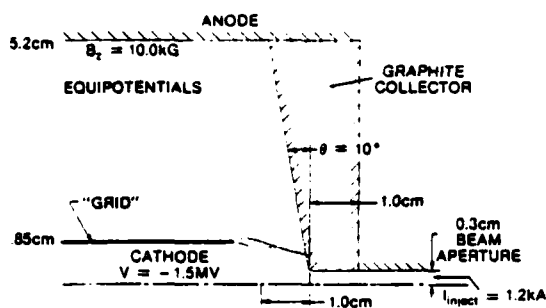


Fig. 3. The VEDA apertured diode with the calculated electron trajectories (only half of the trajectories are shown). Note the paraxial flow close to the axis between the cathode and anode, and the defocusing effect of the aperture.

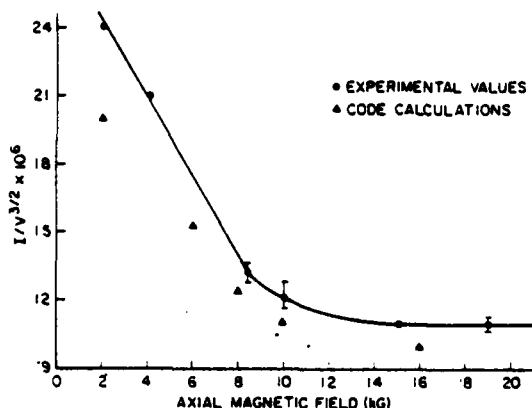


Fig. 4. Perveance of the apertured diode as a function of axial guide field.

tron flow near the axis which exhibits little radial motion until the aperture is reached. The radial electrostatic fields created by the aperture then act to defocus the beam and produce a small, coherent radial oscillation in the extracted beam. Results from these calculations indicated that beams with less than 0.1 percent axial velocity spread could be produced with the apertured diode configuration.

Where possible, code results were compared with laboratory measurements to validate the calculations. In comparing the calculated and experimental values, it should be noted that the code dealt with the "cold" geometry, whereas the effective cathode in the experiment was an expanding plasma. The initial comparisons were made with respect to two parameters which describe the macroscopic properties of the electron flow in the diode. These parameters are the diode perveance [14] and the current transmitted through the aperture. The perveance is calculated from the total diode current and voltage and is shown in Fig. 4 as a function of the axial guide field. The decrease in perveance with increased guide field indicates a change in the effective diode geometry. The observed reduction results from the restricted radial expansion of the electron trajectories and the cathode plasma at the higher fields. At low guide fields where the entire diode gap decreases, the difference between the computed and observed perveance can be used to estimate the plasma expansion velocity. For the values at 2 kG, this gives an expansion velocity of 2-3 cm/ μ s which is in good agreement with previous measurements [15].

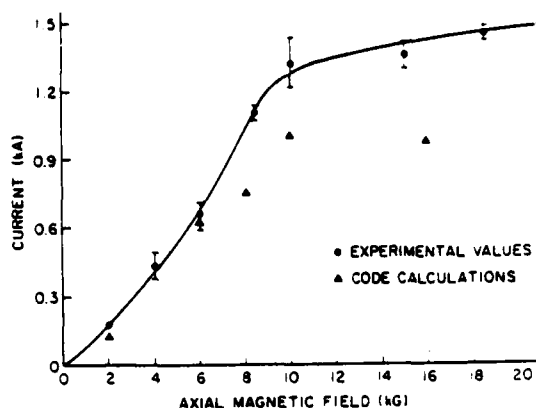


Fig. 5. The current transmitted through the diode aperture as a function of axial guide field.

As the magnetic field is increased, the cathode plasma does not continue to expand at the same rate in all directions. However, the field strength should have no effect on the axial expansion at the cathode face. The effect of cathode expansion on extracted current is apparent in Fig. 5. At the higher magnetic fields, the plasma expansion velocity derived from these values is also consistent with a 2-3 cm/ μ s expansion velocity. Plasma expansion at the lower field levels (< 8 kG) does not show as large an effect because the current is limited by aperture defocusing and not by the available current.

C. Beam Quality Measurements

When corrected for plasma expansion, the predicted values of diode perveance and transmitted current are in excellent agreement with experimental measurements. Although the comparison of macroscopic features provides a tentative verification of the computed results, the more critical issue is the velocity distribution within the transmitted beam. In general, experimental measurement of the velocity distribution within an intense, relativistic electron beam is extremely difficult. However, using the special properties of the apertured diode, a simple method was devised to experimentally verify the code results. For these measurements, the 6 mm diameter anode aperture was extended by 15 cm with a uniform diameter drift tube which terminated in a Faraday cup. The perpendicular velocity of electrons at the beam edge was then calculated by comparing the transmitted current at a given value of axial magnetic field (Fig. 5) with that estimated for an infinite field. The axial velocity spread was then derived from the beam-edge transverse velocity. This analysis requires that the cathode tip emission density and the electron guiding center radius be independent of the axial field, and that the beam be monoenergetic. Analysis of results computed at several values of the guide field indicates that these conditions were well satisfied. In addition, a uniform beam density is assumed, although this method could still be used if the density profile were known. Code results and experimental damage patterns have shown that the assumption of a uniform beam was a good approximation.

The relationship between transmitted current and axial velocity spread was derived as follows. In the limit of an in-

finite field, the electron Larmor radius is zero. As the field is reduced, the electron guiding center remains unchanged, but the Larmor radius becomes finite. Only those electrons for which the sum of the Larmor and guiding center radii is less than the aperture radius can be propagated. The current ratio is therefore given by

$$I(B_o)/I(\infty) = (r_w - r_L)^2 / r_w^2 \quad (1)$$

where r_w and r_L are, respectively, the drift tube wall and Larmor radii, B_o is the axial guide field, and $I(\infty)$ is the transmitted current in the limit of infinite magnetic field. When solved for the perpendicular velocity, this expression becomes

$$\beta_{\perp} = \{1 - [I(B_o)/I(\infty)]^{1/2}\} e B_o r_w / mc^2 \gamma. \quad (2)$$

Numerical analysis of electron trajectories in the diode and drift tube verifies this prediction of the electron perpendicular velocity at the beam periphery. The axial and transverse velocity spreads are related as follows:

$$\Delta\beta_z/\beta_z \approx (\Delta\beta_{\perp})^2/2\beta^2 \approx [\beta_{\perp}(r_w)]^2/4\beta^2. \quad (3)$$

With this relationship, the transverse velocity at the beam periphery can be used to estimate the axial velocity spread. As seen in (2), a measure of $I(\infty)$ is required to complete the estimate. As a lower bound, the transmitted current at 20 kG was measured to be 1.5 kA. The Child-Langmuir current, when corrected for cathode plasma expansion, serves as a reasonable upper bound and is 1.8 kA for this diode geometry. When the applied axial field was set at 10 kG, the transmitted current was 1.3 kA. The resultant beam conditions are estimated, therefore, to be within the following range:

$$0.033 \leq \beta_{\perp}(r_w) \leq 0.072$$

and (4)

$$3 \times 10^{-4} \leq \Delta\beta_z/\beta_z \leq 1.4 \times 10^{-3}.$$

For comparison, the computed value for $\Delta\beta_z/\beta_z$ was 9.5×10^{-4} at 10 kG. Even at the upper limit, the beam axial velocity spread is well below that required for collective effects to dominate the interaction. To place this achievement in proper perspective, it should be noted that these velocity spreads are more than an order of magnitude less than those typically associated with electron beams of this intensity.

III. THEORY

The analysis of the beam-wave interaction in a millimeter-wave free-electron laser is a complex endeavor requiring not only a linear theory to illuminate the interaction physics and to predict gain but also a nonlinear analysis to examine saturation effects and efficiency. To make the linear analysis more tractable, several simplifying assumptions are usually imposed on the model. In the linear theory which follows, a cold electron beam and an ideal helical wiggler field are assumed. Because of the complexity of the saturation phenomena, the nonlinear analysis was performed using a fully electromagnetic numerical simulation of the interaction. Although the code did provide the desired nonlinear capability, the provision for only one spatial dimension limited the analysis to the idealized wiggler fields. To assess the consequences of this limitation in

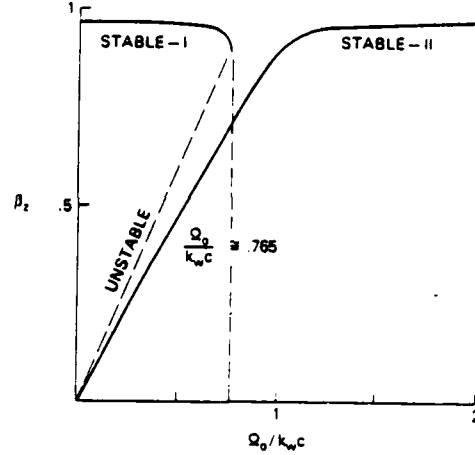


Fig. 6. The two types of stable orbits possible in an ideal wiggler field. The axial velocities are shown as a function of normalized guide field. Note that the Type I orbits become unstable at $\Omega_o/k_w c \approx 0.765$.

the linear and nonlinear analysis, the effects of the realistic wiggler fields were investigated with a multiparticle trajectory code. Using this code, the impact of the wiggler field gradients on the velocity spreads of an initially cold beam were studied as a function of the pump strength and the proximity of the guide field to gyroresonance.

A. Linear Analysis

Recent theoretical work [16], [17], [18] has shed light on the collective interaction in the presence of an axial guide field by perturbation methods about equilibrium orbits. For combined axial guide and helical wiggler magnetic fields, two classes of stable helical equilibrium orbits exist [19], [20] with constant velocity v_z and transverse velocity

$$v_{\perp} = \Omega_o v_z / (\Omega_o - \gamma k_w v_z) \quad (5)$$

where $\Omega_o, \omega \equiv eB_o, r/mc$, $k_w = 2\pi/\lambda_w$, and B_o and B_r are the axial and transverse magnetic fields (see Fig. 6). Group I orbits occur at low values of the guide field ($\Omega_o < \gamma k_w v_z$) and exhibit high v_z which decreases monotonically with increasing B_o . Such orbits become unstable at a critical value of axial field given by $\Omega_o = \gamma(1 + (v_{\perp}/v_z)^2)^{-1} k_w v_z$. Group II trajectories exist for all B_o but exhibit high axial velocities only when $\Omega_o > \gamma k_w c$. The growth rate in the limit of stimulated Raman scattering is given by

$$(\text{Im } k)_{\text{max}} \approx 1/2 |\beta_{\perp}| (\omega_p k_w \gamma_z \Phi^{1/2}/v_z)^{1/2} \quad (6)$$

where ω_p is the invariant plasma frequency, and

$$\Phi \equiv 1 - \Omega_o \gamma_z^2 v_{\perp}^2 / [(v_z^2 + v_{\perp}^2) \Omega_o - \gamma k_w v_z^3]. \quad (7)$$

Note that the presence of the axial guide field leads to gain enhancement both by increasing the transverse velocity and through Φ , which comes from the ponderomotive potential. In the limit of zero beam temperature, the Raman regime is valid as long as

$$\omega_p \Phi^{1/2} \gg \frac{1}{8} \beta_{\perp}^2 \gamma_z^3 \frac{v_z^2}{c} k_w. \quad (8)$$

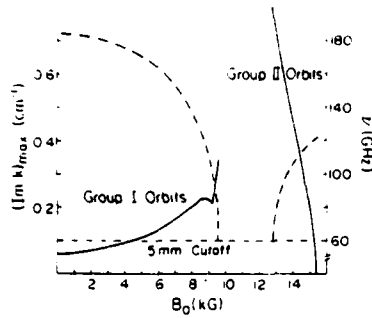


Fig. 7. Calculation of gain (solid lines) and emission frequency (dashed lines) as a function of axial magnetic field for $B_p = 0.63$ kG. The experimental 5 mm cutoff is shown as a horizontal dashed line. Note that below gyroresonance the gain curve is much flatter than above the resonance.

Therefore, the Raman regime, in this limit, is accessible even for lower beam densities when an axial field is present and Φ is large. The strong pump regime occurs in the opposite limit and is characterized by a maximum growth rate of the form

$$(\text{Im } k)_{\text{max}} \approx \frac{\sqrt{3}}{2} \left(\frac{\beta_1^2}{2} \xi^2 \frac{c}{v_z} \Phi \right)^{1/3} k_w \quad (9)$$

where $\xi \equiv \omega_p / ck_w$ is the beam strength parameter.

A calculation of the maximum gain as a function of B_0 for parameters corresponding to the experiment ($\gamma \sim 3.5$, $B_p \sim 0.63$ kG), using the results of the complete stability theory, is shown in Fig. 7. The dashed line in the figure represents the frequency corresponding to peak gain, and the calculation has been performed only for frequencies greater than the 60 GHz cutoff imposed experimentally. As anticipated, the growth rate increases as the gyroresonance ($\Omega_0 \sim \gamma k_w v_z$) is approached from above or below. The apparent discontinuity shown in the growth rate for Group I orbits at $B_0 \sim 9$ kG corresponds to a transition from a Raman to a strong pump interaction [1]. For guide fields below this value, as well as for Group II trajectories, the gain is given predominantly by the Raman-scattering result. It is important to recognize, however, that nonlinear (saturation), finite geometry, and nonideal effects are not included in these calculations. As a result, Fig. 7 cannot be used to predict the detailed variation in the output power with B_0 , and can only be used to obtain the parametric limits of radiation production and to estimate the small-signal gain.

B. Nonlinear Simulation

The effects of beam temperature on the saturated efficiency of the experiment were studied with a fully electromagnetic, relativistic particle code [21] which included one spatial and three velocity components. Although the electron beam was assumed to be monoenergetic, the electrons were allowed to have random velocities in the directions perpendicular to the beam propagation. Such a scattered electron beam can be modeled according to the momentum distribution function

$$f(p) = \delta(p - p_0) \exp(-p_\perp^2 / \Delta p_\perp^2) / [p_0 \Delta p_\perp F(p_0 / \Delta p_\perp)] \quad (10)$$

where $F(x) = \exp(-x^2) \int_0^x \exp(t^2) dt$, p is the particle momentum, $p_0 = mc(\gamma^2 - 1)^{1/2}$, and Δp_\perp is the FWHM of the perpen-

dicular momentum distribution. For this distribution the spread in axial velocity is given by

$$\frac{\Delta \beta_z}{\beta_z} \approx \frac{1}{2} \left(\frac{\Delta p_\perp}{p_0} \right)^2 \quad \text{for} \quad \frac{\Delta p_\perp}{p_0} \ll 1. \quad (11)$$

The velocity spread produced by (10) represents a true, random temperature, unlike the experimental value which represents the radial dependence of the velocity distribution. The exact correspondence between these types of velocity spread is unclear; however, they are expected to have similar effects on the beam-wave interaction.

Electron beams with a momentum distribution given by (10) were initialized self-consistently in the simulations. The simulations had an immobile ion background to provide the necessary electrostatic neutralization and periodic boundary conditions for the electromagnetic fields and the beam particles. The simulation parameters were chosen to match experimental values to the degree possible.

The dependence of the efficiency of energy transfer from the electron beam to the RF wave is illustrated in Fig. 8. The striking result is that the efficiency drops dramatically when the momentum spread increases slightly from 0 to 0.65 percent. However, after the initial sharp drop, it becomes rather insensitive to the spread. It should be noted that the efficiency, as shown in Fig. 8, takes into account the energy of all unstable electromagnetic modes. This rather surprising result from the simulations shows a completely different nonlinear behavior for the free-electron laser interaction than might be expected from the effects of momentum spread on the saturation by electron trapping of the relativistic two-stream instability [22].

The simulations are considered to be accurate representations of the experiment provided that three-dimensional effects are not dominant, and that the code electron beam adequately models the experimental beam. For a beam with the velocity spread observed in the experiment (≈ 0.1 percent), simulations predict an efficiency of roughly 2 percent. This value is remarkably close to the 2.5 percent peak efficiency observed in the experiment. Because of the previously mentioned differences between the simulations and the experiment, some caution should be exercised in applying the code results to interpret the experiment. Nonetheless, the good agreement between the experiment and the simulations is noteworthy, and supports the beam quality calculations and measurements discussed earlier.

As shown in the experimental results section, there are definite combinations of the wiggler and guide magnetic fields which determine the onset, maximum, and cutoff of radiation production. The spatial evolution of the electromagnetic radiation for three sets of experimental parameters which correspond to these conditions is shown in Fig. 9. At radiation onset, the simulation shows that the linear growth rate of the instability was so small that the electromagnetic energy could not achieve an appreciable amplitude within the length of the wiggler. Thus, a change of magnitude of the wiggler field and/or the guide field to enhance the transverse velocity of the electron beam would increase the output of radiation. This is illustrated

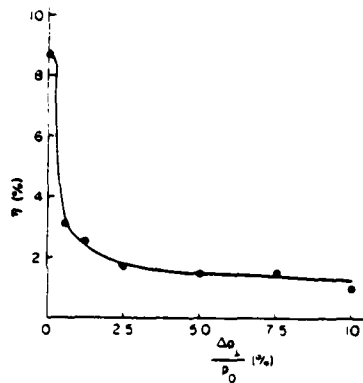


Fig. 8. Electron-beam-power to RF-power conversion efficiency as a function of momentum spread. The 0.1 percent velocity spread observed in the experiment corresponds to a momentum spread of 4.5 percent [see (11)].

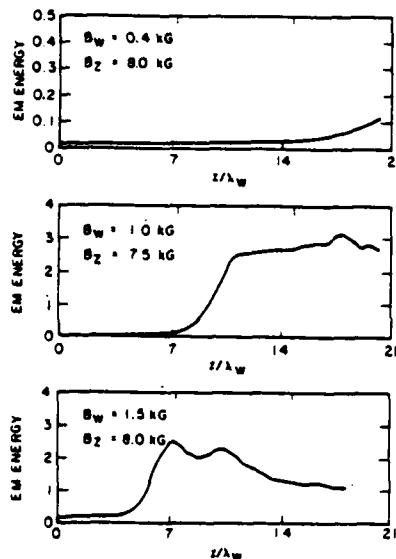


Fig. 9. Spatial growth of electromagnetic energy for field values corresponding to the onset, maximum, and cutoff of power in the experiment. The axial distance is normalized by the wiggler period ($2w = 3$ cm), and the simulations start in the uniform wiggler section.

in the second case in Fig. 9. The electromagnetic energy saturated at a high level at about two-thirds of the wiggler length. The fact that the electromagnetic energy did not decay away as the electron beam continued to interact with the wiggler field indicates that the coherence of the electron bunching was not destroyed. Consequently, the electron beam could still deposit energy into other unstable electromagnetic modes. The third case shown in Fig. 9 had the highest wiggler field, and showed a strong linear growth of the instability. However, the instability saturates in a relatively short distance, and the total electromagnetic energy decays due to strong wave-particle interaction. As a result, the emitted power is significantly reduced.

C. Realistic Wiggler Effects

Neither the linear analysis nor the nonlinear simulations took into account the beam transition into the wiggler and the

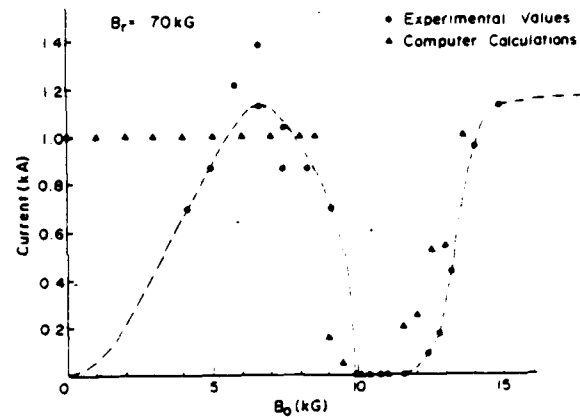


Fig. 10. Transmitted current at the wiggler exit as a function of axial guide field.

spatial variation of the actual wiggler field. To evaluate these effects, a multiple-particle trajectory integration code was developed and used to study beam propagation in the first-order wiggler fields and in a finite geometry waveguide [23]. A comparison of calculated and measured current transmitted through the wiggler is shown in Fig. 10 for an effective wiggler field of 0.7 kG. Since the initial current in the code is normalized to 1 kA and diode phenomena which affect the injected current (see Fig. 5) are not included, a superficial disagreement exists for fields less than 6 kG. With that exception, the agreement is excellent, and the features predicted by the idealized wiggler orbit theory are clearly present. The rapid decrease in current at 9.5 kG results from current loss to the waveguide wall as the Group I orbits become unstable at the critical value of axial magnetic field. Increased propagation in Group II orbits is seen above 11.5 kG as the wall losses progressively decrease.

The wiggler used in the experiment was designed to provide an adiabatic entrance for the beam (see Fig. 2). Calculations incorporating the experimental wiggler profile indicate that the transition is adequate, but not perfect. As a result, the electrons in the uniform section of the helix oscillate about the ideal equilibrium orbits. At modest pump levels and for fields far from resonance, the oscillations are small; however, as gyroresonance is approached or as the pump level is increased, the amplitudes of the oscillations increase dramatically. This velocity oscillation can act as an effective temperature because of the slippage between the beam and the RF wave as the wiggler is traversed.

The spatial variation of the first-order wiggler field induces a cross-sectional velocity spread. The magnitude of this spread depends upon the beam area, wiggler period, pump amplitude, proximity to gyroresonance, and whether the axial field is above or below the "transition" field of the wiggler. The transition field is given by

$$B_T = \frac{mc^2}{e} \gamma k_w (\beta_z^2 + \beta_1^2)^{1/2} \quad (12)$$

and represents the axial field above which the denominator of (5) cannot be driven to zero for any value of pump field. The dependence of the velocity oscillation and the velocity spread

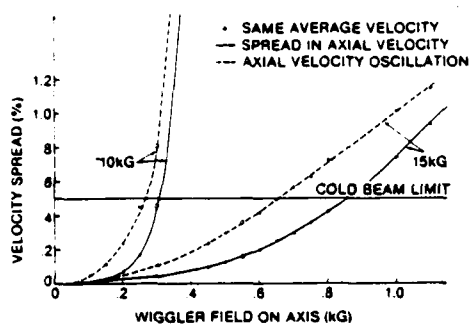


Fig. 11. The two types of velocity spread induced by the actual wiggler field. The solid curves show the cross-sectional velocity spread due to the field gradients and the dashed curves are the velocity oscillations induced by the adiabatic entrance. The 10 kG curves are below, and the 15 kG curves are above the 12 kG transition field of the experiment. The cold beam limit is derived from the theoretical expression $(\gamma - 1)\omega_p/2\gamma^3 c k_w \gg \delta\beta_z$.

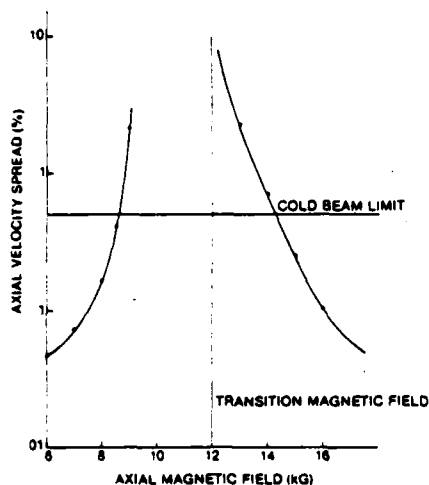


Fig. 12. Axial velocity spread induced by first-order wiggler field gradients near gyroresonance. The wiggler field amplitude is the same as in Fig. 10, $B_p = 0.70$ kG.

on pump strength is shown in Fig. 11 for guide fields above (15 kG) and below (10 kG) the transition field. Note the striking difference in the behavior between the two cases as the pump level approaches a critical value at which the orbits become unstable. The open circles on the graph indicate field values at which the beams have the same average velocity. In general, the code results show that for beams with the same average velocities, operation below the transition field or closer to gyroresonance leads to larger velocity spreads.

The effects of operating near gyroresonance are shown in Fig. 12. Since the resonant denominator in (5) acts to enhance the effects of field differences, the beam becomes more sensitive to field variations near the gyroresonance. This rapid beam thermalization near gyroresonance will act at some point to offset the effects of increased v_1 in producing an enhanced gain. The cold-beam limits shown in Figs. 11 and 12 indicate the ranges of field strengths where this is likely to occur. Experimentally, peak RF emission occurs in the regions before the cold-beam limit is reached (cf. Fig. 13). The effect of these velocity spreads on the interaction is not clear, because the

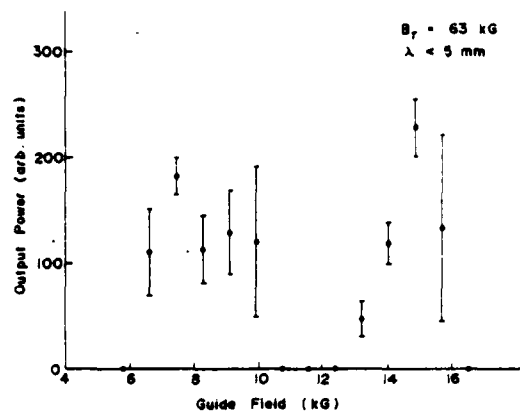


Fig. 13. Measured variation in output power ($\lambda < 5$ mm) with guide field for $B_p = 0.63$ kG. The error bars represent the shot-to-shot reproducibility of the experimental parameters and are based on five or more shots.

spreads are not random. However, at some level, these macroscopic spreads are expected to degrade the interaction in a manner similar to a true temperature.

IV. EXPERIMENTAL RESULTS

A plot of radiated power as a function of axial field strength is shown in Fig. 13 for the interaction parameters used in Fig. 7. This radiated power profile represents a complex overlay of interactive phenomena of which three are thought to dominate. The primary issues are the quality of the injected beam (Figs. 5 and 10); the three-dimensional effects of the wiggler fields on the electron trajectories (this effect is most pronounced near gyroresonance, Figs. 10 and 12); and the variation of the gain with the experimental parameters (Fig. 5). The onset of measurable power at low guide field is related to the increase in transmitted current with increasing B_0 . The subsequent drop in power at 10 kG is consistent with the transition to unstable orbits and the rapid thermalization of the beam. Above gyroresonance ($B_0 \approx 11.5$ kG), the wavelength of the radiation produced by Group II orbits will decrease as the axial velocity is increased. The 5 mm cutoff imposed by the filter corresponds to the theoretically predicted value of $B_0 = 12.5$ kG which is in close agreement with the experimental value. The comparatively slow rise in radiated power from 12.5 kG to 15.0 kG is consistent with the progressive improvement in beam quality shown in Fig. 12. The decrease in power at higher values of B_0 corresponds to a loss of gain as shown in Fig. 7. Note that the power production below gyroresonance is not as peaked in guide field as above gyroresonance. This result is in agreement with the flatter gain curve in Fig. 7 and the more rapid beam thermalization shown in Fig. 12.

Data have been compiled over a range in pump field extending from 0.2 to 2.4 kG. The salient features of the observed parametric variation can be summarized by identifying the pump strength at which thresholds for measurable power and the point of maximum power occur as a function of the guide field. The resultant plot is shown in Fig. 14.

Rewriting (5) yields the following relation between the transverse and longitudinal electron velocities and the pump and guide fields.

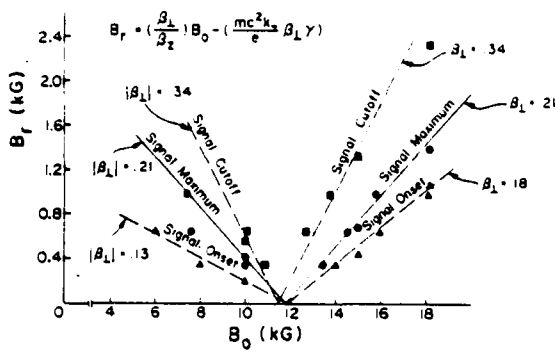


Fig. 14. Signal variation with pump and guide magnetic fields. Signal onset, maximum, and cutoff are plotted as triangles, circles, and squares, respectively. The lines correspond to constant values of β_1 .

$$B_r = (\beta_1/\beta_z) B_0 - (mc^2 k_w / e) \beta_1 \gamma. \quad (13)$$

From this equation, it is evident that the conditions for constant transverse and axial velocities are defined by pairs of straight lines which intersect the horizontal axis at the resonant guide field. The free-electron laser interaction is much more strongly dependent on these velocities than on particular values of magnetic field. Specific experimental features should lie on straight lines characterized by unique values of transverse velocity. Note that the lines in Fig. 14 are not best fits to the data, but are calculated using (13) assuming particular values of transverse velocity. The observed agreement between experimental results and calculations based on ideal single-particle trajectories is another indication that the electron beam is very cold.

The magnitude of the radiated power in the free-electron laser interaction is related through the gain to the transverse velocity and has only a weak dependence on the magnetic fields which occurs through $\Phi^{1/4}$ [see (6)]. The cyclotron maser instability, on the other hand, is sensitive to particular values of the guide field as well as the transverse velocity. Previous intense beam cyclotron maser experiments [24]–[28] have typically shown a power increase of two to three orders of magnitude at specific axial guide fields. In light of this, it is worth noting that the peak power observed along the $\beta_1 \approx 0.21$ lines in Fig. 14 is constant to within a factor of two for all the guide fields tested. The differences in peak power appear to be related to beam quality issues. The highest powers are observed above 15 kG where the injected beam quality is highest and the thermalization effects of the gyroresonance are minimized.

The measure of the constancy of β_z along the lines defined by (13) is the radiated wavelength. To examine this scaling, the wavelength of power generated at 15 and 18 kG was measured at the power threshold conditions of $\beta_1 = 0.18$ and $\beta_1 = 0.34$. The frequency was determined by observing the threshold for transmission through a sequence of high-pass filters. On the high β_1 threshold, the break in transmitted power occurred between cutoff frequencies of 63 and 68 GHz at both values of B_0 . The corresponding bounds for the low β_1 threshold were between 103 and 117 GHz. An analysis of the uncoupled dispersion curves for the pump-shifted,

negative-energy, space-charge wave and the TE_{11} waveguide mode indicates that the intersections of interest occur at 60 and 117 GHz, respectively. Wavelength measurements at the peak power points using both cutoff filters and a grating spectrometer indicate a frequency of 80 GHz which is also in agreement with the dispersion analysis. Independent measurements have established that the observed radiation pattern is consistent with that of the TE_{11} mode.

Calculations of spontaneous emission suggest that the uncorrelated noise spectrum corresponds to a few tens of milliwatts of radiated power. Direct measurement of the emission in the absence of a pump field shows less than 10 W of total power in the range of a W-band detector (60–110 GHz). Calorimetry measurements of the peak observed emission detect 0.68 J, corresponding to ~ 35 MW in a 20 ns output pulse and an instantaneous efficiency of 2.5 percent. This suggests at least fifteen power e -foldings, corresponding to a gain length of approximately 4 cm. Theory (Fig. 7) suggests a gain length of several centimeters, in good agreement with this value.

V. SUMMARY

Initial measurements on a new high-power, short-pulse, millimeter-wave free-electron laser experiment have been completed. These measurements have demonstrated high-power superradiant emission, corresponding to an instantaneous conversion efficiency of electron beam energy into millimeter-wave radiation of 2.5 percent. This efficiency is an order of magnitude improvement over that seen in other millimeter-wave free-electron laser devices. Computer simulations and experimental measurements have shown that the quality of the electron beam extracted from the apertured diode is well in excess of that required to sustain a collective beam-wave interaction. The experiment has shown a regular parametric dependence on guide and pump fields both above and below gyroresonance, a dependence that had not been previously reported. Measurements of radiation onsets and cutoffs agree with predictions based on single-particle orbits and a new cold-beam Raman theory. The observed scaling of wavelength, emitted power, and gain are in excellent agreement with the assumption of a Raman free-electron laser interaction. Computer simulations of the nonlinear effects in the experiment show good agreement with the power scaling and efficiency observed in the experiment. The simulation results taken together with the realistic wiggler analysis indicate that thermal effects are limiting the experimental efficiency. It is not yet known whether this limit is imposed by the injected beam quality, the wiggler gradients, or by some other mechanism.

ACKNOWLEDGMENT

The authors would like to thank L. Friedland, P. Sprangle, A. Drobot, L. Thode, and C. Snell for useful discussions.

REFERENCES

- [1] P. Sprangle, R. A. Smith, and V. L. Granatstein, "Free electron lasers and stimulated scattering from relativistic electron beams," in *Infrared and Millimeter Waves*, vol. 1, K. J. Button, Ed. New York: Academic, 1979, p. 279.

- [2] V. L. Granatstein and P. Sprangle, "Mechanisms for coherent scattering of electromagnetic waves from relativistic electron beams," *IEEE Trans. Microwave Theory Tech.*, vol. MTT-25, p. 545, 1977.
- [3] D. B. McDermott, T. C. Marshall, S. P. Schlesinger, R. K. Parker, and V. L. Granatstein, "High-power free-electron laser based on stimulated Raman backscattering," *Phys. Rev. Lett.*, vol. 41, p. 1368, 1978.
- [4] T. C. Marshall, S. Talmadge, and P. Efthimion, "High-power millimeter radiation from an intense relativistic electron-beam device," *Appl. Phys. Lett.*, vol. 31, p. 320, 1977.
- [5] A. N. Didenko, A. R. Borisov, G. P. Fomenko, E. G. Furman, A. V. Kozhevnikov, A. M-S Le, G. V. Melnikov, Yu. G. Stein, and R. G. Zerlitsin, "Experimental investigation of stimulated microwave radiation from intense relativistic electron beams," in *Abstracts of the International Topical Conference on High Power Electron and Ion Beam Research and Technology*, Palaiseau, France, 1981, unpublished.
- [6] R. H. Jackson and R. K. Parker, "Sources of beam temperature in the electron gun of a Raman FEL," in *Abstr. 1980 IEEE Int. Conf. Plasma Sci.*
- [7] R. K. Parker, R. H. Jackson, S. H. Gold, H. P. Freund, V. L. Granatstein, P. C. Efthimion, M. Herndon, and A. K. Kinkead, "Axial magnetic-field effects in a collective-interaction free-electron laser at millimeter wavelengths," *Phys. Rev. Lett.*, vol. 48, p. 238, 1982.
- [8] J. R. Bettis, J. K. Burton, R. K. Parker, S. H. Gold, M. Herndon, R. H. Jackson, A. K. Kinkead, A. H. Guenther, and E. J. Kobiela, "Laser-triggered switch modification to VEBA," *IEEE Trans. Nucl. Sci.*, vol. NS-28, p. 3091, 1981.
- [9] R. H. Jackson, R. K. Parker, and S. H. Gold, "A new cold beam mm Raman free electron laser experiment," *Bull. Amer. Phys. Soc.*, vol. 25, p. 947, 1980.
- [10] H. Pořitsky, "Helical fields," *J. Appl. Phys.*, vol. 30, p. 1828, 1959.
- [11] R. H. Jackson, Ph.D. dissertation, North Carolina State Univ., Raleigh, in preparation.
- [12] W. B. Herrmannsfeldt, "Electron trajectory program (SLAC program)," SLAC-166 Rep., Sept. 1973, unpublished.
- [13] On the VEBA accelerator, as on other pulse charged machines, prepulse is a capacitively-coupled voltage which appears on the diode during the charging of the pulse-forming line.
- [14] Perveance is defined by $k = I(\text{amps})/V^{3/2}$ (volts) and is invariant for nonrelativistic voltages and space-charge-limited emission, i.e., it depends only on the diode geometry.
- [15] R. K. Parker, R. E. Anderson, and C. V. Duncan, "Plasma-induced field emission and the characteristics of high-current relativistic electron flow," *J. Appl. Phys.*, vol. 45, p. 2463, 1974.
- [16] H. P. Freund, P. Sprangle, D. Dillenburger, E. H. da Jornada, R. S. Schneider, and B. Liberman, "Collective effects on the operation of free electron lasers with an axial guide field," *Phys. Rev. A.*, accepted for publication.
- [17] H. P. Freund, P. Sprangle, D. Dillenburger, E. H. da Jornada, B. Liberman, and R. S. Schneider, "Coherent and incoherent radiation from free electron lasers with an axial guide field," *Phys. Rev. A.*, vol. 24, p. 1965, 1981.
- [18] W. A. McMullin and R. C. Davidson, "Low gain free electron laser near cyclotron resonance," to be published.
- [19] L. Friedland, "Electron beam dynamics in combined guide and pump magnetic fields for free electron laser applications," *Phys. Fluids*, vol. 23, p. 2376, 1980.
- [20] H. P. Freund and A. T. Drobot, "Relativistic electron trajectories in free electron lasers with an axial guide field," *Phys. Fluids*, vol. 25, p. 736, 1982.
- [21] T. Kwan and C. M. Snell, "On the efficiency of free-electron lasers with a scattered electron beam," submitted to *Phys. Fluids*.
- [22] L. E. Thode, "Plasma heating by scattered relativistic electron beams: Correlations among experiment, simulation, and theory," *Phys. Fluids*, vol. 19, p. 831, 1976.
- [23] R. H. Jackson, R. K. Parker, S. H. Gold, V. L. Granatstein, H. P. Freund, P. C. Efthimion, M. Herndon, and A. K. Kinkead, "Axial field effects in a Raman free-electron laser," *Bull. Amer. Phys. Soc.*, vol. 26, p. 909, 1981.
- [24] M. Friedman, D. A. Hammer, W. M. Manheimer, and P. Sprangle, "Enhanced microwave emission due to the transverse energy of a relativistic electron beam," *Phys. Rev. Lett.*, vol. 31, p. 752, 1973.
- [25] V. L. Granatstein, M. Herndon, R. K. Parker, and P. Sprangle,

"Coherent synchrotron radiation from an intense relativistic electron beam," *IEEE J. Quantum Electron.*, vol. QE-10, p. 651, 1974.

- [26] S. Talmadge, T. C. Marshall, and S. P. Schlesinger, "Correlation of intense electron beam dynamics with the operation of the relativistic cyclotron maser," *Phys. Fluids*, vol. 20, p. 974, 1977.
- [27] V. L. Bratman, N. S. Ginzburg, G. S. Nusinovich, M. I. Petelin, and P. S. Strelkov, "Relativistic gyrotrons and cyclotron auto-resonance masers," *Int. J. Electron.*, vol. 51, p. 541, 1981.
- [28] R. E. Shefer and G. Bekefi, "Cyclotron emission from intense relativistic electron beams in uniform and rippled magnetic fields," *Int. J. Electron.*, vol. 51, p. 569, 1981.



Robert H. Jackson was born in Atlanta, GA, in 1952. He received the B.S. degree in physics from North Carolina State University, Raleigh, in 1975, and is finishing the Ph.D. degree in plasma physics at North Carolina State.

He has worked in the areas of intense electron beam physics and high-power microwave generation. From 1980 through 1981 he was a Research Associate with North Carolina State University working at the Naval Research Laboratory, Washington, DC on an intense beam, free-electron laser experiment. His present research activities include development of high-quality electron beams and microwave generation.



Steven H. Gold was born in Philadelphia, PA, on September 3, 1946. He received the B.A. degree from Haverford College, Haverford, PA, in 1968, followed by the M.S. degree in 1970 and the Ph.D. degree in physics in 1978 from the University of Maryland, College Park. His Ph.D. dissertation research included an experimental study of plasma turbulence in a fast theta pinch by means of collective laser scattering techniques.

From 1978 to 1980, he held a National Research Council Resident Research Associateship with the Laser Plasma Branch of the Naval Research Laboratory, Washington, DC. During this period, he studied energy transport through laser-irradiated thin-foil targets using optical diagnostic techniques. Since 1980, he has held the position of Research Physicist with the High Power Electromagnetic Radiation Branch of the Naval Research Laboratory. He is presently studying the generation of very high-power millimeter-wave radiation from intense relativistic electron beams through the Raman or collective free-electron laser interaction.

Dr. Gold is a member of the American Physical Society and the Optical Society of America.



Robert K. Parker was born in Greenville, PA, on October 9, 1942. He received the B.S. degree from Allegheny College, Meadville, PA, in 1964, the M.S. degree from the Air Force Institute of Technology, Wright-Patterson AFB, OH, in 1966, and the Ph.D. degree in nuclear engineering from the University of New Mexico, Albuquerque, in 1973.

Since 1972, he has been a member of the Technical Staff at the Naval Research Laboratory, Washington, DC, where he presently

directs the Microwave and Millimeter Wave Tube Technology Branch. Areas of activity include the research and development of high-power fast-wave amplifiers such as the gyro-TWT and ubitron for Navy applications, extensions of slow-wave device technology to obtain enhanced performance, and the development of ultra-high power component technology.

Dr. Parker is a member of Sigma Xi, Tau Beta Pi, the American Association for the Advancement of Science, and the Plasma Physics Division of the American Physical Society.

Henry P. Freund, for a photograph and biography, see this issue, p. 327.



Philip C. Efthimion received the Ph.D. degree in plasma physics from Columbia University, New York, NY, in 1977. His thesis investigated the generation of millimeter waves by stimulated Raman scattering by relativistic electron beams.

Since graduating he has been with the Princeton University Plasma Physics Laboratory, Princeton, NJ where he investigates wave emission, absorption, and heating in plasmas near the electron cyclotron frequency. In addition, he continues researching the generation of coherent radiation from relativistic electron beams as a consultant with the Naval Research Laboratory, Washington, DC.



Victor L. Granatstein was born in Toronto, Ont., Canada, on February 8, 1935. He received the B.S. and Ph.D. degrees in electrical engineering from Columbia University, New York, NY, in 1960 and 1963, respectively.

From 1964 to 1972, he worked at Bell Laboratories, doing research on the interaction of microwaves with turbulent plasma. Since 1972, he has been with the Plasma Physics Division, the Naval Research Laboratory, Washington, DC, where he is currently Head of the High

Power Electromagnetic Radiation Branch. From 1969 to 1970, he was a Visiting Lecturer in Plasma Physics at the Hebrew University, Jerusalem, Israel. His current research interests include the generation of ultrahigh power microwave pulses with intense relativistic electron beams, the development of electron cyclotron masers (gyrotrons) at millimeter and submillimeter wavelengths, collective processes in free-electron lasers, and the interaction of electromagnetic waves with magnetic fusion plasmas.



Melvin Herndon received the B.S. degree from Tuskegee Institute, Tuskegee Institute, AL, in 1954, and the M.S. degree from Howard University, Washington, DC, in 1976.

He joined the staff of the Naval Research Laboratory, Washington, DC, in 1954, where he worked until his death in October 1981. He played a key role in research studies on ultra-high pulsed power microwave generation and on free-electron lasers.



A. K. Kinhead was born in Bristol, TN, on May 31, 1935. He attended the School of Mechanical Engineering, East Tennessee State University, Johnson City, from 1958 to 1962, and completed additional courses in electrical engineering and electronics at George Washington University, Washington, DC.

From 1958 to 1962, he was employed in the Engineering Design Section of the Raytheon Aerospace Division. From 1962 through 1965, he was employed at the Apollo Space Craft Division of the North American Aviation Company where he was involved in the engineering support effort for the Apollo Program. From 1966 to the present, he has been employed at the Naval Research Laboratory, Washington, DC where he helped build and operate large electron beam pulse generators such as Gamble I, Gamble II, Triton, and VEBA. He is presently working on mm wave and IR FEL experiments.



John E. Kosakowski attended the engineering program at the University of Lowell (formerly Lowell Technological Institute), Lowell, MA.

Following school he worked as an optical thin film engineer, designing and fabricating complex thin film coatings for industrial and military applications. In 1981, his interests were directed towards millimeter wave free-electron laser research at the Naval Research Laboratory (NRL), Washington, DC. Principal duties included providing engineering support for diagnostic components. Recently, he has become involved in the laser fusion research program, also at NRL. His prime responsibility is target fabrication for the study of inertial confinement fusion.



Thomas J. T. Kwan was born in Kwong Tung, China, on November 28, 1947. He received the Ph.D. degree in physics in 1978 from the University of California, Los Angeles.

Presently, he is a staff member at the Los Alamos National Laboratory, Los Alamos, NM, where he is engaged in research on free-electron lasers, microwave generation, and intense particle beam theory.

Dr. Kwan is a member of the American Physical Society.

APPENDIX D

STUDY OF GAIN, BANDWIDTH, AND TUNABILITY OF A
MILLIMETER-WAVE FREE-ELECTRON LASER
OPERATING IN THE COLLECTIVE REGIME

Study of gain, bandwidth, and tunability of a millimeter-wave free-electron laser operating in the collective regime

S. H. Gold, W. M. Black,^{a)} H. P. Freund,^{b)} V. L. Granatstein, R. H. Jackson,^{c)} P. C. Efthimion,^{b)} and A. K. Kinkead

Naval Research Laboratory, Washington, D.C. 20375

(Received 15 March 1983; accepted 12 May 1983)

Frequency-resolved measurements of the emission of a collective free-electron laser operating at millimeter wavelengths have shown emission spectra that agree well with theoretical predictions for the collective free-electron laser instability. Broad tunability, moderate emission linewidths, and high single-frequency gain have been observed. In addition, adjusting the axial field in the end region of the interaction has been found in some cases to cause a large increase in measured power and efficiency.

I. INTRODUCTION

The free-electron laser (FEL) uses a relativistic electron beam traversing a periodic transverse wiggler magnetic field to amplify radiation at a wavelength (λ) corresponding approximately to a double Doppler upshift of the wiggler period (λ_w). The radiation and wiggler fields combine to bunch and decelerate the electrons, and thus to produce gain at the radiation wavelength $\lambda \sim \lambda_w/2\gamma^2$, where γ is the relativistic mass factor. This interaction can operate at any wavelength, and offers the potential of simple, broadly variable tuning of the radiation frequency through variation of the axial velocity of the electron beam.

In the millimeter-wave regime, the FEL interaction, using intense relativistic electron beams of energy approximately 1 MeV and very low velocity spread, can proceed via a collective process that offers the potential of high power and high gain at moderately high intrinsic efficiency.¹ These properties of the collective FEL interaction have been previously demonstrated in a superradiant amplifier (35 MW at ~ 75 GHz, 2.5% efficiency, ~ 1 dB/cm gain), and were reported in earlier publications.^{2,3} On other experiments at lower powers and efficiencies, Birkett *et al.*⁴ have reported the measurement of five discrete emission wavelengths from experiments operating at different currents and voltages on three different machines, all using 8 mm wiggler periods; these wavelengths, ranging from 0.4 to 1.8 mm, have shown the expected $1/\gamma^2$ dependence on electron energy.⁴

We report here on new measurements using frequency-resolved diagnostics that have for the first time explicitly demonstrated the predicted broadband tunability of this interaction on a single device. Additionally, these measurements have demonstrated both broad gain bandwidth and high single-frequency gain, as a superradiant amplifier operating in the collective regime. We also report on measurements that give evidence of an improvement in the previously reported powers and efficiencies by tapering the end conditions of the interaction.

^{a)} Permanent address: George Mason University, Fairfax, Virginia 22030.

^{b)} Permanent address: Science Applications, Inc., McLean, Virginia 22102.

^{c)} Permanent address: Mission Research Corporation, Alexandria, Virginia 22312.

II. EXPERIMENTAL APPARATUS

The basic configuration for these experiments is shown in Fig. 1. A 1.25 MeV ($\gamma \sim 3.4$), 1 kA, 6 mm diameter solid electron beam traverses an 11 mm i.d. stainless steel drift tube under the combined influence of an axial magnetic field and a transverse wiggler magnetic field. The electron beam is provided by a pulseline accelerator with 50 nsec pulse duration and $\sim 10^{-2}$ Hz maximum repetition rate. Through use of a special diode design, the electron beam is produced with an extremely low velocity spread ($\Delta\beta_z/\beta_z \leq 0.1\%$).³ The results of a trajectory integration code,³ which includes the variation of the three-dimensional wiggler fields over the electron beam radius, have shown that low velocity spreads ($< 1\%$) are preserved into the interaction region through careful tapering of the strength of the wiggler magnetic field over an entry region of seven wiggler periods. This statement is valid provided that the axial guide field is not too close to its gyroresonant value and the wiggler field is not too large. For some of the larger transverse velocity cases discussed later in this paper, radial wiggler gradients are expected to produce an axial velocity shear in the range of 1% to 2%. Such velocity shear is not the same as a true beam temperature, and its effects are not completely understood theoretically, but at some level such macroscopic spreads may be

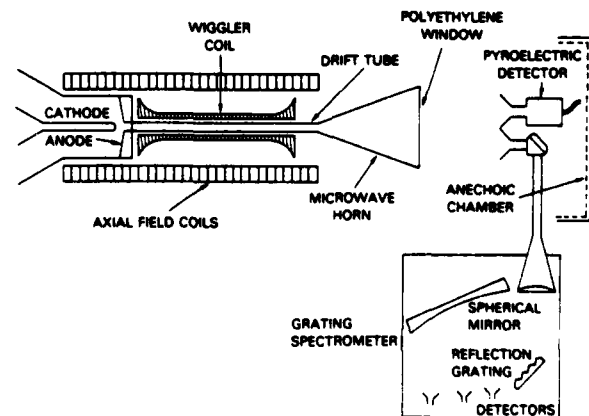


FIG. 1. Diagram of the free-electron laser experimental configuration, showing the system used to make frequency-resolved measurements.

expected to degrade the interaction.

The axial field (B_z) is variable up to 20 kG and is used both to confine the electrons and to provide gyroresonant enhancement of the effects of the wiggler magnetic field. The wiggler magnet provides a helically varying transverse magnetic field (B_r) of period $\lambda_w = 3$ cm and 0–2 kG amplitude over a uniform interaction region of 63 cm, with adiabatic transition regions at both ends. Special care was taken in the calibration of B_r , B_z , and γ for the present paper, since compatibility of these values is essential to produce the correct electron dynamics, and because of the great sensitivity of the output frequency to these experimental parameters.

Spontaneous emission at the injection end of the interaction region is highly amplified by the FEL interaction. The amplified radiation is then radiated into an anechoic chamber by means of a large (30 cm i.d.) microwave horn. Small fractions of this radiation are sampled by a pyroelectric detector with a high-pass filter, to monitor total power in the band of interest, and by a millimeter-wave grating spectrometer,⁵ in order to perform spectrally resolved measurements. The millimeter-wave grating spectrometer is equipped with three *W*-band crystal detectors, and is completely calibrated over the range 60 to 105 GHz. Its resolution is approximately 1 GHz. The use of three simultaneous channels in the spectrometer permits the efficient accumulation of spectra with a limited number of discharges. It also permits simultaneous observations at three discrete frequencies of the effect on the emission of any variation of experimental parameters.

III. THEORY

The operating frequency of an FEL in the collective regime is determined from the intersection of the negative energy electrostatic beam mode dispersion relation,

$$\omega = (k + k_w)v_z - \kappa v_z, \quad (1)$$

and the electromagnetic waveguide mode dispersion relation,

$$\omega^2 = c^2 k^2 + \omega_{co}^2. \quad (2)$$

Here ω_{co} is the cutoff frequency of the particular mode of interest, $k_w (\equiv 2\pi/\lambda_w)$ is the wiggler wave vector, and κv_z is an effective plasma frequency, where⁶

$$\kappa \equiv (\omega_b / \gamma^{1/2} v_z) \Phi^{1/2}, \quad (3)$$

$$\Phi \equiv 1 - \{ \Omega_0 \gamma_z^2 \beta_w^2 / [(1 + \beta_w^2) \Omega_0 - k_w v_z] \}, \quad (4)$$

ω_b is the beam plasma frequency,

$$\gamma \equiv (1 - v^2/c^2)^{-1/2}, \quad \gamma_z \equiv (1 - v_z^2/c^2)^{-1/2},$$

$$\Omega_0 \equiv eB_z / \gamma mc, \quad \beta_w^2 \equiv v_w^2 / v_z^2.$$

Also note for later use that $\beta_z \equiv v_z/c$ and $\beta_l \equiv v_l/c$. Computational analysis of electron orbits in the equilibrium fields³ has shown that the electrons may be assumed to be executing steady-state helical trajectories. For such trajectories, the parallel and perpendicular components of the velocity are given by^{7,8}

$$v_l = \Omega_r v_z / (\Omega_0 - k_w v_z) \quad (5)$$

and

$$v_z^2 + v_l^2 = (1 - \gamma^{-2})c^2, \quad (6)$$

where $\Omega_r \equiv eB_r / \gamma mc$. Equations (5) and (6) give rise to two separate classes of orbits. Figure 2(a) shows the steady-state orbits for typical experimental parameters for an ideal wiggler (i.e., radial gradients neglected), as given in Eqs. (5) and (6), as well as the steady-state orbits in a fully realizable, three-dimensional wiggler.^{9,10} Evidently, for these parameters, the discrepancy between the ideal and realizable wiggler models is small for axial guide fields of the order of 12 kG or greater. However, such a conclusion breaks down for axial fields below the 10 kG level. A one-dimensional theory of the gain is thus expected to be adequate for sufficiently large values of the axial guide field. This condition is expected to apply to all the experimental conditions investigated in this paper.

It should also be noted that the effects of the dielectric polarization of the beam have been neglected in the electromagnetic dispersion relation (2). This is valid as long as $\omega_b^2 / (\gamma \omega_{co}^2) \ll |k_w v_z - \Omega_0| / (k_w v_z)$, which is relevant to all the cases of interest in this paper. It is clear from Eq. (1) that the presence of the wiggler and guide fields have an effect on the characteristics of the space-charge wave. This effect is manifested through the presence of Φ , which reduces to unity if either B_w or B_r vanish. The combination of a wiggler and axial guide field, however, results in significant deviations of Φ from unity, which is equivalent to substantial changes in

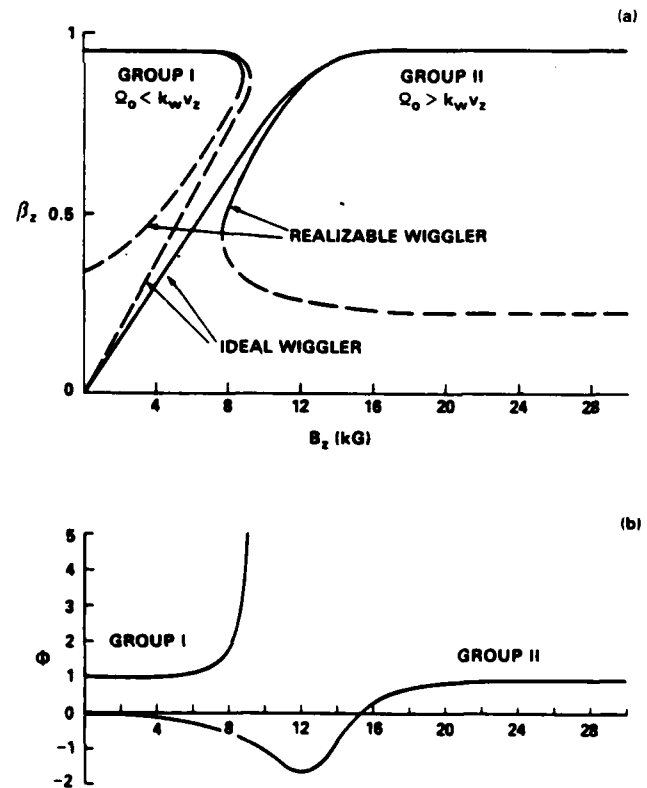


FIG. 2. Plots of (a) β_z and (b) Φ versus axial guide field for $B_w = 630$ G, $\gamma = 3.4$. The axial velocity is shown for both ideal and realizable wigglers. The dashed lines describe unstable orbits. Φ is calculated for an ideal wiggler.

the effective plasma frequency. Typical variation of Φ vs B_z is shown in Fig. 2(b) for constant γ and B_r , assuming an ideal wiggler. Evidently, $\Phi > 1$ for group I trajectories (i.e., $k_w v_z > \Omega_0$). However, the situation is more complex for the group II trajectories (i.e., $k_w v_z < \Omega_0$), for which $\Phi < 0$ whenever $(1 - \gamma^2 v_z^2/c^2)\Omega_0 < k_w v_z$. This is the case for all the data presented in this paper. In this limit the effective plasma frequency (κv_z) is imaginary, and there is no contribution to the real part of the frequency of the electrostatic beam mode due to the electric polarization of the beam. Another way of stating this is to observe that in the beam frame, the electrostatic mode is purely growing (i.e., zero real frequency). This point is discussed in more detail by Freund *et al.*⁶ As a consequence, the resonant frequency satisfies Eq. (2) and $\omega = (k + k_w)v_z$. This yields

$$\omega = \gamma_z^2 k_w v_z [1 \pm (\beta_z^2 - \omega_{co}^2/\gamma_z^2 k_w^2 c^2)^{1/2}], \quad (7)$$

where ω is assumed real. For the parameters discussed in this paper, and over the emission frequencies observed, only the upper intersection is of interest. Note that in the limit in which the waveguide effects are negligible, this expression reduces to $\omega = \beta_z(1 + \beta_z)\gamma_z^2 k_w c$.

It should be stressed that while the plasma frequency does not appear in the resonant frequency (7) for $\Phi < 0$, the interaction may still be in the collective regime. In order to demonstrate this we note that the spatial growth rate $[\text{Im}(k)]$ is given approximately by the dispersion equation^{6,11}

$$(\delta k^2 - \kappa^2)(\delta k - k_w - K_+ + \omega/v_z)(\delta k - k_w - K_- + \omega/v_z) \approx -(\beta_w^2/4)(\omega/c)\kappa^2(\delta k - k_w + \Omega_0/v_z), \quad (8)$$

where $\delta k \equiv k + k_w - \omega/v_z$,

$$K_{\pm} \equiv \frac{1}{2} \left(\frac{\omega}{v_z} (1 + \beta_z) - \frac{\Omega_0}{v_z} \right) \pm \frac{1}{2} \left(\Delta K^2 + 2 \frac{\omega_b^2}{\gamma c^2} \frac{\Omega_0}{\omega \beta_z} \right)^{1/2}, \quad (9)$$

and $\Delta K \equiv [\Omega_0 - \omega(1 - \beta_z)]/v_z$. Note that Eq. (8) is obtained in the limit in which $\omega \gg \omega_b/\gamma^{1/2}$, and describes the coupling between the electrostatic beam modes (for which $\delta k = \pm \kappa$) and the two branches of the electromagnetic dispersion equation given by $\delta k = k_w + K_{\pm} - \omega/v_z$. The strong pump regime is found when the electrostatic wave does not make a strong contribution to the growth rate, that is, when $|\delta k| \gg |\kappa|$. In this limit, Eq. (8) simplifies to a cubic dispersion relation,⁶ and the strong pump condition can be shown to be equivalent to requiring that $|\kappa| \ll \beta_w^2 \gamma_z^2 k_w \beta_z/2$. The collective regime is found in the opposite limit, in which $|\delta k| \lesssim |\kappa|$ and the interaction proceeds via induced scattering between the beam mode and the wiggler field to produce the output radiation. However, it is difficult to obtain an analytical solution to (8) when $\Phi < 0$ and κ is imaginary. In this regime the induced scattering process involves an unstable beam mode and numerical solution shows the collective regime to occur for

$$|\kappa| \gtrsim \frac{1}{2} \beta_w^2 \gamma_z^2 k_w \beta_z. \quad (10)$$

It should be remarked that the theoretical development implicit in Eq. (8) is based upon a model which is one dimensional (i.e., no finite radial effects are included in either the

wiggler or the radiation fields) and describes a monoenergetic electron beam executing orbits which are approximately helical.^{7,8} However, good qualitative agreement has previously been found between this type of analysis and the experimental results,^{2,3} and all cases considered in this work correspond to operation in the collective regime.

IV. EXPERIMENTAL RESULTS

Using the experimental setup described previously, measurements were made of the emission spectrum. Figure 3 shows three spectra. The top spectrum, for $B_z = 13.1$ kG and $B_r = 910$ G, corresponds to $\beta_1 \sim 0.34$. In this case, only coupling to the fundamental TE₁₁ mode of the 11 mm i.d. drift tube is expected from Eq. (7). The predicted frequency, 67 GHz, is in good agreement with the observed radiation. The middle spectrum, with B_r lowered to 630 G, corre-

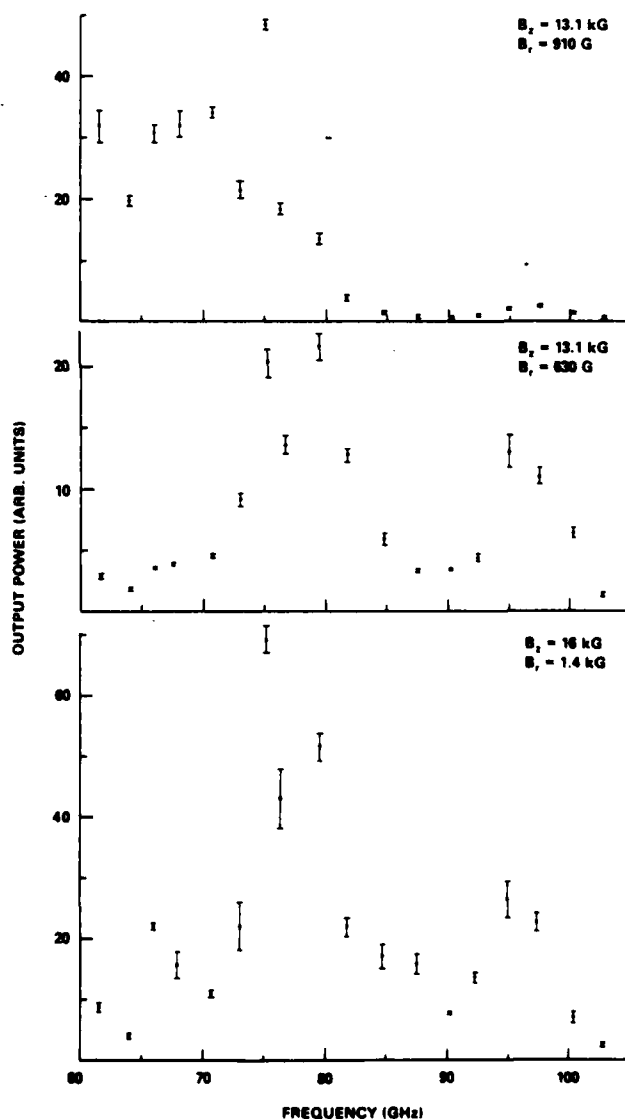


FIG. 3. Free-electron laser emission spectra for (top) $B_z = 13.1$ kG, $B_r = 910$ G; (center) $B_z = 13.1$ kG, $B_r = 630$ G; and (bottom) $B_z = 16.0$ kG, $B_r = 1.4$ kG. Only statistical error bars are shown. The estimated systematic error is ± 2 dB.

sponds to $\beta_1 \sim 0.27$. Equation (7) predicts coupling to the two lowest waveguide modes, the TE_{11} at ~ 96 GHz and the TM_{01} at ~ 78 GHz. The spectrum shows two main peaks, centered at frequencies that are in good agreement with these predictions. Additionally, the lower-frequency emission is observed to be predominantly radially polarized, as would be expected for a TM_{01} mode pattern, while the high-frequency peak is unpolarized, as expected for a (circularly polarized) TE_{11} mode. The bottom spectrum has B_z increased by 20% to 16.0 kG, with B_r increased to 1.4 kG in order to keep β_1 approximately unchanged from the previous case. This spectrum is virtually identical, although its amplitude is doubled. Doubling is also seen in the pyroelectric detector signal. This doubling can occur because gain and saturation are functions of B_z as well as of β_1 .^{6,12}

These results demonstrate that the emission spectrum is strongly affected by changes in β_1 at a single B_z , but is virtually unaffected by a large change in B_z at constant β_1 . This is strong evidence for FEL emission rather than the cyclotron mechanism seen in some other experiments.¹³⁻¹⁵ In addition, the observed emission features do not agree with calculations based on coupling to the positive energy cyclotron (gyron) modes.

Tuning of the spectrum is most easily demonstrated by making single frequency observations of the output power as a function of experimental parameters. This procedure factors out calibration errors for each single frequency sweep so that the only residual errors are because of discharge-to-discharge nonreproducibility of the experiment, which can be dealt with statistically. In essence, an FEL is tuned by varying the axial velocity of the electron beam through the interaction region. Due to the complicated relationship of β_z on both B_z and γ [see Eqs. (5) and (6)], this was most easily done experimentally through variation of B_r .

Figure 4 shows power at six frequencies between 60 and 95 GHz, as a function of B_r . Each curve is plotted in the same power units, subject to the estimated ± 2 dB accuracy of the separate single-frequency calibration factors. Typical statistical error bars for these data are smaller than the symbols used to locate the points. B_z is held constant at 13.1 kG. It is seen that for each frequency, the output power is maximized at a particular value of B_r . The data display a monotonic trend; that is, the lower the frequency of interest, the higher the optimum wiggler field. Through variation of B_r by a factor of 2, superradiant emission is optimized over a 50% variation of frequencies. The pair of vertical arrows associated with each frequency indicate the calculated wiggler field to maximize emission for the TE_{11} mode (right arrow) and the TM_{01} mode (left arrow). In most cases, the coupling seems to be strongest for the TE_{11} mode, as would be expected for a circularly polarized wiggler coupling to an axicentered electron beam. Note that variation of B_r in order to tune the frequency will also affect the total FEL emission through its effect on the gain and possible saturation of the FEL interaction. The wiggler fields that optimize emission in the range 75–80 GHz are the fields that maximize total high-frequency ($f > 60$ GHz) emission, as measured by the pyroelectric detector. That is, the larger emission seen at 75.2 and 79.5 GHz is believed real.

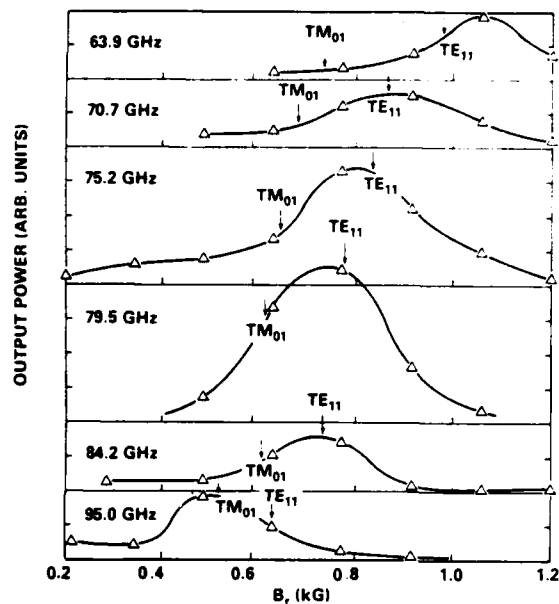


FIG. 4. FEL tuning—emission at six frequencies as a function of B_r , for $B_z = 13.1$ kG. The predicted position of peak emission at each frequency for the TE_{11} mode (right arrow) and TM_{01} mode (left arrow) are shown.

The broad single-frequency tuning peaks shown in Fig. 4 result from the amplification of broadband spontaneous emission by the FEL interaction. For an FEL operating on group II orbits with $\Phi < 0$, theory predicts broad gain bandwidths, since the interaction is coupled to a purely growing electrostatic beam mode.⁶ This broad gain bandwidth, amplifying initially broadband spontaneous emission, results in the moderate emission linewidths seen in Fig. 3, even after the estimated 60 dB of amplification of the original spontaneous emission level has taken place.

Another presentation of the frequency tuning is shown in Fig. 5. Here, the six frequencies of Fig. 4 are plotted versus the calculated value of $\beta_z(1 + \beta_z)\gamma_z^2 c/\lambda_w$ at the peak of each curve in Fig. 4. For a coupling at the light line, the points should lie along the top curve. The lower lines indicate the calculated couplings to waveguide modes. The line corre-

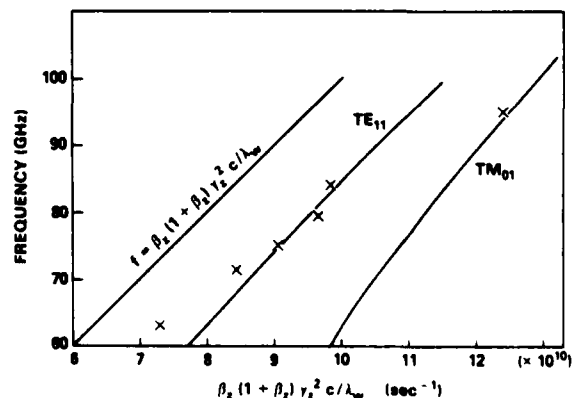


FIG. 5. Emission frequencies plotted against $\beta_z(1 + \beta_z)\gamma_z^2 c/\lambda_w$, calculated from the best measured value of B_r at each frequency. The calculated frequencies of TE_{11} and TM_{01} modes are shown.

sponding to the TE_{11} mode fits most of the points fairly well.

The only direct means to measure the gain of a superradiant amplifier is to vary the length of the interaction region, and to observe the change in frequency-resolved output power as a function of interaction length. Since the wiggler magnet is one continuous coil, the length of wiggler magnet traversed by the electron beam was varied by changing the length of the axial magnetic field. Since Ω_0 is initially greater than $k_w v_z$ for the cases discussed in this paper, the falloff in B_z associated with the end of the axial magnetic field sends the electron beam to the drift tube walls [see Eqs. (5) and (6) and Fig. 2(a)], and note that the electron orbital radius is given by $\beta_1 / (\beta_z k_w)$.

Figure 6 shows the emission at a single frequency, 66 GHz, as a function of the length of the axial field for $B_z = 12.1$ kG and $B_w = 630$ G. The lower axis corresponds to the distance of the last connected axial field coil from the end of the wiggler exit taper. As the axial magnetic field is lengthened (last energized magnet coil changed progressively from -40 to -20 cm), the output power at 66 GHz is seen to exponentiate. The rate of growth is approximately 0.5 dB/cm. This is about 10% of the maximum spatial growth rate calculated from a numerical solution of the dispersion equation given in Eq. (8). The discrepancy can be due to the fact that effects such as the fill factor, finite geometry, finite temperature, wiggler gradients, and mode competition have been emitted from (8). Also, note that the gain measurement was not performed at the peak of the experimental emission spectrum.

The interpretation of the experimental gain measurement is complicated by a very gradual decrease in axial field that begins tens of centimeters upstream from the end of magnet. This results in a gradual increase in β_1 and decrease in β_z that modifies the interaction parameters over this end region, increasing the gain, but lowering its frequency. The length of this nonuniform end region of constant B_w but decreasing B_z is constant, provided that the beam is disposed of within the uniform portion of the wiggler magnet. This will be true when the last energized axial magnet coil is within the

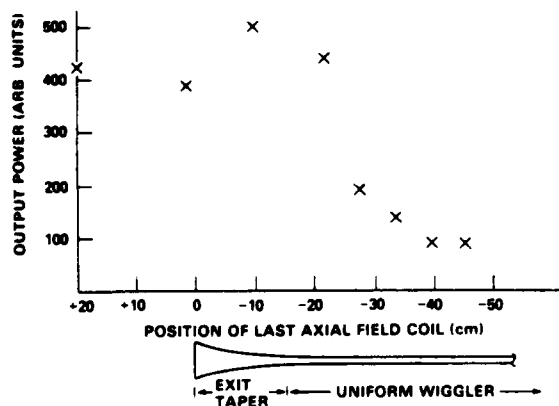


FIG. 6. Variation of output power at 66 GHz as a function of length of axial magnetic field for $B_z = 12.1$ kG, $B_w = 630$ G. Electron beam is traveling right to left. The position of the wiggler magnet is indicated below the plot.

uniform region of the wiggler. Thus, the exponential growth seen as the system is lengthened is believed to characterize the gain in the uniform region of the interaction.

The data in Fig. 6 display a second interesting effect, which is believed due to the nonuniform end region affected by the gradual decrease in axial field. The peak power at 66 GHz appears to occur when the end of the axial field magnet is located near the end of the uniform wiggler section (-10 cm), rather than when the axial field is held constant throughout the wiggler. This increase in measured single-frequency emission is accompanied by a comparable increase in total high-frequency emission. A similar enhancement in emission as the length of uniform axial field is decreased (last axial field coil at -10 cm) is found at several other combinations of axial and wiggler fields. A particularly interesting case is illustrated in Fig. 7, which shows a comparison of the emission spectrum at $B_z = 16.0$ kG and $B_w = 1.4$ kG for the uniform axial field case, with a partial spectrum for the case of B_z shortened to the length producing the maximum effect in Fig. 6. For these experimental parameters the total power in the emission spectrum appears to have increased by a factor of 2, accompanied by a small shift to lower frequencies. The pyroelectric detector data agrees with this factor of 2 increase in frequency-integrated power. For this case, shortening the region of uniform B_z and creating the nonuniform end region increases the total high-frequency emission ($f > 60$ GHz) measured by the pyroelectric detector by approximately 50% over that produced by any combination of wiggler field and uniform axial field. Based on a comparison with pyroelectric detector measurements performed at slightly higher currents and different axial and wiggler magnetic fields, whose total powers and efficiencies were determined calorimetrically,^{2,3} this increases the estimated overall experimental power to near 50 MW at 5% efficiency. It should be noted that this results in larger experimental efficiencies than those predicted for the experiment, at lower axial fields and without an axial field end taper, by a particle-in-cell computer code that includes

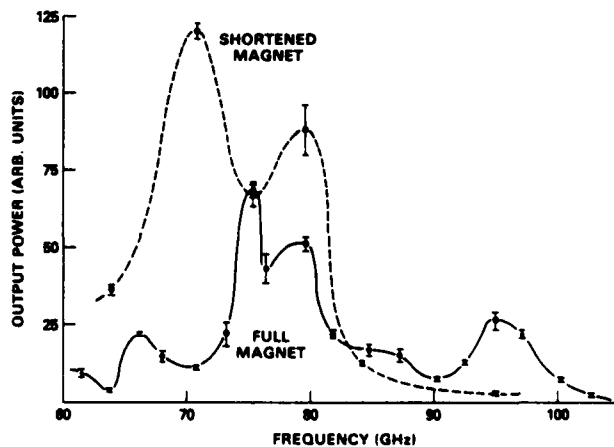


FIG. 7. Emission spectra at $B_z = 16.0$ kG, $B_w = 1.4$ kG for the full system (axial field constant throughout wiggler), and for the shortened system (last connected B_z coil at start of wiggler exit taper).

finite electron velocity spread.^{3,16} However, saturation is expected to be a function of axial guide field,¹² and the effects of the axial end taper are not yet fully understood. These effects are under study.

V. CONCLUSIONS

Initial spectral measurements have been completed on a high-power superradiant millimeter-wave free-electron laser experiment. These measurements have produced emission spectra that agree well with predictions. Coupling has been observed to the two lowest-order modes of the overmoded circular waveguide. Moderate linewidths in the range of 6% to 15% have been measured, demonstrating the broad gain bandwidth of the interaction. Additionally, in this experiment there was observed for the first time the predicted simple broadband tuning of the FEL interaction, with tuning demonstrated over a 50% range of frequencies through variation of the axial electron velocity by means of changing the strength of the wiggler field.

Direct gain measurements have demonstrated a single-frequency gain of approximately 0.5 dB/cm, through variation in the interaction length for the super-radiant emission. Additionally, a frequency shift, accompanied in some cases by a large increase in total power and efficiency, has been observed through shortening the region of uniform axial field and tapering the strength of the axial magnetic field at the end of the uniform wiggler region. The highest power produced in this way is estimated to be ≈ 50 MW at approximately 5% efficiency.

ACKNOWLEDGMENT

This research was supported by the Naval Sea Systems Command under Contract No. SF68-342.

- ¹P. Sprangle, R. A. Smith, and V. L. Granatstein, in *Infrared and Millimeter Waves*, edited by K. J. Button (Academic, New York, 1979), Vol. 1, p. 279; also, V. L. Granatstein, R. K. Parker, and P. Sprangle, in *Handbook of Laser Science and Technology*, edited by M. J. Weber (CRC, Boca Raton, 1982), Vol. I, p. 441.
- ²R. K. Parker, R. H. Jackson, S. H. Gold, H. P. Freund, V. L. Granatstein, P. C. Efthimion, M. Herndon, and A. K. Kinkead, *Phys. Rev. Lett.* **48**, 238 (1982).
- ³R. H. Jackson, S. H. Gold, R. K. Parker, H. P. Freund, P. C. Efthimion, V. L. Granatstein, M. Herndon, A. K. Kinkead, and J. E. Kosakowski, *IEEE J. Quantum Electron.* **QE-19**, 346 (1983).
- ⁴D. S. Birkett, T. C. Marshall, S. P. Schlesinger, and D. B. McDermott, *IEEE J. Quantum Electron.* **QE-17**, 1348 (1981).
- ⁵J. A. Pasour and S. P. Schlesinger, *Rev. Sci. Instrum.* **48**, 1355 (1977).
- ⁶H. P. Freund, P. Sprangle, D. Dillenburg, E. H. daJornada, R. S. Schneider, and B. Liberman, *Phys. Rev. A* **26**, 2004 (1982).
- ⁷L. Friedland, *Phys. Fluids* **23**, 2376 (1980).
- ⁸H. P. Freund and A. T. Drobot, *Phys. Fluids* **25**, 736 (1982).
- ⁹P. Diament, *Phys. Rev. A* **23**, 2537 (1983).
- ¹⁰H. P. Freund, S. Johnston, and P. Sprangle, *IEEE J. Quantum Electron.* **QE-19**, 322 (1983).
- ¹¹L. Friedland and A. Fruchtman, *Phys. Rev. A* **25**, 2693 (1982).
- ¹²H. P. Freund, *Phys. Rev. A* **27**, 1977 (1983).
- ¹³M. Friedman and M. Herndon, *Phys. Rev. Lett.* **28**, 210 (1972); **29**, 55 (1972); and *Phys. Fluids* **16**, 1982 (1973).
- ¹⁴V. L. Granatstein, M. Herndon, P. Sprangle, Y. Carmel, and J. A. Nation, *Plasma Phys.* **17**, 23 (1975).
- ¹⁵R. E. Shefer and G. Bekefi, *Int. J. Electron.* **51**, 569 (1981).
- ¹⁶T. J. T. Kwan and C. M. Snell, *Phys. Fluids* **26**, 835 (1983).

APPENDIX E

NONLINEAR ANALYSIS OF FREE-ELECTRON-LASER AMPLIFIERS
WITH AXIAL GUIDE FIELDS,

Nonlinear analysis of free-electron-laser amplifiers with axial guide fields

H. P. Freund*

Naval Research Laboratory, Washington, D.C. 20375

(Received 21 September 1982)

The nonlinear evolution of free-electron lasers in the presence of an axial guide field is investigated numerically. A set of coupled nonlinear differential equations is derived which governs the self-consistent evolution of the wave fields and particle trajectories in an amplifier configuration. The nonlinear currents which mediate the interaction are computed by means of an average over particle phases, and the inclusion of fluctuating space-charge fields in the formulation permits the investigation of both the stimulated Raman and Compton scattering regimes. The initial conditions are chosen to describe the injection of a cold, axially propagating electron beam into the interaction region which consists of a uniform axial guide field and a helical wiggler field which increases to a constant level adiabatically over a distance of ten wiggler periods. After an initial transient phase, the results show a region of exponential growth of the radiation field which is in excellent agreement with linear theory. Saturation occurs by means of particle trapping. The efficiency of the interaction has been studied for a wide range of axial guide fields, and substantial enhancements have been found relative to the zero-guide-field limit.

I. INTRODUCTION

The use of axial guide magnetic fields in free-electron-laser (FEL) experiments has generally been restricted to low-energy (~ 1 MeV) and high-current (~ 1 kA) devices in which the axial field is necessary in order to confine the electron beam. As a consequence, a great deal of theoretical work has been devoted to the calculation of electron orbits,^{1,2} spontaneous radiation (i.e., noise) spectra,³ and the linear growth rate³⁻⁹ in the presence of an axial guide field. As shown in these works, a fortuitous consequence of the presence of the guide field is that both the noise spectrum and the linear growth rate are enhanced. Such enhancements are due to an increase in the transverse electron velocities and a decrease in the natural response frequency of the electrons. In the latter case, the natural frequency can become comparable to the frequency of the ponderomotive force which results from the beating of the radiation and wiggler fields. When this occurs the linear gain can become very large, and the interaction is analogous to that of driving an oscillator at its natural frequency. In view of the possible enhancements in the gain, the study of the nonlinear phase of the interaction assumes an added importance with a primary focus on possible enhancements in the saturation levels of the instability and the efficiency of the interaction.

The motivation for the present work is to investigate the effects of the guide field on the nonlinear regime of both the stimulated Raman and stimulated Compton scattering regimes of FEL operation. To this end, a set of coupled nonlinear differential equations is derived which describes the evolution of both particle orbits and the electrostatic and electromagnetic fields. The nonlinear currents which mediate the interaction are computed from the microscopic behavior of an ensemble of electrons by means of an average of the electron phases relative to the ponderomotive wave. This is equivalent to a time average over the electron orbits which, in turn, is equivalent to an ensemble average over the microscopic electron distribution. Thus although the macroscopic electron distribution does not explicitly appear, the formulation is equivalent to a fully kinetic treatment of the interaction and is capable of describing effects such as particle trapping in the ponderomotive wave. This is in contrast to the nonlinear analysis described recently by Friedland and Bernstein¹⁰ which is based on the cold-fluid model.

These equations are solved numerically for a configuration in which a uniform, monoenergetic electron beam is injected with purely axial velocities into the interaction region which consists of a uniform axial guide field and a helical wiggler field which increases adiabatically from zero in ten wiggler periods. The analysis is performed in one spatial di-

mension, although the electron trajectories are integrated for three dimensions in the velocity. In addition, since the problem of interest is that of an FEL amplifier, only a single electromagnetic and electrostatic wave is included corresponding to the choice of the fastest growing mode. Thus the analysis self-consistently describes the linear and nonlinear phases of the interaction of a uniform electron beam with a helical wiggler field in one dimension. The results of the simulation show, after an initial transient phase, a region of exponential growth of the radiation and space-charge fields which is in excellent agreement with the linear theory³⁻⁹ over the entire range of parameters studied. The onset of the nonlinear phase of the interaction appears quite suddenly, and saturation occurs by means of particle trapping. Most significantly, substantial enhancements in the interaction efficiency are found to occur.

The organization of the paper is as follows. The general equations are derived in Sec. II. Since the actual adiabatic entry of the electron beam into the wiggler is included in the analysis, we digress in Sec. III to describe the types of orbit which result in the absence of a radiation field. The numerical solutions to the complete set of coupled particle-field

equations are given in Sec. IV, and the conditions under which efficiency enhancements occur are described. A summary and discussion is given in Sec. V.

II. GENERAL EQUATIONS

The physical configuration we employ is one dimensional in that spatial variations are restricted to the z direction. The static magnetic field is taken to be of the form

$$\vec{B}(z) = B_0 \hat{e}_z + B_w(z) [\hat{e}_x \cos(k_w z) + \hat{e}_y \sin(k_w z)] , \quad (1)$$

where B_0 and B_w are the amplitudes of the axial guide field and the wiggler field, respectively, k_w ($\equiv 2\pi/\lambda_w$, where λ_w is the wiggler period) denotes the wiggler wave vector, and it is assumed that $d \ln B_w / dz \ll k_w$. Thus we allow the wiggler amplitude to vary slowly in z while holding the period constant. In practice, we shall allow $B_w(z)$ to vary only over $0 < z < 10\lambda_w$, after which it shall be held constant, so that $d \ln B_w / dz \approx 0.1 k_w$. The variable amplitudes and periods of the radiation and space-charge fields are included by means of the vector and scalar potentials

$$\delta \vec{A}(z, t) = \delta A(z) \left[\hat{e}_x \cos \left[\int_0^z dz' k_+(z') - \omega t \right] - \hat{e}_y \sin \left[\int_0^z dz' k_+(z') - \omega t \right] \right] , \quad (2)$$

$$\delta \Phi(z, t) = \delta \Phi(z) \cos \left[\int_0^z dz' k(z') - \omega t \right] , \quad (3)$$

where ω is the wave frequency, $\delta A(z)$ and $\delta \Phi(z)$ are the amplitudes of the vector and scalar potentials, and $k_+(z)$ and $k(z)$ are the wave vectors. Note that by the choice of parameters (i.e., primarily the pump strength, beam density, and axial field) the amplitudes and wave vectors will be slowly varying functions of z ; however, no such assumption is made *a priori*.

The microscopic current density can be written as the following sum over individual particle trajectories:

$$\delta \vec{J}(z, t) = -en_b \frac{L}{N_T} \sum_{i=1}^{N_T} \vec{v}_i(z, t_{i0}) \frac{\delta(t - \tau_i(z, t_{i0}))}{|v_{zi}(z, t_{i0})|} , \quad (4)$$

where N_T is the total number of electrons within the interaction region of length L , n_b is the average electron density, $\vec{v}_i(z, t_{i0})$ is the velocity of the i th electron at position z which entered the interaction region (i.e., crossed the $z=0$ plane) at time t_{i0} , and

$$\tau_i(z, t_{i0}) \equiv t_{i0} + \int_0^z \frac{dz'}{v_{zi}(z', t_{i0})} . \quad (5)$$

The system is assumed to be quasistatic (i.e., in a temporal steady state) so that particles which enter the interaction region at times t_0 separated by integral multiples of a wave period will execute identical orbits.¹¹ As a result $\vec{v}_i(z, t_{i0}) = \vec{v}_j(z, t_{j0})$, where $t_{i0} = t_{j0} + 2\pi N / \omega$ for integer N .

Substitution of the microscopic fields and current density into Maxwell's equation yields

$$\begin{aligned} \frac{d^2}{dz^2} \delta a + \left[\frac{\omega^2}{c^2} - k_+^2 \right] \delta a \\ = \frac{\omega_b^2}{c^2} \frac{v_{z0}}{c} \left\langle \frac{v_1 \cos \psi - v_2 \sin \psi}{v_3} \right\rangle , \quad (6) \\ 2k_+^{1/2} \frac{d}{dz} (k_+^{1/2} \delta a) = - \frac{\omega_b^2}{c^2} \frac{v_{z0}}{c} \left\langle \frac{v_1 \sin \psi + v_2 \cos \psi}{v_3} \right\rangle , \quad (7) \end{aligned}$$

$$\left(\frac{d^2}{dz^2} - k^2 \right) \delta\phi = 2 \frac{\omega_b^2}{c^2} v_{z0} \left\langle \frac{\cos\psi_1}{v_3} \right\rangle, \quad (8)$$

$$2k^{1/2} \frac{d}{dz} (k^{1/2} \delta\phi) = -2 \frac{\omega_b^2}{c^2} v_{z0} \left\langle \frac{\sin\psi_1}{v_3} \right\rangle, \quad (9)$$

where an average over a wave period has been performed. In Eqs. (6)–(9), $\omega_b^2 \equiv 4\pi e^2 n_b / m$, v_{z0} is the initial axial velocity of the electrons, $\delta a \equiv e \delta A / mc^2$, $\delta\phi \equiv e \delta\Phi / mc^2$,

$$\psi \equiv \psi_0 + \int_0^z dz' (k_+ + k_w - \omega / v_3), \quad (10)$$

$$\psi_1 \equiv \psi_0 + \int_0^z dz' (k - \omega / v_3), \quad (11)$$

$\psi_0 \equiv -\omega t_0$ is the initial phase, and (v_1, v_2, v_3) are the components of the electron velocity in the wiggler frame defined by the basis vectors $\hat{e}_1 = \hat{e}_x \cos(k_w z) + \hat{e}_y \sin(k_w z)$, $\hat{e}_2 = -\hat{e}_x \sin(k_w z) + \hat{e}_y \cos(k_w z)$, $\hat{e}_3 = \hat{e}_z$. Observe that it has been implicitly assumed that the electron beam is monoenergetic and that all electrons have the same initial axial velocity. In addition,

$$\frac{d}{dz} p_1 = - \left[\frac{\Omega_0}{\gamma} - k_w v_3 \right] \frac{p_2}{v_3} + mc \left[\left[\frac{\omega}{v_3} - k_+ \right] \delta a \sin\psi + \cos\psi \frac{d}{dz} \delta a \right], \quad (14)$$

$$\frac{d}{dz} p_2 = \left[\frac{\Omega_0}{\gamma} - k_w v_3 \right] \frac{p_1}{v_3} - m \Omega_w + mc \left[\left[\frac{\omega}{v_3} - k_+ \right] \delta a \cos\psi - \sin\psi \frac{d}{dz} \delta a \right], \quad (15)$$

where $p_{1,2} \equiv \gamma m v_{1,2}$, $\Omega_{0,w} \equiv |e B_{0,w} / mc|$, $\gamma \equiv (1 - v^2/c^2)^{-1/2}$,

$$\begin{aligned} \frac{d}{dz} v_3 &= \frac{\Omega_w}{\gamma} \frac{v_2}{v_3} + \frac{c}{v_3} \frac{\delta a}{\gamma} \left[k_+ - \omega \frac{v_3}{c^2} \right] (v_1 \sin\psi + v_2 \cos\psi) \\ &\quad - \frac{c}{\gamma v_3} \frac{d}{dz} \delta a (v_1 \cos\psi - v_2 \sin\psi) - \frac{c^2}{\gamma \gamma_z^2 v_3} \left[k \delta\phi \sin\psi_1 - \cos\psi_1 \frac{d}{dz} \delta\phi \right], \end{aligned} \quad (16)$$

and $\gamma_z^2 \equiv (1 - v_z^2/c^2)^{-1}$. Both the linear and nonlinear evolution of the FEL amplifier, therefore, are included in Eqs. (6)–(9) for the field quantities and (14)–(16) for the orbits of an ensemble of electrons having initial phases $-\pi \leq \psi_0 \leq \pi$.

III. SINGLE-PARTICLE ORBITS

Since an adiabatic entry region into the wiggler is included in the analysis, it is useful to consider the form which the single-particle orbits take as they emerge into the constant- B_w region as a function of B_0 . It should be remarked here that the radially

$$\langle \mathcal{F} \rangle \equiv \frac{1}{N_w} \sum_{i=1}^{N_w} \mathcal{F} \quad (12)$$

represents a phase average where N_w denotes the number of electrons in a single wave period. Thus following Sprangle *et al.*¹¹ the quasistatic assumption has permitted the reduction of the problem to the consideration of the initial beam segments for which steady-state orbits of the beam electrons are described by particles which enter the wiggler region within a wave period. The actual length of these segments is $2\pi v_{z0} / \omega$ so that $N_w = 2\pi N_T v_{z0} / \omega L$. For sufficiently large N_w , the discrete nature of the phase average (12) can be replaced by an integral over the initial phases ψ_0 as follows:

$$\langle \mathcal{F} \rangle = \frac{1}{2\pi} \int_{-\pi}^{\pi} d\psi_0 \mathcal{F}. \quad (13)$$

In this form the field equations are identical to those derived by Sprangle *et al.*¹¹

In order to complete the formulation, the electron orbit equations in the presence of the static and fluctuating fields must be specified. These equations are of the form

homogeneous wiggler under consideration is neither curl nor divergence free and is a reasonable approximation for a realizable wiggler field only as long as $k_w r \ll 1$ and $d \ln B_w(z) / dz \ll k_w$, where r measures the radial displacement of the electron trajectories from the axis of symmetry. The question we examine in this section, therefore, is the effect of the adiabatic increase in $B_w(z)$ on the trajectories of electrons which enter the wiggler with purely axial motion.

The appropriate equations of motion follow immediately from (14)–(16) in the absence of fluctuating fields,

$$\frac{d}{dz} v_1 = - \left[\frac{\Omega_0}{\gamma} - k_w v_3 \right] \frac{v_2}{v_3}, \quad (17)$$

$$\frac{d}{dz} v_2 = \left[\frac{\Omega_0}{\gamma} - k_w v_3 \right] \frac{v_1}{v_3} - \frac{\Omega_w}{\gamma}, \quad (18)$$

$$\frac{d}{dz} v_3 = - \frac{\Omega_w}{\gamma} \frac{v_2}{v_3}, \quad (19)$$

where γ is now a constant of the motion, and Ω_w is a function of z . The steady-state (or helical) orbits^{1,2} are obtained by requiring the derivatives to vanish in the constant- B_w region and results in solutions $v_1 = v_w \equiv \Omega_w v_{||} / (\Omega_0 - \gamma k_w v_{||})$, $v_2 = 0$, and $v_3 = v_{||}$, where $v_{||}$ is a constant determined by conservation of energy, i.e., $v_{||}^2 + v_{\perp}^2 = (1 - \gamma^{-2})c^2$. This equation is quartic in $v_{||}$ and describes at most four distinct classes of trajectory, of which one is characterized by motion antiparallel to \vec{B}_0 and will be ignored. Of the remaining three classes of trajectory, one is unstable. It is, therefore, difficult to propagate a coherent beam on these orbits, and it is of interest to determine whether, by adiabatic tapering of B_w , these orbits can be avoided. The three types of orbit propagating parallel to \vec{B}_0 are shown in Fig. 1, in which we plot $v_{||}$ vs $\Omega_0/\gamma k_w c$ (i.e., the axial field strength) for $\gamma = 3.5$ and $\Omega_w/\gamma k_w c = 0.05$. Observe that of the two classes of stable orbits, one is characterized by high axial velocities (denoted by group I) for low B_0 and decreases monotonically with the axial field up to a critical B_0 ($\Omega_0/\gamma k_w c \sim 0.76$ for the

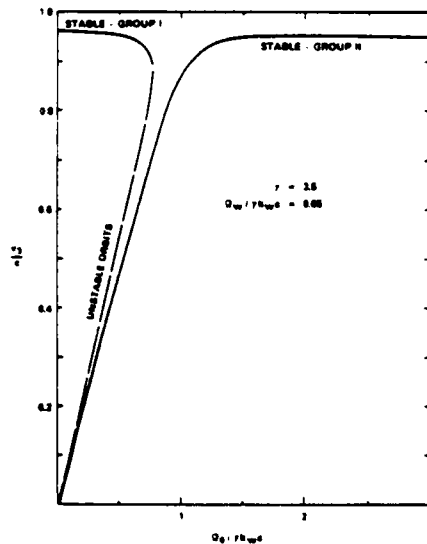


FIG. 1. Graph of the axial velocities corresponding to the steady-state trajectories as a function of the axial guide field.

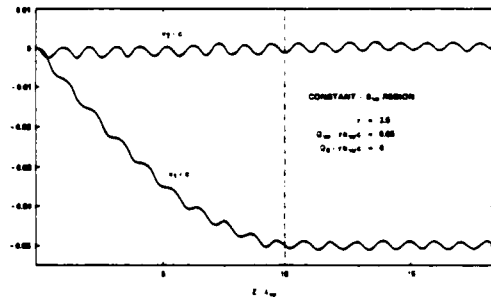


FIG. 2. Plot of the single-particle trajectories vs axial position of $\Omega_0/\gamma k_w c = 0.0$, $\Omega_w/\gamma k_w c = 0.05$, and $\gamma = 3.5$.

case illustrated) at which point there is a transition to the unstable orbits. The second class of stable trajectory (denoted by group II) is characterized by a monotonically increasing axial velocity with B_0 .

In the integration of the orbit equations it shall be assumed that

$$B_w(z) = \begin{cases} \frac{1}{2} B_w [1 - \cos(k_w z / 20)], & 0 \leq z \leq 10\lambda_w \\ B_w, & z > 10\lambda_w \end{cases} \quad (20)$$

which provides for a smooth, adiabatic transition to the constant- B_w region over ten wiggler periods. The results of the integration of the orbits with $B_w(z)$ characterized by (20) are shown in Figs. 2 and 3, where we plot the components of the velocity versus $k_w z$ for $\gamma = 3.5$ and $\Omega_w/\gamma k_w c = 0.05$. Note that the initial conditions on the velocity were chosen to be $v_1 = v_2 = 0$ and $v_3 = (1 - \gamma^{-2})^{1/2}c$. Figure 2 corresponds to parameters consistent with group-I steady-state orbits, and we find that the trajectories in the constant- B_w region differ only slightly from the steady-state case. As is evident in the figures, the bulk values for the magnitude of v_1 increase with the adiabatic rise in B_w , after which small oscillations about mean values corresponding

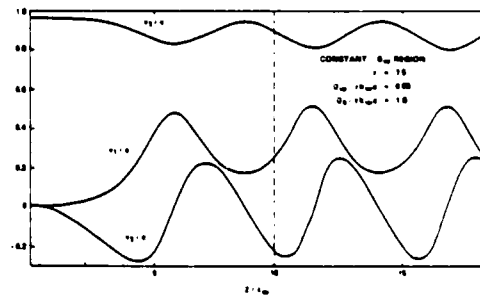


FIG. 3. Plot of the single-particle trajectories vs axial position for $\Omega_0/\gamma k_w c = 1.0$, $\Omega_w/\gamma k_w c = 0.05$, and $\gamma = 3.5$.

to the group-I trajectories are found in the constant- B_w region. Note that $\gamma k_w v_3 > \Omega_0$ for these orbits and, hence, $v_1 < 0$. In addition, $v_2 = 0$ for the steady-state orbits, and the electron trajectories in the constant- B_w region exhibit small oscillations about this value. The behavior of v_3 , while not shown explicitly, also exhibits small oscillations (of less than 1% of the mean value) about the appropriate value for the group-I orbit. Thus we conclude that it is possible to adiabatically inject electrons into the interaction region on near-steady-state orbits. However, it should be observed that as $\Omega_0/\gamma k_w c$ increases from 0 to 0.76 (corresponding to an increase in B_0), the magnitude of the fluctuation relative to the steady-state bulk value increases. This trend is characteristic of group-I-type injection and is indicative of the fact that it becomes increasingly difficult to obtain near-steady-state trajectories as the transition to orbital instability is approached, at which point ($\Omega_0/\gamma k_w c \approx 0.76$) the orbits differ widely from the steady-state trajectories and exhibit large fluctuations in the velocity. As a result, it becomes impossible to either inject or propagate a coherent beam through the system.

Injection corresponding to near-steady-state orbits of the group-II type is illustrated in Fig. 3 for $\Omega_0/\gamma k_w c = 1.0$. Observe that $\gamma k_w v_3 < \Omega_0$ for these orbits and $v_1 > 0$ in this regime. Although orbital instability does not occur for group-II trajectories in one dimension, the orbits are characterized by low axial velocities for sufficiently small B_0 . As a consequence, it is possible for axially injected electrons with relativistic energies to be characterized by initial axial velocities much greater than that of the steady-state orbit. This is the case which corresponds to the orbit shown in Fig. 3, which is characteristic of the resulting trajectories for $\Omega_0/\gamma k_w c \leq 1$. The orbits in this regime may still be described as a perturbation about the steady-state orbits, but the perturbations are large. It is only when B_0 has increased along with the steady-state axial velocity that the perturbations about the helical orbits again become small (i.e., $\Omega_0/\gamma k_w c > 1.3$). As in the case of injection into near-group-I type of orbits in the vicinity of the orbital stability transition, large fluctuations in the equilibrium electron velocity results in a degradation of the FEL interaction.

In view of the preceding results regarding the adiabatic injection of relativistic electron beams into a combined axial guide field and helical wiggler field, we conclude that large-scale fluctuations in the electron velocity may be expected whenever $0.76 \leq \Omega_0/\gamma k_w c \leq 1.0$ for $\gamma = 3.5$ and $\Omega_w/\gamma k_w c = 0.5$. Within this range, the transverse components of the electron velocity may become sufficiently large that the radial excursions of the electron beam

make it difficult for the beam to propagate. In addition, the fluctuations in the axial velocity can cause a breakdown in the FEL wave particle resonance condition which, even if beam propagation is possible, will result in a substantial decrease in the gain.

IV. NUMERICAL SOLUTION

The set of coupled differential equations derived in Sec. II is solved numerically for an amplifier configuration in which a wave (ω, k_+) of arbitrary amplitude is injected into the system in concert with a monoenergetic electron beam. The initial conditions (at $z = 0$) imposed on the electron beam are chosen such that the particles are uniformly distributed in phase for $-\pi \leq \psi_0 \leq \pi$ in order to model the case of a continuous beam (i.e., the beam is not pre-bunched). Difficulties which arise from the inclusion of a necessarily finite number of electrons in the phase averages (12) were found to be overcome by the use of a Simpson's rule integrator for 61 particles per wave period. The use of larger numbers of electrons was found to result in discrepancies of considerably less than 1%. As in the integration of single-particle orbits in Sec. III, the wiggler field is assumed to increase adiabatically to a constant level over ten wiggler periods (20). The electromagnetic mode was chosen to correspond to the wave characterized by the highest linear growth rate. Thus if the equilibrium orbits are characterized by the steady-state trajectories described in Sec. III in the constant- B_w region, then the frequency and wave vector are determined by the intersection of the electrostatic beam mode

$$\omega = (k - \kappa)v_{||} \quad (21)$$

and the transverse electromagnetic mode

$$\omega^2 - k^2 c^2 - \frac{\omega_b^2 (\omega - k_+ v_{||})}{\gamma (\omega - \Omega_0/\gamma - k_+ v_{||})} = 0, \quad (22)$$

where

$$k = k_+ + k_w, \quad \kappa \equiv \omega_b \Phi^{1/2} / \gamma^{1/2} \gamma_z v_{||},$$

$$\Phi \equiv 1 - \frac{\Omega_0 \beta_w^2 \gamma_z^2}{(1 + \beta_w^2) \Omega_0 - \gamma k_w v_{||}}, \quad (23)$$

and $\beta_w \equiv v_w/v_{||}$. Finally, the initial level of fluctuations in the space-charge field is assumed to be zero.

Insofar as the electron orbits approximate the steady-state trajectories, it can be expected that the radiation field will experience a period of exponen-

tial growth (at a rate consistent with the linear theory) prior to saturation. As a consequence, a brief discussion of the linear dispersion equation is

$$[(\omega - kv_{\parallel})^2 - \kappa^2 v_{\parallel}^2](k - k_w - K_+)(k - k_w - K_-) \approx \frac{1}{4} \beta_w^2 \xi^2 k_w^2 \frac{v_{\parallel}}{c} \frac{\omega}{Kc} [\omega \gamma_z^{-2} \Phi(\omega - \Omega_0/\gamma - k_+ v_{\parallel}) - \Omega_0(\omega - kv_{\parallel})/\gamma], \quad (24)$$

where $\xi \equiv \omega_b/\gamma^{1/2} k_w c$ is the beam strength parameter, $K^2 \equiv (\omega^2 - \omega_b^2/\gamma)/c^2$,

$$K_{\pm} \equiv \frac{1}{2} \left[K + \frac{\omega - \Omega_0/\gamma}{v_{\parallel}} \right] \pm \frac{1}{2} \left[(\Delta K)^2 + 2\xi^2 k_w^2 \frac{\Omega_0}{\gamma K v_{\parallel}} \right]^{1/2}, \quad (25)$$

and $\Delta K \equiv K - (\omega - \Omega_0/\gamma)/v_{\parallel}$. If the beam strength parameter is sufficiently small that $\xi \ll \gamma_z \times (B_w/B_0)^{2/3}$ and $\gamma(B_w/B_0)^{2/3} \Phi^{1/2}$, then (24) reduces still further to a more familiar cubic dispersion equation⁹

$$\delta k(\delta k + 2\kappa)(\delta k - \Delta k) \approx -\frac{\beta_w^2}{4} \xi^2 k_w^2 \beta_{\parallel}^{-1} \Phi \frac{\omega}{\gamma_z^2 v_{\parallel}}, \quad (26)$$

where $\delta k \equiv k - \omega/v_{\parallel} - \kappa$, $\beta_{\parallel} \equiv v_{\parallel}/c$, and $\Delta k \equiv k_w + K - \omega/v_{\parallel} - \kappa$ is the frequency mismatch parameter.

The "strong-pump" (or Compton scattering) regime is obtained when $|\delta k| \gg |2\kappa|$. In this limit, (26) can be approximated as

$$(\delta k)^2(\delta k - \Delta k) \approx -\frac{\beta_w^2}{4} \xi^2 k_w^2 \beta_{\parallel}^{-1} \Phi \frac{\omega}{\gamma_z^2 v_{\parallel}}, \quad (27)$$

and peak growth occurs when $\Delta k \approx 0$ at which point

$$(\delta k)_{\max} \approx \frac{1}{2} (1 \pm i\sqrt{3}) \left(\frac{1}{2} \beta_w^2 \xi^2 \beta_{\parallel}^{-1} \Phi \right)^{1/3} k_w. \quad (28)$$

As a consequence, the requirement for Compton scattering to be valid becomes

$$\kappa \ll \frac{1}{16} \beta_w^2 \gamma_z^2 \beta_{\parallel} k_w. \quad (29)$$

The opposite (Raman scattering) regime occurs when $|2\kappa| \gg |\delta k|$, and (26) can be represented in the form

$$(\delta k)^2 - \Delta k \delta k + \frac{\beta_w^2}{4} \gamma_z^2 \beta_{\parallel} \kappa k_w \approx 0. \quad (30)$$

Peak growth is again found for $\Delta k \approx 0$, where

$$(\delta k)_{\max} \approx \frac{1}{2} i \beta_w \gamma_z k_w (\beta_{\parallel} \kappa/k_w)^{1/2}. \quad (31)$$

of interest. The linear dispersion equation can be reduced to the following quartic equation in k_+ (> 0) (Ref. 9):

Therefore the Raman regime is found when

$$\kappa \gg \frac{1}{8} \beta_w^2 \gamma_z^2 \beta_{\parallel} k_w. \quad (32)$$

It should be observed that the criterion defining the Raman and Compton scattering regimes is dependent upon B_0 as well as on the beam and pump strengths. As a result, it is possible to make a transition from one to the other regime as a function solely of axial guide field. Since the principal objective of this paper is to examine the efficiency enhancement of an FEL amplifier in the presence of an axial guide field, the results of the simulation will be compared with the more complete form of the dispersion given by Eq. (24), and not by the idealized Raman and Compton regime approximations. It will be shown at a later stage of the discussion that the agreement between the linear theory as represented by Eq. (24) and the numerical simulation is excellent.

An example of the simulation results is shown in Fig. 4 in which the radiation-field amplitude $\delta a(z)$ and the growth rate $\Gamma(z) (\equiv d \ln \delta a / dz)$ are plotted as functions of axial position for $\Omega_0/\gamma k_w c = 0.0$

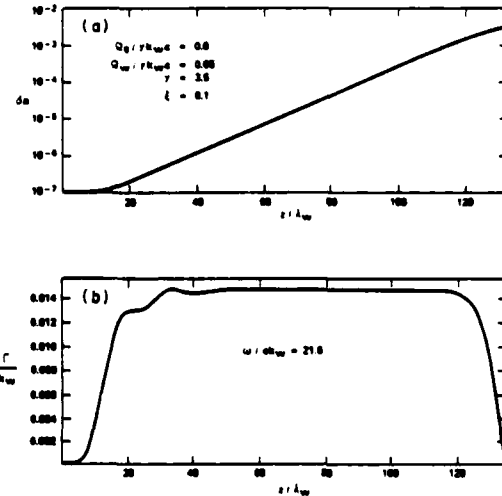


FIG. 4. Graphs of (a) the radiation-field strength and (b) growth rate, vs axial position for $\Omega_0/\gamma k_w c = 0.0$, $\Omega_w/\gamma k_w c = 0.05$, $\gamma = 3.5$, and $\xi = 0.1$.

(i.e., no axial guide field), $\Omega_w/\gamma k_w c = 0.05$, $\gamma = 3.5$, and $\delta\alpha(z=0) = 10^{-7}$. As such, the illustrated calculation corresponds to the orbit calculation shown in Fig. 2. It is evident from the figure that, after an initial transient phase ($z/\lambda_w \leq 29.1$), an extended region of linear (or exponential) growth occurs as evidenced by the constancy of the growth rate. During this phase of the interaction, the growth rate as computed by the simulation is $\Gamma/k_w \approx 0.0146$, which is in good agreement with the linear theory (24) which predicts a growth rate of $\Gamma_{\text{lin}}/k_w \approx 0.0145$. Note that this corresponds to peak growth at a frequency $\omega/ck_w \approx 21.6$.

Fluctuations in the growth rate found in the simulation are $\Delta\Gamma/k_w \approx \pm 0.0002$, which is to be expected on the basis of the orbit calculation (Fig. 2) due to the relatively small fluctuation about the steady-state trajectory. Saturation begins to occur at $z/\lambda_w \approx 114.1$, after which the growth rate rapidly decreases to zero at $z/\lambda_w \approx 127.3$. At saturation, the radiation-field amplitude is $(\delta\alpha)_{\text{sat}} \approx 2.56 \times 10^{-3}$ which corresponds to an efficiency of 3.65%. Saturation occurs by means of particle trapping, and this will be discussed in detail later in this section.

As shown in Sec. II, increases in the axial guide field initially result in increasing fluctuations in the electron orbits about the steady-state trajectories. In addition, it has been shown that the linear growth rate also increases with B_0 for the group-I class of orbits.^{8,9} Therefore in order to determine the nonlinear effects the axial guide field and the adiabatic increase in the wiggler field, a series of calculations has been performed over a wide range of B_0 . The results of the simulation for $\Omega_0/\gamma k_w c = 0.5$ show the average growth rate during the linear phase of the interaction to be $\Gamma/k_w \approx 0.030$ with a fluctuation of $\Delta\Gamma/k_w \approx \pm 0.003$, which remains in good agreement with the linear-theory result (24) of $\Gamma_{\text{lin}}/k_w \approx 0.029$. The increased growth rate leads to a decrease in the distance to saturation, which now occurs at $z_{\text{sat}}/\lambda_w \approx 67.5$ at a field level of $(\delta\alpha)_{\text{sat}} \approx 3.30 \times 10^{-3}$. The wave frequency for this case (at peak growth) was $\omega/ck_w \approx 19.4$, and the efficiency at saturation has increased to 4.92%. The decrease in frequency for this case resulted from a decrease in the axial velocity of the beam (see Fig. 1).

Increases in the axial guide field above this level (but still corresponding to group-I orbits) lead to larger fluctuations in both the orbits and the growth rate in the linear regime which culminates in a chaotic interaction at the transition to orbital instability at $\Omega_0/\gamma k_w c \approx 0.76$. A transitional case is illustrated in Fig. 5 for which $\Omega_0/\gamma k_w c = 0.7$ and a frequency corresponding to peak growth of $\omega/ck_w \approx 14.2$, in which the magnitude of the fluctu-

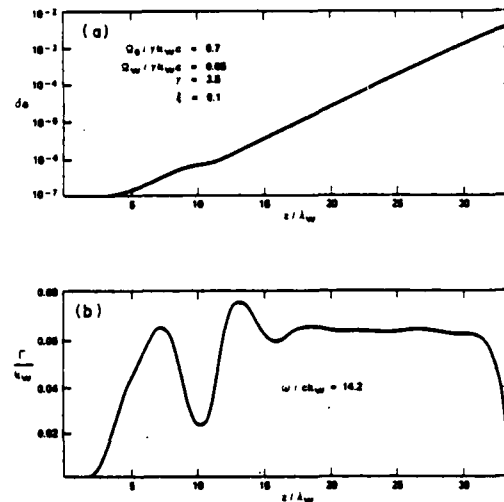


FIG. 5. Graphs of (a) the radiation-field strength and (b) growth rate, vs axial position for $\Omega_0/\gamma k_w c = 0.7$, $\Omega_w/\gamma k_w c = 0.05$, $\gamma = 3.5$, and $\xi = 0.1$.

tations in the growth rate is apparent. It should be noted, though, that for $20 \leq z/\lambda_w \leq 30$ the growth rate is relatively constant and has an average value of $\Gamma/k_w \approx 0.063$, which is comparable to the result of the linear theory of $\Gamma_{\text{lin}}/k_w \approx 0.060$. The increase in the growth rate results in a still further decline in the distance to saturation which now occurs at $z_{\text{sat}}/\lambda_w \approx 32.6$; however, while $(\delta\alpha)_{\text{sat}} \approx 4.09 \times 10^{-3}$ represents a continuing increase in the radiation field, the efficiency at saturation has decreased to 4.02%. The decline in the efficiency is attributable to the decrease in the wave frequency.

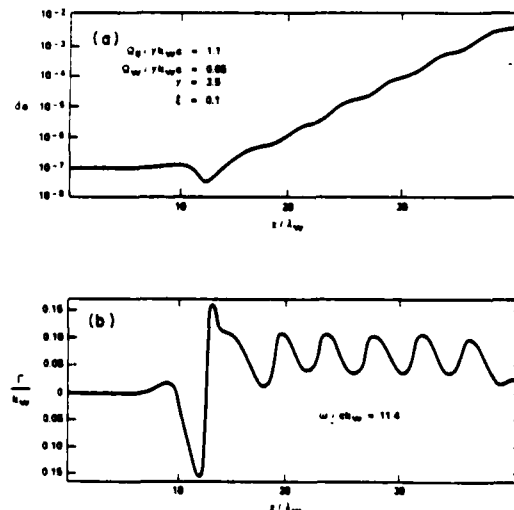


FIG. 6. Graphs of (a) the radiation-field strength and (b) growth rate, vs axial position for $\Omega_0/\gamma k_w c = 1.1$, $\Omega_w/\gamma k_w c = 0.05$, $\gamma = 3.5$, and $\xi = 0.1$.

For levels of B_0 such that $\Omega_0/\gamma k_w c > 0.76$ the electron trajectories correspond to perturbations about group-II-type orbits. However, as seen in Fig. 3, large divergences from the steady-state orbits occur for $\Omega_0/\gamma k_w c = 1.0$ and are characteristic of the low-bulk axial velocities in this regime. The implication of such orbit behavior is that since (1) the growth rate must also exhibit large-scale oscillations and (2) the resonant frequency is relatively low, the interaction efficiency can be expected to be small. Such an expectation is borne out by the simulation results as shown in Fig. 6 for $\Omega_0/\gamma k_w c \simeq 1.1$ and a frequency at peak growth of $\omega/c k_w = 11.4$. The system evidently shows the expected large-scale fluctuations in the growth rate ($\Delta\Gamma/k_w \simeq \pm 0.036$) about a mean value of $\Gamma/k_w \simeq 0.072$ after the transients have decayed ($z/\lambda_w \geq 20$). Note that the linear theory predicts a growth rate of $\Gamma_{\text{lin}}/k_w \simeq 0.056$ on the basis of the steady-state orbits, which is well within this range. Saturation occurs at $z_{\text{sat}}/\lambda_w \simeq 41.1$ for $(\delta a)_{\text{sat}} \simeq 4.91 \times 10^{-3}$; however, while the field amplitude is relatively high, the low frequency of the mode results in an efficiency of 3.88% which is comparable to the zero-axial-field limit. It should be remarked here that the case in which $\Omega_0/\gamma k_w c = 1.0$ (corresponding to Fig. 3) is not shown here since it represents a still more extreme example of the results of the large oscillations in the single-particle orbits and has a still lower efficiency.

Further increases in the axial guide field correspond with increases in the resonant frequency and decreases in the departure from the steady-state single-particle trajectories. As a consequence, the evolution of the radiation fields becomes more regular as well. For $\Omega_0/\gamma k_w c = 1.5$ and a frequency at peak growth of $\omega/c k_w = 20.3$, the simulation gives $\Gamma/k_w \simeq 0.021$ with a variation in the growth rate of less than 1%. It should be noted here that we also recover a growth rate of $\Gamma_{\text{lin}}/k_w \simeq 0.021$ from the linear theory (24). Saturation occurs at $z_{\text{sat}}/\lambda_w = 93.1$ for a field level of $(\delta a)_{\text{sat}} \simeq 3.19 \times 10^{-3}$ and an efficiency of 5.02%.

A summary of the frequencies and growth rates for the various simulations is given in Fig. 7 in which we plot $\omega/c k_w$ and Γ/k_w vs $\Omega_0/\gamma k_w c$. The curves for the frequency represent the variation in the resonant frequency at peak growth found from the intersection of the dispersion relations in Eqs. (21) and (22) for the appropriate value of v_{\parallel} from the steady-state trajectory. These values represent the frequencies used in the simulations. The solid line in the plot of Γ/k_w represents the results of the linear theory (24), again, for the appropriate steady-state trajectory while circles are used to denote the results found from the simulation in the linear re-

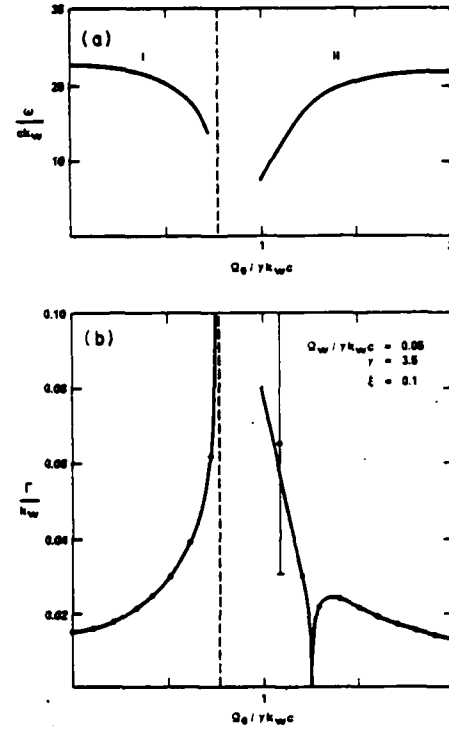


FIG. 7. Plots of (a) the peak growth rate and (b) the corresponding resonant frequency, vs axial field strength. Circles indicate the growth rates obtained from the numerical simulation.

gime. As seen in the figure, the agreement between the simulation and the linear theory is excellent. For the cases shown, it is only when $\Omega_0/\gamma k_w c = 1.1$ that the growth rates differ by more than about 2%, and this is due to the relatively large divergence of the single-particle orbits from the steady state. However, this problem no longer appears for $\Omega_0/\gamma k_w c = 1.2$, and we conclude that (for the parameters under study) difficulties resulting from nonsteady-state single-particle orbits are important only for $0.76 \leq \Omega_0/\gamma k_w c \leq 1.1$, where both the frequency and efficiency are low. Consequently, this regime will be ignored in the discussion of the overall radiation efficiency and saturation mechanism.

The energy-conversion efficiency and the distance to saturation are shown in Fig. 8 as functions of the axial magnetic field. The efficiency is defined to be the ratio of the total energy lost by the electrons through the interaction to the initial energy and may be shown by computation of the Poynting flux to be

$$\eta \simeq \frac{1}{\xi^2 \gamma (\gamma - 1) \beta_{\parallel}} \left[\frac{\omega}{c k_w} (\delta a)_{\text{sat}} \right]^2 \quad (33)$$

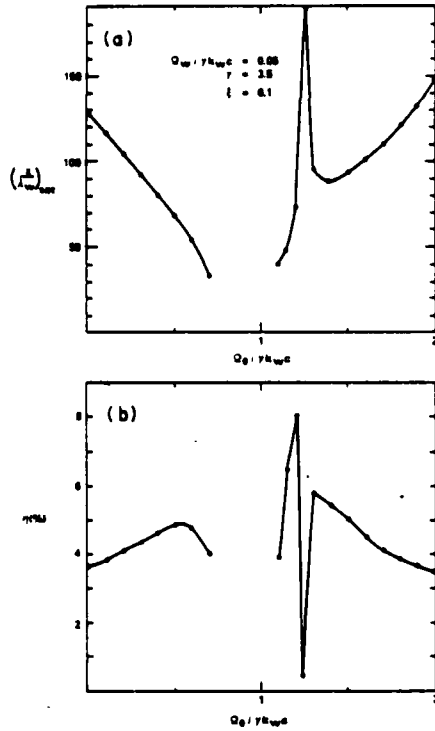


FIG. 8. Graphs of (a) the distance to saturation and (b) saturation efficiency, vs axial field strength.

It is evident from the figure that substantial enhancements of the efficiency are possible over that found in the absence of an axial guide field. For parameters corresponding to the group-I orbits, the peak efficiency is approximately 5% and occurs at $\Omega_0/\gamma k_w c \approx 0.5$ for the chosen parameters and constitutes a 37% enhancement over the efficiency found

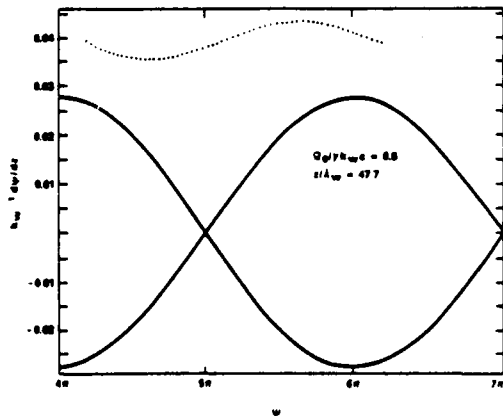


FIG. 9. Plot of the phase-space distribution for $\Omega_0/\gamma k_w c = 0.5$ and $z/\lambda_w = 47.7$ in the linear regime.

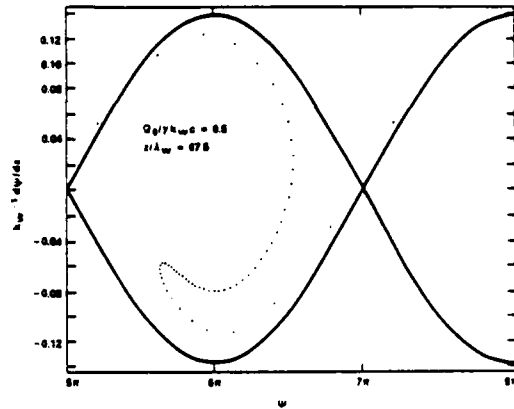


FIG. 10. Graph of the phase-space distribution for $\Omega_0/\gamma k_w c = 0.5$ and $z/\lambda_w = 67.5$ at saturation.

when no guide field is present. Note also that saturation occurs over a much shorter interaction length. However, the greatest enhancements in the efficiency are found for the group-II class of trajectories, for which a peak efficiency of approximately 8.09% is found for $\Omega_0/\gamma k_w c \approx 1.25$ and corresponds to an efficiency enhancement of 122% relative to the $B_0 \rightarrow 0$ limit. It is important to bear in mind, however, that these enhancements in the efficiency occur at the expense of decreases in the resonant frequency of the interaction (see Fig. 7). Finally, the low efficiency found for $\Omega_0/\gamma k_w c \approx 1.25$ corresponds to parameters for which $|\Phi| \ll 1$. In this regime (which is discussed in detail in Refs. 3 and 9) the ponderomotive potential and, hence, the linear growth rate vanish (Fig. 7).

As mentioned previously, saturation occurs by means of particle trapping in the ponderomotive potential which results from the beating of the wiggler and radiation fields. An example of this is shown in Figs. 9 and 10 in which the positions of the particles (represented by the dots) in phase space ($\psi, d\psi/dz$) are plotted for $\Omega_0/\gamma k_w c \approx 0.5$ (i.e., group-I type of orbits) and $z/\lambda_w = 47.7$ and 67.5 , respectively. The solid lines in the figures represent the separatrix which encloses trapped (i.e., bounded) phase-space trajectories. It should be noted, however, that while the positions of the particles represent the results of the simulation, the separatrix represents an approximation as it is derived from a perturbation about the exact steady-state orbits described in Sec. II. As such the separatrix is strictly valid only insofar as the particle velocities are close to those for the helical trajectories, for which¹²

$$\frac{d^2 \psi}{dz^2} = \frac{c^2(k + k_w)^4}{\gamma^2 \omega^2} \frac{v_w}{c} \Phi \delta a \sin \psi. \quad (34)$$

The separatrix, therefore, is given by

$$\frac{d}{dz} \psi = \pm 2 \frac{c(k+k_w)^2}{\gamma_z \omega} \left(\frac{v_w}{\gamma c} \Phi \delta a \right)^{1/2} \sin \left(\frac{\psi}{2} \right), \quad (35)$$

when $v_w \Phi > 0$, and

$$\frac{d}{dz} \psi = \pm 2 \frac{c(k+k_w)^2}{\gamma_z \omega} \left(\frac{v_w}{\gamma c} \Phi \delta a \right)^{1/2} \cos \left(\frac{\psi}{2} \right), \quad (36)$$

when $v_w \Phi < 0$. Because of this, the phase-space evolution of the particle distribution is dependent upon the signs of both v_w and Φ . For the group-I class of orbits (which includes the zero-guide-field limit) $v_w < 0$ and $\Phi > 0$ and the separatrix is determined by Eq. (36). However, the situation is more complicated for the group-II class of trajectories. In this case, while $v_w > 0$ for all the trajectories, Φ is less than zero for $\Omega_0/\gamma k_w c \leq 1.25$ (for the parameters chosen), and greater than zero for axial field strengths above this critical value. Thus one must distinguish between these two regimes in the analysis of the phase-space structure of the interaction. Since the single-particle trajectories are seen to be close to the steady-state orbits, it is expected that the separatrix shown in the figures [given by Eq. (36)] is a reasonable approximation.

The initial phase-space electron distribution (at $z=0$) is uniform in that $d\psi/dz = k+k_w - \omega/v_{z0}$ over $-\pi \leq \psi \leq \pi$ for all the particles. Figure 9 represents the phase-space distribution at a relatively late point in the linear phase of the interaction. It is evident, therefore, that the phase-space bunching of the particles has begun but that the trapping of the electrons has not yet occurred as the trajectories

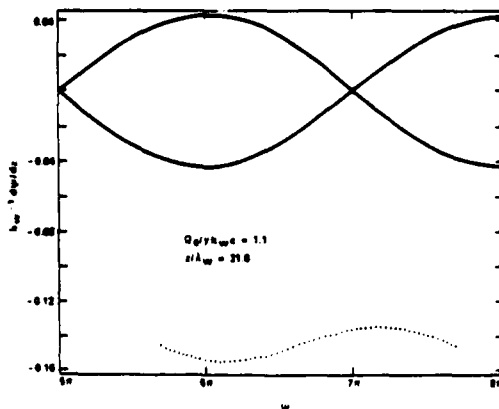


FIG. 11. Plot of the phase-space distribution for $\Omega_0/\gamma k_w c = 1.1$ and $z/\lambda_w = 31.8$ in the linear regime.

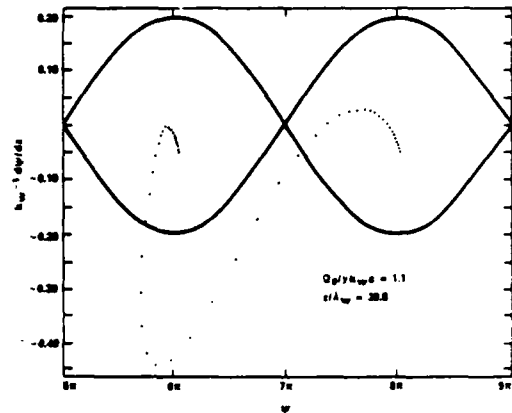


FIG. 12. Graph of the phase-space distribution for $\Omega_0/\gamma k_w c = 1.1$ and $z/\lambda_w = 39.8$ at saturation.

remain unbounded. In contrast, Fig. 10 represents the phase-space distribution at saturation, and it is clear that while two particles remain on unbounded orbits outside the separatrix, the bulk of the electrons has been trapped. The results shown here are in agreement with those found by Sprangle *et al.*¹¹

It was pointed out previously that the phase-space behavior of the electron beam is somewhat different when $\Phi < 0$. This discrepancy arises from the fact that the electron velocity is greater than the phase velocity of the ponderomotive wave [equal to $\omega/(k+k_w)$] at peak growth ($d\psi/dz > 0$) when $\Phi > 0$, but less than the phase velocity of the ponderomotive wave when $\Phi < 0$. This can be illustrated by consideration of the small-signal gain in the single-particle regime,^{3,12}

$$G_L = \frac{\beta_w^2 \xi^2}{16\beta_{||}^2} L^3 k_w^2 k \Phi \frac{d}{d\theta} \left(\frac{\sin\theta}{\theta} \right)^2, \quad (37)$$

where $\theta = -\frac{1}{2} L d\psi/dz$. Therefore when $\Phi > 0$ peak gain occurs for $\theta \approx -1.3$ and $d\psi/dz > 0$. However, in the opposite case when $\Phi < 0$, the peak gain occurs at $\theta \approx 1.3$ and $d\psi/dz < 0$. This type of phase-space behavior is, indeed, found in the simulation and is evident in Figs. 11 and 12 in which we plot the phase-space distributions for $\Omega_0/\gamma k_w c = 1.1$ and $z/\lambda_w = 31.8$ (in the linear regime) and $z/\lambda_w = 39.8$ (at saturation). The separatrix in these figures was calculated from Eq. (36). Note that while the bulk of the particles is trapped on bounded phase-space trajectories at saturation (and that extreme phase bunching has occurred), a greater proportion of the particles appears to be outside the separatrix on unbounded orbits than in the other cases shown. However, this observation must be made in view of the fact that the single-particle orbits resemble those shown in Fig. 3, and the orbits

are widely divergent from the steady-state case. Thus the separatrix is difficult to determine precisely, and may differ greatly from that shown.

V. SUMMARY AND DISCUSSION

The principal objective of the study described in this paper is to examine the effect of an axial guide field on the nonlinear stage of the FEL interaction. Previous studies of the linear regime³⁻⁹ have revealed that large enhancements in the growth rate are possible, and the primary focus of this work is directed toward the question of whether enhancements in the nonlinear efficiency are possible as well. To this end, a self-consistent set of field and particle orbit equations is derived for a FEL amplifier which describes the evolution of both the wave amplitudes and trajectories for an ensemble of particles. It is important to observe that although no particle distribution function is explicitly included in the analysis, the source currents used in Maxwell's equations constitute time averages over the microscopic electron currents, and the level of the formulation is kinetic. The equations are then integrated numerically as functions of axial position subject to initial conditions which describe the interaction of a uniform electron beam with the guide and wiggler system. In fact, entry of the beam into the interaction region is effected by means of an adiabatically increasing wiggler amplitude which reaches a constant level after ten wiggler periods. Finally, inclusion of fluctuating space-charge fields in the formulation permits analysis of both the single-particle (Compton) and collective (Raman) regimes of operation.

The effect of the initial adiabatic increase of the wiggler field on the single-particle orbits was considered by numerical integration of the orbit equations in the absence of electromagnetic and electrostatic fields. The purpose of this phase of the analysis is the determination of the types of orbit which result; in particular, whether the electron orbits resemble the steady-state (helical) trajectories upon which the linear theories of the interaction are based. As such, the question of the relevance of the linear theories to both the simulation and to actual experiments¹³ is addressed. On the basis of this

work it was concluded that, for the configuration used, the electron orbits deviate only slightly from the helical trajectories except when $\Omega_0 \sim \gamma k_w c$, where the orbits are seen to execute large-scale oscillations about the steady-state trajectories. As a result, the linear theories are expected to be relevant over a wide range of parameters.

In fact, the numerical integration of the coupled particle-field equations bears out this conjecture. The results shown in Figs. 4-6 show that (except when $\Omega_0 \sim \gamma k_w c$), after an initial transient phase, an extended region of linear (i.e., exponential) growth occurs with growth rates which are in excellent agreement with the linear theory (see Fig. 7). Even in cases where substantial deviations from the steady-state trajectories occur, the growth rate is seen to oscillate about the predicted linear result (Fig. 6). Saturation is found to occur by means of particle trapping in the ponderomotive potential, and substantial enhancements of more than 100% are observed over the efficiency in the absence of an axial guide field. The greatest enhancements occur for parameters consistent with the group-II type of orbit and relatively large axial guide fields ($\Omega_0 \sim 1.2\gamma k_w c$) which is consistent with the results found in the experiment at the Naval Research Laboratory using the VEBA accelerator.¹³ It should be noted, however, that such enhancements in the efficiency correspond to decreases in the axial velocity of the electrons (and to increases in the transverse velocity) due to the presence of the axial guide field and, therefore, also correspond to decreases in the resonant frequency of the interaction.

Finally, it should also be remarked that these results have been obtained for a monoenergetic electron beam. Introduction of a finite energy spread can have important consequences on the growth rates and saturation levels. In fact, recent results¹⁴ using a full-scale particle simulation indicate that decreases in the efficiency are to be expected when a finite energy spread occurs.

ACKNOWLEDGMENTS

This work was supported under NAVSEA Contract No. SF68-342-602. The author would like to thank Dr. P. Sprangle, Dr. C. M. Tang, and Dr. I. B. Bernstein for helpful and stimulating discussions.

*Permanent address: Science Applications, Inc., 1710 Goodridge Drive, P.O. Box 1303, McLean, VA 22102.

¹L. Friedland, *Phys. Fluids* **23**, 2376 (1980).

²H. P. Freund and A. T. Drobot, *Phys. Fluids* **25**, 736 (1982).

³H. P. Freund, P. Sprangle, D. Dillenburg, E. H. da Jornada, B. Liberman, and R. S. Schneider, *Phys. Rev. A* **24**, 1965 (1981).

⁴P. Sprangle, V. L. Granatstein, and L. Baker, *Phys. Rev. A* **12**, 1697 (1975).

- ⁵T. Kwan and J. M. Dawson, *Phys. Fluids* **22**, 1089 (1979).
- ⁶L. Friedland and J. L. Hirshfield, *Phys. Rev. Lett.* **44**, 1456 (1980).
- ⁷I. B. Bernstein and L. Friedland, *Phys. Rev. A* **23**, 816 (1981).
- ⁸L. Friedland and A. Fruchtman, *Phys. Rev. A* **25**, 2693 (1982).
- ⁹H. P. Freund, P. Sprangle, D. Dillenburg, E. H. da Jornada, R. S. Schneider, and B. Liberman, *Phys. Rev. A* **26**, 2004 (1982).
- ¹⁰L. Friedland and I. B. Bernstein, *Phys. Rev. A* **26**, 2778 (1982).
- ¹¹P. Sprangle, C. M. Tang, and W. M. Manheimer, *Phys. Rev. A* **21**, 302 (1980).
- ¹²S. H. Gold, R. H. Jackson, R. K. Parker, H. P. Freund, V. L. Granatstein, P. C. Efthimion, M. Herndon, and A. K. Kinkead, in *Physics of Quantum Electronics: Free-Electron Generators of Coherent Radiation*, edited by S. F. Jacobs, G. T. Moore, H. S. Pilloff, M. Sargent, M. O. Scully, and R. Spitzer (Addison-Wesley, Reading, Mass., 1982), Vol. 9, p. 741.
- ¹³R. K. Parker, R. H. Jackson, S. H. Gold, H. P. Freund, V. L. Granatstein, P. C. Efthimion, M. Herndon, and A. K. Kinkead, *Phys. Rev. Lett.* **48**, 238 (1982).
- ¹⁴T. J. T. Kwan and C. M. Snell (unpublished).

APPENDIX F

UNSTABLE ELECTROSTATIC BEAM MODES IN
FREE-ELECTRON-LASER SYSTEMS ; 70 2382



Unstable electrostatic beam modes in free-electron-laser systems

H. P. Freund* and P. Sprangle

Naval Research Laboratory, Washington, D.C. 20375

(Received 29 March 1983)

The electrostatic stability of the free-electron laser is studied for a configuration in which a relativistic electron beam propagates through combined helical wiggler and axial guide fields. Instability is found for certain specific parameter regimes which, in the beam frame, is shown to be purely growing and to require the presence of both the wiggler and axial guide fields. The electrostatic stability is also studied for a configuration which consists of a linearly polarized wiggler and an axial guide field, for which analogous results are found.

The stability properties of a free-electron-laser (FEL) configuration in which a relativistic electron beam propagates through a combined helical wiggler and axial guide field was investigated by many authors.¹⁻⁹ It was pointed out by Freund *et al.*⁹ that, in addition to the coherent radiation process, the electrostatic beam modes are intrinsically unstable for a specific class of operating parameters. It is our purpose here to expand upon the discussion in Ref. 1 and to discuss the underlying physical mechanism behind such an instability. To this end, we choose to analyze an idealized model which consists of a cold relativistic fluid described by

$$\frac{\partial}{\partial t} n + \nabla \cdot (n \vec{v}) = 0, \quad (1)$$

$$\frac{d}{dt} \vec{v} = -\frac{e}{\gamma m} \left(\left(\vec{1} - \frac{1}{c^2} \vec{v} \vec{v} \right) \cdot \delta \vec{E} + \frac{1}{c} \vec{v} \times \vec{B} \right), \quad (2)$$

$$\frac{d}{dt} \gamma = -\frac{e}{mc^2} \vec{v} \cdot \delta \vec{E}, \quad (3)$$

where n and \vec{v} describe the electron density and velocity, respectively, $\gamma = (1 - v^2/c^2)^{-1/2}$.

$$\vec{B} = B_0 \hat{e}_z + B_w (\hat{e}_x \cos k_w z + \hat{e}_y \sin k_w z)$$

is the static magnetic field, δE is the electrostatic field (which is assumed to constitute a small perturbation), and $d/dt = \partial/\partial t + \vec{v} \cdot \nabla$ is a convective derivative. The equilibrium state to zeroth order in δE is assumed to be homogeneous (i.e., $\nabla n_0 = 0$), and is characterized by a velocity^{10,11} $\vec{v}_0 = v_w \hat{e}_1 + v_{||} \hat{e}_3$, where $v_{||}$ is a constant, $v_w = \Omega_w v_{||} / (\Omega_0 - k_w v_{||})$, $\Omega_{0,w} = |e B_{0,w} / \gamma m c|$, and

$$\hat{e}_1 = \hat{e}_x \cos k_w z + \hat{e}_y \sin k_w z,$$

$$\hat{e}_2 = -\hat{e}_x \sin k_w z + \hat{e}_y \cos k_w z,$$

and

$$\hat{e}_3 = \hat{e}_z,$$

define an orthogonal coordinate frame rotating with the wiggler field. Observe that conservation of energy imposes the requirement that $v_w^2 + v_{||}^2 = (1 - \gamma_0^{-2}) c^2$.

Under the assumption of plane-wave solutions of the

form $\delta E = \delta \hat{E} \exp(ikz - i\omega t)$, Eqs. (2) and (3) can be reduced to the form

$$-i(\omega - k v_{||}) \delta \hat{v}_1 + (\Omega_0 - k_w v_{||}) \delta \hat{v}_2 = \frac{e}{\gamma_0 m} \beta_w \frac{v_{||}^2}{c^2} \delta \hat{E}, \quad (4)$$

$$(\Omega_0 - k_w v_{||}) \delta \hat{v}_1 + i(\omega - k v_{||}) \delta \hat{v}_2 + \Omega_0 \beta_w \delta \hat{v}_3 = -\frac{i e}{\gamma_0 m} \beta_w \frac{v_{||}^2}{c^2} \frac{k_w v_{||}}{\omega - k v_{||}} \delta \hat{E}, \quad (5)$$

$$\Omega_w \delta \hat{v}_2 + i(\omega - k v_{||}) \delta \hat{v}_3 = \frac{e}{\gamma_0 \gamma_{||} m} \delta \hat{E}, \quad (6)$$

to first order in the electric field, where $\beta_w = v_w/v_{||}$ and $\gamma_{||} = (1 - v_{||}^2/c^2)^{-1/2}$. The stability properties, therefore, are determined by Eqs. (4)-(6) in conjunction with the following combination of the continuity equations and Poisson's equation,

$$\frac{e}{m} \delta \hat{E} = \frac{i \omega_b^2}{\omega - k v_{||}} \delta \hat{v}_3, \quad (7)$$

where $\omega_b = (4\pi e^2 n_0/m)^{1/2}$ is the beam plasma frequency.

It is clear from the z component of the momentum transfer Eq. (6) that in the absence of a wiggler field there is no coupling between the axial and transverse components of the velocity, and the dispersion relation reduces to the well-known positive and negative energy beam modes $\omega = k v_{||} \pm \omega_b / \gamma_{||}^{1/2}$. However, the parallel-transverse coupling in the presence of the static fields can alter the dielectric properties of the medium. Elimination of $\delta \hat{v}_1$ from Eqs. (4) and (5) shows that

$$\begin{aligned} & [(\omega - k v_{||})^2 - (\Omega_0 - k_w v_{||})^2] \delta \hat{v}_2 \\ & = \Omega_0 \beta_w \left[i(\omega - k v_{||}) \delta \hat{v}_3 - \frac{e}{\gamma_0 m} \frac{v_{||}^2}{c^2} \delta \hat{E} \right], \quad (8) \end{aligned}$$

and $\delta \hat{v}_2$ is nonzero only if both the axial guide and wiggler fields are present. Thus, the modification to the dispersion properties of the electrostatic beam modes which is of interest here is possible only through the combination of both magnetic fields. The instability can be readily demonstrated by combination of Eqs. (6)-(8) to obtain the following dispersion equation:

$$(\omega - k v_{||})^2 = \frac{\omega_b^2}{\gamma_0 \gamma_{||}^2} \left[1 - \frac{\gamma_{||}^2 \beta_w^2 \Omega_0 (\Omega_0 - k_w v_{||})}{[(1 + \beta_w^2) \Omega_0 - k_w v_{||}] (\Omega_0 - k_w v_{||}) - (\omega - k v_{||})^2} \right], \quad (9)$$

The regime considered in Ref. 1, and which is most relevant to current FEL experiments, is that in which $|\omega - kv_{\parallel}| \ll |\Omega_0 - kv_{\parallel}|$. As a result, the dispersion equation is of the form

$$(\omega - kv_{\parallel})^2 = \frac{\omega_0^2}{\gamma_0 \gamma_{\parallel}^2} \Phi, \quad (10)$$

where

$$\Phi = 1 - \frac{\gamma_{\parallel}^2 \beta_w^2 \Omega_0}{(1 + \beta_w^2) \Omega_0 - kv_{\parallel}} \quad (11)$$

It is evident that instability results when $\Phi < 0$. Furthermore, the instability is purely growing (i.e., the real part of the frequency is zero) in the beam frame. Additional information on the parameters necessary for instability is given in Ref. 1. Finally, solution of the complete dispersion equation [Eq. (9)] does not qualitatively affect this conclusion.

In order to understand the underlying physics we consider motion in the absence of an axial guide field. It is clear from (6) that the modification of the dielectric properties results from the presence of a $\delta v_2 \hat{e}_2 \times \vec{B}_w$ force in the momentum-transfer equation. Hence, the essential point is to determine a source for an oscillatory velocity in the direction of \hat{e}_2 . The possible sources for such a motion are evident from the two-component of the momentum-transfer equation [Eq. (2)] and includes a $\nabla \times \vec{B}$ force

$$F_{\nabla \times \vec{B}} = -\frac{e}{\gamma_0 mc} (\delta \nabla \times \vec{B}_w) \cdot \hat{e}_2 = -\Omega_w \delta v_2, \quad (12)$$

convection (note that $\nabla \hat{e}_1 = k_w \hat{e}_2$) due to the centripetal force arising from the rotation (or gradient) of the wiggler field,

$$F_{\text{con}} = -(\delta \nabla \cdot \nabla \vec{v}_0) \cdot \hat{e}_2 = -k_w v_w \delta v_2, \quad (13)$$

as well as a relativistic contribution which arises from the variation in the total energy. When no axial field is present, $v_w = -\Omega_w/k_w$ and the convection exactly balances the $\nabla \times \vec{B}$ force with the result that no net velocity in the \hat{e}_2 direction occurs. The relativistic contribution is the sole remaining source, but it can be shown to drive oscillatory motion only in the \hat{e}_1 direction. However, the axial guide field tends to increase the transverse velocity (i.e., v_w), and results in enhanced convection as well as a net source which drives an oscillation in the \hat{e}_2 direction. As mentioned previously, the finite δv_2 causes a $\delta \nabla \times \vec{B}_w$ force in the axial direction which affects partial bunching and modifies the dispersive properties of the medium. As long as $k_w v_{\parallel} > \Omega_0$ the convection acts to oppose the $\nabla \times \vec{B}$ force (12), in part, and causes an effective enhancement in the plasma frequency (10). In contrast, when $k_w v_{\parallel} < \Omega_0$ the direction of the \hat{e}_1 component of the zeroth-order transverse velocity is reversed (i.e., $v_w > 0$), and convection tends to enhance the effect of the $\nabla \times \vec{B}$ force. It is in this regime that instability is found.

The actual motion in the case in which instability occurs may be summarized as follows. The electric field drives a fluctuation in the axial velocity which, in turn, causes a net velocity fluctuation in the \hat{e}_2 direction by the combined action of the Lorentz force and convection. This velocity then feeds back upon the axial velocity via the Lorentz force ($\delta v_2 \hat{e}_2 \times \vec{B}_w$). The feedback provides the dominant contribution to the axial velocity when

$$(1 - \gamma_{\parallel}^2 v_w^2/c^2) \Omega_0 < k_w v_{\parallel} < \Omega_0. \quad (14)$$

(i.e., $\Phi < 0$) and the net effect of the electric field is to drive axial velocity fluctuations counter to that produced by the "direct" action of the electric field. The combined action of the axial guide and wiggler fields results in a phase shift in the axial motion which causes electron bunching to occur in such a way that the electric field is enhanced. Thus, although this is a nonrelativistic effect, the system acts as though the electrons had a negative mass.

It is also of interest to determine whether an analogous instability exists for a configuration in which the static magnetic fields consist of a linearly polarized wiggler in combination with an axial guide field. In this case we represent the magnetic field in the form $\vec{B} = B_0 \hat{e}_z + B_w \sin k_w z \hat{e}_y$. The equilibrium orbits in this field geometry are

$$v_x = \alpha v_{\parallel} \cos k_w z,$$

$$v_y = \alpha \Omega_0 (k_w v_{\parallel})^{-1} v_{\parallel} \sin k_w z,$$

and

$$v_z = v_{\parallel},$$

where $\alpha = \Omega_w k_w v_{\parallel} / (\Omega_0^2 - k_w^2 v_{\parallel}^2)$ and oscillatory terms in $2k_w z$ (and higher) have been neglected. Conservation of energy, therefore, imposes the constraint $(1 + \beta_{\parallel}^2) v_{\parallel}^2 = (1 - \gamma_0^{-2}) c^2$, where $\beta_{\parallel}^2 = \frac{1}{2} \alpha^2 (1 + \Omega_0^2 / k_w^2 v_{\parallel}^2)$. Perturbation analysis of Eqs. (1)–(3) about this equilibrium state to first order in δE , and combination of the result with Eq. (7), therefore, yields the following dispersion equation:

$$(\omega - kv_{\parallel})^2 = \frac{\omega_0^2}{\gamma_0 \gamma_{\parallel}^2} \left[1 - \frac{\gamma_{\parallel}^2 \beta_{\parallel}^2 \Omega_0^2 (\Omega_0^2 + 3k_w^2 v_{\parallel}^2)}{(1 + \beta_{\parallel}^2) \Omega_0^2 - k_w^2 v_{\parallel}^2 (k_w^2 v_{\parallel}^2 - 3\beta_{\parallel}^2 \Omega_0^2)} \right] \quad (15)$$

in the limit in which $|\omega - kv_{\parallel}| \ll |\Omega_0 - kv_{\parallel}|$. This is analogous to the dispersion equation for the helical wiggler field (10), and instability is found when

$$\Omega_0^2 - \beta_{\parallel}^2 (\gamma_{\parallel}^2 - 1) \Omega_0^2 (\Omega_0^2 + 3k_w^2 v_{\parallel}^2) < k_w^2 v_{\parallel}^2 < \Omega_0^2. \quad (16)$$

As in the case of the helical wiggler, the instability is purely growing in the beam frame, and arises from the same physical mechanism.

The central question raised by this analysis is how the instability will affect the performance of the FEL. On the basis of a linearized theory it has been shown that the growth rates for the amplification of radiation are large (and exceed those found in the limit as $B_0 \rightarrow 0$), and the bandwidth is enhanced for the range of parameters leading to the electrostatic beam instability. However, since it might be expected that the electrostatic instability will lead to degradation of beam quality in the nonlinear regime, the effects of this instability on the saturation of the FEL are of prime importance. This question has been addressed by means of a particle simulation of a cold beam in an FEL amplifier,¹² and it was found that (for the parameters considered), the saturation efficiency is greatest when the electrostatic instability is present. It should be remarked that this conclusion is reinforced by experimental results^{13,14} in which maximum power was observed for parameters corresponding to the electrostatic instability. Thus, while the question of the effects of the electrostatic beam instability on the FEL has not been conclusively answered (i.e., a more complete param-

ter study of the nonlinear saturation efficiency is required, as in a knowledge of the effects of a finite velocity spread, it should not be concluded that these effects are necessarily deleterious.

ACKNOWLEDGMENTS

This work was supported, in part, by NAVSEA (PMS 405).

*Permanent address: Science Applications, Inc., McLean, VA 22102.

¹T. Kwan and J. M. Dawson, *Phys. Fluids* **22**, 1089 (1979).

²L. Friedland and J. L. Hirshfield, *Phys. Rev. Lett.* **44**, 1456 (1980).

³I. B. Bernstein and L. Friedland, *Phys. Rev. A* **23**, 816 (1981).

⁴H. P. Freund, P. Sprangle, D. Dillenburg, E. H. da Jornada, B. Liberman, and R. S. Schneider, *Phys. Rev. A* **24**, 1965 (1981).

⁵H. S. Uhm and R. C. Davidson, *Phys. Fluids* **24**, 1541 (1981).

⁶H. S. Uhm and R. C. Davidson, *Phys. Fluids* **24**, 2348 (1981).

⁷L. Friedland and A. Fruchtman, *Phys. Rev. A* **25**, 2693 (1982).

⁸W. A. McMullin and R. C. Davidson, *Phys. Rev. A* **25**, 3130 (1982).

⁹H. P. Freund, P. Sprangle, D. Dillenburg, E. H. da Jornada, R. S. Schneider, and B. Liberman, *Phys. Rev. A* **26**, 2004 (1982).

¹⁰L. Friedland, *Phys. Fluids* **23**, 2376 (1980).

¹¹H. P. Freund and A. T. Drobot, *Phys. Fluids* **25**, 736 (1982).

¹²H. P. Freund, *Phys. Rev. A* **27**, 1977 (1983).

¹³R. K. Parker, R. H. Jackson, S. H. Gold, H. P. Freund, V. L. Granatstein, P. C. Efthimion, M. Herndon, and A. K. Kinkead, *Phys. Rev. Lett.* **48**, 238 (1982).

¹⁴R. H. Jackson, S. H. Gold, R. K. Parker, H. P. Freund, P. C. Efthimion, V. L. Granatstein, M. Herndon, A. K. Kinkead, J. E. Kosakowski, and T. J. T. Kwan, *IEEE J. Quantum Electron.* **QE-19**, 346 (1983).

APPENDIX G

THREE-DIMENSIONAL THEORY OF FREE ELECTRON
LASERS WITH AN AXIAL GUIDE FIELD

Three-Dimensional Theory of Free Electron Lasers with an Axial Guide Field

HENRY P. FREUND, SHAYNE JOHNSTON, AND PHILLIP SPRANGLE

Abstract—The collective interaction in a free electron laser with a combined helical wiggler and uniform axial guide field is presented in the low-gain regime. The wiggler model we employ is fully self-consistent and includes all transverse inhomogeneities. The analysis is performed for a free electron laser (FEL) amplifier in which the radial dependence of the radiation is treated using both the TE and TM waveguide modes. Substantial discrepancies are found to exist between the results for the realizable and ideal wigglers, and a selection rule relating the TE_{1n} and TM_{1n} modes with resonant amplification at the l th harmonic of the FEL Doppler upshift.

A GREAT deal of activity has been directed toward the analysis of free electron laser (FEL) configurations which consist of an axial guide field as well as a transverse, axially periodic wiggler field [1]–[5]. The principal (but by no means only) application of such analyses is to millimeter wave FEL experiments which make use of relatively high current (1 kA) and low-energy (1 MeV) electron beams, in which the guide field is required in order to confine the beam [6]. However, it is of particular significance that one effect of the guide field is to strengthen the FEL interaction, and large enhancements in the gain are found to result when the Larmor period associated with the axial field is close to the wiggler period.

The fundamental difficulty with each of these analyses, however, has been the assumption that radial inhomogeneities in the wiggler field can be neglected when $k_w r_b \ll 1$ (where k_w is the wiggler wavenumber, and r_b is the beam radius). In such a case, the radial variations in the wiggler are of the order of $(k_w r_b)^2$, and were ignored. As pointed out by Diamant [7], however, when radial inhomogeneities are included in a self-consistent analysis of the equilibrium orbits, the transverse velocity associated with the wiggler field (which we denoted by u_w) scales as $|u_w/u_z| \sim k_w r_b$. Since u_w/u_z measures the strength of the oscillatory current which mediates the FEL interaction and the gain is found to scale approximately as $(u_w/u_z)^2$, the assumption of such an ideal radially homogeneous wiggler constitutes a basic inconsistency.

It is our purpose in this work to develop a self-consistent theory of the FEL interaction in the low-gain regime in which the effects of radial inhomogeneities are included. Our results indicate that while the radial variations in a self-consistent

wiggler are generally unimportant in the absence of an axial field as long as $k_w r_b \ll 1$, this is not the case when a guide field is present. In this case radial inhomogeneities introduce fundamental differences, and the problem must be treated in full generality. To this end we employ a realizable wiggler field which is generated by a bifilar helix [7], [8] and write the static magnetic field as

$$B = B_0 \hat{e}_z + 2B_w \left(J_1'(\lambda) \cos \chi \hat{e}_r - \frac{1}{\lambda} I_1(\lambda) \sin \chi \hat{e}_\theta + I_1(\lambda) \sin \chi \hat{e}_z \right) \quad (1)$$

in cylindrical coordinates, where B_0 and B_w are the amplitudes of the axial and wiggler magnetic fields, $\lambda \equiv k_w r$, $k_w \equiv 2\pi/\lambda_w$ (where λ_w denotes the wiggler period), $\chi \equiv \theta - k_w z$, and I_1 and J_1' are the modified Bessel function of the first kind and its derivative, respectively. Since our intention is to treat radial inhomogeneities in a self-consistent manner, these effects must also be included on the coherently amplified radiation fields. As a result, the radiation fields are modeled by the well-known TE and TM modes in a cylindrical waveguide of radius R . The vector potentials for these modes are of the form

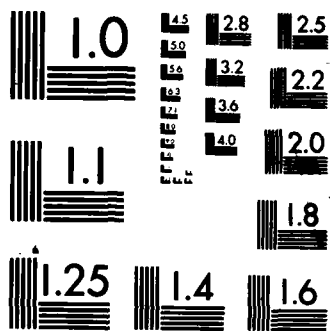
$$\delta A_l(x, t) = \sum_{n=1}^{\infty} \delta A_{1n} \left[\frac{l}{\rho_{1n}} J_l(\rho_{1n}') \hat{e}_r \sin \alpha_l(z, \theta, t) + J_l'(\rho_{1n}') \hat{e}_\theta \cos \alpha_l(z, \theta, t) \right] \quad (2)$$

for the TE mode, and

$$\delta A_l(x, t) = \sum_{n=1}^{\infty} \delta A_{1n} \left[J_l'(\rho_{1n}') \hat{e}_r \cos \alpha_l(z, \theta, t) - \left(\frac{l}{\rho_{1n}} \hat{e}_\theta - \frac{x_{1n}}{kR} \hat{e}_z \right) J_l(\rho_{1n}') \sin \alpha_l(z, \theta, t) \right] \quad (3)$$

for the TM mode. In (2) and (3) J_l and J_l' are the regular Bessel function of the first kind and its derivative, k is the wavenumber of the modes, $\rho_{1n} \equiv x_{1n} r/R$, $\rho_{1n}' \equiv x_{1n}' r/R$, x_{1n} and x_{1n}' are the n th zeros of the J_l and J_l' , respectively, and $\alpha_l(z, \theta, t) \equiv k_z z + \theta - \omega t$ is the phase of the wave. Observe that the sum over n in (2) and (3) describes the complete radial mode structure. Coherent amplification is included by allowing both δA_{1n} and k to be functions of z (such that $\partial_z \ln \delta A_{1n} \ll k$ and $\partial_z \ln k \ll k$). In this case $\alpha_l(z, \theta, t) = \int_0^z dz' k + \theta - \omega t$. In addition, as a result, it is important to note that both

Manuscript received July 29, 1982; revised September 24, 1982. This work was supported in part by NAVSEA under Contract SF68-342-602. H. P. Freund is with Science Applications, Inc., McLean, VA 22102. S. Johnston is with the Plasma Physics Laboratory, Columbia University, New York, NY 10027. P. Sprangle is with the Plasma Theory Branch, Naval Research Laboratory, Washington, DC 20375.



MICROCOPY RESOLUTION TEST CHART
NATIONAL BUREAU OF STANDARDS-1963-A

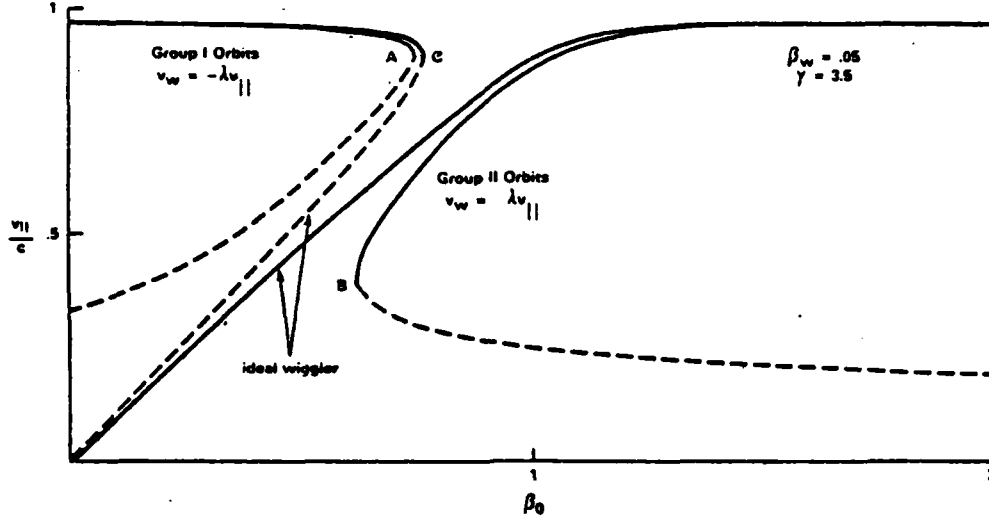


Fig. 1. Graph of the axial velocity versus axial guide for both the ideal and unrealizable wigglers.

modes will predominantly couple to resonant amplification at frequencies $\omega \simeq (k + lk_w)v_z$ (i.e., to the l th harmonic of the FEL Doppler upshift). It should also be remarked that this choice of the radiation field allows for the self-consistent inclusion of the filling factor in the calculation of the gain.

In addition to these field structures, the physical configuration is assumed to consist of an electron beam in which the individual electrons are initially characterized by helical orbits with constant radius and constant axial velocity. Since the stability analysis for the gain involves a calculation of the perturbations of these orbits due to the radiation fields, it will prove useful to review the properties of this class of orbit [7]. The basic equations governing the single-particle trajectories in the static magnetic fields given by (1) are

$$\begin{aligned} \gamma \dot{v}_1 &= -(\Omega_0 - \gamma k_w v_z + 2\Omega_w I_1(\lambda) \sin \chi) v_2 \\ &\quad + \Omega_w v_3 I_2(\lambda) \sin 2\chi, \\ \gamma \dot{v}_2 &= (\Omega_0 - \gamma k_w v_3 + 2\Omega_w I_1(\lambda) \sin \chi) v_1 \\ &\quad - \Omega_w v_3 (I_0(\lambda) + I_2(\lambda) \cos 2\chi), \\ \gamma \dot{v}_3 &= \Omega_w v_2 (I_0(\lambda) + I_2(\lambda) \cos 2\chi) - \Omega_w v_1 I_2(\lambda) \sin 2\chi, \\ \dot{\lambda} &= k_w (v_1 \cos \chi + v_2 \sin \chi), \\ \dot{\chi} &= k_w \lambda^{-1} (-v_1 \sin \chi + v_2 \cos \chi - \lambda v_3) \end{aligned} \quad (4)$$

where $\Omega_{0,w} \equiv |eB_{0,w}/mc|$, $\gamma \equiv (1 - v^2/c^2)^{-1/2}$, and (v_1, v_2, v_3) denote the components of the velocity in a frame rotating with the wiggler and specified by the basis vectors $\hat{e}_1 = \hat{e}_r \cos \chi - \hat{e}_\theta \sin \chi$, $\hat{e}_2 = \hat{e}_r \sin \chi + \hat{e}_\theta \cos \chi$, and $\hat{e}_3 = \hat{e}_z$. Within the context of (4), γ and the total energy are constants of the motion.

The helical orbits are obtained by requiring steady-state solutions in which v_1, v_2, v_3, λ , and χ are constants. As a result, we must have $v_1 = v_w, v_2 = 0, v_3 = v_{||}, \chi = \pm \pi/2$, and $\lambda = \mp v_w/v_{||}$, where $v_{||} (>0)$ is a constant, and

$$v_w = \frac{2\Omega_w v_{||} I_1(\lambda)/\lambda}{\Omega_0 - \gamma k_w v_{||} \pm 2\Omega_w I_1(\lambda)} \quad (5)$$

Equation (5) reduces to the result for an ideal wiggler in the limit as $\lambda \rightarrow 0$; however, since consistency requires that $|\lambda| = |v_w/v_{||}|$ this limit is not strictly valid. Final specification of the orbit requires knowledge of either $v_w, v_{||}$, or λ (a value for any one of which is sufficient to calculate the remaining two). We choose to determine λ , and write

$$\lambda^2 [(1 - \gamma^{-2})(1 + \lambda^2)^{-1}]^{1/2} = \beta_0 \lambda^2 \pm 2\beta_w (1 + \lambda^2) I_1(\lambda) \quad (6)$$

on the basis of the energy constraint, where $\beta_{0,w} \equiv \Omega_{0,w}/\gamma k_w c$. Evidently, (6) determines two distinct branches which may be obtained numerically. The solution for $v_{||}/c$ corresponding to the two classes of orbit implied by (6) are plotted versus β_0 (for $\beta_w = 0.05$ and $\gamma = 3.5$) in Fig. 1. Also, shown in the figure are the corresponding solutions in the case of an ideal wiggler.

There are two principal differences between the orbits for the real and ideal wigglers. The first is that the discrepancies in the velocities increase as $v_{||}$ approaches $\beta_0 c (= \Omega_0/\gamma k_w)$, and the second is that an additional class of unstable orbits exists for the real wiggler. The unstable orbits are denoted in the figure by the dotted lines, and the points A, B, and C represent the orbital stability boundaries for the real and idealized wigglers. The case of the ideal wiggler model has been amply treated in the literature and will not be discussed here; however, a brief analysis of the stability of the helical orbits in a realizable wiggler is necessary. A linear perturbation analysis of (4) about the helical trajectories shows that $\delta v_1, \delta v_3$, and $\delta \lambda$ can be expressed in terms of $\delta \chi$ and δv_2 (where the "δ" denotes the perturbed quantities), which satisfy the equation

$$\left(\frac{d^2}{dt^2} + \Omega_1^2 \right) \left(\frac{d^2}{dt^2} + \Omega_2^2 \right) \begin{pmatrix} \delta \chi \\ \delta v_2 \end{pmatrix} = 0 \quad (7)$$

where

$$\Omega_{1,2}^2 \equiv \frac{1}{2} (\omega_1^2 + \omega_2^2) \pm \frac{1}{2} \sqrt{(\omega_1^2 - \omega_2^2)^2 + 4A_2 B_2} \quad (8)$$

and

$$\begin{aligned}\omega_1^2 &\equiv k_w v_{\parallel} \left[k_w v_{\parallel} \mp 2 \frac{\Omega_w}{\gamma} \left(\frac{1 + \lambda^2}{\lambda} \right) I_2(\lambda) \right], \\ \omega_2^2 &\equiv \left(\frac{\Omega_0}{\gamma} - k_w v_{\parallel} \right) \left(\frac{\Omega_0}{\gamma} - k_w v_{\parallel} \pm 2 \frac{\Omega_w}{\gamma} I_1(\lambda) \right) \\ &\quad \pm 2 \frac{\Omega_w}{\gamma} k_w v_{\parallel} \left(\frac{1 + \lambda^2}{\lambda} \right) I_2(\lambda), \\ A_2 &\equiv -c k_w \frac{v_{\parallel}}{v_w} \left(\frac{\Omega_0}{\gamma} - 2 k_w v_{\parallel} \right), \\ B_2 &\equiv -2 \frac{\Omega_w}{\gamma} \frac{v_{\parallel}}{c} \left[(1 + \lambda^2) \left(\frac{\Omega_0}{\gamma} \pm 2 \frac{\Omega_w}{\gamma} I_1(\lambda) \right) I_2(\lambda) \right. \\ &\quad \left. + \lambda^2 k_w v_{\parallel} \left(I_0(\lambda) - \frac{1}{\lambda} I_1(\lambda) \right) \right].\end{aligned}\quad (9)$$

Evidently $\Omega_{1,2}^2$ must be computed separately for each class of orbit (denoted by group I for $\Omega_0 < \gamma k_w v_{\parallel}$, and II for $\Omega_0 > \gamma k_w v_{\parallel}$ in Fig. 1), and orbital instability occurs whenever either Ω_1^2 or Ω_2^2 are less than zero. The orbital stability boundaries, therefore, occur when either of these characteristic frequencies vanishes. Evaluation of $\Omega_{1,2}^2$ for the group I and II orbits reveals the stability behavior shown in Fig. 1. Since it is expected to be difficult to propagate an electron beam on the unstable orbits, we shall restrict the radiation analysis to cases in which the unperturbed electron trajectories are the stable solutions to (6).

In order to determine the gain, we make use of Maxwell's equations under the assumption that the beam density is sufficiently low that space-charge effects can be ignored. It should be remarked here that our initial use of the waveguide modes in (2) and (3) implicitly assumed that the invariant beam plasma frequency was much lower than the waveguide cutoff, otherwise the model must be extended to include the normal modes in a dielectric-filled waveguide. Under these assumptions, the vector potential satisfies

$$\left(\nabla^2 - \frac{1}{c^2} \frac{\partial^2}{\partial t^2} \right) \delta A_{\parallel}(x, t) = -\frac{4\pi}{c} \delta J(x, t) \quad (10)$$

where the source current is given as

$$\delta J(x, t) = -en_b(r) v_{z0}(r) \int_{-\infty}^{\infty} dt_0 \frac{\eta(t, r, t_0)}{\eta_z(t, r, t_0)} \delta(t - \tau(t_0, r, t)), \quad (11)$$

where $n_b(r)$ is the beam density profile, $\eta(t, r, t_0)$ is the momentum of a particle at radius r and time t which crossed the $z = 0$ plane at time t_0 ,

$$\tau(t_0, r, z) = t_0 + \int_0^z dz' \frac{1}{v_z(t_0, r, z')}, \quad (12)$$

$v_z(t_0, r, z)$ is the axial velocity of a particle at (r, z) which entered the interaction region at time t_0 , and $v_{z0}(r)$ is the initial axial velocity of the beam as a function r . Observe that

we implicitly assume here that all electrons located a distance r from the axis have the same initial axial velocity, and that the initial beam profile is fixed. Equation (11) represents an extension of a model current used previously by Sprangle *et al.* [9] to include a nonuniform radial profile and radial inhomogeneities in the orbits. Under the assumptions that the beam electrons enter the interaction region on the helical orbits, and that the beam density is sufficiently low that operation is in the low-gain regime, the current may be written to lowest order as

$$\begin{aligned}\delta J(x, t) &\approx -en_b(r) \int_{-\infty}^{\infty} dt_0 [v_w(r) (\cos \chi \hat{e}_r - \sin \chi \hat{e}_\theta) \\ &\quad - v_{\parallel}(r) \hat{e}_z] \delta(t - \tau(t, r, t_0)).\end{aligned}\quad (13)$$

Before proceeding with the derivation, it should be pointed out that for given values of B_0 , B_w , λ_w , and γ there is a unique stable helical orbit. More specifically, if the parameters which characterize the axial and wiggler fields are fixed, then a shift in energy implies a shift in radial position (and vice versa), and a finite spread in radial displacements is associated with a finite beam energy spread (i.e., $d\gamma/dr \neq 0$).

For the sake of simplicity, we shall now assume that $kR \gg 1$, which is equivalent to the requirement that resonance occurs far from the waveguide cutoffs. Thus, the principal characteristic of the waveguide structure included is the radial localization of the modes. A more complete analysis valid for arbitrary values of kR is currently in preparation. As a consequence, for the low gain, tenuous beam regime the dispersion relation for both the TE and TM modes is given approximately by the free space limit

$$\omega \approx ck \quad (14)$$

where variations in the wavenumber can be neglected. In addition, the diagonalization of the radial mode structure can be accomplished in (10) by use of the orthogonality properties of the Bessel functions, and we can show that

$$\begin{aligned}\frac{d}{dz} \delta a_{1n} &\approx \frac{x'_{1n}}{kc^3 R^3 J_{l+1}^2(x'_{1n})} \\ &\quad \cdot \int_0^R dr r^2 \omega_b^2(r) v_w(r) J_l(\rho'_{1n}) \langle \cos \psi_l \rangle\end{aligned}\quad (15)$$

for the TE mode, and

$$\begin{aligned}\frac{d}{dz} \delta a_{1n} &\approx \frac{x'_{1n}}{l(l+1) kc^3 R^4 J_{l+1}^2(x'_{1n})} \\ &\quad \cdot \int_0^R dr r^3 \omega_b^2(r) v_w(r) J'_l(\rho'_{1n}) \langle \sin \psi_l \rangle,\end{aligned}\quad (16)$$

for the TM mode. In (15) and (16), $\omega_b^2 \equiv 4\pi e^2 n_b/m$, $\delta a_{1n} \equiv e\delta A_{1n}/mc^2$,

$$\psi_l \equiv \psi_{l0} + \int_0^z dz' \left(k + lk_w - \frac{\omega}{v_z} \right) \quad (17)$$

is the relative phase of the electrons in the ponderomotive frame, and $\langle (\dots) \rangle = (2\pi)^{-1} \int_{-\pi}^{\pi} d\psi_{10} (\dots)$ represents an average over the initial phase ψ_{10} .

In order to compute the gains for the waveguide modes, we must now derive an expression for the phase, ψ_I , to first order in the amplitudes δa_{1n} . Because $d^2 \psi_I / dz^2 = \omega v_z^{-2} dv_z / dz$, this may be accomplished by means of a linear perturbation theory of the orbit equations in the presence of the radiation fields. The unperturbed trajectories in this analysis are assumed to be the helical orbits discussed previously. However, it is evident that the phase will depend linearly upon the amplitudes of each of the TM and TE modes present in the system. Hence, all of the radial modes will be coupled through (15) and (16), and the strength of the coupling will depend upon the amplitudes as well as the overlap of the each specific radial eigenmode with the current. In order to simplify the analysis, we restrict consideration to the treatment of an FEL amplifier in which the initial conditions can be tailored by means of the injection of radiation which results in the presence of a specific TE_{1n} or TM_{1n} radial eigenmode. Within the context of these approximations it can be shown that

$$\frac{d^2 \psi_I}{dz^2} \approx - \frac{(k + lk_w)^2 c v_w}{\gamma \gamma_{II}^2 v_{II}^2} \Phi_I(\lambda) \frac{l}{\rho_{1n}} J_l(\rho'_{1n}) \delta a_{1n} \cos \psi_I \quad (18)$$

for the TE mode, and

$$\frac{d^2 \psi_I}{dz^2} \approx \frac{(k + lk_w)^2 c v_w}{\gamma \gamma_{II}^2 v_{II}^2} \Phi_I(\lambda) \frac{l}{\rho_{1n}} J_l(\rho_{1n}) \delta a_{1n} \sin \psi_I \quad (19)$$

for the TM mode. In addition,

$$\Phi_I(\lambda) = 1 - \frac{l \gamma_{II}^2 k_w}{k + lk_w} + \frac{2 \gamma_{II}^2 \Omega_w}{(k + lk_w) v_w c} \frac{v_w [(\omega_2^2 - \Delta \omega_I^2) A_1 + A_2 B_1] I_2(\lambda) + c [(\omega_1^2 - \Delta \omega_I^2) B_1 + A_1 B_2] \frac{1}{\lambda} I_1(\lambda)}{(\Omega_1^2 - \Delta \omega_I^2) (\Omega_2^2 - \Delta \omega_I^2)} \quad (20)$$

where $\Delta \omega_I \equiv \omega - (k + lk_w) v_{II}$ denotes the frequency mismatch,

$$A_1 \equiv \frac{c k_w}{\gamma} \frac{v_{II}}{v_w} [\omega - k v_{II} (1 + \lambda^2)], \quad (21)$$

and

$$B_1 \equiv \frac{1}{\gamma} \left((\omega - k_w v_{II}) (\Delta \omega_I - k_w v_{II}) + \left(\frac{\Omega_0}{\gamma} \pm 2 \frac{\Omega_w}{\gamma} I_1(\lambda) \right) [\omega - k v_{II} (1 + \lambda^2)] \right). \quad (22)$$

Equations (18) and (19) describe the effect of the ponderomotive potential which results from the beating of the radial and wiggler fields. The presence of the axial guide field acts to enhance the ponderomotive potential. Examination of (20) clearly shows that since $\Delta \omega_I \approx 0$ near resonance, $\Phi_I(\lambda)$ becomes large whenever $\Omega_{1,2}^2$ vanishes. This occurs for $\Omega_0 \sim \gamma k_w v_{II}$ and denotes the transition to orbital instability (7). As a consequence, both the ponderomotive potential and the gain are expected to be significantly enhanced for orbits in this regime.

For operation in the linear regime prior to electron trapping in the ponderomotive potential, we write $\psi_I = \psi_{10} + \Delta k_I z + \delta \psi_I$ and expand (18) and (19) to first order in $\delta \psi_I$, where $\Delta k_I \equiv k + lk_w - \omega / v_{II}$. Using the solutions which result, we find the small-signal gain for a system of length L to be

$$G_L \equiv \frac{1}{\delta a_{1n}(0)} \int_0^L dz \frac{d}{dz} \delta a_{1n}(z) \approx \frac{(k + lk_w)^2 L^3}{8 k c^2 R^2} \int_0^R dr \frac{\omega_b^2}{\gamma \gamma_{II}^2} \frac{v_w^2}{v_{II}^2} \cdot F_{1n} \Phi_I(\lambda) \frac{d}{d\theta_I} \left(\frac{\sin \theta_I}{\theta_I} \right)^2 \quad (23)$$

where $\theta_I \equiv \Delta k_I L / 2$,

$$F_{1n} = -l \frac{J_l^2(\rho'_{1n})}{J_{l+1}^2(x'_{1n})} \quad (24)$$

for the TE_{1n} mode, and

$$F_{1n} = \frac{\rho_{1n}}{l+1} \frac{J_l(\rho_{1n}) J_l'(\rho_{1n})}{J_{l+1}^2(x_{1n})} \quad (25)$$

for the TM_{1n} mode. Observe that the radial integral in (23) describes the overlap between the electron current and the radial profile of the waveguide eigenmode and, hence, includes the effects modeled in the past by a filling factor in a self-consistent way. It also follows that the radial mode structure imposes a selection rule in that the TE_{1n} or TM_{1n} modes undergo resonant amplification at frequencies $\omega \approx (k + lk_w) v_{II}$. This result becomes clear when we consider that to lowest order $\theta \sim k_w v_{II}$ (i.e., $\chi \approx \pm \pi / 2$), so that $\alpha_I(z, \theta, t) \sim \Delta k_I z$ to within

a multiple of $\pi / 2$. In addition, since each radial eigenmode obeys this selection rule, inclusion of a multiplicity of such modes in the formulation would not alter this property. Finally, the gain exhibits large enhancements for frequencies near resonance as the single-particle orbits approach the transition to orbital instability ($\Omega_{1,2}^2 = 0$). The essential differences between this aspect of (23) and the results of the theories [2], [3] based on an ideal wiggler are that 1) for group I orbits ($\Omega_0 < \gamma k_w v_{II}$) the value of B_0 at which orbital instability occurs is shifted downward, and 2) a new class of unstable orbits has appeared for trajectories in group II ($\Omega_0 > \gamma k_w v_{II}$).

It is illustrative to consider the gain for the case of a thin annular beam in which the electron density is assumed to be constant (n_0) within $R_0 - \Delta R \leq r \leq R_0$. As a result, in the limit in which $\Delta R \ll R_0$ the beam density is given approximately by $n_0(r) \approx n_0 \Delta R \delta(r - R_0)$ and the maximum gain becomes

$$G_L^{\text{max}} \approx .54 \pi^3 \xi^2 N_w^3 \frac{\Delta R}{R_0} \left(\frac{v_{II} + c}{v_{II}} \right) \frac{\lambda_0^4}{k_w^2 R^2} |F_{1n} \Phi_I|_{r=R_0} \quad (26)$$

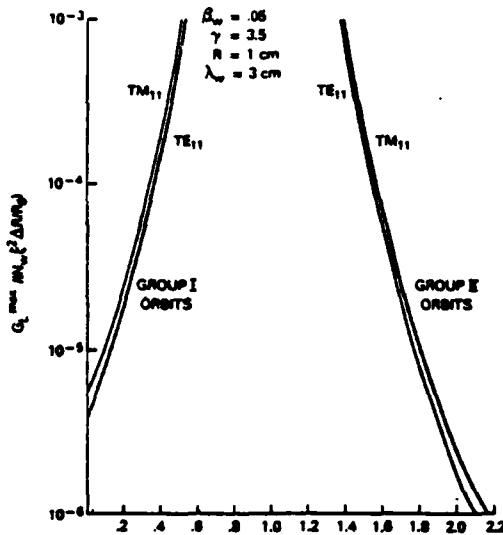


Fig. 2. Graph of the maximum gain versus the axial guide field for both group I and II orbits and the TE_{11} and TM_{11} modes.

where $\xi \equiv \omega_{D0}/\gamma^{1/2}ck_w$ is the beam strength parameter, $N_w \equiv L/\lambda_w$ is the number of wiggler periods within the interaction region, $\lambda_0 \equiv k_w R_0$, and the frequency is given by $\omega = l(1 + v_{||}/c)\gamma^2 k_w v_{||}$. As mentioned previously, specification of B_0 , B_w , λ , and γ defines a unique beam radius for orbits in groups I or II. Hence, if the magnetic field parameters are fixed then finite ΔR implies a finite beam energy spread $\Delta\gamma$; and we estimate from (6) that $\Delta R \sim k_w R_0^2 \Delta\gamma/\gamma\beta_w$ for $\lambda_0 < 1$. Since our analysis is based upon the assumption of a nearly monoenergetic beam which is valid only for $\Delta\gamma < (4\gamma N_w)^{-1}$, we must also require that

$$\frac{\Delta R}{R_0} < \frac{\lambda_0}{4\beta_w \gamma^2 N_w} \quad (27)$$

It should be noted that this requirement is quite stringent; hence this example is meant for illustrative purposes only. The description of an actual experiment requires a numerical integration of (23) over a beam profile. Within the context of (27), we plot the peak gain (26) versus axial magnetic field β_0 in Fig. 2 for both the TE_{11} and TM_{11} modes and $\beta_w = .05$, $\gamma = 3.5$, $\lambda_w = 3$ cm, and $R = 1$ cm. As expected, the gain of both the TE and TM modes is singular as the transition to orbital instability is approached for both the group I and group II orbits and substantial enhancements are found in comparison with the gain in the absence of an axial guide field ($\beta_0 = 0$). In addition, it is evident that amplification of the TM_{11} mode is favored over that for the TE_{11} mode over the range of parameters studied. It should be remarked at this point that the gain for the TE mode becomes dominant only in the limit as the singularity is approached; however, as the linearized low-gain theory breaks down in this regime it has been excluded from consideration here. Finally, it should not be concluded that such a relationship should hold between arbitrary TE_{ln} and TM_{ln} modes. Each case must be examined individually, and will be discussed in more detail in a forthcoming work.

The gain bandwidth described by (23) arises from two effects. The first is the well-known frequency mismatch arising from the form function $d(\sin \theta_1/\theta_1)^2/d\theta_1$, which for a thin annulus yields a frequency spread

$$\frac{\Delta\omega_1}{\omega_1} \approx \frac{1}{2\gamma^2 l N_w} \quad (28)$$

where $\omega_1 = lk_w \beta_z c/(1 - \beta_z)$ is the resonant frequency of the l th FEL Doppler resonance. The second source of spectral broadening stems from the variations of the axial velocity with radial position which results in a radial variation in ω_1 of the form

$$\frac{\Delta\omega_2}{\omega_1} \approx \frac{2\beta_w}{\beta_z^2} \frac{\Delta R}{\lambda_0 R_0} \quad (29)$$

for a thin annulus. Further, in order for the former spectral broadening effect to be dominant, condition (27) must be satisfied. Since this condition is stringent, it is expected that the latter broadening process will be dominant (i.e., $\Delta\omega_2 > \Delta\omega_1$) in most cases of practical interest.

In conclusion, we find that the analysis of the FEL gain with a realizable wiggler introduces fundamental differences in comparison with the usual one-dimensional analyses with an ideal wiggler, such as in [2]–[5]. The three-dimensional analysis presented here describes the effects of 1) the orbital instability for both classes of equilibrium trajectory, 2) the overlap of the radiation and electron beams usually included by means of a phenomenological filling factor, and 3) the selection rule that requires the resonant amplification of the TE_{ln} and TM_{ln} modes at the l th FEL Doppler upshift.

REFERENCES

- [1] T. Kwan and J. M. Dawson, "Investigation of the free electron laser with a guide magnetic field," *Phys. Fluids*, vol. 22, pp. 1089–1103, 1979.
- [2] L. Friedland and J. L. Hirshfield, "Free electron laser with a strong axial magnetic field," *Phys. Rev. Lett.*, vol. 44, pp. 1456–1460, 1980.
- [3] H. P. Freund, P. Sprangle, D. Dillenburg, E. H. daJornada, B. Liberman, and R. S. Schneider, "Coherent and incoherent radiation from free electron lasers with an axial guide field," *Phys. Rev. A*, vol. 24, pp. 1965–1979, 1981.
- [4] H. P. Freund, P. Sprangle, D. Dillenburg, E. H. daJornada, R. S. Schneider, and B. Liberman, "Collective effects on the operation of free electron lasers with an axial guide field," *Phys. Rev. A*, Oct. 1982.
- [5] L. Friedland and A. Fruchtman, "Amplification on relativistic electron beams in combined helical and axial magnetic fields," *Phys. Rev. A*, vol. 25, pp. 2693–2706, 1982.
- [6] R. K. Parker, R. H. Jackson, S. H. Gold, H. P. Freund, V. L. Granatstein, P. C. Efsthimion, M. Herndon, and A. K. Kincaid, "Axial magnetic-field effects in a collective-interaction free-electron laser at millimeter wavelengths," *Phys. Rev. Lett.*, vol. 48, pp. 238–242, 1982.
- [7] P. Diamant, "Electron orbits and stability in realizable and unrealizable wigglers of free-electron lasers," *Phys. Rev. A*, vol. 23, pp. 2537–2552, 1981.
- [8] J. P. Blewitt and R. Chasman, "Orbits and fields in the helical wiggler," *J. Appl. Phys.*, vol. 48, pp. 2692–2698, 1977.
- [9] P. Sprangle, C. M. Tang, and W. M. Manheimer, "Nonlinear theory of free-electron lasers and efficiency enhancement," *Phys. Rev. A*, vol. 21, pp. 302–318, 1980.



Henry P. Freund was born in New York, NY on May 23, 1949. He received the B.S. degree in physics from Rensselaer Polytechnic Institute, Troy, NY, in 1971, and the Ph.D. degree in physics from the University of Maryland, College Park, in 1976.

After graduation he spent a year as a Research Fellow at the Institute for Physical Sciences and Technology, the University of Maryland, and two years as a National Research Council-Naval Research Laboratory Postdoctoral Research Associate. His current research is devoted primarily to free electron lasers at the Naval Research Laboratory, where he is an employee of Science Applications, Inc., McLean, VA.



Shayne Johnston was born in Fort William, Ont., Canada on November 4, 1948. He received the B.Sc. degree in mathematics and physics from McGill University, Montreal, Canada, in 1970, and the Ph.D. degree in plasma physics from Princeton University, Princeton, NJ, in 1975.

From 1974 to 1976, he served as a Research Associate at Lawrence Berkeley Laboratory, the University of California, Berkeley. In 1976, he joined the faculty of Columbia University,

New York, NY as an Assistant Professor of Applied Physics. His research interests include theoretical plasma physics, nonlinear dynamics, and applied mathematics.

Dr. Johnston is a member of the American Physical Society, the University Fusion Association, and Sigma Xi.



Phillip Sprangle was born in Brooklyn, NY on September 27, 1944. He received the B.S. degree in electrical engineering from the Polytechnic Institute of New York, Brooklyn, NY, in 1967, the M.S. degree in physical chemistry from the University of Puerto Rico, Rio Piedras, in 1969, and the Ph.D. degree in applied physics from Cornell University, Ithaca, NY, in 1972.

After graduation he joined the Plasma Physics Division of the Naval Research Laboratory, Washington, DC. He is currently Head of the Plasma Theory Branch at NRL and is conducting research in the fields of free electron lasers, ultra high current accelerators, and electron cyclotron masers.

APPENDIX H

THREE-DIMENSIONAL THEORY OF THE FREE-ELECTRON LASER
IN THE COLLECTIVE REGIME, 40, 3, 1

Three-dimensional theory of the free-electron laser in the collective regime

H. P. Freund* and A. K. Ganguly

Naval Research Laboratory, Washington, D.C. 20375

(Received 23 May 1983)

A fully self-consistent theory of the free-electron laser is derived in the collective regime which includes all transverse variations in the wiggler field as well as the effects of a finite waveguide geometry. A general orbit theory is derived by perturbation about the steady-state trajectories in a configuration which consists of an axial guide field in addition to the helical wiggler field, and used to obtain the source current and charge density for the Maxwell-Poisson equations. By this means, a set of coupled differential equations is found which describes an arbitrary radial beam profile. A dispersion equation is obtained under the assumption of a thin monoenergetic beam, and solved numerically for the growth rates of the TE_{11} and TM_{11} modes in a cylindrical waveguide. A selection rule is found by which the TE_{lm} or TM_{lm} modes are resonant at the l th free-electron-laser Doppler upshift.

I. INTRODUCTION

Interest in the free-electron laser (FEL) as a source of coherent radiation with wavelengths in the millimeter range and below has been maintained by both experimental¹⁻⁸ and theoretical⁹⁻²⁴ studies. Experiments designed to operate in the infrared have, of late, concentrated on the use of a linearly polarized wiggler field composed of permanent magnets.^{5,6} In contrast, experiments at longer wavelengths ($\sim 1-5$ mm) generally make use of helical wiggler fields in concert with an axial guide field. The inclusion of an axial-guide field is necessitated by the high currents (~ 1 kA) employed, and such experiments can be made to operate in the collective regime.^{7,8} Theoretical analyses of the helical wiggler FEL experiments have, hitherto, been able to treat the collective regime only in the limit of an idealized one-dimensional wiggler field which is valid only as long as the electron-beam radius is much shorter than the wiggler period.^{9,12-14,17-21,23} A fully self-consistent, three-dimensional theory which includes all transverse variations of the wiggler field as well as the effects of a finite waveguide geometry has recently appeared²⁴; however, it is restricted to the low-gain, single-particle regime. It is our purpose in this work to extend the three-dimensional theory to the collective regime. In contrast, a nonlinear theory has been developed by Colson and Richardson²⁵ for a helical wiggler/pulsed electron-beam configuration. The radiation mode structure is assumed to be that of an optical resonator and is described in a three-dimensional manner; however, the wiggler field and single-particle orbits are described in the idealized limit in which transverse gradients are ignored. In addition, no axial guide field is included in the treatment.

To this end, we first derive the single-particle trajectories of electrons in the self-consistent static magnetic fields by perturbation about the steady-state, helical orbits.^{24,26-28} These orbits are then used to obtain expressions for the source current and charge density which

drive the FEL interaction by solution of the Vlasov equation. The source current and charge density are then used to obtain Maxwell's equations subject to boundary conditions suitable to describe a loss-free cylindrical waveguide. In this manner, a set of differential equations result which model the presence of an arbitrary radial beam profile of electrons which to lowest order execute the steady-state trajectories. In order to obtain analytic solutions to these differential equations, the approximation of a thin beam (i.e., small radial profile) is imposed which is consistent with the assumption of a nearly monoenergetic beam.

The organization of the paper is as follows. The orbit theory is presented in Sec. II, and applied to obtain the source current and charge density in Sec. III. The coupled field equations are derived in Sec. IV for an arbitrary radial profile. The assumption of a thin, monoenergetic beam is imposed in Sec. V and used to obtain and solve the dispersion equation. A summary and discussion is presented in Sec. VI.

II. SINGLE-PARTICLE ORBITS

The physical configuration we employ is that of a relativistic electron beam propagating through an ambient magnetic field composed of a periodic helical wiggler field and a uniform guide field

$$\vec{B}(\vec{r}) = B_0 \hat{e}_z + \vec{B}_w(\vec{r}), \quad (1)$$

where B_0 denotes the magnitude of the guide field, and the wiggler field is taken to be that generated by a bifilar helix²⁷:

$$\vec{B}_w(\vec{r}) = 2B_w [I_1(\lambda) \cos \chi \hat{e}_r - \lambda^{-1} I_1(\lambda) \sin \chi \hat{e}_z + I_1(\lambda) \sin \chi \hat{e}_z], \quad (2)$$

In Eq. (2), B_w is the amplitude of the wiggler field, $\lambda \equiv k_w r$, $\chi \equiv \theta - k_w z$, $k_w \equiv 2\pi/\lambda_w$ (where λ_w defines the wiggler period), and I_n and I_n' are the modified Bessel

function of the first kind of order n and its derivative, respectively.

The basic equations governing the single-particle orbits in the static magnetic field are

$$\begin{aligned} \gamma \dot{v}_1 &= -[\Omega_0 - \gamma k_w v_3 + 2\Omega_w I_1(\lambda) \sin \chi] v_2 \\ &\quad + \Omega_w v_3 I_2(\lambda) \sin 2\chi, \\ \gamma \dot{v}_2 &= [\Omega_0 - \gamma k_w v_3 + 2\Omega_w I_1(\lambda) \sin \chi] v_1 \\ &\quad - \Omega_w v_3 [I_0(\lambda) + I_2(\lambda) \cos 2\chi], \\ \gamma \dot{v}_3 &= \Omega_w v_2 [I_0(\lambda) + I_2(\lambda) \cos 2\chi] - \Omega_w v_1 I_2(\lambda) \sin 2\chi, \\ \dot{\lambda} &= k_w (v_1 \cos \chi + v_2 \sin \chi), \\ \dot{\chi} &= k_w \lambda^{-1} (-v_1 \sin \chi + v_2 \cos \chi - \lambda v_3), \end{aligned} \quad (3)$$

where $\Omega_{0,w} \equiv |eB_{0,w}/mc|$, $\gamma \equiv (1 - v^2/c^2)^{-1/2}$, and (v_1, v_2, v_3) denote the components of the velocity in a frame rotating with the wiggler and specified by the basis vectors $\hat{e}_1 = \hat{e}_r \cos \chi - \hat{e}_\theta \sin \chi$, $\hat{e}_2 = \hat{e}_r \sin \chi + \hat{e}_\theta \cos \chi$, and $\hat{e}_3 = \hat{e}_z$. It is clear that γ (i.e., the total energy) is a constant of the motion. The class of helical orbits is found by requiring steady-state solutions in which v_1 , v_2 , v_3 , λ , and χ are constants.^{24,27} In this work, the orbits we employ are obtained by expansion about the steady-state trajectories, and a review of the properties of the helical orbits is useful.

The steady-state requirement in (3) results in trajectories in which $v_1 = v_w$, $v_2 = 0$, $v_3 = v_{||}$, $\chi = \pm \pi/2$, and $\lambda = \mp v_w/v_{||}$, where $v_{||} (> 0)$ is a constant and

$$v_w = \frac{2\Omega_w v_{||} I_1(\lambda)/\lambda}{\Omega_0 - \gamma k_w v_{||} \pm 2\Omega_w I_1(\lambda)} \quad (4)$$

Observe that (4) reduces to the result for an ideal wiggler^{25,27} in the limit as $\lambda \rightarrow 0$. Final determination of the orbit requires knowledge of either v_w , $v_{||}$, or λ (specification of any one of these is sufficient to determine the other two) which, in turn, requires an additional equation relating these quantities:

$$\lambda^2 [(1 - \gamma^{-2})(1 + \lambda^2)^{-1}]^{1/2} = \beta_0 \lambda^2 \pm 2\beta_w (1 + \lambda^2) I_1(\lambda), \quad (5)$$

where $\beta_{0,w} \equiv \Omega_{0,w}/\gamma k_w c$. Solution of these equations produces two distinct classes of trajectory as shown in Fig. 1 in which we plot $v_{||}/c$ vs β_0 (for $\beta_w = 0.05$ and $\gamma = 3.5$). Also shown in the figure are the corresponding solutions in the limit of an ideal wiggler.

We now consider the characteristics of particle trajectories which are close to these steady-state trajectories. To this end we write $v_1 = v_w + \delta v_1$, $v_2 = \delta v_2$, $v_3 = v_{||} + \delta v_3$, $\chi = \pm \pi/2 + \delta \chi$, and $\lambda = \mp v_w/v_{||} + \delta \lambda$. To first order in the perturbed quantities, therefore, we find that Eq. (3) implies

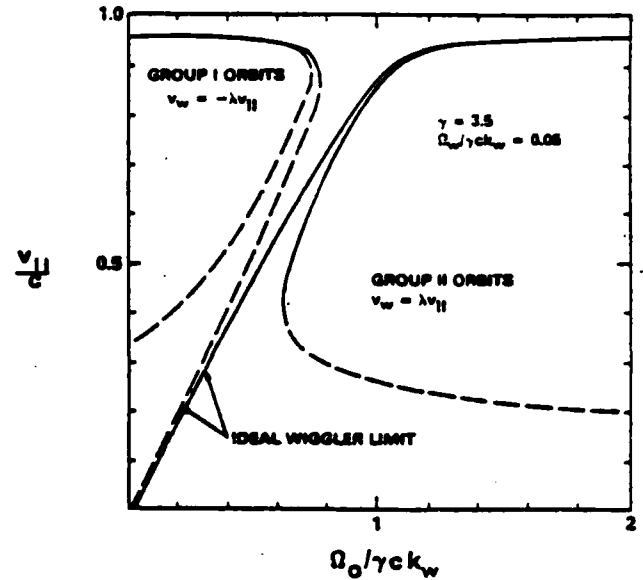


FIG. 1. Graph of the axial velocity of the steady-state orbits vs guide-field strength for ideal and realizable wiggler models.

$$\begin{aligned} \gamma \delta \dot{v}_1 &= -[\Omega_0 - \gamma k_w v_{||} \pm 2\Omega_w I_1(\lambda_0)] \delta v_2 - 2\Omega_w v_{||} I_2(\lambda_0) \delta \chi, \\ \gamma \delta \dot{v}_2 &= [\Omega_0 - \gamma k_w v_{||} \pm 2\Omega_w I_1(\lambda_0)] \delta v_1 \\ &\quad - [\gamma k_w v_w + 2\Omega_w I_1(\lambda_0)] \delta v_3 \\ &\quad - 2\Omega_w v_{||} \lambda_0^{-1} \delta \lambda [I_2(\lambda_0) + \lambda_0^2 I_0(\lambda_0) - \lambda_0 I_1(\lambda_0)], \\ \gamma \delta \dot{v}_3 &= 2\Omega_w v_w I_2(\lambda_0) \delta \chi + 2\lambda_0^{-1} \Omega_w I_1(\lambda_0) \delta v_2, \\ \delta \dot{\chi} &= -k_w (\delta v_3 \pm \lambda_0^{-1} \delta v_1 \mp \lambda_0^{-2} v_w \delta \lambda), \\ \delta \dot{\lambda} &= \pm k_w (\delta v_2 - v_w \delta \chi), \end{aligned} \quad (6)$$

where we denote $\lambda_0 \equiv \mp v_w/v_{||}$. The system of first-order differential equations represented by (6) can be simplified to a pair of fourth-order equations

$$\left[\frac{d^2}{dt^2} + \Omega_1^2 \right] \left[\frac{d^2}{dt^2} + \Omega_2^2 \right] \begin{bmatrix} \delta v_2 \\ \delta \chi \end{bmatrix} = 0, \quad (7)$$

where

$$\Omega_{1,2}^2 \equiv \frac{1}{2}(\omega_1^2 + \omega_2^2) \pm \frac{1}{2}\{(\omega_1^2 - \omega_2^2)^2 + 4A_1 A_2 B_2\}^{1/2}, \quad (8)$$

and

$$\begin{aligned} \omega_1^2 &\equiv k_w^2 v_{||}^2 \mp 2\gamma^{-1} \Omega_w k_w v_{||} \lambda_0^{-1} (1 + \lambda_0^2) I_2(\lambda_0), \\ \omega_2^2 &\equiv \gamma^{-2} (\Omega_0 - \gamma k_w v_{||}) [\Omega_0 \pm 2\Omega_w I_1(\lambda_0) - \gamma k_w v_{||}] \\ &\quad \pm 2\gamma^{-1} \Omega_w k_w v_{||} \lambda_0^{-1} (1 + \lambda_0^2) I_2(\lambda_0), \\ A_2 &\equiv \pm c k_w \lambda_0^{-1} \gamma^{-1} (\Omega_0 - 2\gamma k_w v_{||}), \\ B_2 &\equiv -2\gamma^{-2} \Omega_w \beta_{||} [(1 + \lambda_0^2) [\Omega_0 \pm 2\Omega_w I_1(\lambda_0)] I_2(\lambda_0) \\ &\quad + \lambda_0^2 \gamma k_w v_{||} [I_0(\lambda_0) - \lambda_0^{-1} I_1(\lambda_0)]] , \end{aligned}$$

and $\beta_{||} \equiv v_{||}/c$. Observe that Ω_1^2 and Ω_2^2 must be computed separately for each class of steady-state orbit, and that an orbital instability occurs whenever either Ω_1^2 or Ω_2^2 becomes negative. These frequencies are plotted in Fig. 2

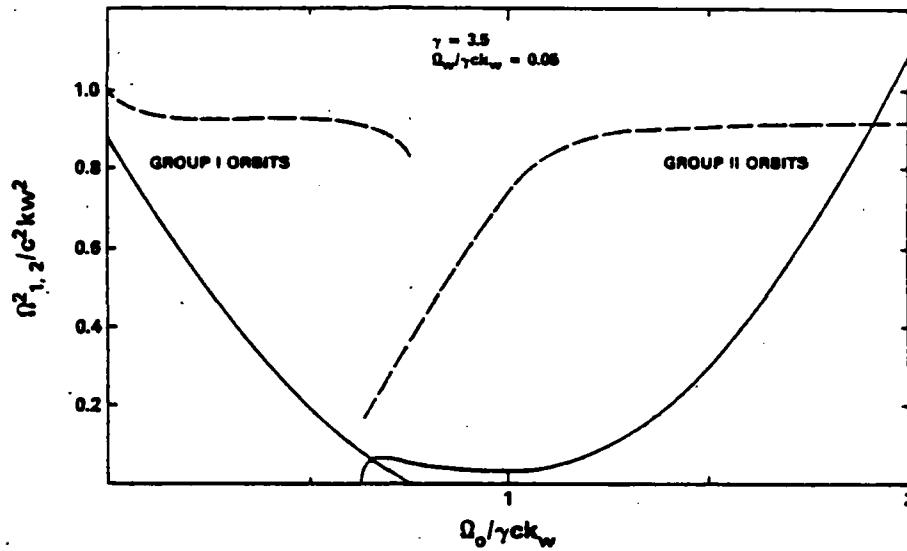


FIG. 2. Graphs of $\Omega_1^2/c^2k_w^2$ (dashed line) and $\Omega_2^2/c^2k_w^2$ (solid line) vs $\Omega_0/\gamma ck_w$ for group I and group II orbits.

versus β_0 (for $\beta_w = 0.05$ and $\gamma = 3.5$) for stable trajectories (i.e., $\Omega_1^2, \Omega_2^2 > 0$). Note that the unstable trajectories are represented in Fig. 1 by the dashed lines. It is evident from Fig. 2 that $\Omega_1^2 \gg \Omega_2^2$ and $\Omega_1 \sim k_w v_{||}$ except for a narrow range of axial fields corresponding to group II orbits in the neighborhood of $\Omega_0 \sim \gamma k_w v_{||}$. Also, Ω_2^2 varies widely and the orbital instability occurs when $\Omega_2^2 < 0$.

The solutions to Eq. (7) are of the form

$$\delta v_2 = -\alpha_1 \sin(\Omega_1 t - \phi_1) - \alpha_2 \sin(\Omega_2 t - \phi_2)$$

and

$$\delta \chi = -\rho_1 \sin(\Omega_1 t - \theta_1) - \rho_2 \sin(\Omega_2 t - \theta_2),$$

where $\alpha_1, \alpha_2, \rho_1, \rho_2, \phi_1, \phi_2, \theta_1,$ and θ_2 are the integration constants. Using these solutions we can derive the appropriate forms for δv_1 and δv_3 from Eqs. (6). However, we note that since $\Omega_1 \leq k_w v_{||}$, such terms will provide for interactions at higher harmonics of the free-electron-laser Doppler upshift. Thus, since we confine ourselves to treatment of the interaction at the fundamental Doppler upshift, we are justified in neglecting oscillatory terms in Ω_1 (which is equivalent to the requirement that $\alpha_1 = \rho_1 = 0$). Within this context, the other components of

the velocity are

$$\delta v_1 = -\frac{2\Omega_w}{\Omega_2} [\mp \lambda_0^{-2} I_1(\lambda_0) \alpha_2 \cos(\Omega_2 t - \phi_2) + \rho_2 v_{||} I_2(\lambda_0) \cos(\Omega_2 t - \phi_2)] \quad (9)$$

and

$$\delta v_3 = \lambda_0 \frac{2\Omega_w}{\Omega_2} [\lambda_0^{-2} I_1(\lambda_0) \alpha_2 \cos(\Omega_2 t - \phi_2) \mp \rho_2 v_{||} I_2(\lambda_0) \cos(\Omega_2 t - \phi_2)]. \quad (10)$$

Observe that $\delta v_1 \mp \lambda_0 \delta v_{||} = \text{const.}$ The further constraint imposed by energy conservation implies that $\theta_2 = \phi_2$, and

$$\alpha_2^2 = \frac{4\Omega_w^2}{\Omega_2^2} (1 + \lambda_0^2) \left[\mp \frac{\alpha_2}{\lambda_0^2} I_1(\lambda_0) + v_{||} \rho_2 I_2(\lambda_0) \right]^2. \quad (11)$$

As a consequence, the orbits can be written in the following form in rectangular coordinates:

$$\begin{aligned} p_x &= p_w \cos k_w z + (1 + \lambda^2)^{-1/2} \alpha_+ [P_x \cos(k_w z - \Omega_2 t) - P_y \sin(k_w z - \Omega_2 t)] \\ &\quad + (1 + \lambda^2)^{-1/2} \alpha_- [P_x \cos(k_w z + \Omega_2 t) + P_y \sin(k_w z + \Omega_2 t)], \\ p_y &= p_w \sin k_w z + (1 + \lambda^2)^{-1/2} \alpha_+ [P_x \sin(k_w z - \Omega_2 t) + P_y \cos(k_w z - \Omega_2 t)] \\ &\quad + (1 + \lambda^2)^{-1/2} \alpha_- [P_x \sin(k_w z + \Omega_2 t) - P_y \cos(k_w z + \Omega_2 t)], \\ p_z &= p_{||} - \frac{p_w}{p_{||}} (1 + \lambda_0^2)^{-1/2} (P_x \cos \Omega_2 t + P_y \sin \Omega_2 t), \end{aligned} \quad (12)$$

where $\alpha_{\pm} \equiv [1 \pm (1 + \lambda_0^2)^{1/2}]/2$, $p_w \equiv \gamma m v_w$, $p_{||} \equiv \gamma m v_{||}$, $P_x \equiv \gamma m \alpha_2 \cos \phi_2$, and $P_y \equiv \gamma m \alpha_2 \sin \phi_2$ are analogs of the canonical momenta. Observe that $\lim_{\lambda_0 \rightarrow 0} \Omega_2 = k_w v_{||} - \Omega_0/\gamma$, $\lim_{\lambda_0 \rightarrow 0} \alpha_+ = 1$, and $\lim_{\lambda_0 \rightarrow 0} \alpha_- = 0$; hence, (12) reduces to the orbit equations used by Freund *et al.*¹⁶ in the one-dimensional limit and (P_x, P_y) are the usual canonical momenta in the limit $B_0 \rightarrow 0$.

Before closing this section, some discussion is in order in regard to the transition to orbital instability at $\Omega_2 = 0$. The gain exhibits large enhancements in this region since the natural response frequency of electron motion (Ω_2 in the wiggler frame) is small and can be comparable to the frequency of the ponderomotive wave which drives the stimulated radiation process in free-electron lasers. For simplicity, we consider the product $\Omega_1^2 \Omega_2^2$ rather than Ω_2^2 independently (since $\Omega_1 - k_w v_{||}$ this cannot affect the orbital instability criterion), and find that

$$\{(1 + \lambda_0^2)[\Omega_0 \pm 2\Omega_w I_1(\lambda_0)] - \gamma k_w v_{||}\} Z(\lambda_0) - \gamma \lambda_0^2 k_w v_{||} Y(\lambda_0) = 0 \quad (13)$$

at the transition to orbital instability, where

$$Z(\lambda_0) \equiv (1 + \lambda_0^2) I_1'(\lambda_0) - \frac{2}{\lambda_2} I_1(\lambda_0) \quad (14)$$

and

$$Y(\lambda_0) \equiv (1 + \lambda_0^2) I_1'(\lambda_0) - \frac{1}{\lambda_0} I_1(\lambda_0). \quad (15)$$

In the limit in which $\lambda_0 \ll 1$ and $B_w \ll B_0$, Eq. (13) reduces to $(1 + \lambda_0^2)\Omega_0 - \gamma k_w v_{||} = 0$, which is the orbital instability threshold found using an idealized one-dimensional wiggler field.^{16,20}

III. THE SOURCE CURRENT AND CHARGE DENSITY

The source current and charge density are obtained from the moments of the perturbed distribution function

$$\delta f_b(\vec{r}(z), z, \vec{p}, \tau(z)) = e \int_0^z \frac{dz'}{v_z(\vec{r}(z'), z')} \left[\delta \vec{E}(\vec{r}(z'), z', \tau(z')) + \frac{1}{c} \vec{v}(\vec{r}(z'), z') \times \delta \vec{B}(\vec{r}(z'), z', \tau(z')) \right] \cdot \frac{\partial F_b}{\partial \vec{p}}, \quad (16)$$

where F_b is the equilibrium distribution, $\delta \vec{E}$ and $\delta \vec{B}$ are the fluctuating electromagnetic fields, $\vec{r}(z')$ is the position of the electron relative to the axis of symmetry at z' , $\tau(z') = t_0 + \int_0^{z'} dz'/v_z(\vec{r}(z'), z')$ is the sum of the time required for an electron to travel from ($\vec{r}(z=0), z=0$) at the start of the interaction region to ($\vec{r}(z=z'), z=z'$) and the entry time t_0 . The equilibrium distribution must be a function of the constants of the motion (P_x, P_y, p), where small P_x and P_y are required. As a consequence, we choose a distribution of the form

$$F_b(P_x, P_y, p) = n_b \delta(P_x) \delta(P_y) G_b(p), \quad (17)$$

where n_b is the average beam density, and $G_b(p)$ is an arbitrary function of the total momentum. In addition, we work with vector and scalar potentials of the form

$$(\delta \vec{A}(\vec{x}, t), \delta \phi(\vec{x}, t)) = \frac{1}{2} (\delta \hat{A}(\vec{x}), \delta \hat{\phi}(\vec{x})) \exp(-i\omega t) + \text{c.c.} \quad (18)$$

With respect to the basis $\hat{e}_\pm = \frac{1}{2}(\hat{e}_x \mp i\hat{e}_y)$, integration of (16) yields

$$\delta \hat{f}_b(\vec{r}(z), z) = \left[D_+ \left[\frac{\partial}{\partial P_x} - i \frac{\partial}{\partial P_y} \right] + D_- \left[\frac{\partial}{\partial P_x} + i \frac{\partial}{\partial P_y} \right] + D_z \frac{\partial}{\partial p} \right] F_b(P_x, P_y, p), \quad (19)$$

where

$$D_\pm \equiv \frac{e}{2cp} \int_0^z dz' \frac{e^{i\omega \tau(z, z')}}{v_z(\vec{r}(z'), z')} \left[-c(p_z \nabla_z + \frac{1}{2} p_- \nabla_+ + \frac{1}{2} p_+ \nabla_-) \delta \hat{\phi} + i\omega(p_z \delta \hat{A}_z + p_- \delta \hat{A}_+ + p_+ \delta \hat{A}_-) \right], \quad (20)$$

$$D_\pm \equiv \frac{e}{2c} \int_0^z dz' \frac{e^{i\omega \tau(z, z')}}{v_z(\vec{r}(z'), z')} \left[\alpha_+ e^{\mp i\theta} \left[-\frac{c}{2} \nabla_\mp \delta \hat{\phi} + (i\omega - v_z \nabla_z) \delta \hat{A}_\mp + \frac{1}{2} v_z \nabla_\mp \delta \hat{A}_z \pm \frac{v_\mp}{2} (\nabla_- \delta \hat{A}_+ - \nabla_+ \delta \hat{A}_-) \right] \right. \\ \left. - \alpha_- e^{\pm i\theta} \left[-\frac{c}{2} \nabla_\pm \delta \hat{\phi} + (i\omega - v_z \nabla_z) \delta \hat{A}_\pm + \frac{1}{2} v_z \nabla_\pm \delta \hat{A}_z \mp \frac{v_\pm}{2} (\nabla_- \delta \hat{A}_+ - \nabla_+ \delta \hat{A}_-) \right] \right], \quad (21)$$

where $\tau(z, z') \equiv \tau(z) - \tau(z')$, $p_\pm \equiv p_x \mp ip_y$, $\delta \hat{A}_\pm \equiv \delta \hat{A}_x \mp i\delta \hat{A}_y$, $\nabla_\pm \equiv \partial_x \mp i\partial_y$, $\nabla_z \equiv \partial_z$, and $\theta_\pm \equiv k_w z \pm \Omega_2 \tau(z)$.

The current and charge density are found by computation of the appropriate moments of (19) as

$$\delta \hat{J}_\pm = -\frac{e}{m} \int dP_x dP_y dp (1 + \lambda^2)^{-1/2} \frac{pp_\pm}{\gamma p_z} \delta \hat{f}_\pm, \quad \delta \hat{J}_z = -\frac{e}{m} \int dP_x dP_y dp (1 + \lambda^2)^{-1/2} \frac{p}{\gamma} \delta \hat{f}_\pm, \quad (22)$$

and

$$\delta\hat{\rho} = -e \int dP_x dP_y dp (1+\lambda^2)^{-1/2} \frac{P_x}{p} \delta\hat{f}. \quad (23)$$

By application of Floquet's theorem, we express the axial and azimuthal structure of the fields and sources in the form

$$\delta\hat{f}(\vec{r}, z) = \sum_{l, n=-\infty}^{\infty} \delta\hat{f}_{l, n}(r) \exp[i(k + nk_w)z + il\theta], \quad (24)$$

in cylindrical coordinates. As might be expected, substitution of (19) into (22) and (23) results in source currents $\delta\hat{J}_{l, n}$ and charge densities $\delta\hat{\rho}_{l, n}$, each of which depends upon a complicated superposition of many harmonics of $\delta\hat{A}_{l, n}$ and $\delta\hat{\phi}_{l, n}$. However, in the limit in which the frequency $\omega \gg \Omega_2$, $\partial|\delta\hat{A}_{l, n}(r)|/\partial r \ll k$, and $\partial|\delta\phi_{l, n}(r)|/\partial r \ll k$ we find the comparatively simple forms

$$\begin{aligned} \delta\hat{J}_{l, n}^{(\pm)} \approx & -\frac{i\omega_b^2}{8\pi c} \int_0^{\infty} dp \frac{1}{\gamma} \left[P_w (\hat{H}_{l, n}^{(\pm)} + \hat{H}_{l, n \mp 2, n \pm 2}^{(\mp)}) - ip_{||} (ck_n \pm \delta\hat{\phi}_{l, n \mp 1, n \pm 1} - \omega \delta\hat{A}_{l, n \mp 1, n \pm 1, z}) \right] \frac{P_w}{\omega - k_n + i\nu_{||}} \frac{1}{p} \frac{\partial}{\partial p} \\ & - \frac{2\alpha_{\pm}^2}{\omega \pm \Omega_2 - k_n + i\nu_{||}} \hat{L}_{l, n}^{(\pm)} \mp \lambda^2 (1+\lambda^2)^{-1/2} \frac{\omega}{\Omega_2} (R_{l, n}^{(\pm)} \hat{L}_{l, n}^{(\pm)} - R_{l, n}^{(\mp)} \hat{L}_{l, n \mp 2, n \pm 2}^{(\mp)}) \Big] G_b(p) \end{aligned} \quad (25)$$

and

$$\begin{aligned} \delta\hat{\rho}_{l, n} \approx & -\frac{i\omega_b^2}{8\pi c} \int_0^{\infty} dp \frac{1}{\gamma v_w} \left[P_w (\hat{H}_{l, n}^{(-)} + \hat{H}_{l, n+1, n-1}^{(+)} - ip_{||} (ck_n \delta\hat{\phi}_{l, n} - \omega \delta\hat{A}_{l, n, z})) \right] \frac{P_w}{\omega - k_n + i\nu_{||}} \frac{1}{p} \frac{\partial}{\partial p} \\ & + \lambda^2 (1+\lambda^2)^{-1/2} \frac{\omega}{\Omega_2} (\hat{L}_{l, n}^{(-)} + R_{l, n}^{(-)} - \hat{L}_{l, n+1, n-1}^{(+)} - R_{l, n+1, n-1}^{(+)} + \frac{1}{2} v_w \hat{K}_{l, n} S_{l, n}) \Big] G_b(p), \end{aligned} \quad (26)$$

where $\delta\hat{J}_{l, n}^{(\pm)} \equiv (\delta\hat{J}_{l, n})_r \mp i(\delta\hat{J}_{l, n})_{\theta}$, $\delta\hat{A}_{l, n}^{(\pm)} \equiv \frac{1}{2}[(\delta\hat{A}_{l, n})_r \mp i(\delta\hat{A}_{l, n})_{\theta}]$, $\omega_b^2 \equiv 4\pi e^2 n_b/m$ is the average plasma frequency, $\nabla_{l, n}^{(\pm)} \equiv \partial/\partial r \pm l/r$,

$$\begin{aligned} \hat{L}_{l, n}^{(\pm)} & \equiv i(\omega - k_n v_{||}) \delta\hat{A}_{l, n}^{(\pm)} - \frac{1}{2} \nabla_{l, n}^{(\pm)} (c \delta\hat{\phi}_{l, n} - v_{||} \delta\hat{A}_{l, n, z}), \\ \hat{H}_{l, n}^{(\pm)} & \equiv i\omega \delta\hat{A}_{l, n}^{(\pm)} - \frac{1}{2} c \nabla_{l, n}^{(\pm)} \delta\hat{\phi}_{l, n}, \quad \hat{K}_{l, n} \equiv \nabla_{l, n}^{(-)} \delta\hat{A}_{l, n}^{(+)} - \nabla_{l, n}^{(+)} \delta\hat{A}_{l, n}^{(-)}, \\ R_{l, n}^{(\pm)} & \equiv \frac{\alpha_{+}}{\omega \pm \Omega_2 - k_n + i\nu_{||}} + \frac{\alpha_{-}}{\omega \mp \Omega_2 - k_n + i\nu_{||}} - \frac{1}{\omega - k_n + i\nu_{||}}, \end{aligned} \quad (27)$$

and

$$S_{l, n} \equiv \frac{1}{\omega - \Omega_2 - k_n + i\nu_{||}} + \frac{1}{\omega + \Omega_2 - k_n + i\nu_{||}} - \frac{2}{\omega - k_n + i\nu_{||}}. \quad (28)$$

Observe that $\delta\hat{J}_{l, n, z}$ has been omitted because the specification of a gauge condition allows us to eliminate one of the components ($\delta\hat{A}_{l, n}$, $\delta\hat{\phi}$), and we choose to deal with $\delta\hat{A}_{\pm}$ and $\delta\hat{\phi}$.

It should also be remarked that our choice of distribution (17) is equivalent to the requirement that the unperturbed orbits are of the steady-state type ($P_x = P_y = 0$). Such orbits are axicentered, and there is a unique mapping between the radius of the orbit and the particle energy (for given B_w , B_0 , and λ_w). As a consequence, a small spread in the energy of the beam will imply a narrow radial profile.

IV. THE MAXWELL-POISSON EQUATIONS

The starting point for the development in this section is the Maxwell-Poisson equations

$$\left[\frac{1}{r} \frac{d}{dr} r \frac{d}{dr} + p_n^2 - \frac{(l \mp 1)^2}{r^2} \right] \delta\hat{A}_{l, n}^{(\pm)} = -\frac{4\pi}{c} \delta\hat{J}_{l, n}^{(\pm)}, \quad (29)$$

$$\left[\frac{1}{r} \frac{d}{dr} r \frac{d}{dr} + p_n^2 - \frac{l^2}{r^2} \right] \delta\hat{\phi}_{l, n} = -8\pi \delta\hat{\rho}_{l, n}, \quad (30)$$

as well as the Lorentz gauge condition

$$k_n \delta\hat{A}_{l, n, z} = \frac{\omega}{c} \delta\hat{\phi}_{l, n} + i(\nabla_{l, n}^{(-)} \delta\hat{A}_{l, n}^{(+)} + \nabla_{l, n}^{(+)} \delta\hat{A}_{l, n}^{(-)}), \quad (31)$$

where $p_n^2 \equiv \omega^2/c^2 - k_n^2$. In order to carry the analysis further, a distribution function must be specified in order to evaluate the sources. We choose $G_b(p) = N(p)\delta[p - p(r)]$, where $p(r)$ is the mapping between the energy and the radius of the steady-state trajectory

$$p(r) = mc(1 + \lambda^2)^{1/2} [\gamma\beta_0 \pm 2\gamma\beta_w \lambda^{-2}(1 + \lambda^2)I_1(\lambda)], \quad (32)$$

$N(p)$ is an arbitrary function of p which is chosen such that $N(p(r))$ models the density profile, and $\omega_b^2(r) \equiv 4\pi e^2 n_0 N(p(r))/m$ is the local plasma frequency. As a consequence, by retaining only the dominant coupling terms, we find

$$\delta\hat{J}_{l,n}^{(\pm)} \approx \frac{c}{4\pi} (\Lambda_{l,n}^{(\pm)} \delta\hat{A}_{l,n}^{(\pm)} + T_{l \mp 1, n \pm 1} \delta\hat{\phi}_{l \mp 1, n \pm 1} + V_{l \mp 2, n \pm 2} \delta\hat{A}_{l \mp 2, n \pm 2}^{(\mp)}) \quad (33)$$

and

$$\delta\hat{\rho}_{l,n} \approx \frac{1}{4\pi} (\chi_{l,n} \delta\hat{\phi}_{l,n} + W_{l+1, n-1} \delta\hat{A}_{l+1, n-1}^{(+)} + W_{l-1, n+1} \delta\hat{A}_{l-1, n+1}^{(-)}), \quad (34)$$

where

$$\Lambda_{l \pm 1, n \mp 1}^{(\pm)} \equiv -\frac{\omega_b^2(r)}{\gamma c^2} \left[\omega - k_n v_{||} \left[1 + \frac{l^2}{2k_n^2 r^2} \right] \right] \left[\frac{\alpha_+^2}{\omega \pm \Omega_2 - k_{n+1} v_{||}} + \frac{\alpha_-^2}{\omega \mp \Omega_2 - k_{n+1} v_{||}} \right] + V_{l \pm 1, n \mp 1}, \quad (35)$$

$$\chi_{l,n} \equiv -\frac{\omega_b^2(r)}{\gamma c^2} \frac{\omega^2 - c^2 k_n^2}{v_{||} k_n} \frac{k_{n+1} v_{||}}{\gamma^2 (1 + \lambda^2) (\omega - k_{n+1} v_{||})^2} \left[1 + \lambda^2 Q(\lambda) \frac{\omega}{k_{n+1} v_{||}} \right], \quad (36)$$

$$T_{l,n}^{(\pm)} \equiv -\frac{\omega_b^2(r)}{2\gamma c^2} \frac{p_w}{p_{||}} \frac{\omega^2 - c^2 k_n^2}{ck_n} \frac{\omega}{\gamma^2 (1 + \lambda^2) (\omega - k_{n+1} v_{||})^2} \left[1 - Q(\lambda) \frac{(1 - \lambda^2)\omega - k_{n+1} v_{||}}{\omega} \right], \quad (37)$$

$$W_{l \pm 1, n \mp 1} \equiv -\frac{\omega_b^2(r)}{\gamma c^2} \frac{p_w}{p_{||}} \frac{\omega k_{n+1} c}{\gamma^2 (1 + \lambda^2) (\omega - k_{n+1} v_{||})^2} \left[1 - Q(\lambda) \frac{\omega - (1 + \lambda^2) k_{n+1} v_{||}}{k_{n+1} v_{||}} \right], \quad (38)$$

$$V_{l \pm 1, n \mp 1} \equiv -\frac{\omega_b^2(r)}{2\gamma c^2} \frac{\lambda^2 \omega^2}{\gamma^2 (1 + \lambda^2) (\omega - k_{n+1} v_{||})^2} \left[1 - Q(\lambda) \frac{2(\omega - k_{n+1} v_{||}) - \lambda^2 k_{n+1} v_{||}}{\omega} \right]. \quad (39)$$

In Eqs. (35)–(39) $(\gamma, v_{||}, p_w)$ are implicit functions of r and

$$Q(\lambda) \equiv \frac{\gamma^3 k_w v_{||} I_1(\lambda)/\lambda}{\{(1 + \lambda^2)[\Omega_0 \pm 2\Omega_w I_1(\lambda)] - \gamma k_w v_{||}\} Z(\lambda) - \lambda^2 \gamma k_w v_{||} Y(\lambda)}, \quad (40)$$

which contains a singularity at the transition to orbital instability for the group I and group II orbits. In the vicinity of these points, therefore, we expect the interaction strength to be greatly enhanced. Analogous results were found in the idealized one-dimensional theory.^{16,20} As a consequence, we obtain the following set of coupled differential equations:

$$\left[\frac{1}{r} \frac{d}{dr} r \frac{d}{dr} + p_{n \mp 1}^2 - \frac{l^2}{r^2} \right] \delta\hat{A}_{l \pm 1, n \mp 1}^{(\pm)} = -\Lambda_{l \pm 1, n \mp 1}^{(\pm)} \delta\hat{A}_{l \pm 1, n \mp 1}^{(\pm)} - T_{l,n}^{(\pm)} \delta\hat{\phi}_{l,n} - V_{l \mp 1, n \pm 1} \delta\hat{A}_{l \mp 1, n \pm 1}^{(\mp)}, \quad (41)$$

$$\left[\frac{1}{r} \frac{d}{dr} r \frac{d}{dr} + p_n^2 - \frac{l^2}{r^2} \right] \delta\hat{\phi}_{l,n} = -\chi_{l,n} \delta\hat{\phi}_{l,n} - W_{l+1, n-1} \delta\hat{A}_{l+1, n-1}^{(+)} - W_{l-1, n+1} \delta\hat{A}_{l-1, n+1}^{(-)}. \quad (42)$$

In order to solve this set of differential equations, we must specify the boundary conditions appropriate to a cylindrical waveguide of radius R_g . We assume the walls to be grounded and at zero potential; hence,

$$\begin{aligned} \delta\hat{\phi}_{l,n}(R_g) &= \delta\hat{A}_{l,n}^{(\pm)}(R_g) \\ &= \frac{d}{dr} [r(\delta\hat{A}_{l,n}^{(+)} + \delta\hat{A}_{l,n}^{(-)})] \Big|_{r=R_g} = 0. \end{aligned} \quad (43)$$

It should be observed that Eqs. (41)–(43) describe a coupling between five harmonic components: $\delta\hat{\phi}_{l,n}$, $\delta\hat{A}_{l \pm 1, n \mp 1}^{(\pm)}$, and $\delta\hat{A}_{l \mp 1, n \pm 1}^{(\mp)}$. Finally, we also assume that the potentials are continuous within the waveguide (i.e.,

across the boundary of the electron beam). The problem, therefore, has been specified with the essential physics of the interaction contained within the radial dependence of the coupling coefficients in (41) and (42). It is important to observe that with the above choice of indices, the azimuthal mode number for the electromagnetic waveguide modes is given by $l \pm 1$, and not simply by l . Thus, if we wish to study the TE_{l,m} or TM_{l,m} modes for the $\delta\hat{A}_{l \pm 1, n \pm 1}^{(\pm)}$ eigenvector, then we must set $l = 0$.

V. THE LIMIT OF A THIN BEAM

A solution to Eqs. (41)–(43) is found for the case of a thin beam in which the density profile is assumed to be

constant (n_0) within the range $R_0 - \Delta R \leq r \leq R_0$. As a result, in the limit in which $\Delta R \ll R_0$ the beam density is given approximately by

$$n_0(r) = n_0 \Delta R \delta(r - R_0). \quad (44)$$

It should be remarked that we have assumed the unperturbed orbits to be the stable steady-state trajectories. These orbits are axicentered and, for orbits of either group I or group II, there is a unique mapping between γ and λ (i.e., the orbit radius) for given B_0 , B_w , and λ_w . Thus, it is sufficient to specify the class of orbit and $R_0(\gamma_0)$ in order to obtain $\gamma_0(R_0)$. In addition, a spread in radius ΔR of the beam is equivalent to an energy spread $\Delta\gamma$ given by

$$\frac{\Delta\gamma}{\gamma_0} = \frac{\gamma_0^2 - 1}{(1 + \lambda_0^2) Q(\lambda_0)} \frac{\Delta R}{R_0}, \quad (45)$$

where $\lambda_0 \equiv k_w R_0$. Observe that within the context of our analysis, a thin beam is equivalent to a relatively small energy spread.

The solutions are of the form

$$\delta\phi_{l,n} = A_{l,n} J_l(p_n r), \quad \delta A_{l,n}^{(\pm)} = A_{l,n}^{(\pm)} J_{l \mp 1}(p_n r), \quad (46)$$

for $0 \leq r < R_0$, and

$$\delta\phi_{l,n} = B_{l,n} J_l(p_n r) + C_{l,n} N_l(p_n r), \quad (47)$$

$$\delta A_{l,n}^{(\pm)} = B_{l,n}^{(\pm)} J_{l \mp 1}(p_n r) + C_{l,n}^{(\pm)} Y_{l \mp 1}(p_n r)$$

for $r > R_0$. In (46) and (47) $J_l(x)$ and $N_l(x)$ are the regular Bessel functions of the first and second kind of order l . Observe that each field quantity (i.e., $\delta\phi_{l,n}$, $\delta A_{l,n}^{(\pm)}$, $\delta A_{l \mp 1, n \mp 1}^{(\pm)}$, $\delta A_{l-1, n+1}^{(\pm)}$, and $\delta A_{l+1, n-1}^{(\pm)}$) requires three coefficients to characterize the solution throughout the waveguide. Two of these coefficients may be determined from the boundary conditions at $r = R_0$, and R_g . The third coefficient is found by multiplying the field equations by r and integrating over $R_0 - \epsilon \leq r \leq R_0 + \epsilon$ in the limit $\epsilon \rightarrow 0^+$. This procedure determines the "jump condition" across the thin beam, and allows us to obtain a 5×5 matrix equation in, for example, the coefficients $A_{l,n}$, $A_{l+1, n-1}^{(\pm)}$, $A_{l-1, n+1}^{(\pm)}$, $A_{l \mp 1, n \mp 1}^{(\pm)}$, and $A_{l \mp 1, n \mp 1}^{(\pm)}$. Observe that the coupling to the field components in $\delta A_{l \mp 1, n \mp 1}^{(\pm)}$ occurs not through the source terms in the field equations but rather through the boundary condition at the waveguide wall.

The matrix equation obtained in this manner can be written as

$$\begin{pmatrix} \epsilon_{l,n} & -\frac{\pi}{2} R_0 \Delta R \bar{W}_{l+1, n-1} & -\frac{\pi}{2} R_0 \Delta R \bar{W}_{l-1, n+1} \\ \frac{\pi}{2} R_0 \Delta R \bar{T}_{l,n} & \epsilon_{l+1, n-1}^{(+)} & \frac{\pi}{2} R_0 \Delta R \bar{V}_{l-1, n+1} \\ \frac{\pi}{2} R_0 \Delta R \bar{T}_{l,n} & \frac{\pi}{2} R_0 \Delta R \bar{V}_{l+1, n-1} & \epsilon_{l-1, n+1}^{(-)} \end{pmatrix} \begin{pmatrix} A_{l,n} \\ A_{l+1, n-1}^{(+)} \\ A_{l-1, n+1}^{(-)} \end{pmatrix} = 0, \quad (48)$$

where the equations for $A_{l-1, n+1}^{(-)}$ and $A_{l+1, n-1}^{(+)}$ have already been eliminated,

$$\epsilon_{l,n} \equiv D_{l,n} - \frac{\pi}{2} R_0 \Delta R \bar{X}_{l,n}, \quad (49)$$

$$\begin{aligned} \epsilon_{l \pm 1, n \mp 1}^{(\pm)} &\equiv D_{l \pm 1, n \mp 1}^{(\pm)} \\ &+ \frac{\pi}{2} R_0 \Delta R (\bar{\Lambda}_{l \pm 1, n \mp 1}^{(\pm)} + \bar{\Lambda}_{l \pm 1, n \mp 1}^{(\mp)} M_{l \mp 1, n \pm 1}^{(l \pm 2)}), \end{aligned} \quad (50)$$

where $\bar{W}_{l \pm 1, n \mp 1}$, $\bar{V}_{l \pm 1, n \mp 1}$, $\bar{\Lambda}_{l \pm 1, n \mp 1}^{(\pm)}$, $\bar{T}_{l,n}$, and $\bar{X}_{l,n}$ denote those quantities specified in Eqs. (35)–(39) in which the substitution $\omega_0^2(r) = 4\pi e^2 n_0 / m$ has been made. In addition,

$$D_{l,n} \equiv \frac{J_l(\xi_n)}{J_l(\xi_n) [J_l(\xi_n) N_l(\xi_n) - J_l(\xi_n) N_l(\xi_n)]}, \quad (51)$$

$$D_{l \pm 1, n \mp 1}^{(\pm)} \equiv \frac{2J_{l \pm 1}(\xi_{n \mp 1}) J_{l \pm 1}(\xi_{n \mp 1})}{J_l(\xi_{n \mp 1}) S_{l \pm 1, n \mp 1}^{(l \pm 2)}}, \quad (52)$$

and

$$M_{l \mp 1, n \pm 1}^{(l \pm 2)} \equiv \frac{J_{l \pm 2}(\xi_{n \mp 1}) \Gamma_{l \pm 2}^{(l \pm 2)}}{J_l(\xi_{n \mp 1}) S_{l \pm 1, n \mp 1}^{(l \pm 2)}}, \quad (53)$$

where $\xi_n \equiv p_n R_0$, $\xi_n \equiv p_n R_g$, and J_l' is the derivative of the Bessel function. In (52) and (53),

$$\begin{aligned} \Gamma_{k,m}^{(n)} &\equiv N_l(\xi_m) \frac{d}{d\xi_m} J_k^2(\xi_m) \\ &- J_l(\xi_m) \frac{d}{d\xi_m} [N_k(\xi_m) J_k(\xi_m)], \end{aligned} \quad (54)$$

$$S_{k,m}^{(l \pm 2)} \equiv \Gamma_{k,m}^{(n)} + \frac{\pi}{2} R_0 \Delta R \bar{\Lambda}_{k,m}^{\mp} J_{l \pm 2}(\xi_m) \Psi_{k,m}^{(l \pm 2)}, \quad (55)$$

and

$$\begin{aligned} \Psi_{k,m}^{(l \pm 2)} &\equiv N_{l \pm 2}(\xi_m) \Gamma_{k,m}^{(n)} \\ &- J_{l \pm 2}(\xi_m) \left[N_l(\xi_m) \frac{d}{d\xi_m} [N_k(\xi_m) J_k(\xi_m)] \right. \\ &\quad \left. - J_l(\xi_m) \frac{d}{d\xi_m} N_k^2(\xi_m) \right]. \end{aligned} \quad (56)$$

The dispersion equation is found by setting the determinant of this interaction matrix to zero.

Substantial simplification occurs in the limit in which $|\omega - k_{n+1} v_{||}| \ll \omega, |k_{n+1} v_{||}|$ and we obtain

$$\bar{X}_{l,n} \approx -\frac{\omega_b^2}{\gamma_0 c^2} \frac{c}{v_{||}} \frac{\omega^2 - c^2 k_n^2}{ck_n} \frac{\omega}{\gamma_0^2 (1 + \lambda_0^2) (\omega - k_n + i v_{||})^2} \Phi, \quad \bar{V}_{l,\pm 1,n \mp 1} \approx \frac{1}{2} \frac{v_w}{c} \bar{W}_{l,\pm 1,n \mp 1}, \quad (57)$$

$$\bar{W}_{l,\pm 1,n \mp 1} \approx -\frac{v_w}{v_{||}} \frac{\omega_b^2}{\gamma_0 c^2} \frac{c}{v_{||}} \frac{\omega^2}{\gamma_0^2 (1 + \lambda_0^2) (\omega - k_n + i v_{||})^2} \Phi, \quad \bar{T}_{l,n} \approx \frac{1}{2} \frac{v_w}{c} \bar{X}_{l,n}, \quad (58) \quad \text{and} \quad (60)$$

$$\bar{\Lambda}_{l,\pm 1,n \mp 1} \approx -\lambda_0^2 \frac{\omega_b^2}{2\gamma_0 c^2} \frac{\omega^2}{\gamma_0^2 (1 + \lambda_0^2) (\omega - k_n + i v_{||})^2} \Phi - \frac{\omega_b^2}{\gamma_0 c^2} \left[\omega - k_n + i v_{||} \left(1 + \frac{l^2}{2k_n^2 R_0^2} \right) \right] \left[\frac{\alpha_+^2}{\omega \pm \Omega_2 - k_n + i v_{||}} + \frac{\alpha_-^2}{\omega \mp \Omega_2 - k_n + i v_{||}} \right], \quad (61)$$

where $\Phi \equiv 1 + \lambda_0^2 Q(\lambda_0)$. Observe that for all cases of practical interest $v_w \ll c$ and $|\bar{V}_{l,\pm 1,n \mp 1}| \ll |\bar{W}_{l,\pm 1,n \mp 1}|$. As a consequence, the terms in $\bar{V}_{l,\pm 1,n \mp 1}$ can be ignored. This is equivalent to the neglect of any direct coupling between the electromagnetic modes $\delta A_{l,\pm 1,n \mp 1}^{(\pm)}$. In addition, we shall neglect the coupling to the $\delta A_{l,\mp 1,n \pm 1}^{(\pm)}$ modes, so that

$$\epsilon_{l,\pm 1,n \mp 1}^{(\pm)} \approx \frac{2J_{l,\pm 1}(\xi_{n \mp 1})J_{l,\pm 1}(\xi_{n \mp 1})}{J_l(\xi_{n \mp 1})\Gamma_l^{(n)}(\xi_{n \mp 1})} + \frac{\pi}{2} R_0 \Delta R \bar{\Lambda}_{l,\pm 1,n \mp 1}^{(\pm)}. \quad (62)$$

Within the context of this approximation, the dispersion equation is of the form

$$\epsilon_{l,n} = \frac{\lambda_0^2}{1 + \lambda_0^2} \Phi \frac{\omega_b^2}{2\gamma_0 c^2} \left[\frac{\pi}{2} R_0 \Delta R \right]^2 \frac{\omega^2}{\gamma_0^2 (\omega - k_n + i v_{||})^2} \bar{X}_{l,n} \left[\frac{1}{\epsilon_{l+1,n-1}^{(+)}} + \frac{1}{\epsilon_{l-1,n+1}^{(-)}} \right]. \quad (63)$$

Finally, if the solution is restricted to the first quadrant in (ω, k_n) space, then $|\epsilon_{l-1,n+1}^{(-)}| \gg |\epsilon_{l+1,n-1}^{(+)}|$ and (63) can be approximated by

$$\epsilon_{l,n} \epsilon_{l+1,n-1}^{(+)} \approx \frac{\lambda_0^2}{1 + \lambda_0^2} \Phi \frac{\omega_b^2}{2\gamma_0 c^2} \left[\frac{\pi}{2} R_0 \Delta R \right]^2 \frac{\omega^2}{\gamma_0^2 (\omega - k_n + i v_{||})^2} \bar{X}_{l,n}. \quad (64)$$

The complete dispersion equation (48) has been solved numerically for $\gamma = 3.5$, $\omega_b/\gamma^{1/2}ck_w = 0.1$, $\Omega_w/\gamma ck_w = 0.05$, $\Delta R/R_0 = 0.1$, $k_w R_0 = 1.5$, and a wide range of axial guide fields for both the TE_{11} and TM_{11} waveguide modes. It should be remarked before we proceed further with a description of the numerical analysis that each of the off-diagonal elements of the dispersion tensor in Eq. (48) is directly proportional to Φ and, hence, the coupling coefficient also depends upon this function. The variation of Φ with the axial guide field, therefore, provides valuable insight into the effect of B_0 on the radiation growth rate. To this end, we plot Φ versus $\Omega_0/\gamma ck_w$ in Fig. 3, in which the distinction between the value of the function for group I and group II orbits is clearly made. As discussed in Sec. II, Φ is characterized by singularities for both groups of orbits at the transitions to orbital instability (13), which occur at $\Omega_0/\gamma ck_w \approx 0.75$ (group I orbits) and $\Omega_0/\gamma ck_w \approx 0.62$ (group II orbits) for the parameters considered. While the growth rates at these points are also singular, it should be recognized that the linear theory itself breaks down in the vicinity of the singularities and a fully nonlinear treatment is required. The difference between Φ in the present three-dimensional theory and the one-dimensional analog²⁰ lies, principally, in the fact that no orbital instability (hence, no singulari-

ty) occurs for the group II orbits in one dimension. In addition, Φ vanishes at $\Omega_0/\gamma ck_w \approx 1.25$ (group II orbits) and the growth rate may be expected to vanish at this point as well.

The growth rate $\text{Im}k_n/k_w$ is plotted versus ω/ck_w in Fig. 4 for the TE_{11} mode and $\Omega_0/\gamma ck_w = 0.0$ and 0.5 . The waveguide cutoff occurs at $\omega/ck_w \approx 1.23$ and the two peaks shown for each value of the axial guide field correspond to the upper and lower intersections between the space-charge wave and the waveguide mode. This figure represents the cases corresponding to group I orbits, and we observe that the unstable spectrum is quite narrow but tends to broaden slightly with increasing B_0 corresponding to decreases in $v_{||}$ as the transition to orbital instability is approached. In addition, the resonant frequency decreases relatively fast with increasing B_0 for the upper intersection, but is not very sensitive to the value of the guide field for the lower intersection. Finally, we observe that the two peaks are well separated and that the growth rate corresponding to the upper intersection is the larger of the two. The peak growth rates and corresponding frequency at peak growth are plotted in Fig. 5 versus $\Omega_0/\gamma ck_w$, in which the singularity at $\Omega_0/\gamma ck_w \approx 0.75$ is evident and that the growth rate for the upper intersection exceeds that of the lower intersection over the entire range

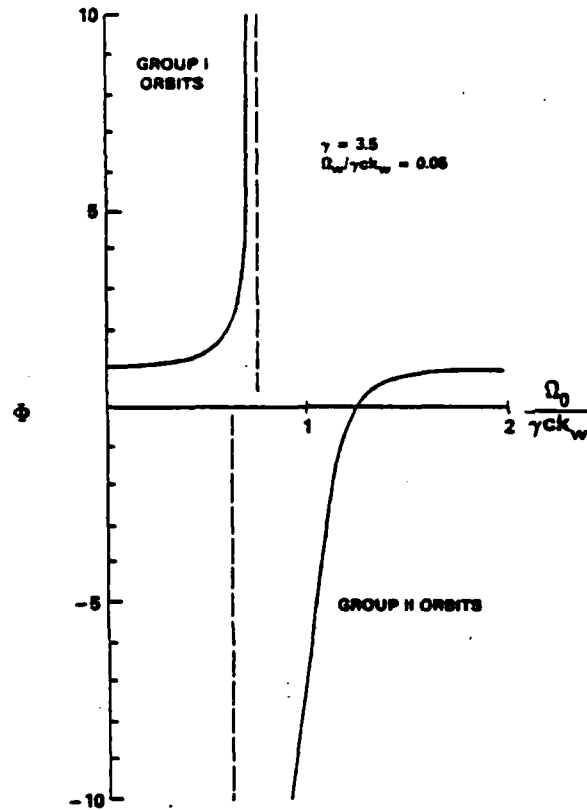


FIG. 3. Graph of $\Phi \equiv 1 + \lambda^2 Q(\lambda)$ vs the axial guide field for both group I and group II steady-state trajectories.

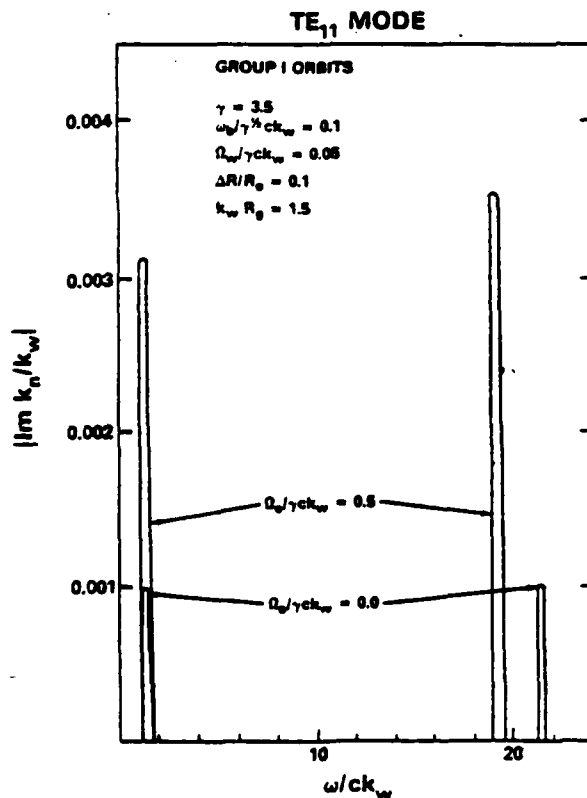


FIG. 4. Plot of the growth rate $|\text{Im } k_n / k_w|$ vs frequency for the TE_{11} mode and group I orbits at $\Omega_0 / \gamma c k_w = 0.0$ and 0.5 .

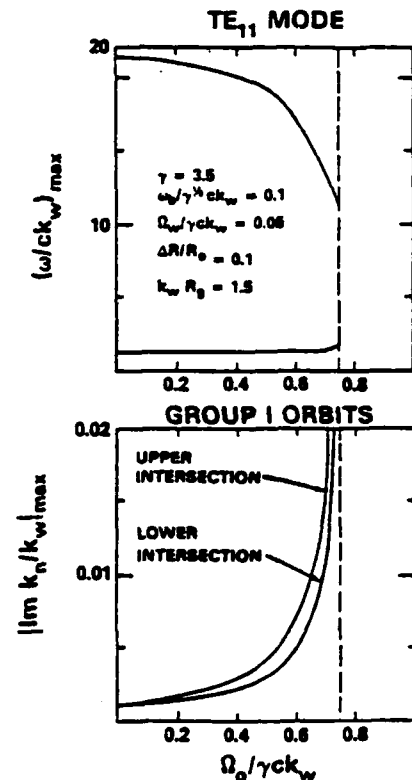


FIG. 5. Plots of the maximum growth rate and corresponding frequency for the TE_{11} mode as a function of the guide field for group I orbits. Both the upper and lower intersections are shown.

of group I orbits. It is also clear that while the frequency at the upper intersection decreases with decreasing $v_{||}$, the frequency at the lower intersections increases. As a result, the interactions tend to coalesce with decreasing $v_{||}$; however, the cutoff of the TE_{11} mode for the parameters considered is sufficiently low that coalescence does not occur for the group I orbits and the two lines remain well separated.

The growth rate for group II orbits is plotted versus frequency for $\Omega_0 / \gamma c k_w = 1.0$ and 1.5 in Fig. 6 for the TE_{11} mode. It is again clear that two peaks are found which correspond to the upper and lower intersections. However, in the case of $\Omega_0 / \gamma c k_w = 1.0$ the axial velocity ($v_{||}/c \approx 0.87$) is sufficiently low that the two peaks are not well separated and overlap. This results in a substantially broadened spectrum of unstable waves. As the guide field is increased the axial velocity also increases and the separation between the peaks becomes more distinct. This is illustrated for $\Omega_0 / \gamma c k_w = 1.5$ ($v_{||} \approx 0.95$) in which the two peaks are seen to be well separated. The peak growth rates and frequencies corresponding to the group II orbits are shown in Fig. 7 versus $\Omega_0 / \gamma c k_w$. As in the case of group I orbits, the growth rates for the upper intersection everywhere exceed those of the lower intersection. In addition, it is clear that the growth rates vanish for $\Omega_0 / \gamma c k_w \approx 1.25$ corresponding to the zero of Φ . Finally, it is seen that as $\Omega_0 / \gamma c k_w$ decreases below unity the coalescence continues rapidly and the resonance is lost for

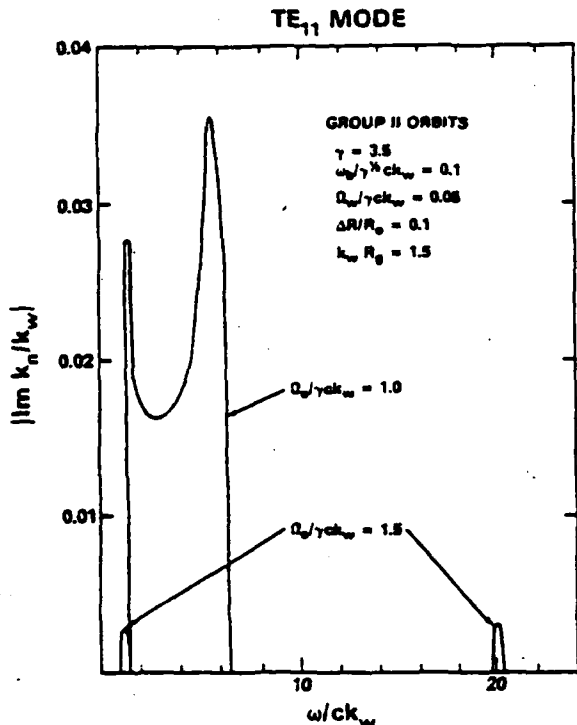


FIG. 6. Plot of the growth rate vs frequency for the TE₁₁ mode and group II orbits at $\Omega_0/\gamma ck_w = 1.0$ and 1.5.

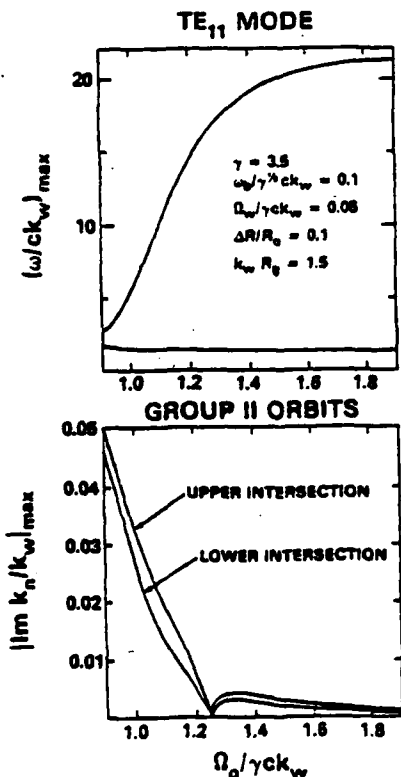


FIG. 7. Plots of the maximum growth rate and corresponding frequency for the TE₁₁ mode as a function of the guide field for group II orbits.

$\Omega_0/\gamma ck_w \leq 0.89$ by which point the double peak in the unstable spectrum has merged to form a single line. As a result, the interaction is lost at a value of the axial guide field greater than that corresponding to the singularity in Φ at $\Omega_0/\gamma ck_w \approx 0.62$ and no difficulties arising from the singularity occur.

One characteristic of the resonant nature of the interaction which must be emphasized is that the *l*th Doppler upshift describes interactions for all radial eigenmodes TE_{*lm*} and TM_{*lm*} (*m* = 1, 2, 3, . . .). This constitutes a selection rule²⁴ which stems from the azimuthal variation of the steady-state orbits; specifically, that $\theta = k_w z$ and the phase of the waveguide modes varies as

$$\exp(ik_w z + il\theta - i\omega t) \sim \exp(ik_w z + ilk_w - \omega t).$$

The behavior of the growth spectrum for the TM₁₁ mode as a function of the axial guide field is qualitatively similar to that shown for the TE₁₁ mode. However, the TM₁₁ mode is characterized by a higher cutoff frequency (at $\omega/ck_w \approx 2.55$ for the parameters chosen); therefore, the upper (lower) intersection frequency is lower (higher) for the TM₁₁ mode than for the TE₁₁ at a given axial velocity. The maximum growth rate and corresponding frequency of the TM₁₁ modes are plotted versus $\Omega_0/\gamma ck_w$ in Figs. 8 and 9 for the group I and group II orbits, respectively. The growth rates are found to be comparable to those found for the TE₁₁ mode. It is evident, however, that the upper and lower intersections coalesce for the TM₁₁ before the singularity in Φ occurs on both the group I and group II orbits. Such coalescence was found only on the group

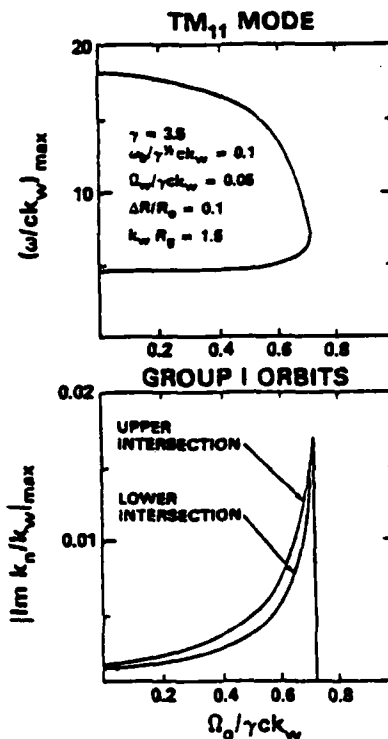


FIG. 8. Graph of the maximum growth rate and corresponding frequency for the TM₁₁ mode vs axial guide field for group I orbits.

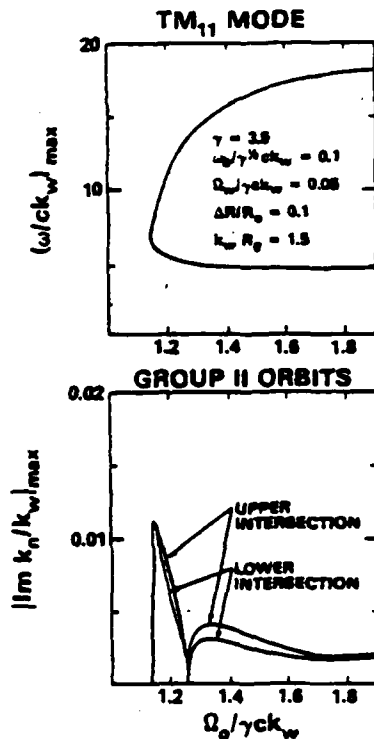


FIG. 9. Graph of the maximum growth rate and corresponding frequency for the TM_{11} mode vs axial guide field for group II orbits.

II orbits for the TE_{11} mode due to the lower value of the cutoff frequency.

VI. SUMMARY AND DISCUSSION

In this paper we have developed a collective theory of the free-electron laser which includes the effects of finite waveguide geometry and transverse gradients in the wiggler field. To this end, a Vlasov-Maxwell formulation has been employed which is equivalent to a perturbation expansion of the single-particle orbits to first order in the radiation and space-charge fields. The single-particle orbits are assumed to be helical, steady-state trajectories.^{24,27}

The principal difference between the orbits in the ideal (one-dimensional) and realizable (three-dimensional) wigglers is that in three dimensions unstable trajectories are found for both group I ($\Omega_0 < \gamma k_w v_{||}$) and group II ($\Omega_0 > \gamma k_w v_{||}$) orbits, while in one dimension only the group I trajectories can become unstable. Because of this feature, singularities are found in the linear growth rates for both types of trajectory in the realizable wiggler, which contrasts with the one-dimensional theory in which such a singularity occurs only for the group I class of orbit.

An additional feature of the three-dimensional theory arises from the fact that for given B_w , B_0 , λ_w , and γ at most one stable, steady-state orbit of each type exists. Thus for a specific guide and wiggler-field combination there is a unique mapping between γ and the orbit radius which implies that a nearly monoenergetic beam will be characterized by a small spread in the radii of the orbits described by the constituent electrons. As a result, we have solved the coupled Maxwell-Poisson equations in a "thin-beam" limit, and obtained the growth rates for the TE_{11} and TM_{11} modes. Wave amplification is found, in general, at both the upper and lower intersections of the waveguide and space-charge modes, although for sufficiently low axial velocities these two unstable regions of the spectrum are found to coalesce just prior to the point at which the intersections are lost.

It should also be reiterated that amplification of the TE_{lm} or TM_{lm} modes ($m=1,2,3,\dots$) occurs only for the resonance corresponding to the l th Doppler upshift. This constitutes a selection rule, and occurs because the azimuthal variation of the steady-state orbits varies as $\theta = k_w z$ and the phase of the waveguide modes vary as $\exp(ik_w z + i l \theta - i \omega t)$. It is important to recognize, however, that not all beam electrons in an experimental device can be expected to execute the steady-state trajectories and, as a consequence, other waveguide modes (i.e., TM_{0m} or TE_{0m}) may be excited as well.

ACKNOWLEDGMENT

This work was supported in part by Naval Sea Systems Command and in part by Naval Electronic Systems Command.

*Permanent address: Science Applications, Inc., McLean, VA 22102.

¹L. R. Elias, W. M. Fairbank, J. M. J. Madey, H. A. Schwettman, and T. I. Smith, Phys. Rev. Lett. **36**, 717 (1976).

²D. A. G. Deacon, L. R. Elias, J. M. J. Madey, G. J. Ramian, H. A. Schwettman, and T. I. Smith, Phys. Rev. Lett. **38**, 892 (1977).

³V. L. Granatstein, S. P. Schlesinger, M. Herndon, R. K. Parker, and J. A. Pasour, Appl. Phys. Lett. **30**, 384 (1977).

⁴D. B. McDermott, T. C. Marshall, S. P. Schlesinger, R. K. Parker, and V. L. Granatstein, Phys. Rev. Lett. **41**, 1368 (1978).

⁵H. Boehmer, M. Z. Caponi, J. Edighoffer, S. Fornaca, J. Munch, G. R. Neil, B. Saur, and C. Shih, Phys. Rev. Lett. **48**, 141 (1982).

⁶J. M. Slater, IEEE J. Quant. Electron. **QE-17**, 1476 (1981).

⁷R. K. Parker, R. H. Jackson, S. H. Gold, H. P. Freund, V. L. Granatstein, P. C. Efthimion, M. Herndon, and A. K. Kinkaid, Phys. Rev. Lett. **48**, 238 (1982).

⁸S. H. Gold, W. M. Black, H. P. Freund, V. L. Granatstein, R. H. Jackson, P. C. Efthimion, and A. K. Kinkaid, Phys. Fluids **26**, 2683 (1983).

⁹P. Sprangle, V. L. Granatstein, and L. Baker, Phys. Rev. A **12**, 1697 (1975).

¹⁰P. Sprangle and V. L. Granatstein, Phys. Rev. A **17**, 1792 (1978).

¹¹T. Kwan and J. M. Dawson, Phys. Fluids **22**, 1089 (1979).

¹²I. B. Bernstein and J. L. Hirshfield, Phys. Rev. A **20**, 1661 (1979).

¹³P. Sprangle and R. A. Smith, Phys. Rev. A **21**, 293 (1980).

- ¹⁴R. C. Davidson and H. S. Uhm, *Phys. Fluids* **23**, 2076 (1980).
¹⁵L. Friedland and J. L. Hirshfield, *Phys. Rev. Lett.* **44**, 1456 (1980).
¹⁶H. P. Freund, P. Sprangle, D. Dillenburg, E. H. da Jornada, B. Liberman, and R. S. Schneider, *Phys. Rev. A* **24**, 1965 (1981).
¹⁷I. B. Bernstein and L. Friedland, *Phys. Rev. A* **23**, 816 (1981).
¹⁸H. S. Uhm and R. C. Davidson, *Phys. Fluids* **24**, 1541 (1981).
¹⁹H. S. Uhm and R. C. Davidson, *Phys. Fluids* **24**, 2348 (1981).
²⁰H. P. Freund, P. Sprangle, D. Dillenburg, E. H. da Jornada, R. S. Schneider, and B. Liberman, *Phys. Rev. A* **26**, 2004 (1982).
²¹L. Friedland and A. Fruchtman, *Phys. Rev. A* **25**, 2693 (1982).
²²W. A. McMullin and R. C. Davidson, *Phys. Rev. A* **25**, 3130 (1982).
²³H. P. Freund, *Phys. Rev. A* **27**, 1977 (1983).
²⁴H. P. Freund, S. Johnston, and P. Sprangle, *IEEE J. Quant. Electron.* **QE-19**, 322 (1983).
²⁵W. B. Colson and J. L. Richardson, *Phys. Rev. Lett.* **50**, 1050 (1983).
²⁶L. Friedland, *Phys. Fluids* **23**, 2376 (1980).
²⁷P. Diament, *Phys. Rev. A* **23**, 2537 (1981).
²⁸H. P. Freund and A. T. Drobot, *Phys. Fluids* **25**, 736 (1982).

APPENDIX I

RAPID ELECTRON BEAM ACCELERATORS, *55*

(REBA-TRONS)

Rapid Electron Beam Accelerators (REBA-TRONS)

C. A. KAPETANAKOS, P. SPRANGLE, S. J. MARSH,*
D. DIALETIS,† C. AGRITELLIS,† AND A. PRAKASH,‡

*Advanced Accelerator Program
Plasma Physics Division*

**Sachs/Freeman Associates
Bowie, MD 20715*

*†Science Applications International Corp.
McLean, VA 22102*

*‡Ballistic Research Laboratory
Aberdeen, MD 21005*

April 25, 1985

This work was supported by the Office of Naval Research
and the U.S. Army Ballistic Research Laboratory.



NAVAL RESEARCH LABORATORY
Washington, D.C.

Approved for public release; distribution unlimited.

SECURITY CLASSIFICATION OF THIS PAGE

REPORT DOCUMENTATION PAGE				
1a. REPORT SECURITY CLASSIFICATION UNCLASSIFIED		1b. RESTRICTIVE MARKINGS		
2a. SECURITY CLASSIFICATION AUTHORITY		3. DISTRIBUTION / AVAILABILITY OF REPORT		
2b. DECLASSIFICATION / DOWNGRADING SCHEDULE		Approved for public release; distribution unlimited.		
4. PERFORMING ORGANIZATION REPORT NUMBER(S) NRL Memorandum Report 5503		5. MONITORING ORGANIZATION REPORT NUMBER(S)		
6a. NAME OF PERFORMING ORGANIZATION Naval Research Laboratory	6b. OFFICE SYMBOL (If applicable) Code 4704	7a. NAME OF MONITORING ORGANIZATION Office of Naval Research		
6c. ADDRESS (City, State, and ZIP Code) Washington, DC 20375-5000		7b. ADDRESS (City, State, and ZIP Code) Arlington, VA 22217		
8a. NAME OF FUNDING / SPONSORING ORGANIZATION ONR and BRL	8b. OFFICE SYMBOL (If applicable)	9. PROCUREMENT INSTRUMENT IDENTIFICATION NUMBER		
8c. ADDRESS (City, State, and ZIP Code) Arlington, VA 22217 Aberdeen, MD 21005		10. SOURCE OF FUNDING NUMBERS		
		PROGRAM ELEMENT NO. 61153N	PROJECT NO.	TASK NO. RR011-09-4E WORK UNIT ACCESSION NO. DN180-207
11. TITLE (Include Security Classification) Rapid Electron Beam Accelerators (REBA-TRONS)				
12. PERSONAL AUTHOR(S) Kapetanakos, C.A., Sprangle, P., Marsh, S.J.,* Dialektis, D.,† Aggitellis, C.,‡ and Prakash, A.‡				
13a. TYPE OF REPORT Interim	13b. TIME COVERED FROM TO	14. DATE OF REPORT (Year, Month, Day) 1985 April 25	15. PAGE COUNT 55	
16. SUPPLEMENTARY NOTATION *Sachs/Freeman Associates, Bowie, MD 20715 †Science Applications International Corp., McLean, VA 22102 (Continues)				
17. COSATI CODES		18. SUBJECT TERMS (Continue on reverse if necessary and identify by block number)		
FIELD	GROUP	SUB-GROUP		
19. ABSTRACT (Continue on reverse if necessary and identify by block number) <p>We have carried out an extensive numerical and analytical investigation of the beam dynamics in a rebratron accelerator. In this device acceleration occurs by a localized, high gradient electric field and beam confinement is achieved by a strong focusing torsatron magnetic field. In a rebratron, beam acceleration occurs in a few microseconds and limitations imposed by instabilities, field errors and radiation losses can be relaxed. Our studies indicate that both the bandwidth and the maximum electron beam current than can be confined by these devices is remarkably high.</p>				
20. DISTRIBUTION / AVAILABILITY OF ABSTRACT <input checked="" type="checkbox"/> UNCLASSIFIED/UNLIMITED <input type="checkbox"/> SAME AS RPT <input type="checkbox"/> DTIC USERS		21. ABSTRACT SECURITY CLASSIFICATION UNCLASSIFIED		
22a. NAME OF RESPONSIBLE INDIVIDUAL C. A. Kapetanakos		22b. TELEPHONE (Include Area Code) (202) 767-2838	22c. OFFICE SYMBOL Code 4704	

DD FORM 1473, 84 MAR

83 APR edition may be used until exhausted

All other editions are obsolete.

SECURITY CLASSIFICATION OF THIS PAGE

i

16. SUPPLEMENTARY NOTATION (Continued)

‡Ballistic Research Laboratory, Aberdeen, MD 21005

This work was supported by the Office of Naval Research and the U.S. Army Ballistic Research Laboratory.

CONTENTS

I. INTRODUCTION 1

II. THE APPLIED FIELDS 3

III. NUMERICAL RESULTS 9

IV. THEORETICAL MODEL 11

V. SELF FIELDS 19

VI. CONCLUSIONS 23

ACKNOWLEDGMENTS 48

REFERENCES 48

RAPID ELECTRON BEAM ACCELERATORS
(REBA-TRONS)

I. Introduction

Ultra-high current accelerators are rapidly becoming an active area of research.^{1,2} The development of these devices is mainly motivated by a variety of potential applications^{1,3,4} that are extended over several areas, including environment, food processing, radiation sources, x-ray radiography and national defense.

Among the various accelerating schemes that have the potential to produce ultra-high power electron beams, induction accelerators^{1,2} appear to be the most promising. Induction accelerators are inherently low impedance devices and thus are ideally suited to drive high current beams. The acceleration process is based on the inductive electric field produced by a time varying magnetic field.

Quite naturally, induction accelerators are divided into linear⁵⁻¹³ and cyclic¹⁴⁻¹⁹ devices. In linear devices the accelerating field is localized in the gap, while in their cyclic counterparts the electric field is continuous along the orbit of the accelerated particles. Both cyclic and linear devices require the same total magnetic flux change to achieve a given energy increment. However, in linear accelerators the total change of flux occurs in one transit time, typically in less than 100 nsec, while in cyclic accelerators the same change occurs over several thousand revolutions in a typical time of one msec.

As a consequence of the slow acceleration, the accelerated beam must be confined by the focusing magnetic field over long periods of time and thus field errors, instabilities and radiation losses impose limitations on the cyclic accelerators. These limitations can be substantially relaxed if the acceleration could occur rapidly as in

Manuscript approved February 7, 1985.

linear accelerators. Therefore, a device that combines the rapid acceleration of linear accelerators and the compact size of cyclic accelerators is highly desirable. In this paper, we propose such a hybrid scheme that combines most of the advantages of linear and cyclic accelerators. This device has been named REBA-TRON (Rapid Electron Beam Accelerator). The rebatron is similar to the racetrack induction accelerator.²⁰

A rebatron is shown schematically in Fig. 1. The high gradient localized field that is responsible for the rapid acceleration is produced by convoluted parallel transmission lines, although, other transmission lines may be more appropriate in an actual system. Since the acceleration occurs over a few usec, the constraints imposed on the vertical field are very stringent. In an actual device the vertical field is generated by two coaxial, cylindrical plates that carry current in the opposite direction. The axes of these lines coincide with the major axis of the toroidal vessel and they are located symmetrically around the minor axis of the torus. These transmission lines change mainly the local, vertical magnetic field, while the magnetic flux through the beam orbit remains approximately constant. The mismatch between the beam energy and the vertical field is alleviated by a strong focusing field. This field is generated by a set of $\ell = 2$ torsatron windings, i.e., two twisted wires that carry current in the same direction. In addition to the transverse components of the field, the torsatron windings provide a zero order toroidal magnetic field. The purpose of the resistive chamber wall is to facilitate the beam trapping²¹ in the applied magnetic field. Beam capture in the rebatrons is very difficult, because the strong focusing field makes the particle orbit insensitive to the energy mismatch and thus small changes

in the betatron (vertical) magnetic field are not sufficient to move the beam from the injection position near the wall to the minor axis of the torus.

The superior confining properties of twisted quadrupole fields have been recognized for several years.²² Recently, it has been reported¹⁹ that the $\ell=2$ Stellarator configuration has an energy bandwidth of ~50%.

In this report, we are presenting results from our studies of the beam dynamics in a rebatron accelerator when the magnetic fields are not a function of time. In addition, the local vertical magnetic field has been replaced by a betatron magnetic field. Our results indicate that both the bandwidth and the maximum electron current that can be confined by a rebatron are very high. Results with the local, fast varying vertical field will be reported in a forthcoming publication.

II. The Applied Fields

a. Magnetic Fields

In the local cylindrical coordinate system $\hat{e}_\theta, \hat{e}_\phi, \hat{e}_s$ shown in Fig. 2, the magnetic field components of the $\ell = 2$ torsatron are given by

$$B_\theta = B_\theta^{(0)} + B_{\theta+}^{(1)} + B_{\theta-}^{(1)}, \quad (1a)$$

$$B_\phi = B_\phi^{(0)} + B_{\phi+}^{(1)} + B_{\phi-}^{(1)}, \quad (1b)$$

$$B_s = \frac{1}{1 + (\rho/r_0) \cos \theta} [B_s^{(0)} + B_{s+}^{(1)} + B_{s-}^{(1)}], \quad (1c)$$

where

$$B_{\phi}^{(0)} = B_0 \sum_{m=1}^{\infty} A_m^{(0)} m x_0 I_{2m}^{\prime}(mx) \sin[2m(\phi - \alpha s)], \quad (2a)$$

$$B_{\phi}^{(0)} = B_0 \sum_{m=1}^{\infty} A_m^{(0)} 2m \frac{x_0}{x} I_{2m}^{\prime}(mx) \cos[2m(\phi - \alpha s)], \quad (2b)$$

$$B_s^{(0)} = B_0 \left[1 - \sum_{m=1}^{\infty} A_m^{(0)} m x_0 I_{2m}^{\prime}(mx) \cos[2m(\phi - \alpha s)] \right], \quad (2c)$$

and²⁵

$$B_{\phi \pm}^{(1)} = \frac{1}{4} \frac{\rho_0}{r_0} B_0 \sum_{m=1}^{\infty} \left[A_m^{(1)} I_{2m \pm 1}^{\prime}(mx) - A_m^{(0)} \{2(1 \pm m)mx I_{2m}^{\prime}(mx) + [(mx)^2 + 2m(2m \pm 1) + 1] I_{2m}^{\prime}(mx)\} \sin[(2m \pm 1)\phi - 2m\alpha s] \right], \quad (3a)$$

$$B_{\phi \pm}^{(1)} = \frac{1}{4} \frac{\rho_0}{r_0} B_0 \sum_{m=1}^{\infty} (2m \pm 1) \left[A_m^{(1)} \frac{1}{mx} I_{2m \pm 1}^{\prime}(mx) - A_m^{(0)} \{mx I_{2m}^{\prime}(mx) + (1 \pm 2m) I_{m \mp 1}^{\prime}(mx)\} \cos[(2m \pm 1)\phi - 2m\alpha s] \right], \quad (3b)$$

$$B_{s \pm}^{(1)} = -\frac{1}{4} \frac{\rho_0}{r_0} B_0 \sum_{m=1}^{\infty} \left[A_m^{(1)} I_{2m \pm 1}^{\prime}(mx) - A_m^{(0)} \{mx [mx I_{2m}^{\prime}(mx) + (1 \pm 2m) I_{2m}^{\prime}(mx)]\} \cos[(2m \pm 1)\phi - 2m\alpha s] \right]. \quad (3c)$$

The coefficients $A_m^{(0)}$, $A_m^{(1)}$ and C_m are given by the expressions

$$A_m^{(0)} = K \frac{1}{2m} (mx_0) C_m, \quad (4a)$$

$$A_m^{(1)} = \left[(mx_0)^2 K_{2m}^{\prime}(mx_0) - K_{2m\pm 1}^{\prime}(mx_0) \right. \\ \left. + (1 \pm 4m) mx_0 K_{2m\pm 1}^{\prime}(mx_0) \right] C_m, \quad (4b)$$

$$C_m = \frac{2 \sin 2m\delta}{2m\delta}. \quad (4c)$$

The remaining parameters are defined as follows:

$$B_0 = \frac{8\pi I}{cL}, \quad (5)$$

$$x_0 = 2a\alpha_0, \quad (6a)$$

$$x = 2a\alpha, \quad (6b)$$

$$\alpha = \frac{2\pi}{L}, \quad (7)$$

where I is the current flowing in the windings, $2\delta a_0$ is the width of the current carrying conductor, a_0 is the radius and L is the period of the windings, r_0 is the major radius of the torus, B_s^{ex} is the external toroidal magnetic field and $I_n(x)$, $K_n(x)$, $I_n^{\prime}(x)$ and $K_n^{\prime}(x)$ are the Bessel functions and their derivatives. In a toroidal device, the period should satisfy the relation

$$\frac{2\pi r_0}{L} = N, \quad (8)$$

where N is an integer. The zero order fields $B_0^{(o)}$, $B_\phi^{(o)}$ and $B_s^{(o)}$ are the field components produced by the helical windings in a straight (cylindrical) configuration^{23,24} and the terms proportional to a_0/r_0 are

the first order toroidal corrections. These corrections, as given in Eqs. (3), have been obtained for the surface current density

$$J_{\rho} = 0, J_{\phi} = \left(\frac{I}{2\delta\rho_0} \right) \left[\frac{\alpha_0}{1 + (\rho_0/r_0) \cos \phi} \right] \text{ and } J_s = \frac{I}{2\delta\rho_0} .$$

The three magnetic field components for $s = 0$ are plotted in Figs. 3a and 3b for $\phi = 0$ and $\phi = \pi/2$ respectively. The various parameters for these plots are listed in Table I. At $\phi = 0$, the radial component of the field is zero. The B_{ϕ} component increases linearly with ρ near the minor axis and considerably faster near the wires. The toroidal correction at $\rho = 0$ is approximately -36 G. In the results shown in Fig. 3, in addition to the toroidal field produced by the torsatron windings, there is a - 6 kG field produced by a set of toroidal coils. At $\rho = 0$, $B_s = B_s^{\text{ex}} + B_0 = - 6 + 2.5 = - 3.5$ kG. It is apparent from these results that the toroidal field B_{ϕ} does not vary as $1/r$. The reason is that B_s is a function of s or the toroidal angle. Figure 3c gives the magnetic field lines in the r, z and ρ, s planes. Because of the toroidal corrections, the magnetic axis does not coincide with the minor axis of the torus, which is located at $r = 100$ cm. The magnetic axis is always shifted toward the major axis of the torus, because the field on the minor axis generated by the axial current flowing on the section of the torus to the left of the major axis reinforces the field generated by the axial current flowing in the outside edge of the torus that is located to the right of the major axis.

Equations (1) to (7) are used to compute the magnetic field

components in the numerical integration of the orbit equations. It has been determined that the first two non zero terms in the expansion are sufficient to describe the field in the region $\rho/a < 0.5$ with an accuracy better than 95%.

In the analytical work described in Section IV, the toroidal corrections have been neglected as well as all the terms with $m > 2$. Furthermore, it has been assumed that $\delta \ll 1$. Under these simplifications the torsatron magnetic field becomes

$$B_{\rho} = 2B_s^{ex} \epsilon_t I_2(x) \sin [2(\phi - \alpha s)], \quad (9)$$

$$B_{\phi} = \frac{4B_s^{ex}}{x} \epsilon_t I_2(x) \cos [2(\phi - \alpha s)], \quad (10)$$

$$B_s = B_0 - 2B_s^{ex} \epsilon_t I_2(x) \cos [2(\phi - \alpha s)], \quad (11)$$

where $B_s^{ex} \epsilon_t = B_0 x_0 K_2(x_0)$.

For $x \ll 1$, Eqs. (9), (10) and (11) become

$$B_{\rho} = \frac{B_s^{ex} \epsilon_t x}{2} \sin [2(\phi - \alpha s)], \quad (12)$$

$$B_{\phi} = \frac{B_s^{ex} \epsilon_t x}{2} \cos [2(\phi - \alpha s)], \quad (13)$$

$$B_s = B_0. \quad (14)$$

In addition to the torsatron field, the rebatron accelerator includes a betatron or vertical magnetic field and a toroidal field, B_s^{ex} , that is produced by a set of toroidal coils. The two

components of the betatron field are described by the linearized equations

$$B_z = B_{z0} [1 - n x/r_0], \quad (15)$$

$$B_r = - B_{z0} n y/r_0, \quad (16)$$

where B_{z0} is the betatron field at the reference orbit, i.e., at $x = y = 0$ and n is the external field index.

The toroidal field produced by a set of toroidal coils is independent of toroidal angle and therefore varies as $1/r$. This toroidal field can be chosen to have either the same or opposite polarity to the torsatron toroidal field.

b. The Electric Field in the Gap

Consider two cylinders with their axes lying along the same line and separated by a distance d as shown in Fig. 4a. Since the cylinder on the left is charged to $-V_0$ and the cylinder to the right is charged to $+V_0$ the average electric field in the gap is $\langle E_s \rangle = 2V_0/d$. The local electric field is given by the solution of Laplace equation, i.e., $\nabla^2 \phi = 0$. For $|s| > d/2$, the exact components of the electric field are:

$$E_s = - \frac{4V_0}{d} \sum_{n=1}^{\infty} \frac{\sinh(\lambda_n d/2) J_0(\lambda_n a)}{\lambda_n a J_1(\lambda_n a)} e^{-\lambda_n |s|}, \quad (17)$$

$$E_o = - \frac{s}{|s|} \frac{4V_0}{d} \sum_{n=1}^{\infty} \frac{\sinh(\lambda_n d/2) J_1(\lambda_n a)}{\lambda_n a J_1(\lambda_n a)} e^{-\lambda_n |s|}. \quad (18)$$

Similarly, for $|s| < d/2$, the two components of the electric field are:

$$E_s = - \frac{4V_0}{d} \left[\frac{1}{2} - \sum_{n=1}^{\infty} \frac{J_0(\lambda_n a) e^{-\lambda_n d/2} \cosh(\lambda_n s)}{a \lambda_n J_1(\lambda_n a)} \right], \quad (19)$$

and

$$E_\phi = - \frac{4V_0}{d} \sum_{n=1}^{\infty} \frac{J_1(\lambda_n a) e^{-\lambda_n d/2} \sinh(\lambda_n s)}{\lambda_n a J_1(\lambda_n a)}, \quad (20)$$

where $J_0(\lambda_n a) = 0$, a is the radius of the cylinders and J_0 and J_1 are the Bessel functions.

The electric field lines that correspond to the field components given by Eqs. (17) to (20) are plotted in Fig. 4b. These electric fields are a good representation of the fields produced inside the torus by a transmission line, since in this region the inductive magnetic field is zero and therefore the potential is described by $\nabla^2 \phi = 0$.

III. Numerical Results

To investigate the confining properties of the torsatron magnetic field, we have integrated the relativistic equations of motion using Eqs. (1) to (7) for the torsatron magnetic field and Eqs. (15) and (16) for the betatron field. The accelerating gap is 2 cm wide and as shown in Fig. 5, the electric field is limited to a 0.60 radian wide toroidal sector. For reasons that are discussed later on, the self fields have been omitted in these runs.

In the first run, the current in the torsatron windings is chosen

to be zero. Figure 6a shows the normalized particle energy (γ) as a function of time and Fig. 6b the projection of the particle orbit in the transverse plane. The various parameters for this run are listed in Table II. Since ϵ_c is zero, the magnetic field configuration is that of the modified betatron. As a consequence of the curvature drift, the gyrating particle drifts out of the system in about 26 nsec, i.e., in about a revolution around the major axis. As expected, the guiding center of the particle moves mainly in the vertical direction, while the particle gyrates around its guiding center with a frequency corresponding to the local toroidal field.

Figures 7a and 7b show the normalized energy of the particle and its orbit when approximately -124.7 kA of current flows through the torsatron windings. The rest of the parameters for this run are listed in Table III. The particle remains confined for eight revolutions. Figures 8a and 8b show similar results when the current in the windings is increased to approximately -250 kA. The corresponding torsatron field strength factor ϵ_c is -0.8. The remainder of the parameters are listed in Table IV. In all three runs the betatron magnetic field was held constant at 118 G. These results clearly demonstrate that the confining properties of the system are substantially improved by the addition of the torsatron field. The particle strikes the chamber wall when its gamma approaches approximately 65. The total time the particle remains in the system is about 320 nsec, i.e., more than an order of magnitude longer than when the torsatron field is absent.

Further improvement in the particle confinement is observed when the period of the windings is reduced or the current in the windings increased. An additional modest improvement in the confinement of the

system is observed when the betatron field is increased above its matching value. This is shown in Fig. 9. The betatron field for this run is 236 G and the remainder of the parameters are identical to those in Fig. 8. The confinement time increased by 20 nsec, i.e., from 320 to 340 nsec. However, when the betatron field increased to 472 G the confinement time was reduced to 290 nsec.

IV. Theoretical Model

To gain a better understanding of the focusing properties of the torsatron fields, we have developed a theoretical model that is based on linear external fields. Obviously, these fields are appropriate only near the minor axis of the torus, i.e., when $2a_0 \ll 1$.

The components of the torsatron field in the coordinate system $\hat{e}_r, \hat{e}_\phi, \hat{e}_z$ shown in Fig. 2 are

$$B_{r\phi} = B_0 \cos\phi - B_1 \sin\phi = B_s^{\text{ex}} \epsilon_t a \left[z \cos 2ar_0^a + (r-r_0) \sin 2ar_0^a \right], \quad (21)$$

$$B_{z\phi} = B_0 \sin\phi + B_1 \cos\phi = B_s^{\text{ex}} \epsilon_t a \left[(r-r_0) \cos 2ar_0^a - z \sin 2ar_0^a \right], \quad (22)$$

$$B_{\theta z} = -B_0, \quad (23)$$

where $-r_0^a = s$.

In addition, the betatron magnetic field is given by

$$B_{zb} = B_{z0} \left[1 - \frac{n(r-r_0)}{r_0} \right], \quad (24)$$

and

$$B_{rb} = -nB_{z0} z/r_0, \quad (25)$$

where n is the external field index. The total field components are

$$B_r = B_{rt} + B_{rb}, \quad (26)$$

$$B_z = B_{zt} + B_{zb}, \quad (27)$$

$$B_\theta = B_{\theta t} - B_s^{ex}, \quad (28)$$

where B_s^{ex} indicates any additional toroidal field that may be applied.

The accelerating electric field components are approximated by

$$E_r = \frac{(r-r_0)}{2r_0} \ddot{\gamma} \left(\frac{mc^2}{e} \frac{r_0}{v_\theta^2} \right), \quad (29)$$

$$E_z = \frac{z}{2r_0} \ddot{\gamma} \left(\frac{mc^2}{e} \frac{r_0}{v_\theta^2} \right), \quad (30)$$

$$E_\theta = - \frac{mc^2}{ev_\theta} \dot{\gamma}, \quad (31)$$

where $\dot{\gamma} = d\gamma/dt$, $\ddot{\gamma} = d^2\gamma/dt^2$ and v_θ is the toroidal velocity, which is assumed constant.

Using Eqs. (26) to (31) for the fields, the equations of motion in the laboratory frame become

$$\ddot{R} + \omega_R^2 R + \frac{\omega_0 \omega_w}{2} (R \cos \omega_w t - Z \sin \omega_w t) - \left(Z - \frac{\dot{\gamma}}{2\gamma} Z \right) \frac{v_\theta}{\gamma} = \lambda^2(\tau), \quad (32)$$

$$\ddot{Z} + \omega_z^2 Z - \frac{\omega_0 \omega_w}{2} (Z \cos \omega_w t + R \sin \omega_w t) + \left(\dot{R} - \frac{\dot{\gamma}}{2\gamma} R \right) \frac{\Omega_A}{\gamma} = 0, \quad (33)$$

where

$$R = \gamma^{1/2} (r - r_0), \quad Z = \gamma^{1/2} z,$$

$$\Omega_A = eB_A/mc, \quad \Omega_{z0} = eB_{z0}/mc,$$

$$\omega_0 = \Omega_s^{\text{ex}} \varepsilon_t / \gamma, \quad \omega_w = 2\alpha v_A,$$

$$\lambda^2(t) = \frac{c^2}{r_0} \gamma^{1/2} \frac{v_A}{c} \left(\frac{v_A}{c} - \frac{r_0 \Omega_{z0}}{c\gamma} \right),$$

$$\omega_R^2 = 1/4 \left(\frac{\dot{\gamma}}{\gamma} \right)^2 - 1/2 \left(\frac{\ddot{\gamma}}{\gamma} \right) + \frac{\ddot{\gamma}}{\gamma} \left(\frac{c^2}{2v_A^2} \right) - \frac{v_A \Omega_{z0}}{\gamma} \frac{n}{r_0} + \frac{v_A^2}{r_0^2},$$

and

$$\omega_z^2 = 1/4 \left(\frac{\ddot{\gamma}}{\gamma} \right)^2 - 1/2 \left(\frac{\ddot{\gamma}}{\gamma} \right) + \frac{\ddot{\gamma}}{\gamma} \left(\frac{c^2}{2v_A^2} \right) + \frac{v_A \Omega_{z0} n}{\gamma r_0}.$$

Equations (32) and (33) become more tractable when transformed to a frame rotating with angular frequency $\omega_w/2$. Using the transformation

$$R = \tilde{R} \cos \left(\frac{\omega_w t}{2} \right) + \tilde{Z} \sin \left(\frac{\omega_w t}{2} \right), \quad (34)$$

$$Z = -\tilde{R} \sin \left(\frac{\omega_w t}{2} \right) + \tilde{Z} \cos \left(\frac{\omega_w t}{2} \right), \quad (35)$$

equations (32) and (33) become

$$\ddot{\tilde{R}} + \left[\omega_1^2 - \delta\omega^2 \cos\omega_w t + \frac{\omega_0 \omega_w}{2} - \left(\frac{\omega_w}{2} \right)^2 + \left(\frac{\omega_w}{2} \right) \frac{\Omega_a}{\gamma} \right] \tilde{R} + \left(\omega_w - \frac{\Omega_a}{\gamma} \right) \dot{\tilde{Z}} + \left(\frac{\dot{\gamma}}{2\gamma} \frac{\Omega_a}{\gamma} - \delta\omega^2 \sin\omega_w t \right) \tilde{Z} = \lambda^2 \cos \left(\frac{\omega_w t}{2} \right), \quad (36)$$

$$\ddot{\tilde{Z}} + \left[\omega_1^2 + \delta\omega^2 \cos\omega_w t - \frac{\omega_0 \omega_w}{2} - \left(\frac{\omega_w}{2} \right)^2 + \left(\frac{\omega_w}{2} \right) \frac{\Omega_a}{\gamma} \right] \tilde{Z} - \left(\omega_w - \frac{\Omega_a}{\gamma} \right) \dot{\tilde{R}} - \left(\frac{\dot{\gamma}}{2\gamma} \frac{\Omega_a}{\gamma} + \delta\omega^2 \sin\omega_w t \right) \tilde{R} = \lambda^2 \sin \left(\frac{\omega_w t}{2} \right), \quad (37)$$

where

$$\omega_1^2 = 1/4 \left(\frac{\dot{\gamma}}{\gamma} \right)^2 - 1/2 \left(\frac{\ddot{\gamma}}{\gamma} \right) + \frac{\ddot{\gamma}}{\gamma} \left(\frac{c^2}{2v_a^2} \right) + \frac{v_a^2}{2r_0^2} = 1/4 \left(\frac{\dot{\gamma}}{\gamma} \right)^2 + \frac{v_a^2}{2r_0^2},$$

and

$$\delta\omega^2 = \frac{v_a n}{r_0} \left(\frac{\Omega_{z0}}{\gamma} - \frac{v_a}{2nr_0} \right)$$

Since at the start of the acceleration $|\omega_0 \omega_w / 2| \gg |\delta\omega^2|$ and $(\dot{\gamma}/2\gamma) |(\frac{\Omega_a}{\gamma})| \gg |\delta\omega^2|$, the two coupled equations (36) and (37) can be combined into a single equation by introducing the complex variable $\tilde{\psi} = \tilde{R} + i\tilde{Z}$. Multiplying Eq. (37) by i and adding it to Eq. (36), it is obtained

$$\ddot{\tilde{\psi}} + f_1 \dot{\tilde{\psi}} + f_3 \tilde{\psi}^* - if_2 \dot{\tilde{\psi}} = \lambda^2 e^{i\omega_w t/2}, \quad (38)$$

where

$$f_1 = \omega_1^2 - \left(\frac{\omega_w}{2}\right)^2 + \frac{\omega_w}{2} \frac{\Omega_a}{\gamma} - \frac{i\dot{\gamma}}{2\gamma} \frac{\Omega_a}{\gamma}, \quad f_2 = \left(\omega_w - \frac{\Omega_a}{\gamma}\right) \quad \text{and}$$

$$f_3 = \frac{\omega_0 \omega_w}{2}.$$

Equations (36) and (37) have been solved numerically. After integration the orbit is transferred back to the laboratory frame. The results are shown in Fig. 10. The projection of the orbit in the r, z plane is shown in Fig. 10a, the particle radial distance from the minor axis as a function of time is shown in Fig. 10b and γ as a function of time in Fig. 10c. The various parameters for this run are identical to those listed in Table IV. The particle strikes the wall at about 325 nsec, when its gamma is approximately 68. These results are in good agreement with those of Fig. 8 that have been obtained using the more accurate expressions for the torsatron fields. As will be discussed later, the particle was lost because at $\gamma = 65$ it entered the unstable region that extends from $\gamma = 65$ to $\gamma = 121$.

When $\dot{\gamma} = 0$, the homogeneous part of Eq. (38) becomes

$$\tilde{\psi}^{(4)} + [2f_1 + f_2^2] \tilde{\psi}'' + [f_1^2 - f_3^2] \tilde{\psi} = 0, \quad (39)$$

i.e., a fourth order equation with constant coefficients. The solutions of Eq. (39) are of the type $\tilde{\psi} = \tilde{\psi}_0 e^{i\omega t}$, where ω^2 , is given by

$$\omega_{\pm}^2 = 1/4 \left(\omega_w - \frac{\Omega_a}{\gamma}\right)^2 + \frac{\Omega_a^2}{4\gamma^2} \pm \frac{\Omega_a}{2\gamma} \left(\omega_w - \frac{\Omega_a}{\gamma}\right)^2 + \omega_w^2 \epsilon_t^2 \left(\frac{\Omega_s^{\text{ex}}}{\Omega_a}\right)^2)^{1/2}, \quad (40)$$

when $|\omega_1^2| \ll |\omega_0 \omega_w / 2|$.

The particle orbits are stable when ω is real, i.e., when

$$u(\gamma) \equiv \left(\Omega_A - \frac{\omega_w \gamma}{2} \right)^2 - \epsilon_t^2 \Omega_s^2 \text{ex}^2 > 0. \quad (41)$$

The two roots of (40) are given by

$$\gamma_{\pm} = \frac{2\Omega_A}{\omega_w} \left(1 \pm \epsilon_t \frac{\Omega_s \text{ex}}{\Omega_A} \right). \quad (42)$$

The function $u(\gamma)$ is plotted in Fig. 11 for three values of B_A and B_s^{ex} . In Fig. 11a $B_s^{\text{ex}} = -6\text{kG}$, $B_0 = 5\text{KG}$ and thus $B_A = -(B_s^{\text{ex}} + B_0) = 1\text{KG}$. For this value of toroidal magnetic field and for $\epsilon_t = 0.4$ and $\omega_w/2 = 3 \times 10^9 \text{ sec}^{-1}$, Eq. (42) gives 19.96 and -8.2 for the two roots of Eq. (41). Therefore, at $\gamma = 7$ the particle orbit should be unstable. Results from the numerical integration of nonlinear orbit equations for $\dot{\gamma} = 0$, and $\gamma = 7$ and using the same values for the rest of the parameters as in Fig 11a are shown in Fig. 12. As expected, the orbit is indeed unstable and the particle is lost in less than one nsec.

By reversing the direction of the current in the torsatron wires B_0 and ϵ_t change sign and the two roots of Eq. (41) become 50.5 and 78.7. Therefore, for $\gamma = 7$ the orbit is stable. This is in agreement with the results from the numerical integration of nonlinear orbit equations shown in Fig. 13.

When $|\gamma_{\pm}| < 1$, the orbits are stable for all values of γ . For

$B_s^{ex} = 6KG$, $B_o = 5KG$ and $\epsilon_c = -0.4$ the two roots of Eq. (41) are -50.5 and -78.7. For this case the orbits were found stable for all the values of γ considered.

The numerical and theoretical results are in excellent agreement when the linearized theoretical model is valid. However, when B_s^{ex} and B_o have opposite signs and $|B_s^{ex}| > |B_o|$, the toroidal field vanishes at some radial distance and the field lines form magnetic cusps. In this case the linear theory does not properly describe the fields and the predictions of the theory are not in agreement with the numerical results.

When

$$\frac{\omega_o^2 \omega_w^2}{(\omega_w - \frac{\omega_a}{\gamma})^2} \left(\frac{\omega_a}{\gamma^2} \right)^2 \ll 1 ,$$

Equation (40) gives

$$\omega_{\pm}^2 = \left\{ \begin{array}{l} (\omega_w/2)^2 \left[1 + \frac{\omega_o^2}{(\omega_w - \omega_a/\gamma)(\omega_a/\gamma)} \right] , \quad (\text{slow mode}) \\ -\frac{\omega_w^2}{4} + \frac{\omega_a^2}{\gamma^2} - \omega_w \frac{\omega_a}{\gamma} - \frac{\omega_o^2 \omega_w^2}{4(\omega_w - \omega_a/\gamma)(\omega_a/\gamma)} . \quad (\text{fast mode}) \end{array} \right.$$

In the laboratory frame the slow mode ω_+ becomes

$$\omega_+ = \omega_+ - \frac{\omega_w}{2} = \frac{\omega_0^2}{4(1 - \frac{\Omega_a}{\gamma\omega_w})(\frac{\Omega_a}{\gamma})} \quad (43)$$

The particular solution of Eq. (38) in the rotating frame, for $\dot{\gamma} = 0$ and ω_+^2 small, is $\tilde{\psi}_p = \tilde{R}_p + i\tilde{Z}_p$

where

$$\tilde{R}_p = \frac{4\lambda^2(\omega_w - \Omega_a/\gamma + \omega_0/2)}{\omega_0^2 \omega_w} \cos\left(\frac{\omega_w t}{2}\right), \quad (44)$$

and

$$\tilde{Z}_p = \frac{4\lambda^2(\omega_w - \Omega_a/\gamma - \omega_0/2)}{\omega_0^2 \omega_w} \sin\left(\frac{\omega_w t}{2}\right). \quad (45)$$

Transforming back to the laboratory frame using the transformation $\psi = \tilde{\psi} e^{-i\omega_w t/2}$, we find that the particle orbit is displaced along the horizontal axis by

$$\Delta r = \frac{4\lambda^2}{\omega_0^2 \gamma/2} (1 - \Omega_a/\gamma\omega_w). \quad (46)$$

Figure 14 shows the projection of the particle orbit in the transverse plane for

$\gamma = 11$, $\epsilon_c = -0.4$, $B_a = 11\text{KG}$, $\omega_w = 6 \times 10^9 \text{ sec}^{-1}$, $r_0 = 100\text{cm}$,

$B_{z0} = 118 \text{ G}$ and $v_a = c$. For these parameters Eq. (43) gives a slow

period $\tau_+ = 2\pi/\omega_+ = 62$ nsec. For the same parameters the code gives $\tau_+ = 60$ nsec.

In addition, Eq. (46) gives a displacement $\Delta r = 1.74$ cm, which is identical to the orbit displacement of Fig. 14.

Let's now return to discuss briefly the results of Fig. 10. For the parameters of the run, Eq. (42) gives $\gamma_+ = 121$ and $\gamma_- = 65$. When the γ of the particle reaches 65 i.e., at about 300 nsec, it becomes unstable and strikes the wall in one revolution.

In addition, at $t=0$ the ratio $\omega_a/\omega_w \gamma = 6.67$ and according to Eq. (46) the orbit displacement is negative. As γ increases $\omega_a/\omega_w \gamma$ is reduced and when $\omega_a/\omega_w \gamma < 1$ the orbit displacement becomes positive. At $\gamma = 46.6$, $\omega_a/\omega_w \gamma = 1$ and $\Delta r = 0$. According to Fig. 10b this occurs at $t = 210$ nsec, which corresponds to $\gamma = 47$ (see Fig. 10c).

V. Self Fields

An accurate self consistent determination of self fields of a high current electron ring confined in a rebatron is difficult, because the minor cross section of the ring has, in general, a complex shape that varies along the toroidal direction.

Since we are interested in the macroscopic motion of the ring and therefore on the self fields that act on the ring centroid, we assume that the ring has a circular cross section and its particle density is uniform. Neglecting toroidal corrections, the fields at the center of the beam, which is located at the distance $(r - r_0)$ and z from the minor axis are^{18,26}

$$E_r^s = -2\pi|e| n_o r_o \frac{r_b^2}{a^2} \frac{(r - r_o)}{r_o} \quad (47)$$

$$E_z^s = -2\pi|e| n_o r_o \frac{r_b^2}{a^2} \frac{z}{r_o} \quad (48)$$

$$B_r^s = 2\pi|e| n_o^2 r_o \frac{r_b^2}{a^2} \frac{z}{r_o} \quad (49)$$

and

$$B_z^s = 2\pi|e| n_o^2 r_o \frac{r_b^2}{a^2} \frac{(r - r_o)}{r_o} \quad (50)$$

where n_o is the particle density, r_b the beam radius and a the minor radius of the perfectly conducting torus.

When $\dot{\gamma} = 0$, $n = 1/2$ and the beam energy is matched to the vertical field, the equation describing the beam centroid motion in the transverse rotating plane is given by

$$\ddot{\tilde{\psi}} + \hat{f}_1 \tilde{\psi} + f_3 \tilde{\psi}^* - if_2 \dot{\tilde{\psi}} = \lambda^2 e^{i\omega_w \tau/2} \quad (51)$$

where f_2 and f_3 have been defined under Eq. (38) and

$$\hat{f}_1 = \omega_l^2 - \left(\frac{\omega_w}{2}\right)^2 + \frac{\omega_w}{2} \frac{\eta_A}{\gamma} \quad (52)$$

where

$$\omega_l^2 = \frac{v_A^2}{2 r_o^2} - \frac{v_b^2}{2\gamma^3} \left(\frac{r_b}{a}\right)^2 \quad (53)$$

and $\omega_b^2 = 4\pi e^2 n_o / m$.

The solution of Eq. (51) when $\lambda^2 = 0$ is $\tilde{\psi} = \sum_i \tilde{\psi}_{oi} e^{i\omega_i t}$,

where

$$\omega_{\pm}^2 = 1/4 \left(\omega_w - \frac{\Omega_A}{\gamma} \right)^2 + \left(\frac{\Omega_A^2}{4\gamma^2} + \omega_l^2 \right) \pm \left[\left(\omega_w - \frac{\Omega_A}{\gamma} \right)^2 \left(\frac{\Omega_A^2}{4\gamma^2} + \omega_l^2 \right) + \frac{\omega_o^2 \omega_w^2}{4} \right]^{1/2}. \quad (54)$$

The orbits are stable provided

$$\frac{\Omega_A^2}{4\gamma^2} + \omega_l^2 > 0, \quad (55)$$

and

$$\left[\omega_l^2 - \left(\frac{\omega_w}{2} \right)^2 + \frac{\omega_w}{2} \frac{\Omega_A}{\gamma} \right]^2 - \frac{\omega_o^2 \omega_w^2}{4} > 0. \quad (56)$$

Equation (56) can be written as

$$\hat{u} = \omega_l^4 + 2\omega_l^2 \left(\frac{\omega_w}{2} \right) \left(\frac{\Omega_A}{\gamma} - \frac{\omega_w}{2} \right) + \left(\frac{\omega_w}{2} \right)^2 \left[\left(\frac{\Omega_A}{\gamma} - \frac{\omega_w}{2} \right)^2 - \omega_o^2 \right] > 0, \quad (57)$$

and its roots are given by

$$\frac{\omega_{l\pm}^2}{(\omega_w/2)} = - \left[\left(\frac{\Omega_A}{\gamma} - \frac{\omega_w}{2} \right) \pm \omega_o \right]. \quad (58)$$

When $\left| \left(\frac{\Omega_A}{\gamma} - \frac{\omega_w}{2} \right) \right| > \left| \omega_o \right|$, the two roots of inequality (57) are both either positive or negative depending upon the sign of $\left(\frac{\Omega_A}{\gamma} - \frac{\omega_w}{2} \right)$ and ω_o . The results are summarized in Table V.

For $\gamma \gg 1$, Eq. (58) becomes

$$\omega_{l\pm}^2 = (\omega_w/2)^2, \quad (59)$$

i.e. the orbits are always stable provided inequality (55) is satisfied.

The maximum amount of space charge that can be confined by a rebatron can be determined from Eq. (55). When

$$v_A^2 / 2r_0^2 \ll \left(\frac{\omega_b^2}{2\gamma^3} \right) \left(\frac{r_b}{a} \right)^2 ,$$

Eq. (55) gives

$$\frac{v}{\gamma} < \frac{\Omega_A^2 a^2}{8c^2} . \quad (60)$$

For $a = 10$ cm, $B_A = 10$ KG, $\gamma = 7$, Eq. (60) gives $v = 3,000$ or $I = 50$ MA.

When the current of the beam is large, $\hat{\omega}_l^2 \ll 0$. However, as γ increases $\hat{\omega}_l^2$ approaches its asymptotic value $v_A^2 / 2r_0^2$. Similarly, the two roots $\hat{\omega}_{l\pm}^2$ approach their asymptotic value given by Eq. (59).

Figure 15 shows the stability diagram at $t = 0$, when $\left(\frac{\Omega_A}{\gamma} - \frac{\omega_w}{2} \right) < 0$

and $\omega_0 < 0$. For this case the stability condition

$$\text{is } -\frac{\omega_w}{2} \left[\left(\frac{\Omega_A}{\gamma} - \frac{\omega_w}{2} \right) \right] + \frac{\omega_0 \omega_w}{2} > \hat{\omega}_l^2 > -\frac{\Omega_A^2}{4\gamma^2} .$$

During acceleration γ increases and therefore both $-\Omega_A^2 / 4\gamma^2$ and $\hat{\omega}_l^2$ move to the right of the diagram. Therefore, it may be argued that before $\hat{\omega}_l^2$ crosses the vertical axis, $-\Omega_A^2 / 4\gamma^2$ catches up with it and the ring becomes unstable. A similar situation would occur when $\hat{\omega}_l^2$ becomes equal to $\hat{\omega}_{l+}^2$. However, we have shown that when the system is stable at $t = 0$ it will remain stable for any γ that exceeds the initial γ .

VI. Conclusions

We have carried out an extensive numerical and analytical investigation of the beam dynamics in a rebatron accelerator. Although the analytical work is based on simple, linear approximations for the various fields, the two approaches give very similar results when these approximations are valid.

Our studies indicate that when self field effects can be ignored, the particle normalized energy can be increased from $\gamma = 7$ to $\gamma = 70$, at constant betatron field, before confinement is lost. This implies that the device has a bandwidth that approaches 1000%. This bandwidth can be further increased by increasing the current in the torsatron wires.

Even in the absence of the space charge, there is a range of parameters [see Eq. (42)] for which the rebatron is unstable. However, this orbit instability can be easily avoided by a judicious choice of the various parameters.

As far as orbit stability is concerned, the maximum electron beam current that can be confined in a rebatron accelerator is given by Eq. (60) and is impressively high. Therefore, it is expected that the limiting beam current in a rebatron would be determined from collective instabilities and not from the macroscopic stability of beam orbits.

Although the bandwidth of rebatron accelerators is very high, the maximum energy that can be obtained by these devices, with time independent magnetic fields, is rather limited. To achieve very high energies ($\gamma > 1000$) the betatron magnetic field should be replaced by a local vertical magnetic field that varies rapidly with time and approximately in synchronism with the beam energy. Such a fast vertical field can be generated by two coaxial, cylindrical lines that carry

current in the opposite direction. The axes of these lines coincide with the major axis of the toroidal vessel and they are located symmetrically around the minor axis of the torus. These transmission lines change mainly the local vertical magnetic field, while the magnetic flux through the beam orbit remains approximately constant. The mismatch between the beam energy and the vertical field is alleviated by the strong focusing field. The effect of the rapidly varying vertical magnetic field on the beam dynamics will be reported in a forthcoming publication.

Table II

Parameters of the run shown in Fig. 6

Torus Major Radius	r_0 (cm)	= 100
Winding Minor Radius	ρ_0 (cm)	= 12
Toroidal Chamber Minor Radius	a (cm)	= 10
	$\alpha = 2\pi/L$ (cm^{-1})	= 0.1
Field Strength Factor	ϵ_c	= 0
Winding Current	I (kA)	= 0
	ℓ	= 2
Additional Toroidal Field	B_s^{ex} (kG)	= -6
Betatron Field	B_{z0} (G)	= 118
Ext. Field Index	n	= 0.5
Initial	γ	= 7.0
Initial Positions	$\rho = \theta = s$	= 0
Initial Velocities	$v_\rho = v_\theta = 0, v_s = c$	

Table I

Parameters relevant to the torsatron fields shown in Fig. 3. Only two terms retained in the series of Eqs. (1) to (3).

Torus major radius	r_0 (cm)	= 100
Windings minor radius	ρ_0 (cm)	= 12
Toroidal chamber minor radius	a (cm)	= 10
	$\alpha = 2\pi/L$ (cm^{-1})	= 0.1
Field Strength Factor	ϵ_t	= 0.2
Winding Current	I (kA)	= 62.37
	z	= 2
Additional Toroidal Field	B_s^{ex} (kG)	= - 6

Table IV

Parameters of the run shown in Fig. 8.

Torus Major Radius r_0 (cm)		= 100
Winding Minor Radius ρ_0 (cm)		= 12
Torodial Chamber Minor Radius a (cm)		= 10
$\alpha = 2\pi/L$ (cm^{-1})		= 0.1
Field Strength Factor ϵ_c		= -0.8
Winding Current I (kA)		= -250
	ℓ	= 2
Additional Torodial Field B_s^{ex} (kG)		= -6
Betatron Field B_{z0} (G)		= 118
Ext. Field Index	n	= 0.5
Initial γ		= 7.0
Initial Positions	$\rho = \phi = s$	= 0
Initial Velocities	$v_\rho = v_\phi = 0, v_s = c$	

Table III

Parameters of the run shown in Fig. 7.

Torus Major Radius r_0 (cm)	=	100
Winding Minor Radius a_0 (cm)	=	12
Toroidal Chamber Minor Radius a (cm)	=	10
$\alpha = 2\pi/L$ (cm^{-1})	=	0.1
Field Strength Factor ϵ_t	=	-0.4
Winding Current I (kA)	=	-124.7
l	=	2
Additional Toroidal Field B_s^{ex} (kG)	=	-6
Betatron Field B_{z0} (G)	=	118
Ext. Field Index n	=	0.5
Initial γ	=	7.0
Initial Positions $\rho = \phi = s$	=	0
Initial Velocities $v_\rho = v_\phi = 0, v_s = c$		

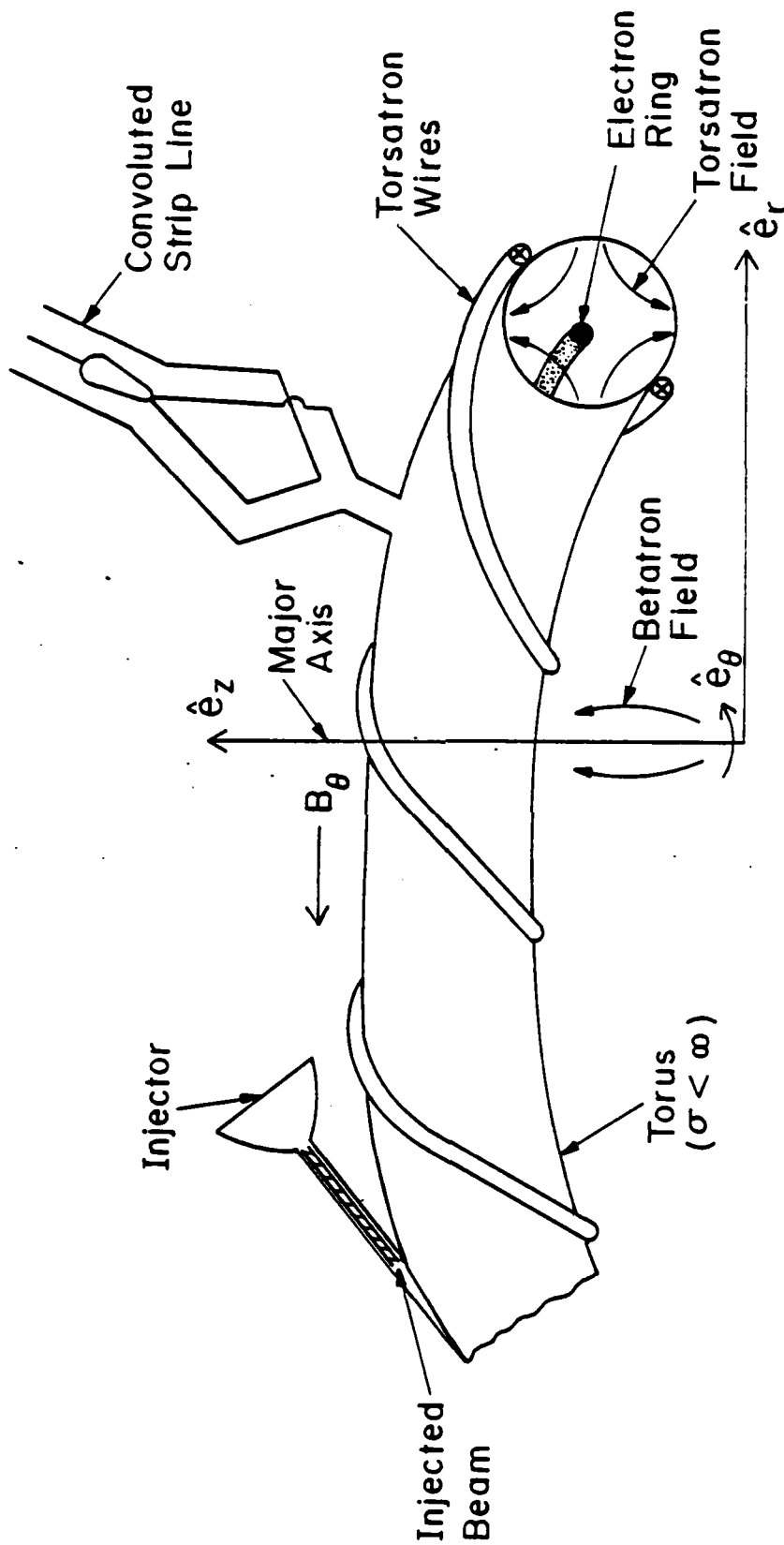


Fig. 1 — Schematic of a rebatron. The accelerating gap is energized by two or more transmission lines that are symmetrically distributed around the minor axis.

Table V

Roots of inequality (57) as given by Eq. (58), when

$$\left| \left(\frac{\omega_R}{\gamma} - \frac{\omega_W}{2} \right) \right| > |\omega_0| .$$

$\left(\frac{\omega_R}{\gamma} - \frac{\omega_W}{2} \right)$	ω_0	$2\omega_{\pm}^2 / \omega_W$
+	+	both negative
-	-	both positive
-	+	both positive
+	-	both negative

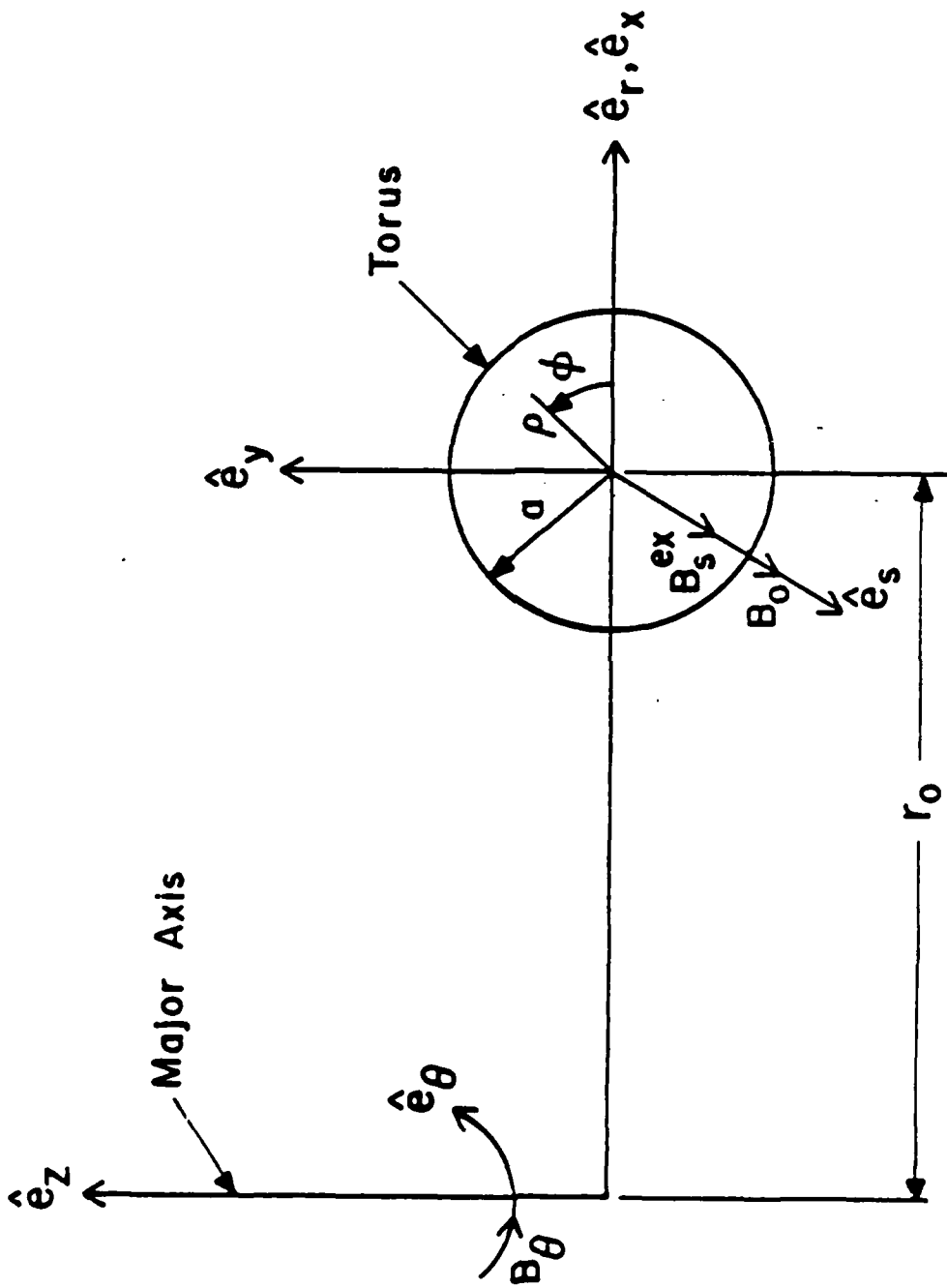
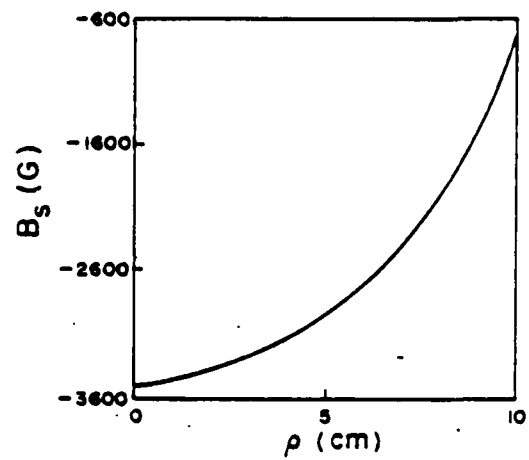
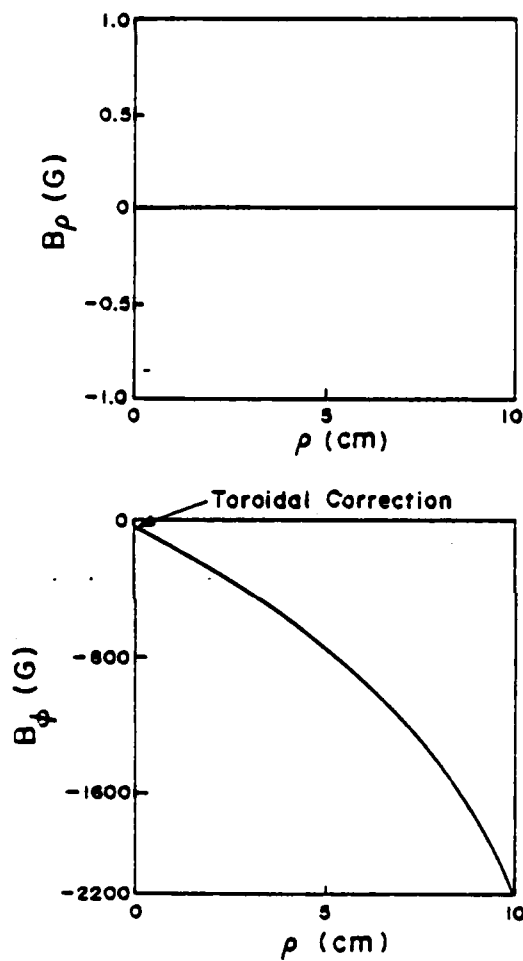


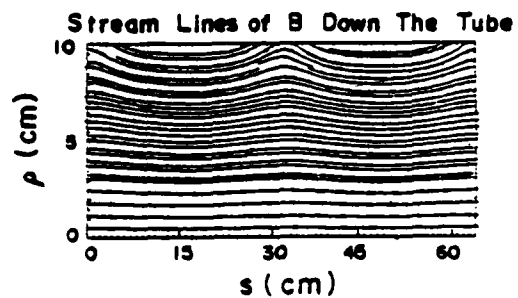
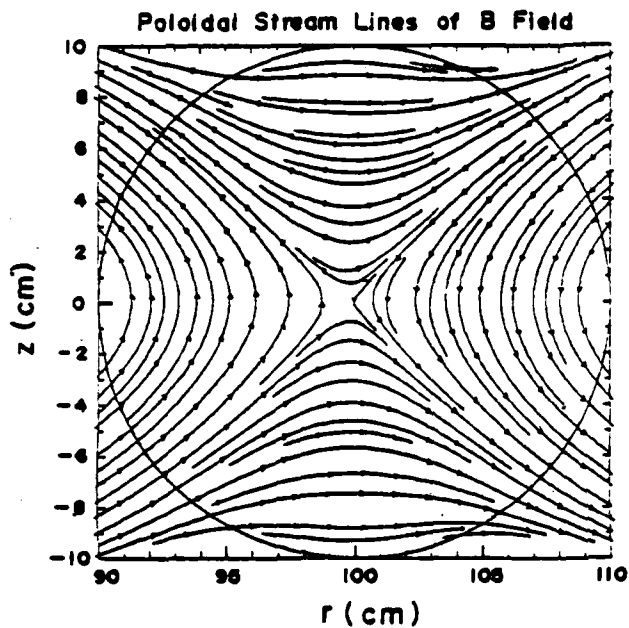
Fig. 2 — Systems of coordinates



Torsatron Field Components
 $\phi = s = 0$

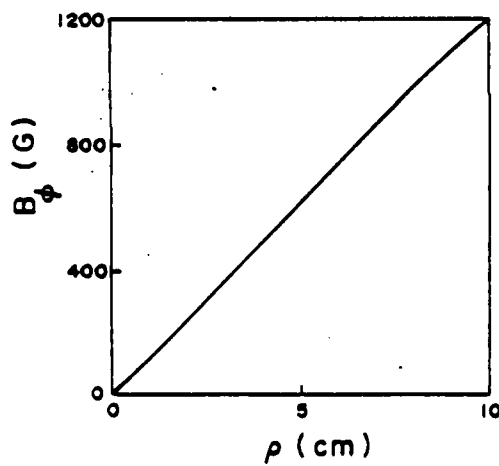
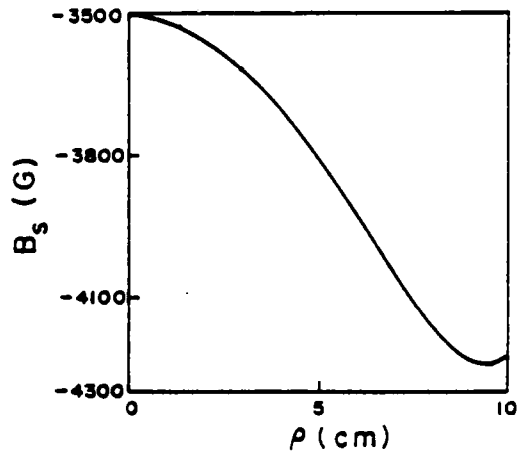
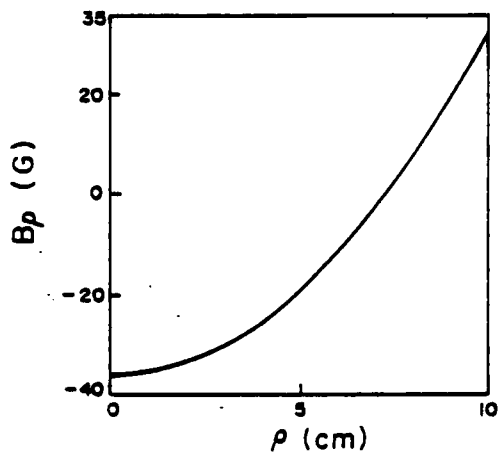
(a)

Fig. 3 - Torsatron magnetic field components (a) at $\phi = s = 0$ and (b) at $s = 0, \phi = \pi/2$. In addition to the torsatron field there is toroidal field $B_z^{ex} = -6$ kG that is produced by a set of toroidal coils. (c) magnetic field lines in r, z and ρ, s planes.



(c)

Fig. 3 (Cont'd) — Torsatron magnetic field components (a) at $\phi = s = 0$ and (b) at $s = 0$, $\phi = \pi/2$. In addition to the torsatron field there is toroidal field $B_{\theta}^{\text{ex}} = -6$ kG that is produced by a set of toroidal coils. (c) magnetic field lines in r, z and ρ, s planes.

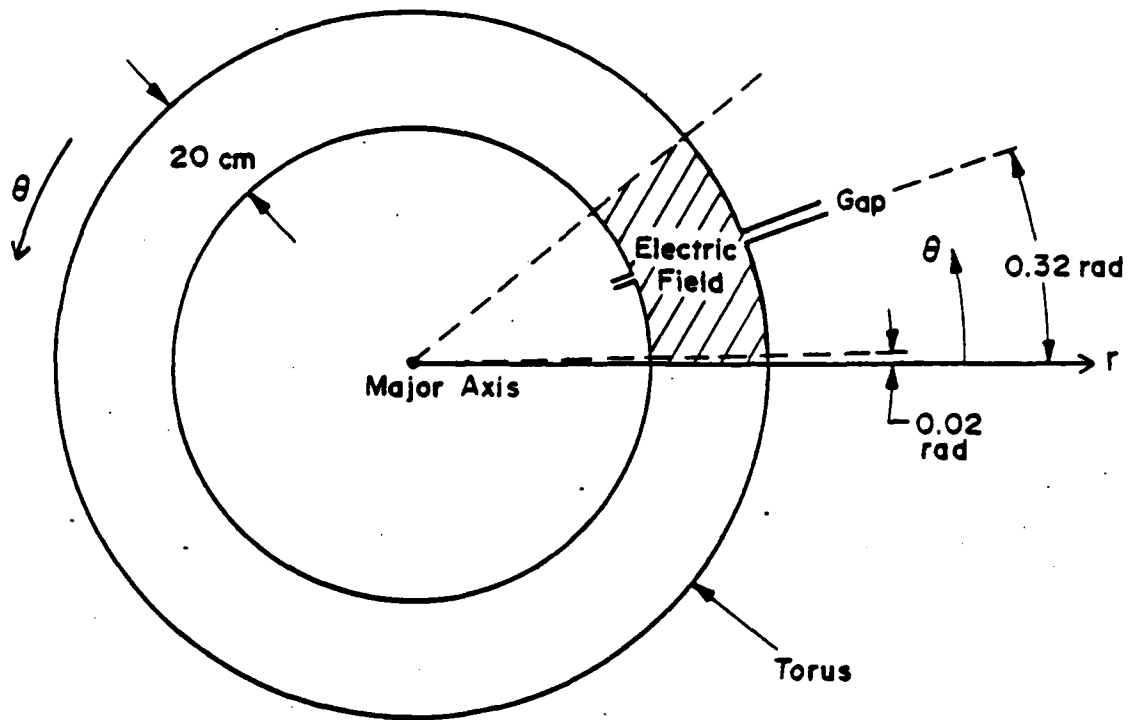


Torsatron Field Components

$s = 0$
 $\phi = 90^\circ$

(b)

Fig. 3 (Cont'd) — Torsatron magnetic field components (a) at $\phi = s = 0$ and (b) at $s = 0, \phi = \pi/2$. In addition to the torsatron field there is toroidal field $B_z^{\text{ext}} = -6$ kG that is produced by a set of toroidal coils. (c) magnetic field lines in r, z and ρ, s planes.



Top View

Fig. 5 — Top view of the torus. The accelerating field is limited to $\pm 30\text{cm}$ around the gap.

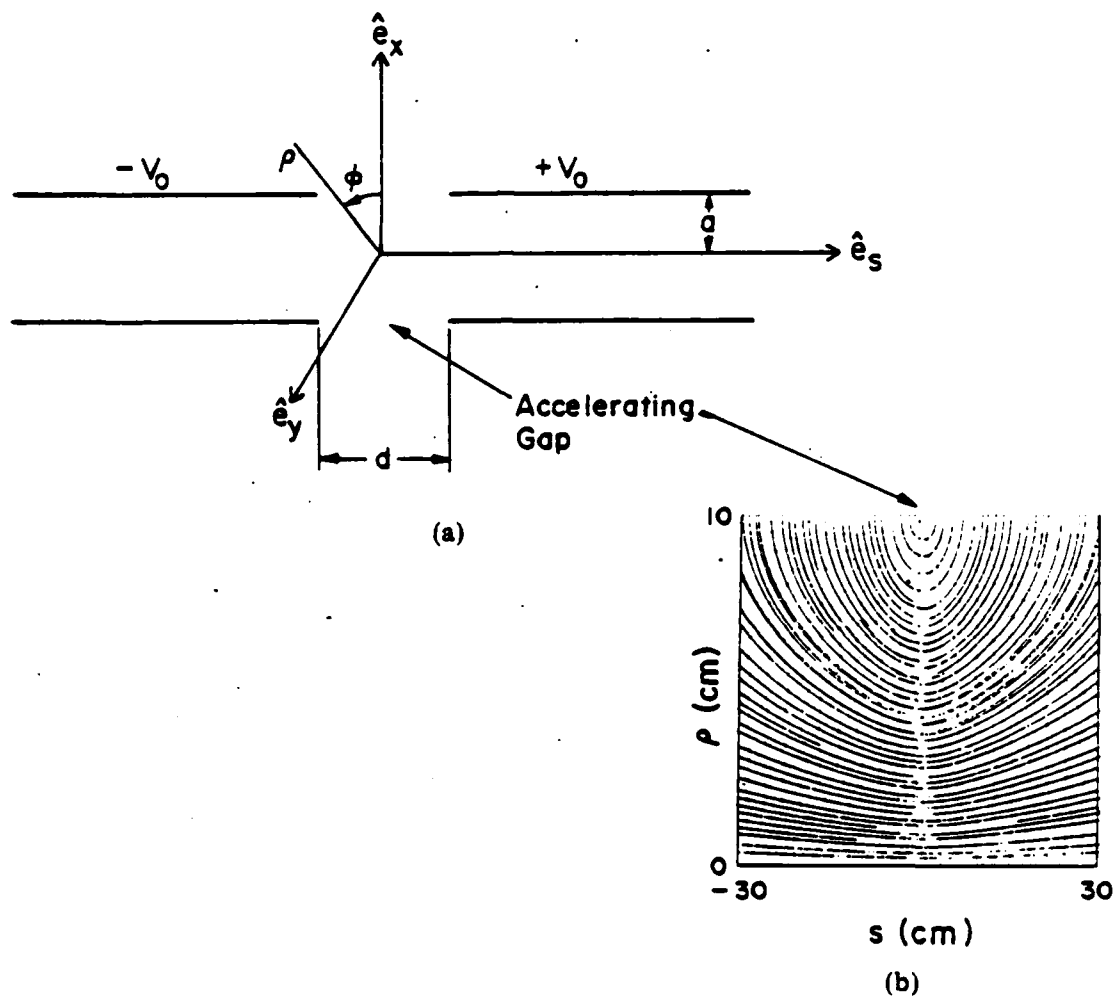
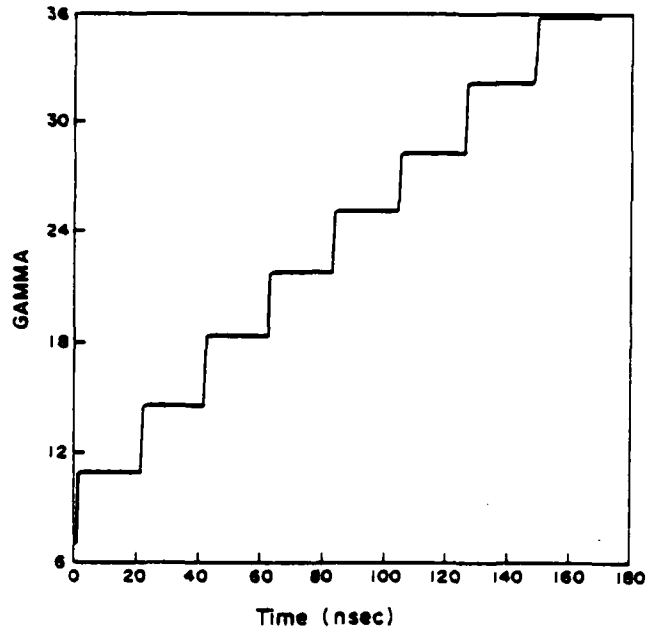
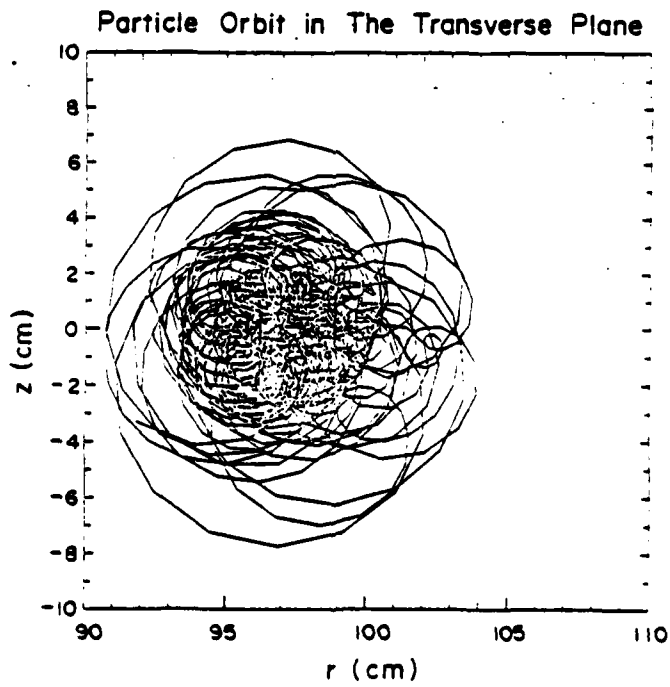


Fig. 4 — (a) Configuration and (b) field lines of the accelerating electric field.

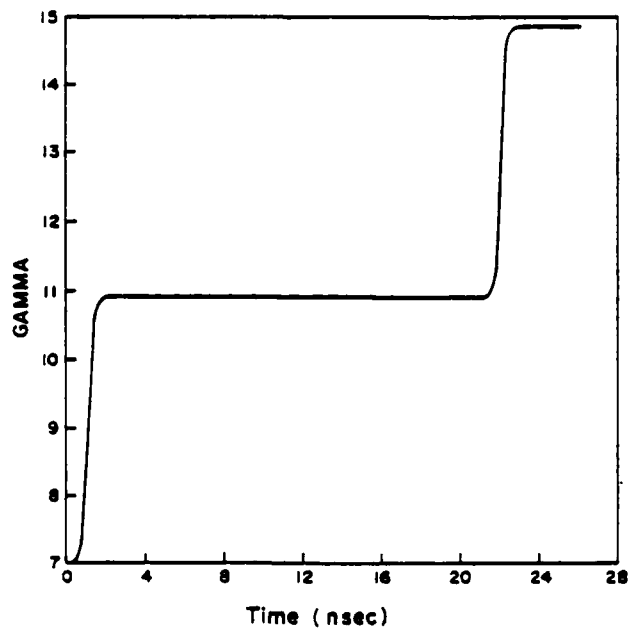


(a)

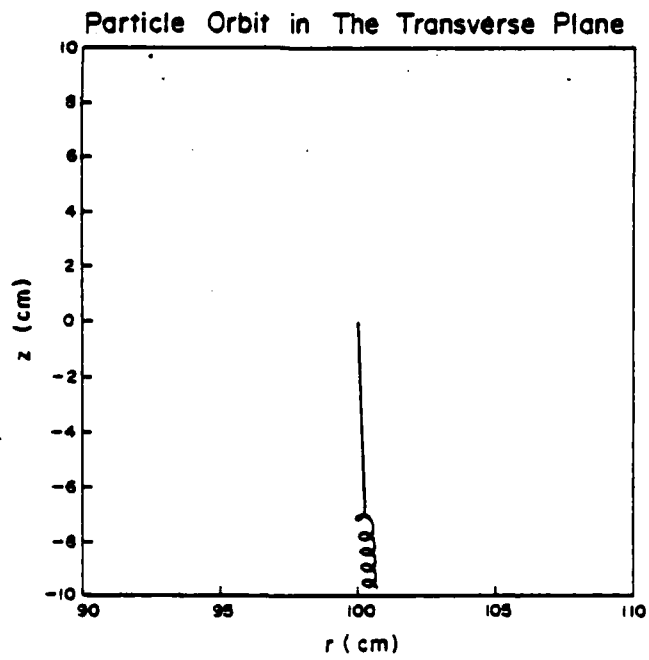


(b)

Fig. 7 - (a) γ of particle as a function of time and (b) particle orbit in the r, z plane for moderate ($\epsilon_1 = -0.4$) torsatron field. The various parameters for this run are listed in Table III.

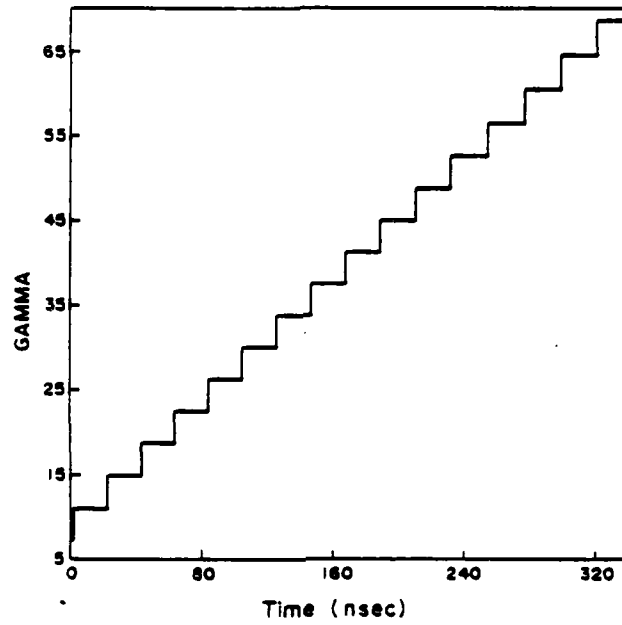


(a)

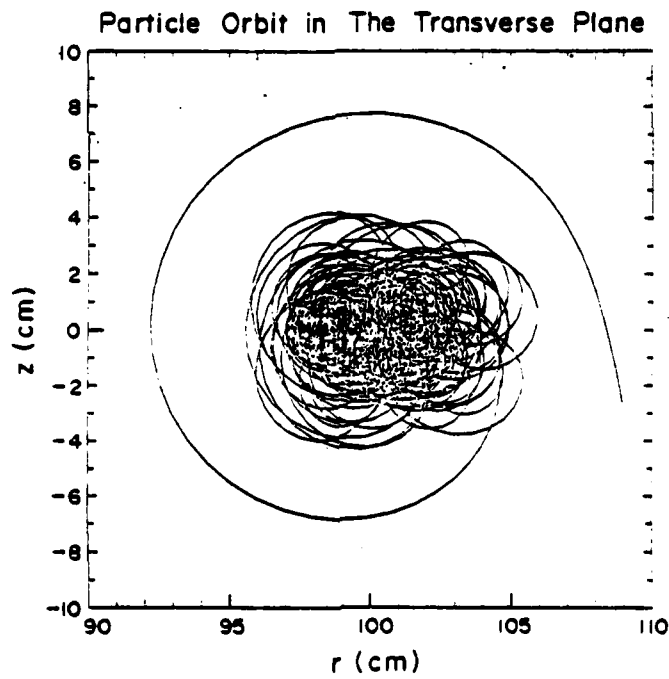


(b)

Fig. 6 — (a) γ of particle as a function of time and (b) particle orbit in the r, z plane in the absence ($\epsilon_r = 0$) of torsatron field. The various parameters for this run are listed in Table II.

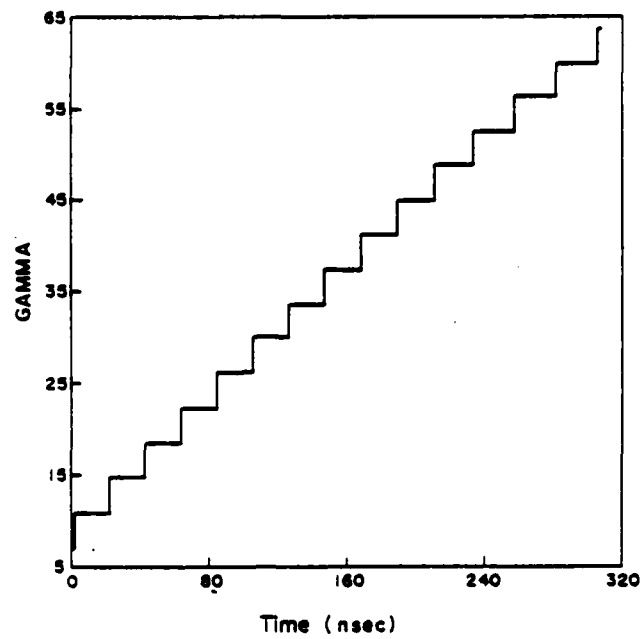


(a)

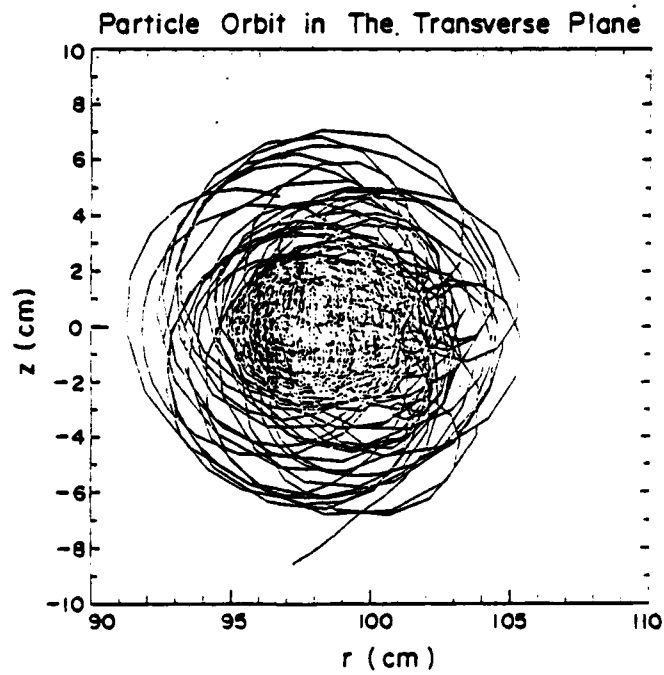


(b)

Fig. 9 — (a) γ of particle as a function of time and (b) particle orbit in the r, z plane for the same parameters as Figure 8 except at a higher betatron field.

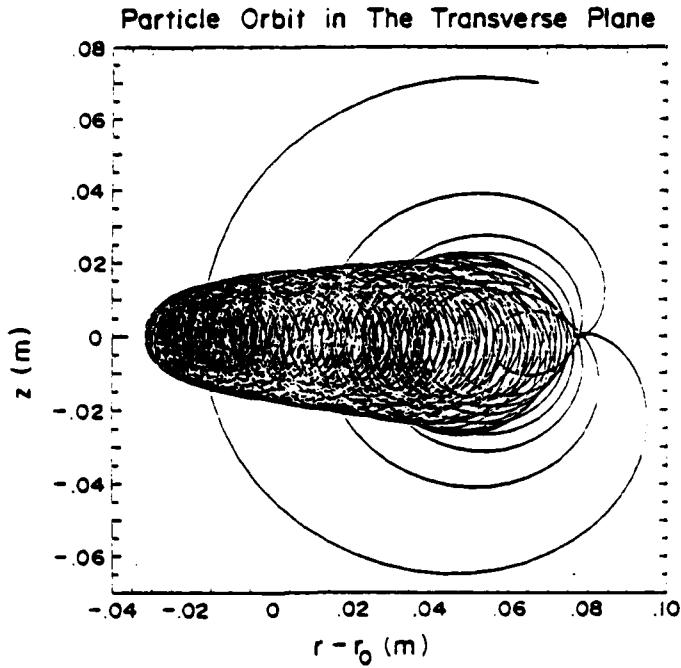


(a)

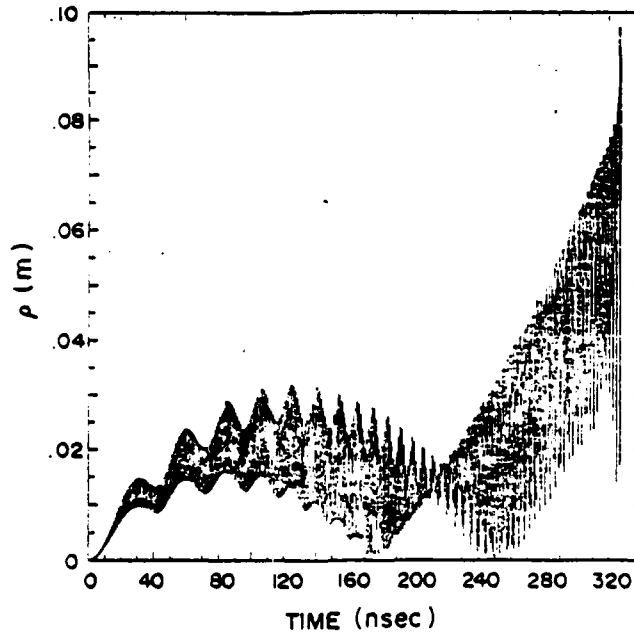


(b)

Fig. 8 — (a) γ of particle as a function of time and (b) particle orbit in the r, z plane for high ($\epsilon_r = -0.8$) torsatron field. The various parameters for this run are listed in Table IV.

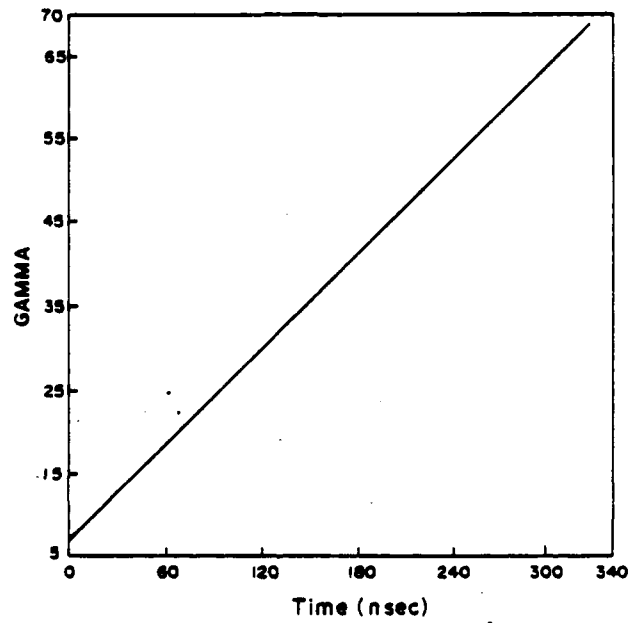


(a)



(b)

Fig. 10 — (a) Particle orbit in the r, z plane; (b) particle radius as a function of time and (c) γ of particle as a function of time. These results have been obtained from the linear equations (36) and (37). The results shown are in the Lab. frame. The various parameters for this run are the same with those of Figure 8.



(c)

Fig. 10 (Cont'd) — (a) Particle orbit in the r, z plane; (b) particle radius as a function of time and (c) γ of particle as a function of time. These results have been obtained from the linear equations (36) and (37). The results shown are in the Lab. frame. The various parameters for this run are the same with those of Figure 8.

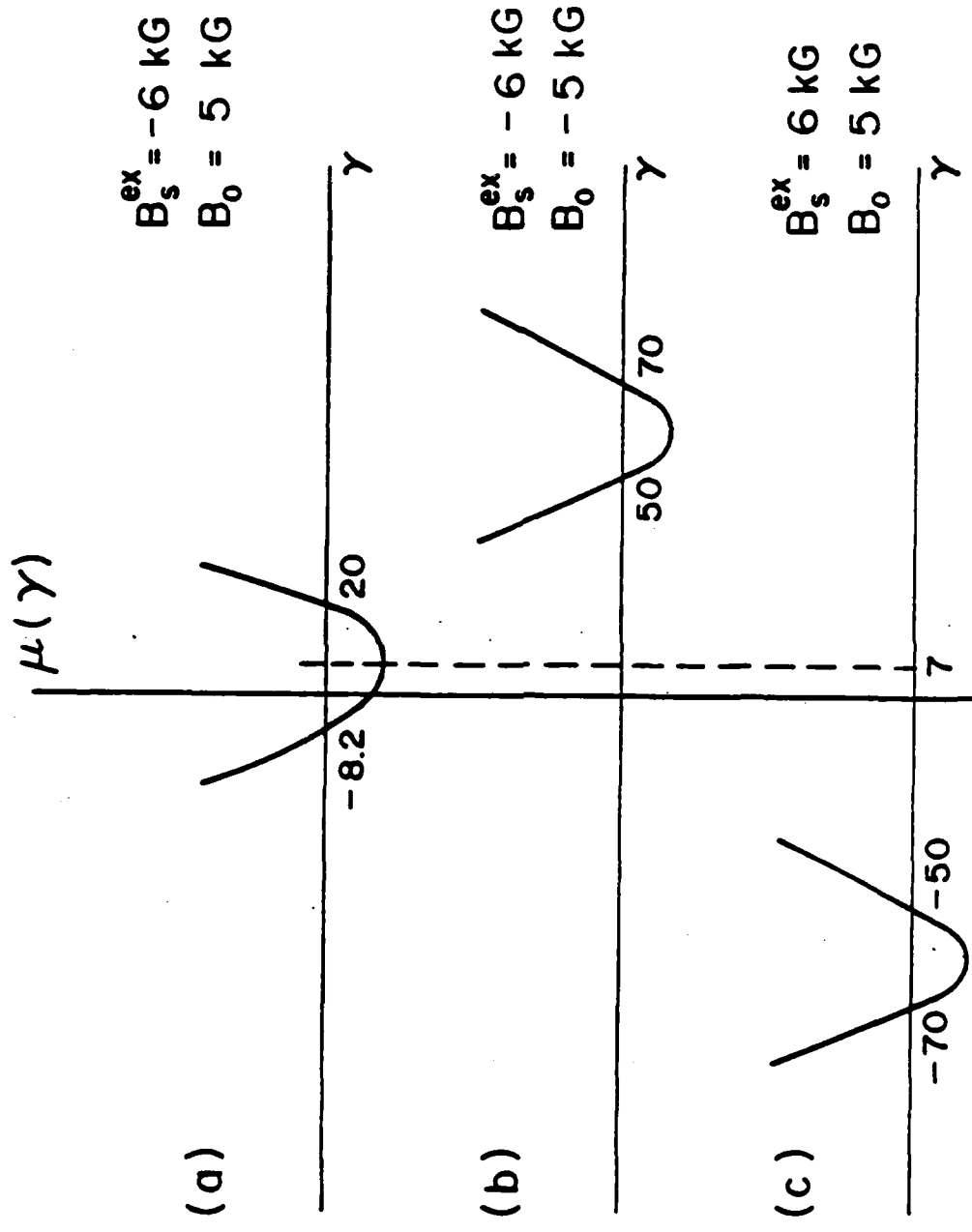


Fig. 11 — Plot of $\mu(\gamma)$ given in Equation (41) for three different combinations of B_s^{ex} and B_0 .

Particle Orbit in The Transverse Plane

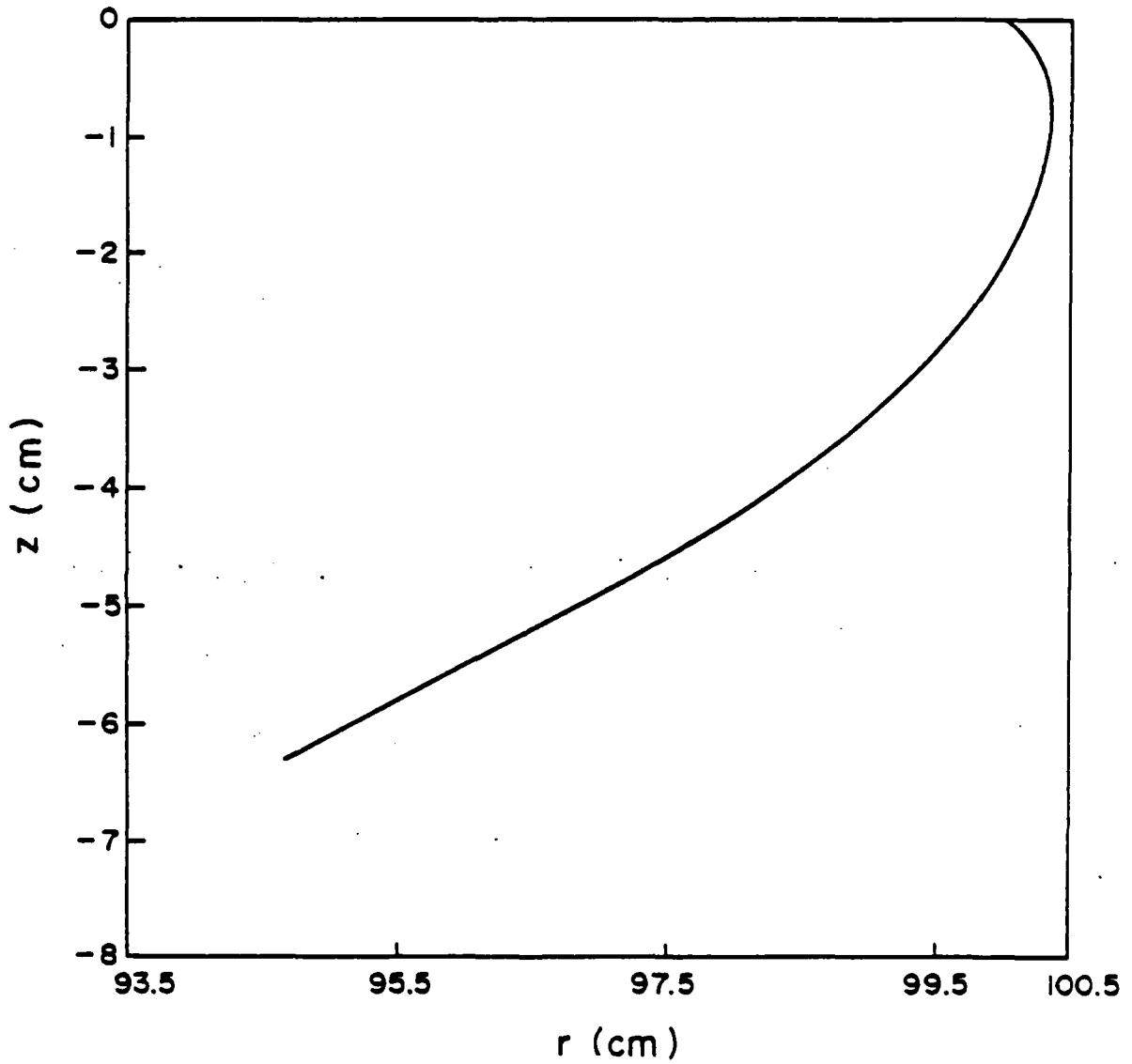


Fig. 12 — Particle orbit in the r, z plane for the same parameters as those in Figure 11a.

Particle Orbit in The Transverse Plane

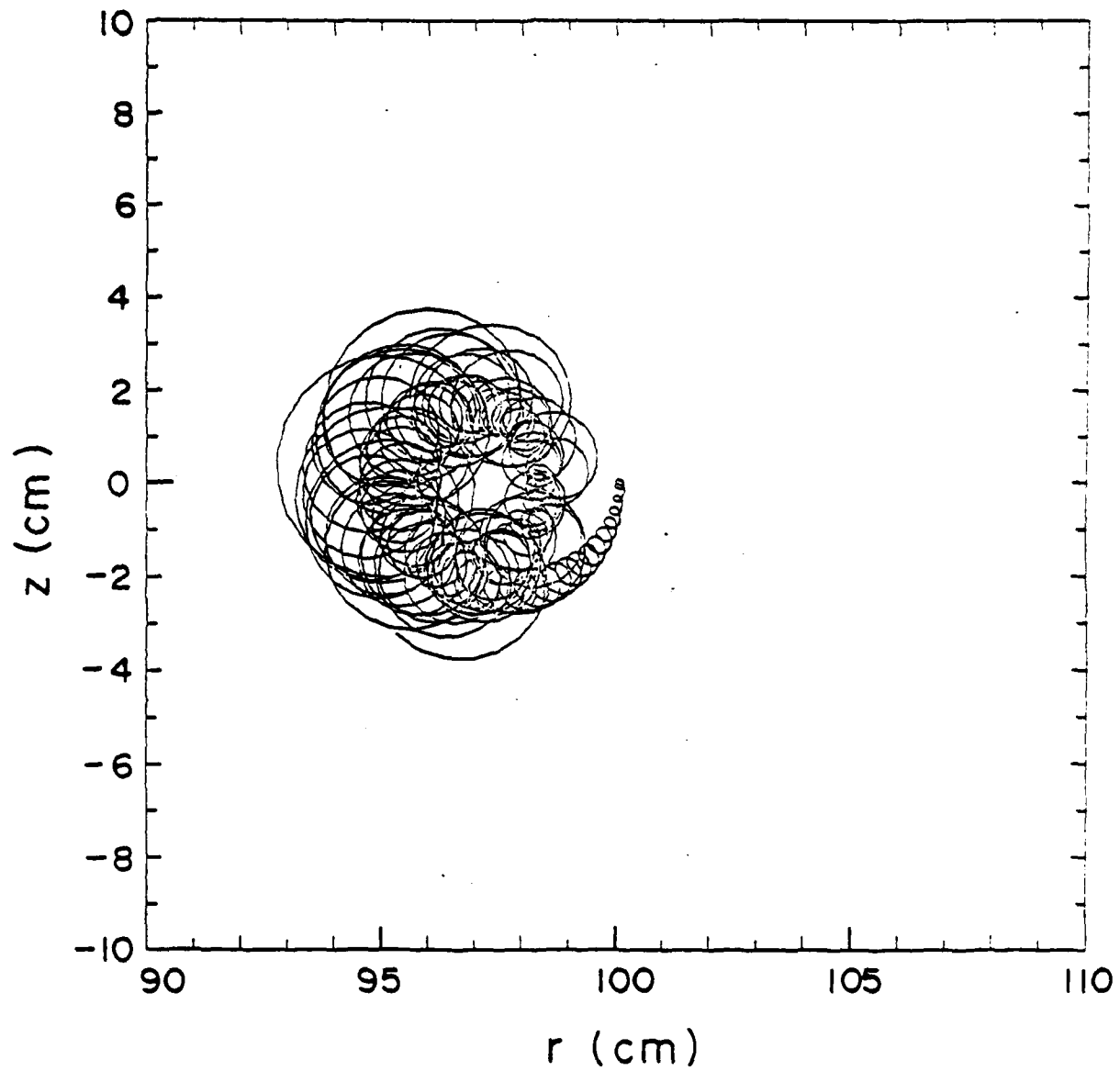


Fig. 13 — Particle orbit in the r, z plane for the same parameters as those in Figure 11b.

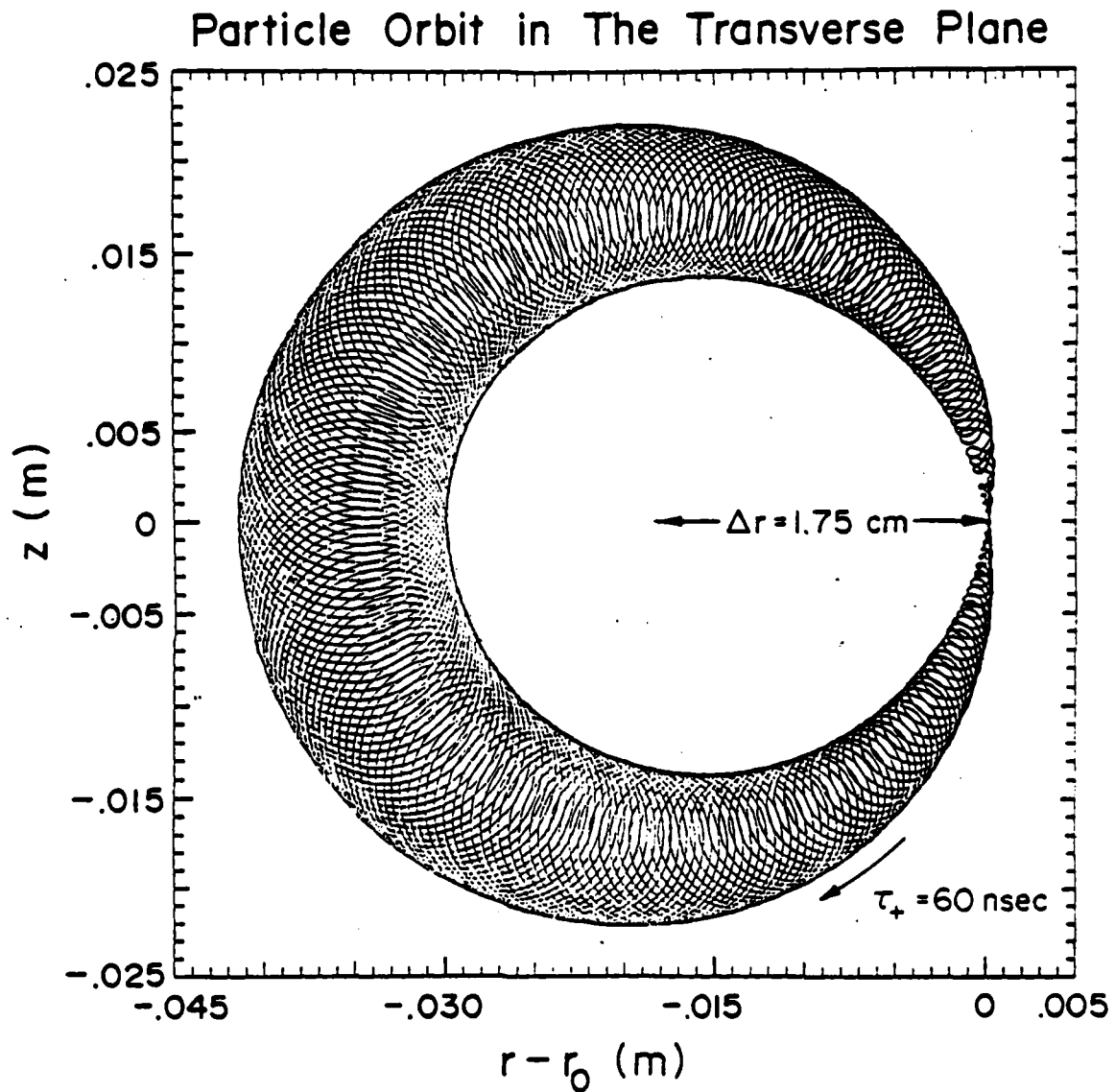


Fig. 14 — Particle orbit in the r, z plane for an initially mismatched beam and $\dot{\gamma} = 0$. The particle rotated around the equilibrium position four times with a period of 60 nsec. The theory [Equation (43)] predicts a period of 62 nsec and the nonlinear equations give similar orbits with a period of about 55 nsec.

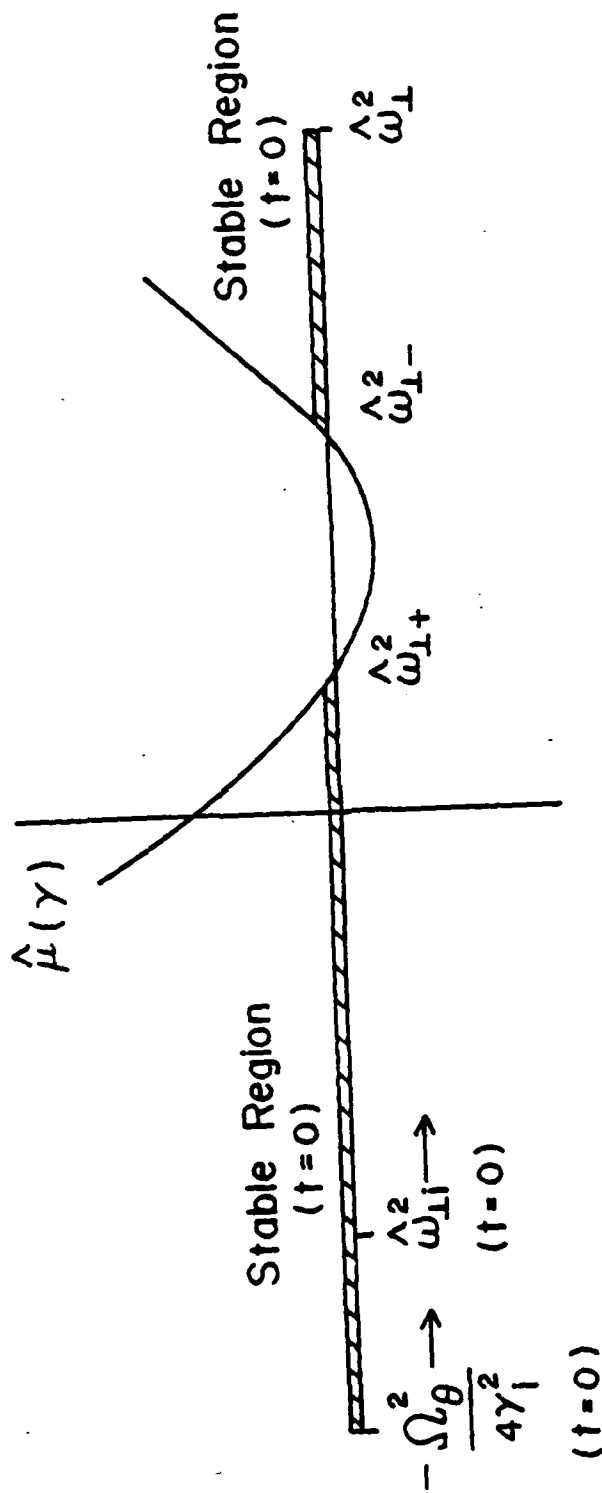


Fig. 15 — Plot of $\hat{\mu}(\gamma)$ of Equation (57) as a function of ω_1^2 . If the system is stable at $t = 0$, it will remain stable for any γ that exceeds the initial γ .

Acknowledgments

*Work is jointly supported by the Office of Naval Research and U. S. Army Ballistic Research Laboratory, Aberdeen, Md.

(a) Permanent Address: Sachs/Freeman Associates, Bowie, Md. 20715

(b) Permanent Address: Science Applications, Inc., McLean, Va. 22102

References

1. C. A. Kapetanakos and P. Sprangle, Phys. Today, V. 38, #2 (Feb 1985), p. 58.
2. C. A. Kapetanakos and P. Sprangle, NRL Memo Report No. 5259, 1984 AD-A142303.
3. E. T. Gerry and S. A. Mani, W. T. Schafer Associates Report No. DOE/ER-0176 (1983).
4. P. Sprangle and T. Coffey, Phys. Today, V. 36, #12 (Dec 1983).
5. D. Keefe, Part. Acc. 11, 187 (1981).
6. N. C. Christofilos, et al., Rev. Sci. Instrum. 35, 886 (1964).
7. J. E. Leiss, N. J. Norris and M. A. Wilson, Part. Acc. 10, 223 (1980).
8. T. J. Fessenden, et al., Proc. of the Int. Top. Conf. on High-Power Electron and Ion Beam Research and Technology; Palaiseau, France, June 29-July 3, 1981, p. 813. AD-A057 218 Vol I, AD A057 219 Vol. II, March 78, edition.
9. R. J. Briggs, et al., Proc. 1981 Particle Accel. Conf.; IEEE Trans.

- Nucl. Sci. NS-28 (June 1981), p. 3360.
10. A. I. Pavlovskii, et al., Sov. Phys. Dokl. 25, 120 (1980).
 11. K. R. Prestwich, et al., IEEE Trans. on Nucl. Sci. NS-30, 3155 (1983).
 12. L. N. Kazanskii, A. V. Kisletsov and A. N. Lebedev, Atomic Energy 30, 27 (1971).
 13. M. Friedman, Appl. Phys. Lett. 41, 419 (1982).
 14. D. W. Kerst, Nature 157, 90 (1946).
 15. A. I. Pavlovskii, et al., Sov. Phys. Tech. Phys. 22, 218 (1977).
 16. P. Sprangle and C. A. Kapetanacos, J. Appl. Phys. 49, 1 (1978).
 17. N. Rostoker, Comments on Plasma Physics, Vol. 6, p. 91 (1980).
 18. C. A. Kapetanacos, P. Sprangle, D. P. Chernin, S. J. Marsh and I. Haber, Phys. Fluids 26, 1634 (1983).
 19. C. W. Roberson, A. Mondelli and D. Chernin, Phys. Rev. Lett. 50, 507 (1983).
 20. A. A. Mondelli and C. W. Roberson, Particle Accelerators 15, 221 (1984).
 21. P. Sprangle and C. A. Kapetanacos, NRL Memo Report No. 5458 (1984).
 22. L. Teng, Argonne Nat. Lab. Report No. ANLAB-55 (1959); G. Salardi, et al., Nucl. Instr. and Methodes 59, 152 (1968); R. M. Pearce, Nucl. Instr. and Methodes 83, 101 (1970); R. L. Gluckstern, Proc. Kinear Accel. Conf., 1979, p. 245.
 23. P. A. Politzer, MIT Report No. 77-1 (1977).
 24. R. E. Potok, H. Becker, L. Bromberg, D. Cohn, N. Diatchenko, P. B. Roemer and J.E.C. Williams MIT Report PFC/RR-82-10 (1982).
 25. I. S. Danilkin, in Stellarators, Proc. of the P.N. Lebedev Inst. (Consultants Bureau, N.Y. 1974) Vol. 65, p. 23. [Note: We have

rederived the toroidal correction and found that two signs in the expression for the potential are different than those given by Danilkin in his Eqs. (24) and (26)].

26. P. Sprangle, C.A. Kapetanacos and S.J. Marsh NRL memo report no. 4666 (1981), (AD-A108359).

APPENDIX J

EXCITATION OF THE PLASMA WAVES IN THE
LASER BEAT WAVE ACCELERATOR

Excitation of the plasma waves in the laser beat wave accelerator

C. M. Tang and P. Sprangle

Plasma Theory Branch, Plasma Physics Division, Naval Research Laboratory, Washington, D.C. 20375

R. N. Sudan

Laboratory for Plasma Studies, Cornell University, Ithaca, New York 14853

PREVIOUS PAGE
IS BLANK

(Received 5 March 1984; accepted for publication 30 May 1984)

The excitation of plasma waves by two laser beams, whose frequency difference is approximately the plasma frequency, is analyzed. Our nonlinear analysis is fully relativistic and includes mismatching of the laser beat frequency to the plasma frequency, time dependent laser amplitudes, and an applied transverse magnetic field (surfatron). For a given beat frequency, laser power, and plasma density, we find the peak accelerating electric field and its phase velocity. The transverse magnetic field is found to increase the effective plasma frequency, but has little effect on the plasma dynamics.

The laser beat wave accelerator concept is a promising collective acceleration scheme which utilizes a large amplitude plasma wave generated by the nonlinear coupling of two intense laser beams to accelerate electrons.¹⁻⁷ We analyzed the formation and saturation of the plasma waves by two laser beams, whose frequencies are separated by approximately the plasma frequency.

Our model consists of a spatially one-dimensional plasma containing infinitely massive ions. Initially the plasma is assumed to be cold, uniform in density, and stationary. The temporal evolution of the plasma wave over a single spatial period is studied at a fixed axial position. This analysis treats the following topics: (1) nonlinear behavior of plasma waves, (2) relativistic effects, (3) effect of finite duration laser pulses, (4) mismatching of the laser beat frequency to the plasma frequency, and (5) the effect of an applied transverse magnetic field (surfatron).⁷

The vector potential associated with the linearly polarized laser pulses within the plasma is

$$A_L(z, t) = \sum_{i=1,2} A_i(z - v_g t) \cos(k_i z - \omega_i t + \phi_i) \hat{e}_x,$$

where $\omega_i > \omega_p$, ω_i is the laser frequency; $\omega_p = (4\pi|e|^2 n_0 / m_0)^{1/2}$ is the ambient plasma frequency, n_0 is the ambient electron density, and $v_g = (\omega_1 - \omega_2) / (k_1 - k_2)$ is the group velocity. In our model, we assume k_i to be constant and A_i specified, i.e., the imposed laser fields are assumed unaffected by the plasma density fluctuations. This is a good approximation if $\omega_i > \omega_p$, $|e|A_i / (m_0 c^2) \ll 1$, and $\delta n / n_0 < 1$, where δn is the plasma density fluctuation. Also included in our model is an applied transverse static magnetic

field, which is represented by the vector potential $A_0 = B_0 z \hat{e}_y$. In this configuration, the electric field of the lasers is parallel to the imposed transverse magnetic field, $E_L \parallel B_0$.

In our one-dimensional model, the transverse electron dynamics possess two constants of motion, i.e., $-|e|c^{-1}(A_L + A_0) + p_x = \text{constant}$. Assuming that $p_x = 0$ prior to the arrival of the laser pulses, it follows that the electron's transverse momentum is given by $p_x = |e|c^{-1}A_L \cdot \hat{e}_x$, and $p_y = |e|c^{-1}B_0(z - z_0)$, where z_0 is the initial axial position of the electron.

It proves convenient to transform to Lagrangian variables,^{8,9} such that $t = \tau$, and $z = z_0 + \xi(z_0, \tau)$, where z_0 and τ are the new independent variables, and $\xi(z_0, \tau)$ is the axial displacement at time τ relative to the electron's initial position z_0 . Using Lagrangian variables, the axial electric field takes on a simple form, $E_z(z_0, \tau) = 4\pi|e|n_0 \xi(z_0, \tau)$.

We normalize the parameters in the following manner, $T = \Delta\omega\tau$, $Z_0 = \Delta k z_0$, $E = (\Delta k / \omega_p^2)(|e|/m_0)E_z = \Delta k \xi$ is the normalized electric field amplitude, $f = \Delta\omega / \omega$ is the frequency mismatch parameter, and $G = (\Omega^2 / \gamma_{10}^2)(\omega_p^2 / \gamma_{10})^{-1}$ is the transverse magnetic field parameter, where

$$\gamma_{10} = [1 + (a_1^2 + a_2^2) / 2]^{1/2},$$

$$a_i = |e|A_i / m_0 c^2, \quad \omega_i = [(\omega_p^2 / \gamma_{10}) + (\Omega^2 / \gamma_{10}^2)]^{1/2}$$

is the effective plasma frequency, $\Omega = |e|B_0 / m_0 c$, $\Delta k = k_1 - k_2$, and $\Delta\omega = \omega_1 - \omega_2$ is the laser beat wave frequency.

Using the axial component of the Lorentz force equation, the evolution of the plasma oscillation is found to be given by

$$\begin{aligned} \ddot{E} + \frac{1}{f^2(1+G)}(1-\beta_g^2 \dot{E}^2) \frac{\gamma_{10}}{\gamma_1} \left((1-\beta_g^2 \dot{E}^2)^{1/2} + G \frac{\gamma_{10}}{\gamma_1} \right) E \\ = - \frac{(1-\beta_g^2 \dot{E}^2)(1-\beta_g^2 \dot{E})}{2\beta_g^2 \gamma_1^2} \left((a_1 + a_2 \cos \Delta\psi) \frac{\partial a_1(\alpha)}{\partial \alpha} + (a_2 + a_1 \cos \Delta\psi) \frac{\partial a_2(\alpha)}{\partial \alpha} - a_1 a_2 \sin \Delta\psi \right), \end{aligned} \quad (1)$$

where

$$\gamma_1 = \left(1 + \frac{\beta_g^2}{f^2} \frac{G}{1+G} \gamma_{10}^2 E^2 + \frac{1}{2}(a_1^2 + a_2^2) + a_1 a_2 \cos \Delta\psi \right)^{1/2},$$

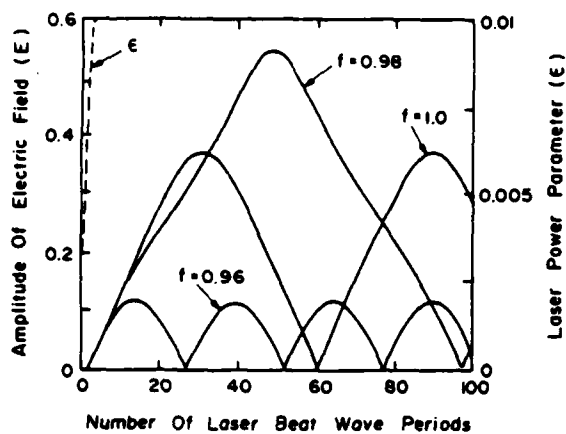


FIG. 1. Normalized amplitude of the accelerating electric field E as a function of number of laser beat wave periods obtained with the fully relativistic equations for laser powers built up over three laser beat wave periods.

$\Delta\psi = E - T + Z_0 + \Delta\phi$, $\dot{E} = \partial E(Z_0, T)/\partial T$,
 $\alpha = Z_0 + E - T$, and $\beta_z = \Delta\omega/c\Delta k$. Our model is valid prior to electron trapping, i.e., trajectory crossing, which occurs when the amplitude $|E|$ is approximately unity.

The equation of motion described by Eq. (1) is fully relativistic in both the axial and transverse directions. Equation (1) permits us to analyze the plasma dynamics for laser pulses having a beat frequency approximately equal to the plasma frequency. By varying the parameter associated with the transverse magnetic field G , we can also model the surfatron configuration.

Using Eq. (1), analytical results in the saturated regime for weak laser fields, i.e., mildly relativistic electron motion, can be obtained. First, we consider the case where the two laser powers are constant in time and define the laser power parameter

$$\epsilon = a_1 a_2 / [1 + (a_1^2 + a_2^2)/2]. \quad (2)$$

Assuming E to be a slowly varying function of time, it can be represented in the form

$$E(Z_0, T) = \Delta E(T) \sin[Z_0 - T + \theta(T) + \Delta\phi], \quad (3)$$

where $\Delta E(T)$ and $\theta(T)$ are slowly varying functions of time

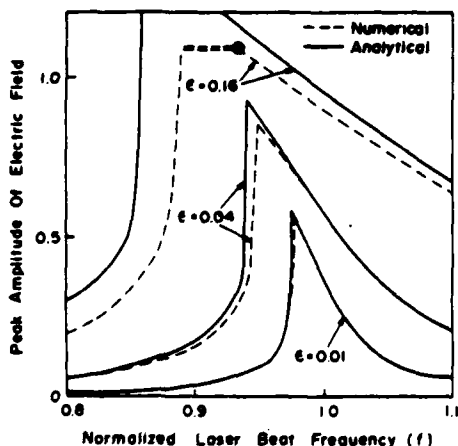


FIG. 2. Normalized peak amplitude of the accelerating electric field for $\epsilon = 0.01, 0.04$, and 0.16 .

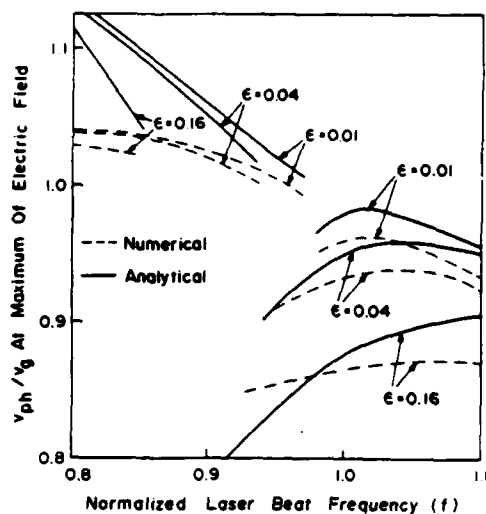


FIG. 3. Plots of the phase velocity associated with the peak electric field for $\epsilon = 0.01, 0.04$, and 0.16 .

compared to the plasma oscillation period. Furthermore, we assume that $\omega_1, \omega_2 > \omega_p$, $\Delta\omega/c\Delta k \approx 1$, and $1 > \Delta E > \epsilon$.

With these assumptions, we obtain

$$d\Delta E/dT = (\epsilon/4)\sin\theta, \quad (4)$$

$$d\theta/dT = (4f^2)^{-1}(f^2 - 1 + 9\Delta E^2/16), \quad (5)$$

where the initial conditions are $\Delta E = 0$ and $\theta = \pi/2$. A constant of motion associated with Eqs. (4) and (5) is

$$\Delta E [\Delta E^3 + \frac{1}{4}(f^2 - 1)\Delta E + \frac{1}{4}f^2\epsilon \cos\theta] = C, \quad (6)$$

where $C = 0$ since initially $\Delta E = 0$.

We obtain analytical results for ΔE and for θ in the saturated regimes by solving Eq. (6). The maximum ΔE at saturation occurs at $\cos\theta = -1$, giving

$$\Delta E_{\max} = 4(\epsilon/3)^{1/3}, \quad (7)$$

and the maximum field in cgs units is

$$E_{z, \max} = 4(\omega_p/\omega_s)(\beta_g/f)(m_0 c/|e|)(\epsilon/3)^{1/3}.$$

As the laser power is increased, relativistic effects on the electron motion become significant. These relativistic effects cause the accelerating field to maximize at a laser beat frequency which is less than the effective plasma frequency,

$$f_{\text{opt}} = 1 - 2^{-1}(9\epsilon/8)^{2/3}. \quad (8)$$

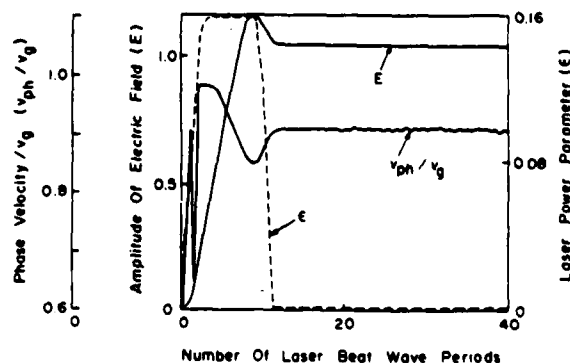


FIG. 4. Temporal evolution of the amplitude of the normalized electric field E and the phase velocity v_{ph}/v_g produced by pulsed laser beams ϵ at a normalized frequency $f = 0.925$.

During the acceleration process the injected electrons must be nearly synchronized with the phase velocity of the plasma wave. To obtain the phase velocity v_{ph} , we follow a null of the electric field and find that

$$v_{ph} = c\beta_g(1 - d\theta/dT). \quad (9)$$

The phase velocity of the plasma wave at the maximum electric field amplitude is at a local minimum and given by

$$v_{ph, min} = c\beta_g(1 - 1.89\epsilon^{2/3}). \quad (10)$$

Figure 1 shows the amplitude of E as a function of time obtained from Eq. (1), with $\epsilon = 0.01$, $G = 0$, and three different beat frequencies: $f = 0.96$, 0.98 , and 1.0 . In Fig. 1 the laser power was increased gradually over three periods of the laser beat frequency. In this case the amplitudes of the electric fields are almost identical to those obtained using Eqs. (4) and (5).

Plots of the normalized peak amplitudes of the accelerating electric field for $\epsilon = 0.01$, 0.04 , and 0.16 in the frequency range $0.8 < f < 1.1$ is given in Fig. 2. The phase velocities associated with the peak amplitudes are plotted in Fig. 3. The dashed curves are the numerical results obtained from Eq. (1), while the solid curves are the analytical results obtained from solving the cubic polynomial in ΔE , Eq. (6). We note that both the amplitudes and phase velocities undergo discontinuities at f_{opt} . For $f > f_{opt}$, ΔE has one real root and the phase velocity associated with the peak electric field is less than the speed of light. For $f < f_{opt}$, ΔE has three real roots and the root closest to the numerical result is the smallest. The phase velocity associated with the peak electric field is generally greater than the speed of light.

In the region marked by (= =) in Fig. 2, the large amplitude plasma oscillations cause the electrons to become highly relativistic and the electric field steepens until wave breaking.^{4,5,8,9} Since the electric field produced by turbulent plasma is unlikely to be desirable for acceleration, the upper limit for ΔE is 1.1. The laser power parameter required to achieve this value is $\epsilon \sim 0.06$.

The saturated oscillatory electric field amplitudes and

the phase velocities are not desirable for accelerating electrons. Thus, the laser pulse duration should be chosen to equal the plasma build up time. After the laser pulses pass through the plasma, the plasma wave will continue to oscillate until disrupted by various instabilities.⁶ Figure 4 shows the temporal profiles of the normalized stimulated electric field amplitude, a short laser beat wave pulse ϵ , and the corresponding phase velocity v_{ph}/v_g at the normalized frequency $f = 0.925$.

For the purpose of accelerating electrons, it is desirable to have large accelerating electric fields with a phase velocity v_{ph} very close to c . As the laser power increases, we find that as the maximum amplitude of the plasma wave increases (scaling as $\epsilon^{1/3}$), and the corresponding phase velocity decreases ($v_g - v_{ph}$ scales as $\epsilon^{2/3}$). The final electron energy is limited by desynchronization of the accelerated electrons and the plasma wave. An imposed transverse magnetic field⁷ can increase the total kinetic energy by maintaining synchronism while accelerating the electron in the transverse direction. The imposed transverse magnetic field increases the effective plasma frequency, but has little effect on the dynamics of the plasma wave.

We have enjoyed stimulating discussions with I. B. Bernstein. This work is sponsored by DOE, under Contract No. DE-AI05-83ER40117.

¹T. Tajima and J. M. Dawson, IEEE Trans. Nucl. Sci. NS-28, 3416 (1981).

²Laser Acceleration of Particles, edited by Paul J. Channell (AIP, New York, 1982), AIP Conf. Proc. No. 91.

³J. D. Lawson, Rutherford Appleton Laboratory, Report No. RL-83-057, 1983.

⁴D. J. Sullivan and B. B. Godfrey, in *The Challenge of Ultra High Energies*, edited by J. Mulvey (ECFA 83/68, Rutherford Appleton Laboratory, Oxford, United Kingdom, 1983), p. 209.

⁵R. J. Noble, Presented at Proceedings of the 12th International Conference on High Energy Accelerators, Fermi National Laboratory, 1983.

⁶R. Bingham (private communication, 1983).

⁷T. Katsouleas and J. M. Dawson, Phys. Rev. Lett. 51, 392 (1983).

⁸R. C. Davidson, *Methods in Nonlinear Plasma Theory* (Academic, New York, 1972).

⁹M. N. Rosenbluth and C. S. Liu, Phys. Rev. Lett. 29, 701 (1972).

APPENDIX K

DYNAMICS OF SPACE-CHARGE WAVES IN THE
LASER BEAT WAVE ACCELERATOR

Dynamics of space-charge waves in the laser beat wave accelerator

C. M. Tang and P. Sprangle

Plasma Theory Branch, Plasma Physics Division, U. S. Naval Research Laboratory, Washington, D. C. 20375-5000

R. N. Sudan

Laboratory for Plasma Studies, Cornell University, Ithaca, New York 14853

(Received 7 June 1984; accepted 17 January 1985)

The excitation of plasma waves by two laser beams, whose frequency difference is approximately the plasma frequency, is analyzed. Our nonlinear analysis is fully relativistic in the axial and transverse directions and includes mismatching of the laser beat frequency to the plasma frequency, time dependent laser amplitudes, and an applied transverse magnetic field (surfatron configuration). Our analytical results for the large amplitude plasma waves include an axial constant of motion, accelerating electric field, and its phase velocity. The analytical results in the weak laser power limit are in good agreement with numerical results obtained from the complete equations. The imposed transverse magnetic field is found to increase the effective plasma frequency, but has little effect on the plasma dynamics.

1. INTRODUCTION

The laser beat wave accelerator is one of a number of laser driven particle accelerating schemes,^{1,2} which is currently receiving considerable attention. Existing types of synchrotron and linear accelerators are nearing their economic limits in going much beyond a few TeV in energies. The availability of high power laser beams ($> 10^{14}$ W) with electric fields as high as 10^9 V/cm brings about the possibility of using these high fields to accelerate particles. Direct use of these fields for continuous particle acceleration is not possible because of the transverse polarization and rapid oscillation of the fields. A number of laser driven acceleration schemes have been suggested over the past two dozen years.

Before describing the laser beat wave accelerator concept, a brief description of some of the other generic laser acceleration concepts is mentioned. These include the inverse free-electron laser accelerator, the grating accelerator, the inverse Čerenkov accelerator, the cyclotron resonance accelerator, and the use of high gradient short wavelength structures.

In the inverse free-electron laser accelerator scheme,³⁻⁵ an electron beam together with an intense laser pulse is propagated through a spatially periodic magnetic field known as a wiggler field. The wiggler period and laser wavelength are such that the transverse particle velocity caused by the wiggler field is in phase with the transverse electric field of the laser radiation. By appropriately contouring both the wiggler amplitude and period, the injected particles can be continually accelerated. The inverse of this process has been used to generate radiation and is the well-known free-electron laser mechanism.

The grating accelerator mechanism⁶ relies on the fact that when electromagnetic radiation propagates along a diffraction grating a slow electromagnetic surface wave is excited along the grating's surface. This scheme utilizes the slow, phase velocity less than the speed-of-light, electromagnetic wave to trap and accelerate a beam of injected electrons.

The inverse Čerenkov accelerator^{7,8} approach takes ad-

vantage of the fact that the index of refraction of a neutral gas is slightly greater than unity. The laser radiation within the gas has a phase velocity less than the speed of light making it possible to trap and accelerate an injected beam of particles.

In the cyclotron resonance accelerator mechanism^{9,10} an electron beam is injected along a uniform magnetic field together with a parallel propagating laser beam. Because of a self-resonance effect, the phase of the electron's transverse velocity can be synchronized with the radiation electric field. This synchronism is maintained throughout the acceleration length.

The high gradient short wavelength structure concept¹¹ is basically a scaled down version of a conventional slow wave accelerator structure. Radiation power sources in the centimeter wavelength range appear appropriate for this approach. The potential advantage of this scheme is that because of the short wavelength employed, relatively low radiation energy per unit length is needed to fill the small structure, and breakdown field limits appear to be higher.

The laser beat wave accelerator concept is a collective acceleration scheme which utilizes a large amplitude plasma wave with phase velocity slightly less than the velocity of light to accelerate charged particles. The large amplitude plasma wave is generated by the nonlinear coupling of two intense laser beams propagating through the plasma.^{1,2,12-22} In this process the two laser beams with frequencies ω_1 , ω_2 and corresponding wavenumbers k_1 , k_2 couple through the plasma to produce a ponderomotive wave with frequency $\omega_1 - \omega_2$ and wavenumber $k_1 - k_2$. See Fig. 1. If $\omega_1 - \omega_2 \approx \omega_p$, the plasma wave will initially grow linearly in time. If the laser frequencies are much greater than the ambient plasma frequency ω_p , then the phase velocity of the ponderomotive wave is nearly equal to the group velocity of the laser wave. In this scheme a beam of injected electrons with axial velocity close to the plasma wave phase velocity can be accelerated until synchronism is lost.

A potentially attractive variation of the plasma beat wave accelerator is the surfatron scheme.²² In the surfatron

Schematic Of Plasma Beat Wave Accelerator

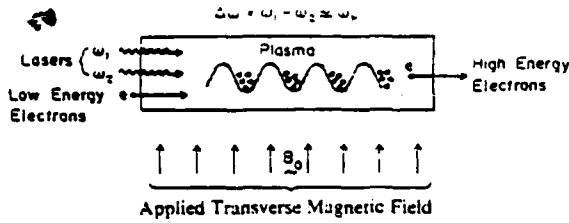


FIG. 1. The schematic of electron acceleration by plasma waves excited by two lasers with a beat frequency approximately equal to the plasma frequency.

configuration a transverse magnetic field is externally applied permitting the accelerated particles to effectively $E \times B$ drift in a direction transverse to the laser propagation direction. In this configuration the electrons can remain in phase with the plasma wave allowing, in principle, higher electron energies to be achieved.

In this paper we analyze the buildup of the plasma waves, extending the analysis of Rosenbluth and Liu.^{23,24} Our nonlinear, fully relativistic treatment of the plasma wave includes mismatching of the laser beat frequencies to the plasma frequency, applied transverse magnetic field as well as time-dependent laser pulses. The resultant equations in Sec. II describe the growth of the excited plasma waves up until saturation. We find that the effective plasma frequency is increased from the ambient plasma frequency when a transverse magnetic field is applied. On the other hand, the effective plasma frequency can be decreased as the transverse motion, induced by intense laser powers, becomes relativistic.

Making the weak laser power approximation in Sec. III, we obtain analytical results for the initial growth rate for the large-amplitude plasma wave, the maximum accelerating electric field, the laser beat frequency requirement, and the corresponding phase velocity. As the combined laser powers (measured by ϵ) increase, the maximum amplitude of the plasma electric field increases as $\alpha\epsilon^{1/3}$. The variable α is a function of frequency mismatch between the laser beat frequency and the effective plasma frequency. The relativistic effect associated with the transverse motion is incorporated in the parameter ϵ . In the limit of exact resonance and nonrelativistic motion in the transverse direction, we confirm the results of Rosenbluth and Liu.²⁴ For the purpose of accelerating electrons, it is desirable not only to have the largest accelerating electric field but also the phase velocity v_{ph} less than but close to the speed of light. We find, however, that as the amplitude of the plasma wave gets larger, the corresponding phase velocities become slower, i.e., $v_g - v_{ph}$ scales as $\epsilon^{2/3}$, where v_g is the group velocity of the lasers in the plasma. The maximum accelerating field for a given laser power parameter ϵ is achieved when the laser beat frequency is less than the effective plasma frequency. The difference between the effective plasma frequency and the optimal laser beat frequency is proportional to $\epsilon^{2/3}$. The plasma buildup time is proportional to $\epsilon^{-2/3}$. The analytical results also show that the transverse magnetic field has little effect on the plasma dynamics to the lowest order.

In Sec. IV we obtained numerical results from the full treatment and compared them with the analytical results. In the weak laser power limit, the results are in excellent agreement. We observe the wave steepening phenomenon caused by relativistic effects. As the laser power increases, the waves eventually break and become turbulent. We show that for laser pulse lengths much longer than the plasma wave buildup time, the amplitude and the phase velocity of the plasma waves are oscillatory. By applying lasers with pulse lengths approximately equal to the plasma wave buildup time, both the amplitude and phase velocity can be approximately maintained at a constant value.

II. PLASMA BEAT WAVE ACCELERATOR

Our model consists of a spatially one-dimensional plasma containing infinitely massive ions. Initially the plasma is assumed to be cold, uniform in density, and stationary. Large amplitude plasma waves are excited by the ponderomotive force associated with the two laser pulses. Using a Lagrangian formulation, the temporal evolution of the plasma wave over a single spatial period is studied at a fixed axial position.

This analysis treats the following topics: (1) nonlinear behavior of plasma waves, (2) relativistic effects, (3) effect of finite duration laser pulses, (4) mismatching of the laser beat frequency to the plasma frequency, and (5) the effect of an applied transverse magnetic field.

A. Nonlinear, relativistic plasma dynamics

The vector potential associated with the linearly polarized laser pulses within the plasma is

$$A_L(z, t) = \sum_{i=1,2} A_i(z - v_g t) \cos(k_i z - \omega_i t + \phi_i) \hat{e}_x, \quad (1)$$

where $A_i(z - v_g t)$ denotes the pulse amplitude of the i th laser, $\omega_i \gg \omega_p$, ω_i is the laser frequency, $\omega_p = (4\pi e^2 n_0 / m_0)^{1/2}$ is the ambient plasma frequency, n_0 is the ambient electron density, and $v_g = (\omega_1 - \omega_2) / (k_1 - k_2)$ is the group velocity of the laser radiation. In our model we assume k_i to be constant and A_i specified, i.e., the imposed laser fields are assumed to be unaffected by the plasma density modulations. This is a good approximation if $\omega_i \gg \omega_p$, $|e|A_i / (m_0 c^2) < 1$ and $\delta n / n_0 < 1$, where δn is the plasma density modulation. Also included in our model is an applied transverse static magnetic field which is represented by the vector potential

$$A_0 = B_0 z \hat{e}_y. \quad (2)$$

The electric and magnetic fields in terms of the vector potential are $E = -(1/c)(\partial/\partial t) A_L$ and $B = \nabla \times (A_L + A_0)$ respectively. In our configuration the electric field vector is parallel to the transverse magnetic field, $E_L \parallel B_0$.

In our one dimensional model, the transverse particle dynamics possesses two constants of motion, i.e., the canonical momentum in the x and y direction,

$$C_1 = -(|e|/c)(A_L + A_0) + p_1. \quad (3)$$

Assuming that $p_1 = 0$ prior to the arrival of the laser pulses, it follows that the electron's transverse momenta are given by

$$p_x = (|e|/c)A_L \cdot \hat{e}_x, \quad (4)$$

and

$$p_y = (|e|/c)B_0(z - z_0), \quad (5)$$

where z_0 is the initial axial position of the electron.

The momentum equation in the axial direction can now be written as

$$\frac{dp_z}{dt} = -|e|E_z - \frac{|e|}{\gamma m_0 c} \left(p_x \frac{\partial A_x}{\partial z} + p_y \frac{\partial A_y}{\partial z} \right), \quad (6)$$

where E_z is the self-consistent plasma induced electric field, $A_x = A_L \cdot \hat{e}_x$, and $A_y = B_0 z$. The particle energy equation is

$$\frac{d\gamma}{dt} = \frac{|e|}{\gamma m_0 c^2} \left(p_x \frac{\partial A_x}{\partial t} + p_y \frac{\partial A_y}{\partial t} \right) - \frac{|e|}{\gamma m_0 c^2} p_z E_z. \quad (7)$$

Combining (6) and (7), we obtain the equation governing the axial motion of the electrons.

$$\begin{aligned} \frac{d\beta_z}{dt} = & -\frac{|e|}{m_0 c} \frac{(1 - \beta_z^2)^{3/2}}{(1 + U_x^2 + U_y^2)^{1/2}} E_z \\ & - \frac{c(1 - \beta_z^2)}{2(1 + U_x^2 + U_y^2)} \left(\frac{\partial}{\partial z} + \frac{\beta_z}{c} \frac{\partial}{\partial t} \right) (U_x^2 + U_y^2), \end{aligned} \quad (8)$$

where $\beta_z = v_z/c$, $U_x = (|e|/m_0 c^2)A_L \cdot \hat{e}_x$, and $U_y = -(|e|/m_0 c^2)B_0(z - z_0)$. Neglecting nonresonant terms we find that

$$\begin{aligned} U_x^2 + U_y^2 = & (\Omega^2/c^2)(z - z_0)^2 + \frac{1}{2}(a_1^2 + a_2^2) \\ & + a_1 a_2 \cos(\Delta k z - \Delta \omega t + \Delta \phi), \end{aligned} \quad (9)$$

where $\Omega = |e|B_0/m_0 c$ is the cyclotron frequency, $a_i = |e|A_i(z - v_g t)/m_0 c^2$, $\Delta k = k_1 - k_2$, $\Delta \omega = \omega_1 - \omega_2$, $\Delta \phi = \phi_1 - \phi_2$, and $\beta_g = \Delta \omega/c\Delta k$. The difference in the laser frequencies is assumed to be close to the plasma frequency, $\Delta \omega \approx \omega_p$. Substituting (9) into (8) yields

$$\begin{aligned} \frac{d\beta_z}{dt} = & -\frac{|e|}{m_0 c} \frac{(1 - \beta_z^2)^{3/2}}{\gamma_i} E_z - \frac{(1 - \beta_z^2)}{\gamma_i^2} \frac{\Omega^2}{c} (z - z_0) \\ & + c \frac{(1 - \beta_z^2)}{2\gamma_i^2} \left(\frac{\partial}{\partial z} + \frac{\beta_z}{c} \frac{\partial}{\partial t} \right) \\ & \times \left[\frac{1}{2}(a_1^2 + a_2^2) + a_1 a_2 \cos(\Delta k z - \Delta \omega t + \Delta \phi) \right], \end{aligned} \quad (10)$$

where

$$\begin{aligned} \gamma_i = & (1 + U_x^2 + U_y^2)^{1/2} \\ = & [1 + (\Omega^2/c^2)(z - z_0)^2 + \frac{1}{2}(a_1^2 + a_2^2) \\ & + a_1 a_2 \cos(\Delta k z - \Delta \omega t + \Delta \phi)]^{1/2} \end{aligned} \quad (11)$$

is a measure of the magnitude of the transverse oscillations induced by the laser beams.

B. Transformation to Lagrangian variables

Equation (10) is expressed in terms of Eulerian independent variables z and t . It proves convenient at this point to perform a transformation to Lagrangian variables,^{23,24} because the plasma induced field E_z takes on a particularly simple form. In the Lagrangian variables, the independent variables are z_0 and τ , such that

$$t = \tau,$$

(12)

$$z = z_0 + \xi(z_0, \tau),$$

where z_0 is the initial position of the electrons at $\tau = 0$ and $\xi(z_0, \tau)$ is the axial displacement at time τ relative to its initial position z_0 . The axial electric field written in terms of the new variables (z_0, τ) is

$$E_z(z_0, \tau) = 4\pi|e|n_0 \xi(z_0, \tau). \quad (13)$$

The equation governing the plasma oscillations can now be written completely in terms of $\xi(z_0, \tau)$, i.e.,

$$\begin{aligned} \ddot{\xi} + \left[\omega_p^2 \left(1 - \frac{\xi^2}{c^2} \right)^{1/2} + \frac{\Omega^2}{\gamma_i} \right] \frac{(1 - \xi^2/c^2)^{1/2}}{\gamma_i} \xi \\ = -\frac{(1 - \xi^2/c^2)}{2\gamma_i^2} \left[c^2 \left(1 - \frac{\beta_z \dot{\xi}}{c} \right) (a_1 + a_2 \cos \Delta \psi) \right. \\ \times \frac{\partial a_1(\alpha)}{\partial \alpha} + (a_2 + a_1 \cos \Delta \psi) \frac{\partial a_2(\alpha)}{\partial \alpha} \\ \left. - \left(\beta_g^{-1} - \frac{\dot{\xi}}{c} \right) c \Delta \omega a_1 a_2 \sin \Delta \psi \right], \end{aligned} \quad (14)$$

where $\dot{\xi} = \partial \xi(z_0, \tau)/\partial \tau$, $\alpha = z_0 + \xi - v_g \tau$, and $\Delta \psi(z_0, \tau) = \Delta k [z_0 + \xi(z_0, \tau)] - \Delta \omega \tau + \Delta \phi$.

The imposed laser field and the applied transverse magnetic field modify the plasma frequency and hence we define an effective plasma frequency

$$\omega_i = (\omega_p^2/\gamma_{i0} + \Omega^2/\gamma_{i0}^2)^{1/2}, \quad (15)$$

where

$$\gamma_{i0} = [1 + \frac{1}{2}(a_{1,\max}^2 + a_{2,\max}^2)]^{1/2}. \quad (16)$$

The effective plasma frequency ω_i is the relativistic upper-hybrid frequency. An increase in the transverse oscillations results in a decrease in the velocity of the axial oscillation, which in turn leads to an effective reduction in the plasma frequency. On the other hand, the transverse magnetic field results in an increase in the effective plasma frequency

C. Normalized plasma wave equation

To further study the dynamics of the plasma oscillations, we normalize the parameters in the following manner,

$$T = \Delta \omega \tau, \quad (17)$$

$$E = (\Delta k/\omega_p^2)(|e|/m_0)E_z = \Delta k \xi,$$

$$Z_0 = \Delta k z_0,$$

$$f = \Delta \omega/\omega_i,$$

and

$$G = (\Omega^2/\gamma_{i0}^2)(\omega_p^2/\gamma_{i0})^{-1}.$$

The evolution of the plasma oscillation is now given by

$$\begin{aligned} \ddot{E} + \frac{1}{f^2(1+G)} (1 - \beta_g^2 \dot{E}^2)^{\gamma_{i0}} \left((1 - \beta_g^2 \dot{E}^2)^{1/2} + G \frac{\gamma_{i0}}{\gamma_i} \right) E \\ = -\frac{(1 - \beta_g^2 \dot{E}^2)(1 - \beta_g^2 \dot{E})}{2\beta_g^2 \gamma_i^2} \left((a_1 + a_2 \cos \Delta \psi) \frac{\partial a_1(\alpha)}{\partial \alpha} \right. \\ \left. + (a_2 + a_1 \cos \Delta \psi) \frac{\partial a_2(\alpha)}{\partial \alpha} - a_1 a_2 \sin \Delta \psi \right), \end{aligned} \quad (18)$$

where

$$\gamma = \left(1 + \frac{\beta_x^2}{f^2} \frac{G}{1-G} \gamma^2 E^2 + \frac{1}{2}(a_1^2 + a_2^2) + a_1 a_2 \cos \Delta\psi \right)^{1/2}, \quad (19)$$

$$\Delta\psi = E - T + Z_0 + \Delta\phi, \quad (20)$$

$\alpha = Z_0 + E - T$, and $\dot{E} = \partial E(Z_0, T) / \partial T$. The total relativistic mass factor associated with the plasma motion becomes

$$\gamma(Z_0, T) = \gamma_1 (1 - \beta_x^{-2} E^2)^{-1/2}. \quad (21)$$

Since the plasma oscillation amplitude is single valued, our model is valid prior to electron trapping, i.e., trajectory crossing. Trajectory crossing occurs when the amplitude $|E|$ is approximately unity.

The equation of motion described by Eq. (18) is fully relativistic in both the axial and transverse directions and permits us to model laser pulses with a beat frequency other than the plasma frequency. Also, by varying the parameter G associated with the transverse magnetic field we can also model the surfatron configuration.

III. ANALYTICAL THEORY IN THE WEAK LASER FIELD

In this section we derive the scaling laws appropriate for weak laser fields, i.e., electron transverse motion is mildly relativistic. Here we consider the case where the two laser powers are constant in time and define the small parameter

$$\epsilon = a_1 a_2 / [1 + \frac{1}{2}(a_1^2 + a_2^2)], \quad (22)$$

where the denominator of ϵ is associated with the relativistic motion in the transverse direction, $\gamma_{\perp 0}^2$. When $a_1 = a_2$, ϵ is proportional to the laser powers.

Assuming E to be a slowly varying function of time, it can be represented in the form

$$E(Z_0, T) = \Delta E(T) \sin[Z_0 - T + \theta(T) + \Delta\phi], \quad (23)$$

where $\Delta E(T)$ and $\theta(T)$ are slowly varying functions of time compared to the plasma oscillation period. Furthermore, we assume that $\omega_1, \omega_2 \gg \omega_p$, so that $\Delta\omega/c\Delta k \approx 1$.

A. Small parameter expansion

Expanding Eq. (18) in terms of the small parameters ϵ and E , we obtain the following equation for E :

$$\dot{E} + (1/f^2)E = (\epsilon/2)\sin \Delta\psi + F, \quad (24)$$

where

$$F(Z_0, T) = \left\{ 1/f^2 - [(1-G)/f^2](1 - \frac{1}{2}E^2) \right. \\ \times [1 - (\epsilon/2)\cos \Delta\psi] \\ \left. - (G/f^2)(1 - \epsilon \cos \Delta\psi) \right\} E \\ - (\epsilon/2)(\dot{E} + \epsilon \cos \Delta\psi)\sin \Delta\psi.$$

$\Delta\psi = \Delta E(T)\sin \Phi(Z_0, T) - T + Z_0 + \Delta\phi$, and $\Phi = Z_0 - T + \Delta\phi + \theta(T)$. Using the identities

$$\sin \Delta\psi = \sum_{l=-\infty}^{\infty} J_l(\Delta E)\sin[(l+1)\Phi - \theta], \quad (25a)$$

$$\cos \Delta\psi = \sum_{l=-\infty}^{\infty} J_l(\Delta E)\cos[(l+1)\Phi - \theta], \quad (25b)$$

and keeping only terms that are proportional to $\sin \Phi$ and $\cos \Phi$, we obtain

$$\left(1 - \frac{1}{f^2} - 2 \frac{d\theta}{dT} \right) \Delta E \sin \Phi - 2 \frac{d\Delta E}{dT} \cos \Phi \\ = -(\epsilon/2)J_0(\Delta E)\sin(\Phi - \theta) - F, \quad (26)$$

where

$$F = \left[\frac{3}{8} \frac{\Delta E^3}{f^2} - \frac{\epsilon}{4} \Delta E \left(\frac{3(1-3G)}{f^2} + 1 \right) \right] J_1(\Delta E)\cos \theta \\ + \frac{\epsilon^2}{4} J_1(2\Delta E)\cos 2\theta \Big\} \sin \Phi \\ + \left[\frac{\epsilon \Delta E}{4} \left(\frac{1-3G}{f^2} + 1 \right) J_1(\Delta E)\sin \theta \right. \\ \left. - \frac{\epsilon^2}{4} J_1(2\Delta E)\sin 2\theta \right] \cos \Phi.$$

Using the small parameter expansions for the Bessel functions, i.e., $J_0(x) \approx 1 - x^2/4$ and $J_1(x) \approx x/2$, Eq. (26) becomes

$$2 \frac{d\theta}{dT} \Delta E \sin \Phi - 2 \frac{d\Delta E}{dT} \cos \Phi \\ = \Delta E \left(1 - \frac{1}{f^2} \right) \sin \Phi + \frac{\epsilon}{2} \left(1 - \frac{\Delta E^2}{4} \right) \\ \times (\sin \Phi \cos \theta - \cos \Phi \sin \theta) + F, \quad (27)$$

where

$$F = \left(\frac{3}{8} \frac{\Delta E^3}{f^2} - \frac{\epsilon}{8} \frac{\Delta E^2}{f^2} (2 - 9G) \cos \theta \right. \\ \left. + \frac{\epsilon^2}{4} \Delta E \cos(2\theta) \right) \sin \Phi \\ + \left(\frac{\epsilon}{8} \frac{\Delta E^2}{f^2} (2 - 3G) \sin \theta - \frac{\epsilon^2}{4} \Delta E \sin(2\theta) \right) \cos \Phi.$$

Separating the terms proportional to $\sin \Phi$ and $\cos \Phi$, we obtain two simultaneous coupled equations for the amplitude and phase variation of the excited plasma wave.

$$\frac{d\Delta E}{dT} = \epsilon \left[\frac{1}{4} - \frac{\Delta E^2}{16} \left(1 + \frac{2}{f^2} - \frac{3G}{f^2} \right) \right] \sin \theta + \frac{\epsilon^2 \Delta E}{8} \sin 2\theta, \quad (28a)$$

$$\Delta E \frac{d\theta}{dT} = \frac{\Delta E}{2} \frac{f^2 - 1}{f^2} + \frac{3}{16} \frac{\Delta E^3}{f^2} \\ + \epsilon \left[\frac{1}{4} - \frac{\Delta E^2}{16} \left(\frac{2}{f^2} + 1 - \frac{9G}{f^2} \right) \right] \cos \theta \\ + \frac{\epsilon^2}{8} \Delta E \cos 2\theta. \quad (28b)$$

B. Constant of motion

Analytical expressions for ΔE and phase velocity v_{ph} of the plasma wave can be obtained by assuming $1 \gg \Delta E \gg \epsilon$. It will be shown later that this assumption is well founded. Neglecting terms proportional to $\epsilon \Delta E^2$ and $\epsilon^2 \Delta E$ in Eq. (28) we obtain,

$$\frac{d\Delta E}{dT} \approx \frac{\epsilon}{4} \sin \theta, \quad (29a)$$

$$\Delta E \frac{d\theta}{dT} \approx \frac{\Delta E}{2} \frac{f^2 - 1}{f^2} + \frac{\epsilon}{4} \cos \theta + \frac{3}{16} \frac{\Delta E^3}{f^2}. \quad (29b)$$

Multiplying Eq. (29a) by $\cos \theta$ and Eq. (29b) by $\sin \theta$ and adding the two equations yield

$$\frac{d}{dT}(\Delta E \cos \theta) = \left(-\frac{\Delta E}{2} \frac{f^2 - 1}{f^2} - \frac{3}{16} \frac{\Delta E^3}{f^2} \right) \sin \theta. \quad (30)$$

Using (29a) and (30), the following constant of the motion is obtained:

$$\Delta E [\Delta E^3 + (16/3)(f^2 - 1)\Delta E + (16/3)f^2 \epsilon \cos \theta] = C, \quad (31)$$

where $C = 0$, since initially $\Delta E = 0$.

Employing (30), Eqs. (29a) and (29b) become

$$\frac{d\Delta E}{dT} = \frac{\epsilon}{4} \sin \theta, \quad (32a)$$

and

$$\frac{d\theta}{dT} = \frac{1}{4f^2} \left(f^2 - 1 + \frac{9}{16} \Delta E^2 \right), \quad (32b)$$

where the initial conditions are $\Delta E = 0$ and $\theta = \pi/2$. An alternate way to solve ΔE and θ in time is outlined in the Appendix. At exact resonance $f = 1$ and nonrelativistic motion in the transverse direction, i.e., $\gamma_{10}^2 \approx 1$ and $\epsilon \approx a_1 a_2$, the expressions (32a) and (32b) agree with that of Rosenbluth and Liu.²⁴

C. Analytical results

We obtain analytical results for the startup as well as the saturated regimes of the plasma wave. The plasma wave initially grows linearly in time, i.e., the initial amplitude of E_z in cgs units is proportional to Γt , where

$$\Gamma = (\beta_g/4)(m_0 c / |e|) \omega_p^2 \epsilon. \quad (33)$$

The most interesting results are associated with the saturated regime. In the remainder of this section, we obtain maximum accelerating electric fields, the appropriate laser beat frequencies, the corresponding phase velocities, and the plasma wave profiles.

The amplitude of the electric field is proportional to a real root of the cubic polynomial (31). The roots are

$$\Delta E = A + B, \quad -\frac{A+B}{2} + \frac{A-B}{2} \sqrt{-3}, \quad -\frac{A+B}{2} - \frac{A-B}{2} \sqrt{-3}, \quad (34)$$

where $A = (-b/2 + h)^{1/3}$, $B = (-b/2 - h)^{1/3}$, $h = (b^2/4 + a^3/27)^{1/2}$, $a = 16/3(f^2 - 1)$, and $b = 16/3f^2 \epsilon \cos \theta$. For $h > 0$, there is one real root given by $\Delta E = A + B$. When $h < 0$, there are three real roots, and numerical results show that the relevant ΔE corresponds to the smallest real root. At $h = 0$, ΔE undergoes a discontinuity.

For a given laser power parameter ϵ , the maximum ΔE occurs at $h = 0$ and $\cos \theta = -1$, giving

$$\Delta E_{\max} = 4(\epsilon/3)^{1/3}, \quad (35)$$

where ϵ is defined in Eq. (22). The actual maximum field in cgs units is

$$E_{z,\max} = 4 \left(\frac{\omega_p^2}{\Delta \omega} \right) \beta_g \frac{m_0 c}{|e|} \left(\frac{\epsilon}{3} \right)^{1/3}. \quad (36)$$

As the laser power is increased, relativistic effects on the electron motion become significant. These relativistic effects cause the accelerating field to maximize at a laser beat frequency which is less than the effective plasma frequency. For example, when the beat frequency is exactly equal to the effective plasma frequency, i.e., $f = 1$, the maximum normalized field is

$$\Delta E = [(16/3)\epsilon]^{1/3} < \Delta E_{\max}. \quad (37)$$

It can be shown that the electric field maximizes to the value in Eq. (35), when the normalized laser beat frequency is

$$f_{\text{opt}} = 1 - \frac{1}{2}(\frac{2}{3}\epsilon)^{2/3}, \quad (38)$$

which corresponds to a laser beat frequency in cgs units given by

$$\Delta \omega_{\text{opt}} = \omega_s (1 - 0.54\epsilon^{2/3}). \quad (39)$$

During the acceleration process in injected electrons must be nearly synchronized with the phase velocity of the plasma wave. To obtain the phase velocity, we follow a null in the plasma wave. We find that the phase velocity of the plasma wave and the associated relativistic mass factor are

$$v_{\text{ph}} = v_g \left(1 - \frac{d\theta}{dT} \right), \quad (40a)$$

and

$$\gamma_{\text{ph}} = \gamma_g \left(1 + 2\gamma_g^2 \frac{d\theta}{dT} \right)^{-1/2}, \quad (40b)$$

where $d\theta/dT$ is given by (32b) and $\gamma_g = [1 - (v_g/c)^2]^{-1/2}$. As the amplitude of the plasma wave becomes larger, the phase velocity of the plasma wave decreases. The phase velocity of the plasma wave at the maximum electric field amplitude is a minimum and given by

$$v_{\text{ph,min}} = v_g (1 - 1.89\epsilon^{2/3}). \quad (41)$$

The time it takes the amplitude of the plasma wave to reach the first peak is called the plasma buildup time and in normalized units is given by

$$\bar{T}(f, \epsilon) = 4 \int_{\pi/2}^{\pi} \frac{d\theta}{f^2 - 1 + (9/16)\Delta E^2}, \quad (42)$$

where ΔE is expressed in terms of θ in Eq. (34). The equation above can be integrated at exact resonance, i.e., $f = 1$. Using the fact that $\Delta E = [-(16/3)\epsilon \cos \theta]^{1/3}$ at $f = 1$, we can write

$$\bar{T}(1, \epsilon) = \frac{64}{9} \left(\frac{3}{16} \right)^{2/3} \epsilon^{-2/3} \int_{\pi/2}^{\pi} \frac{d\theta}{(-\cos \theta)^{2/3}}. \quad (43)$$

Evaluating the integral in (43), we obtain

$$\begin{aligned} \bar{T}(1, \epsilon) &= \frac{32}{9} \left(\frac{3}{16} \right)^{2/3} \frac{\Gamma(1/6)\Gamma(1/2)}{\Gamma(2/3)} \epsilon^{-2/3} \\ &= 8.48\epsilon^{-2/3}. \end{aligned} \quad (44)$$

Taking $\epsilon = 0.01$ as an example, the plasma buildup time at exact resonance is 29.1 plasma periods, i.e., $\bar{T}(1, 0.01) = 29.1(2\pi)$. For $\epsilon = 0.1$, the plasma buildup time is reduced to only 6.3 plasma periods. The plasma buildup time shortens as laser power parameter ϵ increases.

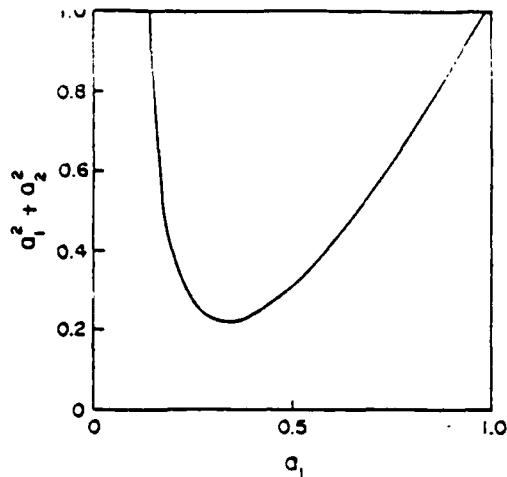


FIG. 2. Plot of $a_1^2 + a_2^2$ as a function of a_1 , for $\epsilon = 0.1$.

Finally, we discuss the effect of unequal applied laser pulse powers on the plasma wave dynamics. Suppose a given value of ϵ is desired, the total power required for the laser is at a minimum when $a_1 = a_2 = a$ where $a = [\epsilon/(1 - \epsilon)]^{1/2}$. The expression for a_2 given a_1 and ϵ is

$$a_2 = a_1/\epsilon - [a_1^2/\epsilon - (2 + a_1^2)]^{1/2}. \quad (45)$$

The range for a_1 given ϵ is

$$a_{\min} = \left(\frac{2\epsilon^2}{1 - \epsilon^2}\right)^{1/2} < a_1 < a_{\max} = \left(\frac{2}{1 - \epsilon^2}\right)^{1/2}. \quad (46)$$

A plot of $a_1^2 + a_2^2$ is given in Fig. 2 for $\epsilon = 0.1$. The use of unequal laser powers can be advantageous in controlling the value of the parameter ϵ .

IV. NUMERICAL RESULTS

Numerical examples are given for the complete nonlinear and fully relativistic equations obtained in Sec. II, and these results are compared to the analytical results obtained in Sec. III in the weak laser field limit, i.e., $\epsilon < 1$.

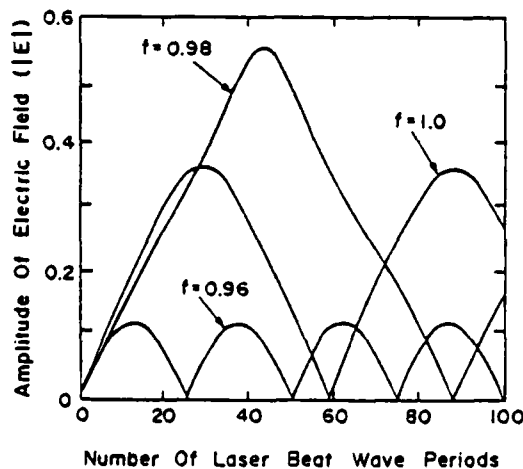


FIG. 3. Plot of $|\Delta E|$ as a function of the number of laser beat wave periods for $\epsilon = 0.01$, $G = 0$ and three different beat frequency parameters $f = 0.96$, 0.98 , and 1.0 .

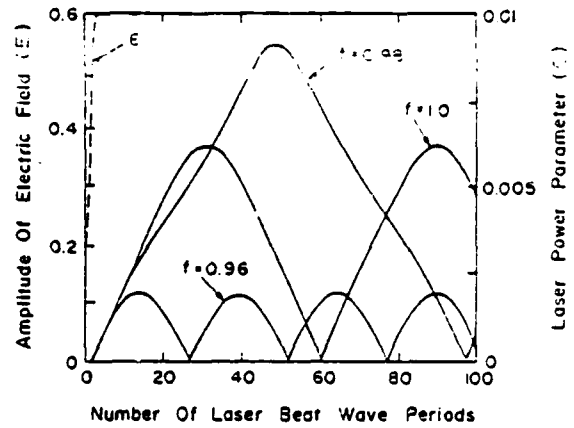


FIG. 4. Normalized amplitude of the accelerating electric field E as a function of the number of laser beat wave periods obtained with the fully relativistic equations for laser powers built up over three laser periods.

Equations (32a) and (32b) were numerically solved in order to verify our approximation $|\Delta E| \gg \epsilon$ used in deriving the constant of motion. Figure 3 is a plot of $|\Delta E|$ as a function of time for the parameters $\epsilon = 0.01$, $G = 0$, and three different normalized frequencies: $f = 0.96$, $f = 0.98$, and $f = 1.0$. The curves show that the approximation, $|\Delta E| \gg \epsilon$, is indeed well satisfied. The curves for $|\Delta E|$ in Fig. 3 are periodic in time and show that the plasma wave periodically exchanges its energy with the laser field. The plasma buildup time is longest when the frequency is f_{opt} , and is 29 plasma periods with $f = 1$ and $\epsilon = 0.01$, agreeing with the calculations in Sec. III C.

Figure 4 is a plot of the amplitude of E as a function of time for the complete equations (18)–(20), with the same parameters as used in Fig. 3. The laser power was built up gradually over three periods of the laser beat frequency. We used $\beta_z = 0.9999$ for the purpose of comparing with analytical results. In this case, the amplitudes of the plasma electric

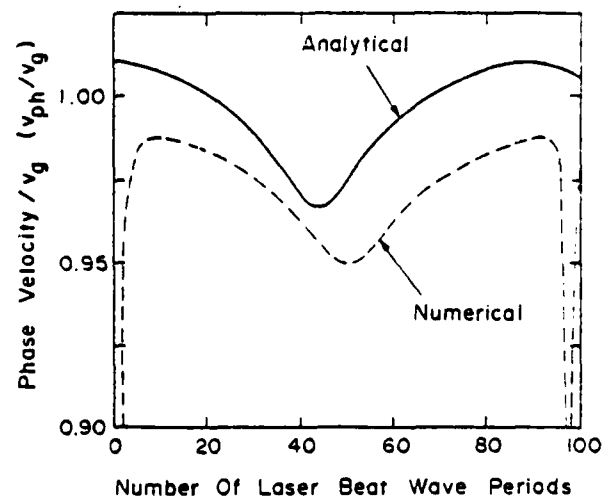


FIG. 5. Phase velocities obtained from the simplified equations (solid curve) and numerically obtained from the fully relativistic nonlinear equations (dashed curve) for $\epsilon = 0.01$, $G = 0$ and $f = 0.98$.

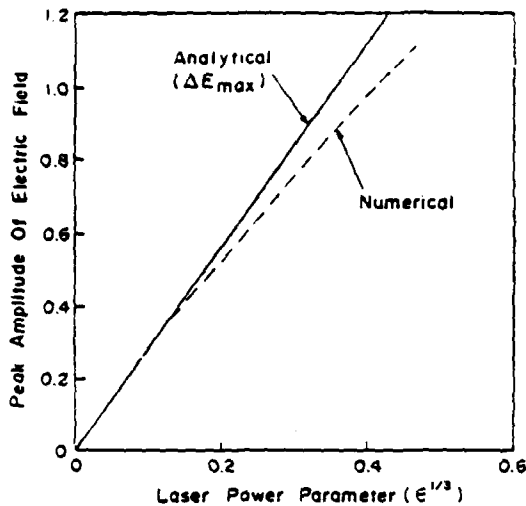


FIG. 6. Comparison of ΔE_{\max} based on the analytical result (solid curve), and the peak amplitude of E numerically obtained from the fully relativistic nonlinear equations (dashed curves).

fields are only slightly changed, showing that the analytical equations are excellent in the small ϵ limit.

In Fig. 5, the phase velocities given by the analytical results (solid curve) are compared to the numerical values (dashed curve) for $\epsilon = 0.01$ and $f = 0.98$. The shift of the two curves is caused by the three periods of laser buildup time in the numerical calculation. The phase velocity v_{ph} is at a local minimum when $|\Delta E|$ is maximum and decreases as ΔE increases.

The plots of the numerically calculated peak amplitude of E (dashed curve) and the analytical expression $\Delta E_{\max} = 4(\epsilon/3)^{1/3}$ (solid curve) are plotted as a function of $\epsilon^{1/3}$ in Fig. 6. The plots of the normalized laser beat frequency f (dashed curve), at which the largest accelerating electric field is numerically obtained, and the analytical expression for f_{opt} (solid curve) are shown in Fig. 7 as a function of $\epsilon^{2/3}$.

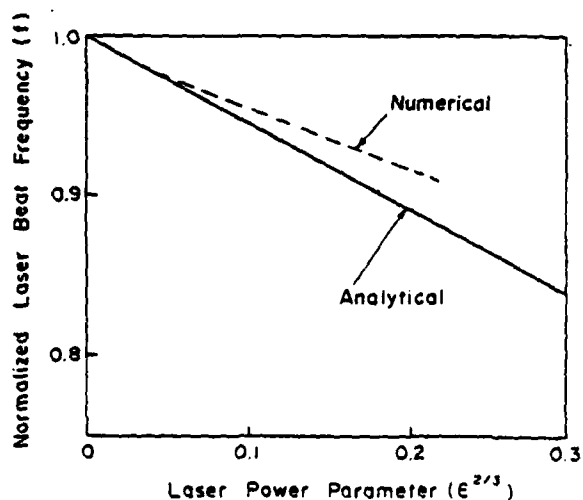


FIG. 7. Comparison of the frequency at which the largest accelerating electric field is obtained. The solid curve is a plot of f_{opt} obtained analytically and the dashed curve is found numerically from the fully relativistic nonlinear equations.

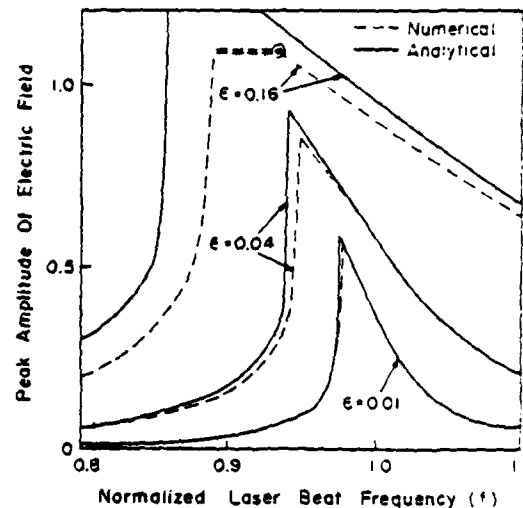


FIG. 8. Normalized peak amplitude of the accelerating electric field for $\epsilon = 0.01, 0.04,$ and 0.16 within the normalized laser beat frequency range $0.8 < f < 1.1$. The solid curves are analytical results of peak ΔE obtained from Eq. (34) and the dashed curves are numerical results of peak amplitude of E obtained from the complete analysis of Eqs. (18)–(20).

The normalized peak amplitudes of the accelerating electric field for $\epsilon = 0.01, 0.04,$ and 0.16 in the frequency range $0.8 < f < 1.1$ are given in Fig. 8. The phase velocities associated with the peak amplitude are plotted in Fig. 9. The dashed curves are the numerical results obtained from the complete nonlinear and fully relativistic equations (18)–(20), while solid curves are the analytical results obtained from Eq. (34). The agreement for small ϵ is excellent.

We note that the analytical solutions for the amplitude of the plasma wave and the phase velocity have discontinuities at f_{opt} . For $f > f_{opt}$, ΔE has one real root and the phase

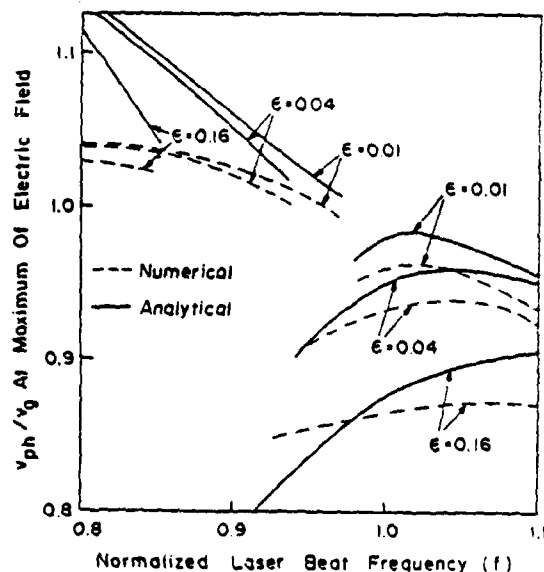


FIG. 9. Plots of the phase velocity associated with the peak electric field for $\epsilon = 0.01, 0.04,$ and 0.16 within the normalized beat frequency range $0.8 < f < 1.1$. The solid curves are obtained from the analytical equations and the dashed curves are obtained from the complete equations at the maximum of E .

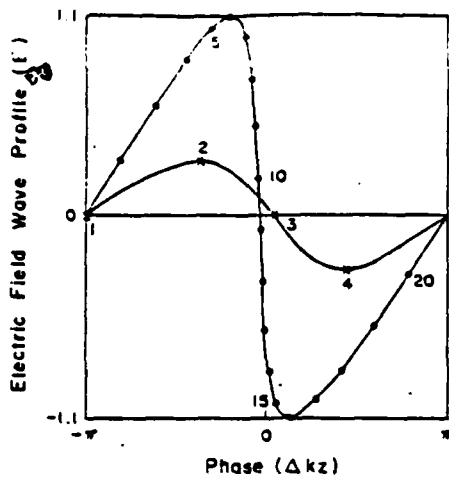


FIG. 10. Normalized electric field for one period of the laser beat wave at two different amplitudes obtained at two different instants in time with $\epsilon = 0.16$, $f = 0.925$, and $G = 0$. The point is marked by (*) in Fig. 8.

velocity associated with the peak electric field is less than the speed of light. For $f < f_{opt}$, ΔE has three real roots. The smallest value of the root is closest to the numerical result. For $f < f_{opt}$, the phase velocity associated with the peak electric field is generally greater than the speed of light.

In the region marked by (==) in Fig. 8, the analysis is not applicable because of particle mixing. Here, the large amplitude oscillations cause the electrons to become relativistic in wave steepening,^{20,24} which phenomenon is illustrated in Fig. 10. Two curves of the normalized electric field at two instants of time are plotted for one wavelength of the laser beat wave with parameters $\epsilon = 0.16$ and $f = 0.925$; the point is marked by (*) on Fig. 8. The curve with the circular dots showing wave steepening is the normalized electric field just before wave breaking. On the other hand, the wave profile is almost sinusoidal when the amplitude of the electric field is small, i.e., $|\Delta E| \ll 1$, as illustrated by the curve with the crosses in Fig. 10. As $|\Delta E|$ becomes larger than 1.1, the

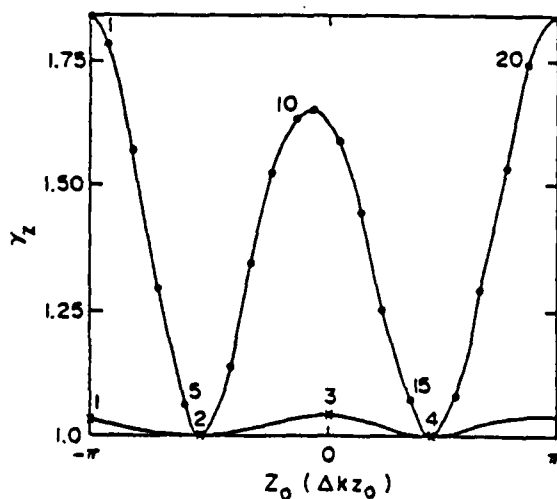


FIG. 11. Plots of the relativistic gamma associated with the axial motion γ_z for one period of the plasma oscillation for the same parameters and at the same instants in time as in Fig. 10.

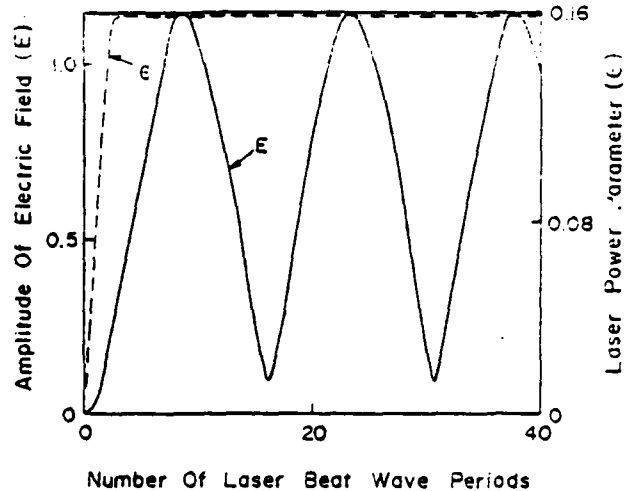


FIG. 12. Time evolution of the amplitude of the normalized electric field (solid curve) and the time-dependent laser power parameter ϵ (dashed curve) for $f = 0.925$.

electric field in our representation becomes multivalued and the Lagrangian model breaks down. Since the electric field produced by a turbulent plasma is unlikely to be desirable for acceleration of electrons, the upper limit for $|\Delta E|$ is $\Delta E_{lim} = 1.1$. The minimum ϵ necessary to obtain ΔE_{lim} is approximately $\epsilon_{min} = 0.06$.

To illustrate the relativistic phenomenon, Fig. 11 shows a plot of $\gamma_z = [1 - (v_z/c)^2]^{-1/2}$ for one wavelength of the laser beat wave for the same parameters and at the same instants in time as Fig. 10.

Numerically calculated time evolution of the electric field and the corresponding phase velocity for $f = 0.925$ are plotted in Figs. 12 and 13, respectively, where ϵ is adiabatically increased from 0 to 0.16 in three plasma periods.

Since the saturated oscillatory electric field amplitudes and phase velocities are not desirable for accelerating electrons, the laser pulse duration should be chosen to equal the plasma buildup time. After the laser pulses pass through the

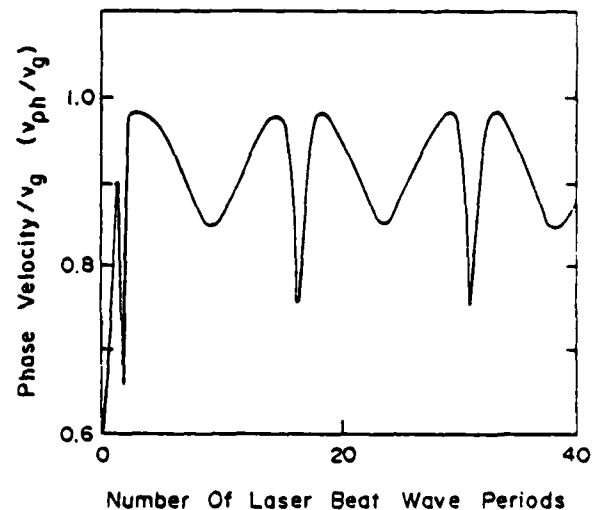


FIG. 13. The temporal dependence of the phase velocity associated with Fig. 12.

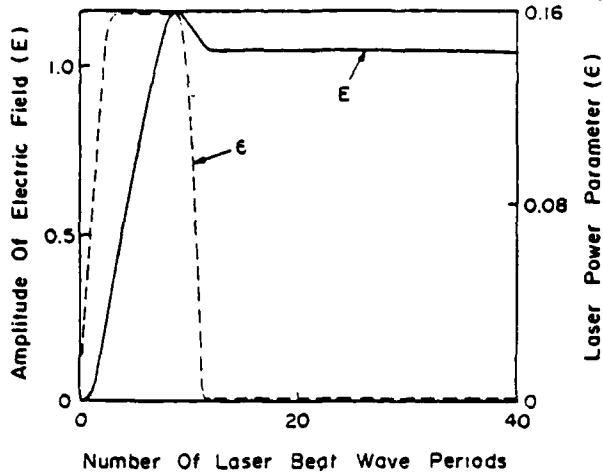


FIG. 14. The temporal evolution of the amplitude of the normalized electric field E (solid curve) produced by pulsed laser beams $\epsilon(t)$ (dashed curve) for $f = 0.925$.

plasma, the plasma wave will continue to oscillate until disrupted by various instabilities. Figure 14 plots the temporal profiles of the normalized stimulated electric field amplitude (solid curve) for $f = 0.925$ and a short laser beat wave pulse $\epsilon(t)$ (dashed curve). The corresponding phase velocity is shown in Fig. 15. After the laser pulse passed, the amplitude and the phase velocity of the plasma oscillation remained roughly constant.

Next, we examined the effect of the perpendicular magnetic field on the plasma oscillation in the surfatron configuration. An imposed transverse magnetic field can increase the total electron energy by maintaining synchronism while accelerating the electron in the transverse direction.²² The analytical calculation shows that the transverse magnetic field has a higher order effect on the plasma dynamics. The numerical result of the peak electric field and the corresponding phase velocity are plotted as a function of G for $\epsilon = 0.16$ and $f = 0.925$ in Fig. 16, and results changed little for $0 < G < 1$. The imposed transverse magnetic field increases

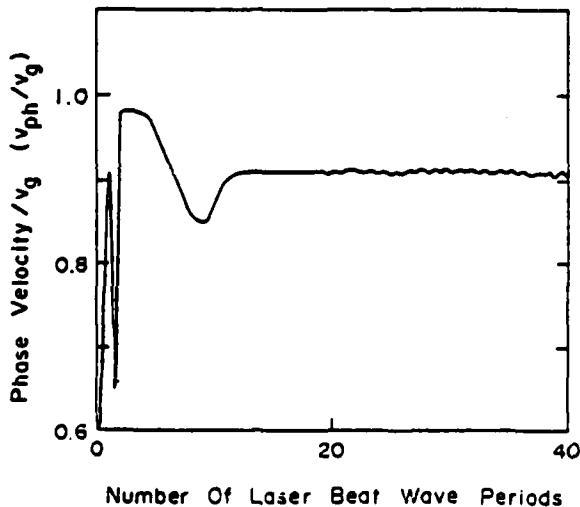


FIG. 15. The phase velocity associated with the pulsed laser beam shown in Fig. 14.

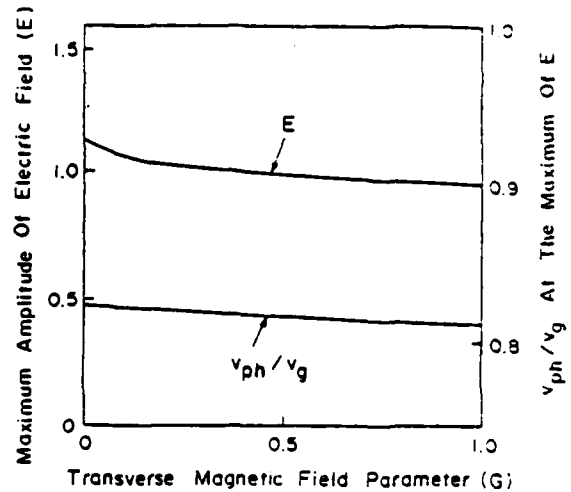


FIG. 16. Plot of the maximum amplitude of the normalized electric field E (solid curve) and the corresponding phase velocity variation v_{ph}/v_g (dashed curve) as a function of G for $\epsilon = 0.16$ and $f = 0.925$.

the effective plasma frequency, but has little effect on the dynamics of the plasma wave.

V. SUMMARY AND DISCUSSION

We have obtained nonlinear, fully relativistic results for the plasma waves excited by the beating of two laser beams. We found that the effective plasma frequency is a function of the laser power as well as the imposed transverse magnetic field in the surfatron configuration. In the ideal situation analyzed here, the amplitude of plasma waves becomes oscillatory. Since it is desirable to maintain the accelerating electric field at the largest value, the laser pulse duration should be approximately equal to the plasma wave buildup time.

In the weak laser power limit, we obtained analytical results for the saturated plasma wave for a range of frequencies around the effective plasma frequency. As the laser power increases, the maximum amplitude of the plasma electric field increases as $\epsilon^{1/3}$, confirming the previous work of Rosenbluth and Liu²⁴ at exact resonance when the transverse motion is nonrelativistic, i.e., $\gamma_{10} \approx 1$, and the corresponding phase velocity decreases, i.e., $v_g - v_{ph}$ scales as $\epsilon^{2/3}$. The maximum accelerating field is achieved when the laser beat frequency is less than the effective plasma frequency. The difference between the effective plasma frequency and the optimal laser beat frequency is proportional to $\epsilon^{2/3}$. The plasma buildup time is proportional to $\epsilon^{-2/3}$.

Given a plasma density, the desirable range of normalized laser beat frequency for growth of large amplitude plasma waves is small, i.e., $1.05 \gtrsim f \gtrsim f_{op}$. If the laser beat frequency is given, this condition can be translated to plasma density requirements. Defining $n_0 = \Delta n + n_{f=1}$, where $n_{f=1}$ is the ambient plasma density that will provide exact resonance at $f = 1$, i.e., $\omega_r(n_{f=1}) = (\omega_{p0}^2/\gamma_{10} + \Omega^2/\gamma_{10}^2)^{1/2} = \Delta\omega$, where $\omega_{p0} = (4\pi|e|^2 n_{f=1}/m_n)^{1/2}$. The density criteria for stimulating large amplitude plasma waves is

$$-0.1(1 + G_0) \leq \Delta n/n_{f=1} < 1.1\epsilon^{2/3}(1 + G_0). \quad (47)$$

where $G_0 = (\Omega^2/\gamma_{10}^2)(\omega_{p0}^2/\gamma_{10})^{-1}$. We now consider two examples of plasma density variation requirements without

imposed transverse magnetic field, i.e., $G_0 = 0$. The largest tolerable plasma density variation is about 25% for $\epsilon = 0.06$. The tolerable density variation is reduced to 15% for $\epsilon = 0.01$. The application of transverse magnetic field B_0 in the surfatron configuration can increase the allowable density fluctuation limit by a factor $(1 + G_0)$. In an experimental situation, B_0 not only overcomes the problem of desynchronization, but allows more flexibility in the tuning of plasma density.

A comparison of the numerical results from the complete equations with the simple analytical results for the weak laser power limit is excellent for $\epsilon \ll 0.1$, and is in fair agreement for larger ϵ . Numerical results show that the largest amplitude for the accelerating electric field in cgs units without electrons overtaking each other is

$$|E_z| \simeq (\omega_p^2 / \Delta\omega) \beta_s (m_0 c / |e|).$$

The laser power required to reach this value without wave breaking is $\epsilon \sim 0.06$.

For the purpose of accelerating electrons, it is desirable not only to have the largest accelerating electric field but also to have v_{ph}/c less than but close to unity. Instead, we find that as the amplitude of plasma waves gets larger, the corresponding phase velocities become smaller. An applied transverse magnetic field can overcome the problem of desynchronization of the accelerating electrons in the accelerative electric field. Since the transverse magnetic field only modifies the effective plasma frequency, but has little effect on the plasma dynamics, the surfatron configuration may be the desirable way to operate the laser beat wave accelerator.

Finally, we would like to point out that the laser plasma interaction contains a rich source of instabilities, many of which may be detrimental for the formation of the large amplitude plasma waves studied in this paper for the laser beat wave accelerating scheme. Some of the processes¹⁹ that have large growth rates are three-wave forward Raman scattering, four-wave forward Raman scattering, and processes associated with background ions. Other areas requiring investigations are the effects of the transverse Weibel instability induced by energy anisotropy, the influence of kinetic effects, self-focusing of laser radiation, and filamentation. Detailed studies of them are necessary to evaluate feasibility of the long term goals of the laser beat wave accelerating scheme.

ACKNOWLEDGMENT

This work is sponsored by U. S. Department of Energy, Office of Energy Research, under Interagency Agreement No. DE-AI05-83ER40117.

APPENDIX: ALTERNATIVE VIEW OF EQUATIONS (32a) AND (32b)

The simplified equations in (32a) and (32b) can be written in the form

$$\frac{dx}{dT} = \frac{1}{2f^2} \left(1 - f^2 - \frac{3}{8}(x^2 + y^2) \right) y, \quad (A1)$$

$$\frac{dy}{dT} = \frac{\epsilon}{4} - \frac{1}{2f^2} \left(1 - f^2 - \frac{3}{8}(x^2 + y^2) \right) x, \quad (A2)$$

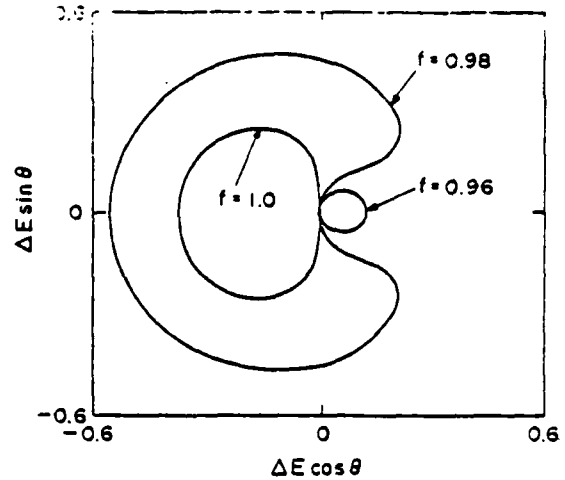


FIG. 17. Plot of $\Delta E \sin \theta$ vs $\Delta E \cos \theta$ for $\epsilon = 0.01$ and three different normalized laser beat frequencies.

where $x = \Delta E \cos \theta$, $y = \Delta E \sin \theta$ and the initial conditions are $x = y = 0$ at $T = 0$. The amplitude and the phase of the electron displacement are

$$\Delta E = (x^2 + y^2)^{1/2}, \quad (A3a)$$

$$\theta = \tan^{-1}(y/x). \quad (A3b)$$

Figure 17 is a plot of x and y for $\epsilon = 0.01$ and three different normalized laser beat frequencies: $f = 0.96$; 0.98 , and 1.0 . For $f > f_{opt}$, the enclosed area is to the left of $x = 0$, and to the right of $x = 0$ for $f < f_{opt}$.

¹Laser Acceleration of Particles, AIP Conference Proceedings No. 91, edited by P. J. Channell (American Institute of Physics, New York, 1982).

²The Challenge of Ultra-High Energies, Proceedings of ECFA-RAL meeting, Oxford, 1982 (Rutherford Appleton Laboratory, England, 1983).

³H. Motz, *Contemp. Phys.* 20, 547 (1979).

⁴P. Sprangle and C.-M. Tang, *IEEE Trans. Nucl. Sci.* NS-28, 3346 (1981).

⁵C. Pellegrini, in Ref. 1, p. 138 and in Ref. 2, p. 249.

⁶R. B. Palmer, in Ref. 1, p. 179 and in Ref. 2, p. 267.

⁷R. H. Pantell and T. I. Smith, *Appl. Phys. Lett.* 40, 753 (1982).

⁸J. R. Fontana and R. H. Pantell, *J. Appl. Phys.* 54, 4255 (1983).

⁹A. A. Kolomenskii and A. N. Lebedev, *Sov. Phys. Dokl.* 7, 745 (1963).

¹⁰P. Sprangle, L. Vlahos, and C. M. Tang, *IEEE Trans. Nucl. Sci.* NS-30, 3177 (1983).

¹¹A. M. Sessler, in Ref. 1, p. 154.

¹²T. Tajima and J. M. Dawson, *Phys. Rev. Lett.* 43, 267 (1979).

¹³T. Tajima and J. M. Dawson, *IEEE Trans. Nucl. Sci.* NS-26, 4188 (1979).

¹⁴T. Tajima and J. M. Dawson, *IEEE Trans. Nucl. Sci.* NS-28, 3416 (1981).

¹⁵C. Joshi, T. Tajima, J. M. Dawson, H. A. Baldis, and N. A. Ebrahim, *Phys. Rev. Lett.* 47, 1285 (1981).

¹⁶M. Ashour-Abdalla, J. N. Leboeuf, T. Tajima, J. M. Dawson, and C. F. Kennel, *Phys. Rev. A* 23, 1906 (1981).

¹⁷D. J. Sullivan and B. B. Godfrey, *IEEE Trans. Nucl. Sci.* NS-28, 3395 (1981).

¹⁸J. D. Lawson (private communication).

¹⁹R. Bingham (private communication).

²⁰R. J. Noble, *Proceedings of the 12th International Conference on High Energy Acceleration*, edited by F. T. Cole and R. Donaldson (Fermi National Laboratory, Batavia, IL, 1983), p. 467.

²¹B. I. Cohen (private communication).

²²T. Katsouleas and J. M. Dawson, *Phys. Rev. Lett.* 51, 392 (1983).

²³R. C. Davidson, *Methods in Nonlinear Plasma Theory* (Academic, New York, 1972).

²⁴M. N. Rosenbluth and C. S. Liu, *Phys. Rev. Lett.* 29, 701 (1972).

APPENDIX L

FINITE LARMOR RADIUS DIODOTRON INSTABILITY

Finite Larmor radius diocotron instability

Robert G. Kleva and Edward Ott^{a)}

Laboratory for Plasma and Fusion Energy Studies, University of Maryland, College Park, Maryland 20742

Wallace M. Manheimer

Plasma Physics Division, Naval Research Laboratory, Washington, D.C. 20375

(Received 30 March 1984; accepted 4 December 1984)

The diocotron instability of an electron layer in which the electron Larmor radius is of the order of the layer thickness is studied. Remarkably, exact analytical solutions are obtainable in a nontrivial special case. These results allow an examination of the effects of finite Larmor radius for arbitrary ratios of Larmor radius to wavelength and of Larmor radius to layer thickness. In addition, an energy principle which yields a necessary and sufficient condition for instability for general distribution functions is derived.

I. INTRODUCTION

The physics of unneutralized, single species plasmas is of great basic interest, as well as being inherently related to a number of applications. These applications include collective electromagnetic wave generators (e.g., gyrotrons and free-electron lasers), particle accelerators (e.g., the modified betatron), diode devices, etc. In all of these situations stability of the plasma is a key consideration. Perhaps the most basic instability of an unneutralized plasma is the diocotron instability.¹ The mechanism driving this instability is the shear in the $E \times B$ velocity resulting from spatial dependence of the self-electric field E_0 created by the equilibrium charge density.

In this paper we consider the diocotron instability of an electron layer in which the typical electron is allowed to have a Larmor radius of the order of the layer width. The results of our analysis are as follows:

(1) An integral equation eigenvalue problem for the Fourier transform of the electrostatic potential is formulated (Sec. III).

(2) An exact analytical solution to the full problem is given for a special case which, however, is general enough to encompass the full range of ratios of Larmor radius to layer thickness and of Larmor radius to wavelength (Sec. IV). We

believe that the results obtained for this special case are representative of what happens in general.

(3) Using the results of the analytical solution we find the following:

(a) Finite Larmor radius does not stabilize a beam wherein the guiding centers are localized (i.e., $\Delta = 0$, where Δ is the half-thickness of the guiding center spread), and instability persists at all wavelengths, although the growth rates are reduced (cf. Figs. 1 and 2).

(b) Beams of fixed thickness $\delta = 2(\Delta + \rho)$ (where ρ is the Larmor radius) are destabilized by increasing the relative fraction $2\rho/\delta$ of beam thickness due to gyroradius (cf. Figs. 1 and 2).

(c) For a beam of fixed guiding center spread Δ , increasing ρ is stabilizing, in that the growth rates are reduced and the range of unstable wavenumber becomes smaller (cf. Fig. 3).

(4) A necessary and sufficient condition for instability in the form of an energy principle is derived for the case of a general symmetric distribution of guiding centers that decreases monotonically away from the center of the layer (Sec. V).

(5) As in the case of zero Larmor radius, the diocotron instability occurs only if the component of the propagation direction along the magnetic field is less than a certain small critical value (Sec. VI).

Finally we note that the techniques and results of this study may be useful in the context of other problems with

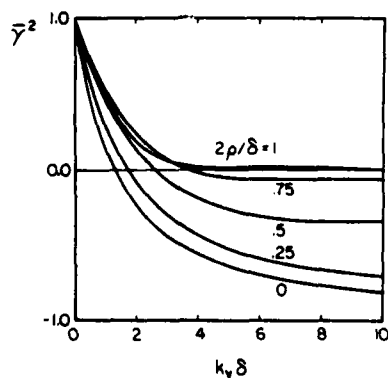


FIG. 1. The $k_y \delta$ dependence of the normalized growth rate $\bar{\gamma}^2$. Each curve is parameterized by $2\rho/\delta$.

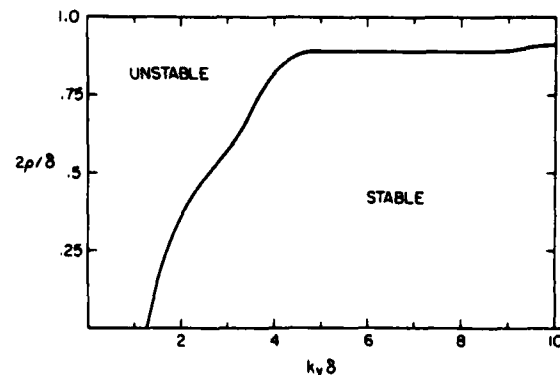


FIG. 2. Stability diagram in the $(k_y \delta, 2\rho/\delta)$ plane.

^{a)} Also at Departments of Electrical Engineering and of Physics.

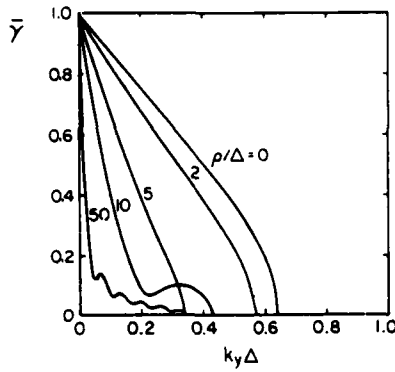


FIG. 3. The $k_y \Delta$ dependence of \bar{v} . Each curve is parameterized by ρ/Δ .

large self-electric fields, such as resistive wall and ion resonance instabilities² of azimuthal mode number $m > 2$.

II. EQUILIBRIUM

Consider a nonrelativistic, single species, low β (\equiv ratio of plasma pressure to magnetic field pressure) plasma immersed in a uniform magnetic field $\mathbf{B} = B_0 \hat{z}$, where \hat{z} is a unit vector in the z direction of a Cartesian coordinate system (x, y, z) . Suppose that the plasma is in an equilibrium which is uniform and unbounded in y and z , and localized in x with a particle density $n(x)$. By Gauss's law there is an accompanying electric field $\mathbf{E} = E_0(x) \hat{x}$,

$$\frac{dE_0(x)}{dx} = 4\pi q n(x); \quad (1)$$

$E_0(x)$ is odd about $x = 0$ if $n(x)$ is even.

The single particle equations of motion in this equilibrium are

$$\frac{d\mathbf{x}}{dt} = \mathbf{v}, \quad (2a)$$

$$\frac{d\mathbf{v}}{dt} = \frac{q}{m} E_0(x) \hat{x} + \Omega \mathbf{v} \times \hat{z}, \quad (2b)$$

where $\Omega \equiv qB_0/mc$ is the gyrofrequency. Assume that the density and, hence, the electric field are sufficiently small so that the dominant motion in x is the gyromotion

$$v_x(t) = v_1 \cos(\Omega t + \zeta) \\ x(t) = (v_1/\Omega) \sin(\Omega t + \zeta) + X.$$

Then, the velocity in the y direction,

$$v_y = v_{gy} + V(X, v_1),$$

is the sum of the velocities due to the gyromotion $v_{gy} = -v_1 \times \sin(\Omega t + \zeta)$ and the finite Larmor radius $\mathbf{E} \times \mathbf{B}$ drift. The latter quantity is just $-cE_0[x(t)]/B_0 \equiv V_y[x(t)]$ averaged over a gyro-orbit,

$$V(X, v_1) \equiv T^{-1} \int_0^T dt \int dy \int dx \\ \times V_y(x) p(x, y, t; X, \rho), \quad (3)$$

where the gyroperiod $T \equiv 2\pi/\Omega$ and

$$p(x, y, t; X, \rho) = \delta\{x - X - \rho \sin(\Omega t + \zeta)\} \\ \times \delta\{y - \rho \cos(\Omega t + \zeta)\}$$

is the probability that a particle with guiding center position X and Larmor radius $\rho \equiv v_1/\Omega$ is at (x, y) at time t . After integration over y and t , expression (3) becomes

$$V(X, v_1) = \int dx V_y(x) p(x; X, \rho), \quad (4)$$

where the probability density in x

$$p(x; X, \rho) = p(x - X; \rho) \\ = \begin{cases} \frac{1}{\pi} \frac{1}{[\rho^2 - (x - X)^2]^{1/2}}, & |x - X| < \rho, \\ 0, & \text{otherwise.} \end{cases} \quad (5)$$

The essential approximation used above is that, in a frame moving at the velocity $V(X, v_1)$, the equilibrium electric field, $E'_0(x)$, makes a perturbation on the lowest-order fast circular gyromotion which is small. In this frame the electric field is $E'_0 = E_0 + VB_0/c$, and the maximum E'_0 seen by a particle is of the order of $\rho dE_0/dx$. Thus we can estimate the size of the perturbation in velocity due to E'_0 to be of the order of

$$q\rho \frac{dE_0(x)}{dx} \frac{1}{m\Omega}.$$

Requiring that this be small compared to v_1 and making use of Gauss's law (1), we find that our drift approximation is valid provided that

$$\omega_p^2 \ll \Omega^2, \quad (6)$$

where $\omega_p = (4\pi n q^2/m)^{1/2}$ is the plasma frequency. This condition is also sufficient to neglect the modification of the equilibrium magnetic field caused by the diamagnetic currents of the gyrating electrons.

Direct integration of Eqs. (2) shows that the x coordinate of the guiding center position $X \equiv x + v_y/\Omega$ is an invariant of the motion. When the limitation (6) on the plasma density is satisfied, the invariant X reduces to $x + v_{gy}/\Omega$. The equilibrium particle distribution function $f_0(X, v_x, v_1)$ is a function of the invariants of the motion: the guiding center position X and the speeds v_x and v_1 , parallel and perpendicular to the magnetic field.

III. KINETIC THEORY—INTEGRAL EQUATION

The evolution of the particle distribution function $f(\mathbf{x}, \mathbf{v}, t)$ is described by the collisionless Boltzmann equation

$$\frac{\partial f}{\partial t} + \mathbf{v} \cdot \nabla f + \frac{q}{m} \left(\mathbf{E} + \frac{\mathbf{v}}{c} \times \mathbf{B} \right) \cdot \frac{\partial f}{\partial \mathbf{v}} = 0.$$

For electrostatic perturbations of the equilibrium, the perturbed distribution function \tilde{f} satisfies the equation

$$\frac{\partial \tilde{f}}{\partial t} + \mathbf{v} \cdot \nabla \tilde{f} + \left(\frac{q}{m} E_0(x) \hat{x} + \Omega \mathbf{v} \times \hat{z} \right) \cdot \frac{\partial \tilde{f}}{\partial \mathbf{v}} \\ = - \frac{q}{m} \tilde{\mathbf{E}} \cdot \frac{\partial f_0}{\partial \mathbf{v}}, \quad (7)$$

where $\tilde{\mathbf{E}} = -\nabla \tilde{\phi}$. Equation (7) can be solved in the usual manner by means of the method of characteristics. In terms of the equations of motion for the unperturbed orbit,

$$\frac{d\mathbf{x}'}{dt} = \mathbf{v}', \quad (8a)$$

$$\frac{d\mathbf{v}'}{dt} = \frac{q}{m} E_0(x') \hat{x} + \Omega \mathbf{v}' \times \hat{z}, \quad (8b)$$

with the initial conditions $x'(t' = t) = x$ and $v'(t' = t) = v$, the solution of Eq. (7) is

$$\tilde{f}(x, v, t) = \frac{q}{m} \int_{-\infty}^t dt' \nabla \cdot \tilde{\phi}(x', t') \cdot \frac{\partial}{\partial v'} f_0(X', v'_z, v'_1). \quad (9)$$

In this section, as well as Secs. IV and V, we shall take the wavenumber parallel to B to be zero, $k_z = 0$. The case $k_z \neq 0$ will be considered in Sec. VI. For perturbations of the form $\tilde{f}(x, v, t) = \tilde{f}(x, v) \exp[i(k_y y - \omega t)]$, Eq. (9) becomes

$$\tilde{f}(x, v) = \frac{q}{m} \int_{-\infty}^t dt' \left[\left(\hat{x} \frac{\partial}{\partial x'} + ik_y \hat{y} \right) \tilde{\phi}(x') \cdot \frac{\partial}{\partial v'} f_0(X', v'_z, v'_1) \right] \times \exp\{i[k_y(y' - y) - \omega(t' - t)]\}. \quad (10)$$

The Fourier transform in x of Eq. (10) is

$$\tilde{f}(k, v) = \frac{q}{m} \int_{-\infty}^t dt' \int_{-\infty}^{\infty} \frac{dk'}{2\pi} \int_{-\infty}^{\infty} dx \times i(k' \hat{x} + k_y \hat{y}) \tilde{\phi}(k') \cdot \frac{\partial}{\partial v'} f_0(X', v'_z, v'_1) \times \exp\{i[k'x' - kx + k_y(y' - y) - \omega(t' - t)]\}, \quad (11)$$

where k is the transform variable. It is useful to transform the integral over x in Eq. (11) into an integral over the guiding center constant of the motion X ; the result of this transformation is

$$\tilde{f}(k, v) = \frac{q}{m} \int_{-\infty}^t dt' \int_{-\infty}^{\infty} \frac{dk'}{2\pi} \int_{-\infty}^{\infty} dX \tilde{\phi}(k') \times i(k' \hat{x} + k_y \hat{y}) \cdot \frac{\partial}{\partial v'} f_0(X, v_z, v_1) \times \exp\{i[(k' - k)X + \Omega^{-1}[k v_{\parallel}(t' = t) - k' v_{\parallel}(t')] + k_y(y' - y) - \omega(t' - t)]\}. \quad (12)$$

The unperturbed particle orbits are obtained from the equations of motion (8). As discussed in Sec. II, with the density limitation (6) the particle orbit consists of the gyro-motion together with a mean $E \times B$ drift motion

$$y' - y = (v_1/\Omega) \{ \cos[\Omega(t' - t) + \zeta] - \cos \zeta \} + V(x, v_1)(t' - t), \quad (13a)$$

$$v_{\parallel}(t') = -v_1 \sin[\Omega(t' - t) + \zeta], \quad (13b)$$

where ζ is the gyroangle and the mean drift $V(X, v_1)$ is defined in Eq. (4). It is useful to transform to polar coordinates in wavenumber space,

$$k = k_1 \cos \theta, \quad k_y = k_1 \sin \theta,$$

and

$$k' = k'_1 \cos \theta', \quad k_y = k'_1 \sin \theta'.$$

Then, inserting the orbit (13) into Eq. (12) and using the Bessel function identity

$$\exp(iz \sin \psi) = \sum_{n=-\infty}^{\infty} J_n(z) \exp(in\psi),$$

we find that the perturbed distribution function \tilde{f} is

$$\tilde{f}(k, v) = \frac{q}{m} \int_{-\infty}^t dt' \int_{-\infty}^{\infty} dX \int_{-\infty}^{\infty} \frac{dk'}{2\pi} \tilde{\phi}(k') \times i \left(k'_1 \cos[\Omega(t' - t) + \zeta - \theta'] \frac{\partial}{\partial v_1} + \frac{k_y}{\Omega} \frac{\partial}{\partial X} \right) \times f_0(X, v_z, v_1) \exp\{i(k' - k)X - [\omega - k_y V(X, v_1)](t' - t)\} \times \sum_{n=-\infty}^{\infty} \sum_{m=-\infty}^{\infty} J_n \left(\frac{k'_1 v_1}{\Omega} \right) J_m \left(\frac{k_1 v_1}{\Omega} \right) \times \exp\{i[n[\Omega(t' - t) + \zeta + \theta'] + m(\zeta + \theta + \pi)]\}, \quad (14)$$

where $k_1 = (k^2 + k_y^2)^{1/2}$ and $k'_1 = (k'^2 + k_y^2)^{1/2}$.

The perturbed density $\tilde{n}(k)$ is defined in terms of $\tilde{f}(k, v)$ by

$$\tilde{n}(k) = \int_{-\infty}^{\infty} dv_{\parallel} \int_0^{\infty} v_1 dv_1 \int_0^{2\pi} d\zeta \tilde{f}(k, v),$$

and the potential $\tilde{\phi}(k)$ is self-consistently determined through Poisson's equation

$$k_1^2 \tilde{\phi}(k) = 4\pi q \tilde{n}(k).$$

Integrating \tilde{f} in Eq. (14) over the gyroangle ζ and keeping only the term of lowest order in $|\omega - k_y V|/\Omega < 1$, we find that the self-consistent integral equation for $\tilde{\phi}(k)$ is

$$k_1^2 \tilde{\phi}(k) = - \frac{4\pi k_y q c}{B_0} \int_{-\infty}^{\infty} dk' \tilde{\phi}(k') \times \int_0^{\infty} v_1 dv_1 J_0 \left(\frac{k_1 v_1}{\Omega} \right) J_0 \left(\frac{k'_1 v_1}{\Omega} \right) \times \int_{-\infty}^{\infty} dX \frac{\exp[i(k' - k)X]}{\omega - k_y V(X, v_1)} \frac{\partial}{\partial X} f_0(X, v_1). \quad (15)$$

Previous work has dealt only with the laminar, zero Larmor radius diocotron instability. To recover this limit, set $f_0(X, v_1) = \psi(X) \delta(v_1)/(2\pi v_1)$ in Eq. (15), where $\psi(X)$ is the particle density. After integration over v_1 , the inverse Fourier transform of Eq. (15) becomes the known differential equation eigenvalue problem for the zero Larmor radius diocotron instability,¹

$$\frac{d^2 \tilde{\phi}(x)}{dx^2} - k_y^2 \tilde{\phi}(x) = \frac{4\pi k_y q c}{B_0} \frac{\tilde{\phi}(x)}{\omega - k_y V_y(x)} \frac{d\psi(x)}{dx}. \quad (16)$$

IV. DIOCOTRON STABILITY—A SOLUBLE MODEL

Consider a plasma in which all the particles have the same v_1 and the guiding centers of the particles are uniformly distributed in a slab $|X| < \Delta$. The equilibrium distribution function f_0 can be written in the form

$$f_0(X, v_1) = \psi(X) \chi(v_1), \quad (17a)$$

where

$$\psi(X) = (N/2\Delta) [H(X + \Delta) - H(X - \Delta)], \quad (17b)$$

$$\chi(v_1) = \delta(v_1 - v_{10})/2\pi v_{10}, \quad (17c)$$

and $H(X)$ is the Heaviside step function,

$$H(X) = \begin{cases} 1, & X > 0, \\ 0, & X < 0. \end{cases}$$

Insertion of Eqs. (17) into the integral equation (15) for $\bar{\phi}(k)$ and subsequent integration over the guiding center position X and the velocity v_1 yields the integral eigenmode equation

$$k_1^2 \bar{\phi}(k) = -\frac{k_y V_0}{\Delta} \int_{-\infty}^{\infty} \frac{dk'}{2\pi} \bar{\phi}(k') J_0(k_1 \rho) J_0(k_1 \rho) \times \left(\frac{\exp[-i(k' - k)\Delta]}{\omega + k_y V(\Delta, \rho)} - \frac{\exp[i(k' - k)\Delta]}{\omega - k_y V(\Delta, \rho)} \right), \quad (18)$$

where $V_0 \equiv 2\pi N q c / B_0$, the Larmor radius $\rho = v_{10} / \Omega$, and we have noted that the $E \times B$ drift $V(-\Delta, \rho) = -V(\Delta, \rho)$ since $E_x(x)$ is odd about $x = 0$. The right-hand side of this integral equation is the sum of two terms, each of which has a kernel $K(k, k')$ which is separable: $K(k, k') = K_1(k) K_2(k')$. As a consequence, Eq. (18) can be written in the form

$$\bar{\phi}(k) = [J_0(k_1 \rho) / k_1^2] (\alpha e^{ik\Delta} + \beta e^{-ik\Delta}), \quad (19)$$

where

$$\alpha = -\frac{(k_y V_0 / \Delta)}{\omega + k_y V(\Delta, \rho)} \int_{-\infty}^{\infty} \frac{dk'}{2\pi} \bar{\phi}(k') J_0(k_1 \rho) e^{-ik'\Delta}$$

and

$$\beta = \frac{(k_y V_0 / \Delta)}{\omega - k_y V(\Delta, \rho)} \int_{-\infty}^{\infty} \frac{dk'}{2\pi} \bar{\phi}(k') J_0(k_1 \rho) e^{ik'\Delta}$$

are numbers which are independent of k . Substitution of expression (19) for $\bar{\phi}(k)$ into Eq. (18) yields a pair of linear homogeneous equations for α and β :

$$\alpha = -\frac{(k_y V_0 / \Delta)}{\omega + k_y V(\Delta, \rho)} \times \int_{-\infty}^{\infty} \frac{dk'}{2\pi} \frac{J_0^2(k_1 \rho)}{k_1'^2} (\alpha + \beta e^{-2ik'\Delta}), \quad (20a)$$

$$\beta = \frac{(k_y V_0 / \Delta)}{\omega - k_y V(\Delta, \rho)} \times \int_{-\infty}^{\infty} \frac{dk'}{2\pi} \frac{J_0^2(k_1 \rho)}{k_1'^2} (\alpha e^{2ik'\Delta} + \beta). \quad (20b)$$

The numbers α and β in Eqs. (20) can be nonzero only if the determinant of the system (20) is zero. Thus the frequency $\omega = i\gamma$ satisfies the dispersion relation

$$\gamma^2 = -k_y^2 \left[\left(V(\Delta, \rho) + V_0 \int_{-\infty}^{\infty} \frac{dk}{2\pi\Delta} \frac{J_0^2(k_1 \rho)}{k_1^2} \right)^2 - V_0^2 \left| \int_{-\infty}^{\infty} \frac{dk}{2\pi\Delta} \frac{J_0^2(k_1 \rho)}{k_1^2} e^{-i2k\Delta} \right|^2 \right]. \quad (21)$$

To proceed further with (21) we need to evaluate

$V(\Delta, \rho)$. The mean $E \times B$ drift velocity $V(X, \rho)$ is given in Eq. (4),

$$V(X, \rho) = -\frac{c}{B_0} \int dx E_x(x) p(x - X; \rho), \quad (22)$$

where the probability density p is given in Eq. (5). An expression for V in terms of the guiding center distribution function $\psi(X)$ is obtained as follows. Let us take the derivative of Eq. (22) with respect to X and then integrate by parts; the result is

$$\frac{dV(X, \rho)}{dX} = -\frac{c}{B_0} \int dx p(x - X; \rho) \frac{d}{dx} E_x(x).$$

Using Gauss's law (1) and noting that the particle density $n(x)$ is related to the guiding center distribution $\psi(X)$ by the equation

$$n(x) = \int dX' \psi(X') p(x - X'; \rho),$$

we find that

$$\frac{dV(X, \rho)}{dX} = -\frac{4\pi q c}{B_0} \int dx p(x - X; \rho) \times \int dX' p(x - X'; \rho) \psi(X'). \quad (23)$$

By the convolution theorem, the Fourier transform of Eq. (23) is

$$ikV(k, \rho) = -(4\pi q c / B_0) p(k; \rho) p(-k; \rho) \psi(k), \quad (24)$$

where the Fourier transform of the probability $p(x; \rho)$ given in Eq. (5) is $p(k; \rho) = J_0(k\rho)$. For the uniform guiding center distribution (17b), the transform $\psi(k) = N \sin(k\Delta) / (k\Delta)$ and Eq. (24) becomes

$$V(k, \rho) = 2iV_0 J_0^2(k\rho) \sin(k\Delta) / k^2 \Delta. \quad (25)$$

The inverse Fourier transform of (25) yields the final result

$$V(X, \rho) = -2V_0 \int \frac{dk}{2\pi\Delta} J_0^2(k\rho) \frac{\sin(k\Delta)}{k} \frac{\sin(kX)}{k}. \quad (26)$$

With expression (26) for V , the dispersion relation (21) for the growth rate γ can be written in the form

$$\frac{\bar{\gamma}^2}{4} = \left(\int_{-\infty}^{\infty} \frac{dk}{2\pi} \frac{J_0^2(k_1 \rho)}{k_1^2} \right) \times \left[\int_{-\infty}^{\infty} \frac{dk}{2\pi} \left(J_0^2(k\rho) - \frac{k^2}{k_1^2} J_0^2(k_1 \rho) \right) \frac{\sin^2(k\Delta)}{(k\Delta)^2} \right] + \left(\int_{-\infty}^{\infty} \frac{dk}{2\pi} \frac{J_0^2(k_1 \rho)}{k_1^2} \frac{\sin^2(k\Delta)}{\Delta} \right)^2 - \left(\int_{-\infty}^{\infty} \frac{dk}{2\pi} \frac{J_0^2(k\rho)}{k^2} \frac{\sin^2(k\Delta)}{\Delta} \right)^2, \quad (27)$$

where $\bar{\gamma} \equiv \gamma / k_y V_0$ is the normalized growth rate. When $\rho = 0$ we recover the guiding center result

$$\bar{\gamma}^2 = [e^{-2k\delta} - 1 + 2k\delta - (k\delta)^2] / (k\delta)^2,$$

where $\delta \equiv 2\Delta$ is the plasma width in x . A guiding center plasma slab is unstable to long wavelength perturbations with $k, \delta < 1.28$.

For a sheet distribution of guiding centers ($\Delta = 0$), the dispersion relation (27) reduces to

$$\bar{\gamma}^2 = 4 \left(\int_{-\infty}^{\infty} \frac{dk}{2\pi} \frac{J_0^2(k_1 \rho)}{k_1^2} \right) \times \left[\int_{-\infty}^{\infty} \frac{dk}{2\pi} \left(J_0^2(k\rho) - \frac{k^2}{k_1^2} J_0^2(k_1 \rho) \right) \right]. \quad (28)$$

Transforming the integration variable in $-\int dk (k^2/k_1^2) J_0^2(k_1 \rho)$ from k to k_1 , we can rewrite expression (28) for $\bar{\gamma}^2$ as

$$\bar{\gamma}^2 = 16 \left(\int_0^{\infty} \frac{dk}{2\pi} \frac{J_0^2(k_1 \rho)}{k_1^2} \right) \left[\int_0^{k_1} \frac{dk}{2\pi} J_0^2(k\rho) + \int_{k_1}^{\infty} \frac{dk}{2\pi} J_0^2(k\rho) \left(1 - \frac{(k^2 - k_1^2)^{1/2}}{k} \right) \right],$$

which is manifestly positive. Hence a sheet distribution of particle guiding centers is always unstable to perturbations of any wavelength no matter how large the Larmor radii of the particles are.

In general, the width δ of the plasma slab is $\delta = 2(\Delta + \rho)$. Figure 1 is a plot of the k, δ dependence of $\bar{\gamma}^2$. Each curve is parameterized by the quantity $2\rho/\delta$ which measures the fraction of the plasma width which is due to the particle Larmor radius. A diagram of the region of stability in the $(k, \delta, 2\rho/\delta)$ plane is shown in Fig. 2. The range of unstable wavenumbers increases as the Larmor radius becomes a larger fraction of the total plasma width.

For a plasma with fixed guiding center width Δ , an increase in the particle Larmor radius is stabilizing. Figure 3 is a plot of the k, Δ dependence of $\bar{\gamma}$ for several values of the ratio ρ/Δ . Typically, the growth rate is reduced as ρ increases.

V. ENERGY PRINCIPLE

A. Sufficient condition for instability

Multiplying Eq. (15) through by the conjugate of $\bar{\phi}(k)$, and integrating over all k , we have the quadratic form,

$$\int k_1^2 |\bar{\phi}(k)|^2 dk = -\gamma_0 \int v_1 dv_1 \times \int dX \frac{\partial f_0}{\partial X} \frac{I(X, v_1, k_y)}{\omega - k_y V(X, v_1)}, \quad (29)$$

where $I(X, v_1, k_y) = \left| \int dk \bar{\phi}(k) J_0(k_1 v_1 / \Omega) \exp(ikX) \right|^2$ and $\gamma_0 = 4\pi k_y q c / B_0$. In all of what follows we shall take $f_0(X, v_1)$ to be symmetric and monotonically decreasing away from $X = 0$: $f_0(X, v_1) = f_0(-X, v_1)$, and $\partial f_0 / \partial X \geq 0$ for $X \leq 0$. We now derive a condition for Eq. (15) to have an unstable solution for which the corresponding eigenfunction $\bar{\phi}(k)$ is real. Since unstable solutions may also conceivably exist for which $\bar{\phi}(k)$ is not purely real, the condition so derived will only be sufficient for instability. Subsequently we shall prove that it is also necessary.

Assume that there exists an unstable solution with $\bar{\phi}$ real. Because $\bar{\phi}(k)$ is real, $I(X, v_1, k)$ is seen to be even in X . Since $\partial f_0 / \partial X$ is odd, we may replace $(\omega - k_y V)^{-1}$ in (29) by its odd part in X . Then, taking the imaginary part of the quadratic form, Eq. (29), we obtain

$$\omega_r \int \int \frac{I k_y V \partial f_0 / \partial X}{[(\omega_r - k_y V)^2 + \gamma^2][(\omega_r + k_y V)^2 + \gamma^2]} \times 2\pi v_1 dv_1 dX = 0,$$

where $\omega_r = \text{Re}(\omega)$, $\gamma = \text{Im}(\omega) > 0$, and we have utilized the odd symmetry of $V[V(X, v_1) = -V(-X, v_1)]$. Since $V \partial f_0 / \partial X > 0$ for $X \neq 0$ (assuming $q > 0$), and since $I > 0$, we see that the integral above is always positive. Thus $\omega_r = 0$, and we conclude that if $\bar{\phi}(k)$ is real, then the instability is purely growing.

With this information we can rewrite the quadratic form Eq. (29) as

$$1/\gamma_0 = \Lambda[\bar{\phi}; \gamma], \quad (30)$$

where the functional $\Lambda[\bar{\phi}; \gamma]$ is given by

$$\Lambda[\bar{\phi}; \gamma] = \frac{\int \int v_1 dv_1 dX [k_y V \partial f_0 / \partial X / (\gamma^2 + k_y^2 V^2)] I}{\int k_1^2 \bar{\phi}^2 dk}, \quad (31)$$

and the function $\bar{\phi}$ is real. It is easy to verify that the equation, $1/\gamma_0 = \Lambda[\bar{\phi}; \gamma]$, is variational (that is, setting $\delta\gamma_0 / \delta\bar{\phi} = 0$ yields the original integral equation).

We now wish to show that $\Lambda[\bar{\phi}; \gamma]$ is bounded from above. To do this we make use of Schwartz's inequality,

$$(\eta, \zeta)^2 \leq (\eta, \eta)(\zeta, \zeta),$$

applied to the quantity I ,

$$I = \left| \int dk [k_1 \bar{\phi}(k)] \left(\frac{J_0(k_1 v_1 / \Omega)}{k_1} e^{ikX} \right) \right|^2 < \left(\int dk k_1^2 \bar{\phi}^2 \right) \left(\int dk \frac{J_0^2(k_1 v_1 / \Omega)}{k_1^2} \right).$$

Thus

$$0 < \Lambda[\bar{\phi}; \gamma] < \Lambda_{\max}(\gamma), \quad (32)$$

where

$$\Lambda_{\max}(\gamma) = \int \int \int 2\pi v_1 dv_1 dX dk \times \frac{k_y V \partial f_0 / \partial X}{\gamma^2 + k_y^2 V^2} \frac{J_0^2(k_1 v_1 / \Omega)}{k_1^2}. \quad (33)$$

Say we find a trial function $\bar{\phi}_*$ and a trial growth rate γ_* , such that

$$\Lambda[\bar{\phi}_*; \gamma_*] > 1/\gamma_0,$$

then we claim that this is a sufficient condition for an instability with growth rate greater than γ_* . To see that this is so, we represent the situation schematically as in Fig. 4. Since $\Lambda[\bar{\phi}; \gamma]$ is bounded from above by $\Lambda_{\max}(\gamma_*)$, we see that $\Lambda[\bar{\phi}; \gamma_*]$ must have a maximum (as shown). From (31) we see that $\Lambda[\bar{\phi}; \gamma]$ is monotonically decreasing with γ and tends to zero as $\gamma \rightarrow \infty$. Thus as γ increases past γ_* , the "curve" $\Lambda[\bar{\phi}; \gamma]$ lowers until, eventually, at some value of γ (here denoted γ_{**}), the maximum of Λ is $1/\gamma_0$, occurring at $\bar{\phi} = \bar{\phi}_{**}$. Since (30) is variational, $\bar{\phi} = \bar{\phi}_{**}$, $\omega = i\gamma_{**}$ satisfies the original integral equation, Eq. (15), with a growth rate in excess of the original trial growth rate, $\gamma_{**} > \gamma_*$. In particular, a sufficient condition for instability is

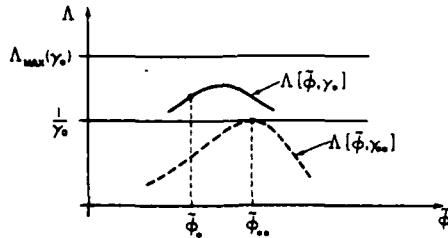


FIG. 4. Schematic illustration of the argument for sufficiency. Note that the horizontal axis is meant to represent an infinite dimensional function space [the space of all $\bar{\phi}(k)$].

$$\Lambda\{\bar{\phi}_*, 0\} = \frac{\int \int v_1 dv_1 dX (I/k, V) \partial f_0 / \partial v_1}{\int k_1^2 \bar{\phi}_*^2 dk} > \frac{1}{\gamma_0} \quad (34)$$

for some real trial function $\bar{\phi}_*$.

B. Necessity of (34) for instability

We now wish to demonstrate that (34) is also necessary for instability. That is, if there is no trial function which satisfies (34), then the plasma is stable. The technique for showing necessity is based on the Nyquist criterion and is similar to one used by Antonsen and Lee for a different problem.³ To utilize the Nyquist criterion, we introduce a dispersion relation $D(\omega, k_y) = 0$ for Eq. (15) as follows:

$$\begin{aligned} k_1^2 \left(\frac{1}{\gamma_0} - D(\omega, k_y) \right) \bar{\phi}(k) \\ = - \int dk' \bar{\phi}(k') \\ \times \int_0^\infty v_1 dv_1 J_0 \left(\frac{k_1 v_1}{\Omega} \right) J_0 \left(\frac{k'_1 v_1}{\Omega} \right) \\ \times \int_{-\infty}^\infty dX \frac{\exp[i(k' - k)X]}{\omega - k_y V(X, v_1)} \frac{\partial f_0}{\partial X} \end{aligned} \quad (35)$$

For given (ω, k_y) , we regard (35) as an eigenvalue problem and D as the eigenvalue. This defines $D(\omega, k_y)$. The solutions of $D(\omega, k_y) = 0$ represent solutions of (15). Again making (35) into a quadratic form by multiplying through by $\bar{\phi}^*(k)$ and integrating over all k , we obtain an equation of the form

$$D(\omega, k_y) = 1/\gamma_0 - \bar{\Lambda}(\omega, k_y), \quad (36)$$

where

$$\bar{\Lambda}(\omega, k_y) = - \frac{\int \int v_1 dv_1 dX [(\partial f_0 / \partial X) / (\omega - k_y V)] I}{\int k_1^2 |\bar{\phi}(k)|^2 dk}, \quad (37)$$

and we emphasize that the $\bar{\phi}$ appearing in (37) is the solution of the eigenvalue problem (35).

Now consider the Nyquist contour in the complex ω plane shown in Fig. 5(a) and follow the corresponding contour in the complex D plane. Using the Schwartz inequality, we see that (37) has no poles in the upper half ω plane. Thus the net counterclockwise encirclement of the origin of the D plane by the contour is the number of unstable solutions of the dispersion relation. To show that Eq. (34) is necessary for instability, we need to demonstrate that if there is no $\bar{\phi}$ which

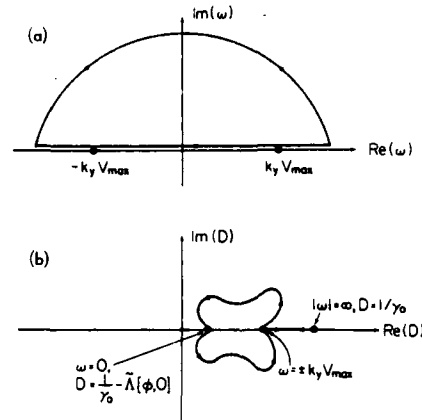


FIG. 5. Nyquist contour in (a) the complex ω plane and (b) the complex D plane.

satisfies (34), then there is no counterclockwise encirclement of the origin.

Now consider the part of the ω plane contour that is along the real ω axis. From (37), where $\text{Im}(\omega) = 0^+$,

$$\text{Im}(D) = \pi \frac{\int \int v_1 dv_1 dX I \delta(\omega_r - k_y V) \partial f_0 / \partial X}{\int k_1^2 |\bar{\phi}(k)|^2 dk} \quad (38)$$

For $x \rightarrow \pm \infty$, we have $E_0 \rightarrow \pm E_{max}$, where $E_{max} = 2\pi q \int_0^\infty 2\pi v_1 dv_1 dX$. Thus there are no particles with $|V| > V_{max} \equiv cE_{max}/B_0$. Furthermore, the resonant X value is positive for ω_r in (38) positive, and it is negative for ω_r negative. Thus (38) shows that

$$\text{Im}(D) = 0, \quad \text{for } |\omega_r| > k_y V_{max}, \quad (39a)$$

$$\text{Im}(D) > 0, \quad \text{for } 0 > \omega_r > -k_y V_{max}, \quad (39b)$$

$$\text{Im}(D) = 0, \quad \text{for } \omega_r = 0, \quad (39c)$$

$$\text{Im}(D) < 0, \quad \text{for } k_y V_{max} > \omega_r > 0, \quad (39d)$$

where we have utilized $\partial f_0 / \partial X \geq 0$ for $X \leq 0$, and $\partial f_0 / \partial X = 0$ at $X = 0$.

Now say we start our circuit in the ω plane at $\omega_r = +\infty$, $\text{Im}(\omega) = 0$. We then travel around the semicircle in the upper-half ω plane shown in Fig. 5(a). In the D plane Eq. (37) shows that this semicircle maps to the point $D = 1/\gamma_0$ [cf. Fig. 5(b)]. We then travel along the real ω axis from $\omega_r = -\infty$ to $\omega_r = -k_y V_{max}$. From (39a) the D plane contour remains on the real axis. Assume, in addition, that there are no roots of the dispersion relation for ω purely real and in the range $[-\infty, -k_y V_{max}]$ (this will be verified later). With this assumption the D contour corresponding to ω_r traveling from $-\infty$ to $-k_y V_{max}$ does not cross the origin of the D plane. As ω_r increases from $-k_y V_{max}$, the contour remains in $\text{Im}(D) > 0$ [cf. Fig. 5(a) and Eq. (39b)]. At $\omega_r = 0$, the contour crosses the real D axis. The situation, which is symmetric about the real D axis, is shown schematically in Fig. 5(b). It is seen that if $\bar{\Lambda}(\bar{\phi}, 0) < 1/\gamma_0$, then there is no unstable mode. Furthermore, when $\omega = 0$,

$$\begin{aligned} \int_{-\infty}^{+\infty} \frac{\exp[i(k' - k)X]}{\omega - k_y V(X, v_1)} \frac{\partial f_0}{\partial X} dX \\ = - \int_{-\infty}^{+\infty} \frac{\cos[(k' - k)X]}{k_y V} \frac{\partial f_0}{\partial X} dX \end{aligned}$$

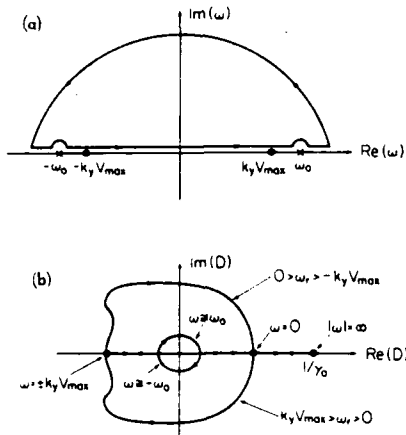


FIG. 6. Nyquist contour in (a) the complex ω plane and (b) the complex D plane when the dispersion function D has a zero on the real ω axis at $\omega = \omega_0$.

and the solution to (35) has a purely real eigenfunction. Thus, we see that $\Lambda[\bar{\phi}_*, 0] > 1/\gamma_0$, for some real $\bar{\phi}_*$, is necessary for instability. QED

It remains to verify that $D(\omega, k_y) = 0$ has no solutions on the real ω axis for ω , in $[-\infty, -k_y V_{\max}]$ and $[k_y V_{\max}, \infty]$. For illustrative purposes, assume that there is one such solution (similar considerations apply if there are any number), and denote this solution $\omega = \omega_0$. Figures 6(a) and 6(b) show the situation for this case corresponding to Figs. 5(a) and 5(b) for the case where the $\omega = \omega_0$ root does not exist. As seen from Fig. 6(b) there are two clockwise encirclements of $D = 0$, implying two poles of D in the upper half ω

$$(k_1^2 + k_2^2)\bar{\phi}(k) = -\frac{4\pi k_y q c}{B_0} \int_{-\infty}^{+\infty} dk' \bar{\phi}(k') \int_0^{+\infty} v_1 dv_1 J_0\left(\frac{k_1 v_1}{\Omega}\right) J_0\left(\frac{k_1' v_1}{\Omega}\right) \int_{-\infty}^{+\infty} dv_2 \int_{-\infty}^{+\infty} dX \frac{[\partial f_0(X, v_1, v_2)/\partial X] + (k_z/k_y)\Omega [\partial f_0(X, v_1, v_2)/\partial v_z]}{\omega - k_y V(X, v_1) - k_z v_2} e^{ik' \cdot -k \cdot X} \quad (42)$$

To solve (42) we take the case of a beam with all gyrocenters located at $X = 0$, neglect thermal spread along B , and again assume a delta function in v_1 ,

$$f_0(X, v_1, v_2) = N\delta(X)\delta(v_2)\delta(v_1 - v_{10})/(2\pi v_{10}).$$

Performing the v_2 and X integrations by parts and using our assumed form of f_0 , we find that Eq. (42) yields

$$(k_1^2 + k_2^2)\bar{\phi}(k) = \frac{4\pi k_y q c N}{B_0} \int_{-\infty}^{+\infty} \frac{dk'}{2\pi} \bar{\phi}(k') J_0(k_1 \rho) J_0(k_1' \rho) \left[\frac{1}{\omega^2} \left(k_y V' + \frac{k_z^2}{k_y} \Omega \right) + \frac{i(k' - k)}{\omega} \right], \quad (43)$$

where $V' \equiv dV(X, v_{10})/dX$ evaluated at $X = 0$, and $\rho = v_{10}/\Omega$. Examining the k dependence of the right side of (43) we see that $\bar{\phi}(k)$ has the form

$$\bar{\phi}(k) = (k_1^2 + k_2^2)^{-1} J_0(k_1 \rho) [\hat{\alpha} + ik\hat{\beta}].$$

Substituting this expression for $\bar{\phi}$ back into (43) and proceeding as in Sec. III we obtain the dispersion relation

$$\bar{\gamma}^2 = 4 \left(\int_{-\infty}^{+\infty} \frac{dk}{2\pi} \frac{J_0^2(k_1 \rho)}{k_1^2 + k_2^2} \right) \left[\left(\int_{-\infty}^{+\infty} \frac{dk}{2\pi} \times \left(J_0^2(k\rho) - \frac{k^2}{k_1^2 + k_2^2} J_0^2(k_1 \rho) \right) - \frac{1}{2} \frac{k_z^2}{k_y^2} \frac{\Omega}{V_0} \right) \right]. \quad (44)$$

plane. Since there are no such poles, there can be no $\omega = \omega_0$ root.

Finally, we note that our proof of necessity implies that $\Lambda_{\max}(0) < 1/\gamma_0$ is a sufficient condition for stability.

VI. FINITE WAVENUMBER PARALLEL TO B

In Secs. III–V we have taken $k_z = 0$. We now return to a discussion of the effect of finite k_z . First we recall the known zero Larmor radius dispersion relation for a sheet beam with finite k_z (cf. Pierce¹),

$$\bar{\gamma}^2 = 1 - \frac{k_z^2}{k_y^2} \frac{\Omega}{(k_y^2 + k_z^2)^{1/2} V_0}, \quad (40)$$

where $\bar{\gamma}$ is the growth rate normalized to $k_y V_0$ and $V_0 \equiv 2\pi N q c / B_0$ (cf. Sec. IV). From (40) we see that the mode is purely growing for waves with

$$\left(\frac{k_z}{k_y} \right)^2 < \frac{(k_y^2 + k_z^2)^{1/2} V_0}{\Omega}. \quad (41)$$

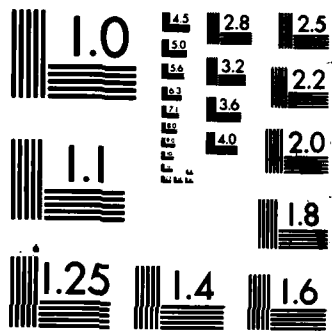
Since our analysis is in the guiding center limit $\Omega \gg \gamma$, the right-hand side of (41) is small, indicating that instability occurs only for nearly perpendicular propagation. When (41) is violated, (40) indicates that the modes become purely oscillatory. We wish to see what effect finite Larmor radius has on this result. We find that the situation is qualitatively unchanged, although there are, of course, quantitative changes.

Inclusion of finite k_z in the integration over unperturbed particle orbits is a straightforward extension of the treatment of Sec. III. The integral equation eigenvalue problem Eq. (15) then generalizes to

Note that (28) is recovered for $k_z \rightarrow 0$, while (40) is recovered for $\rho \rightarrow 0$. As in (41), instability will occur only if k_z^2 is sufficiently small compared to k_y^2 . The condition for instability, generalizing (41) to finite gyroradius is

$$F(s) = \frac{1}{\pi} \frac{k_y}{(k_y^2 + k_z^2)^{1/2}} \int_{-\infty}^{+\infty} du \left(J_0^2(us) - \frac{u^2}{u^2 + 1 + (k_z/k_y)^2} \times J_0^2[s(u^2 + 1)^{1/2}] \right) > \frac{k_z^2}{k_y^2} \frac{\Omega}{(k_y^2 + k_z^2)^{1/2} V_0}, \quad (45)$$

where $s \equiv |k_y \rho|$ and $F(0) = 1$ in agreement with (41). Here $F(s)$ can be evaluated asymptotically for $s \gg 1$ and is found to decrease slowly with increasing s , thus narrowing the unstable range of propagation angles.



MICROCOPY RESOLUTION TEST CHART
NATIONAL BUREAU OF STANDARDS-1963-A

$$F(s) \sim \frac{2}{\pi^2} \frac{k_y}{(k_y^2 + k_z^2)^{1/2}} \frac{\ln s}{s}, \quad s \gg 1.$$

Thus we see from (45) that, as in the zero ρ case, the diocotron mode is stabilized by a small parallel component of the wavenumber.

The dispersion relation for a relativistic beam in which all the particles have the same parallel velocity v_z close to the speed of light can be easily obtained from the nonrelativistic result assuming $v_z^2/c^2 \ll 1$. In the rest frame of the beam, let ω be the eigenfrequency determined by solution of Eq. (42). Then, the frequency ω' and wavenumber k'_z in the laboratory frame are related to ω and k_z by the Lorentz transformations

$$\begin{aligned} \omega' &= \gamma(\omega + v_z k_z), & \omega &= \gamma(\omega' - v_z k'_z), \\ k'_z &= \gamma[k_z + (v_z/c^2)\omega], & k_z &= \gamma[k'_z - (v_z/c^2)\omega'], \end{aligned}$$

where the relativistic factor $\gamma \equiv [1 - (v_z/c)^2]^{-1/2}$. For example, say we have a dispersion relation calculated in the beam frame, $D(\omega, k_z) = 0$. Then the dispersion relation in the laboratory frame, $D'(\omega', k'_z) = 0$, is simply obtained via the Lorentz transformations,

$$D'(\omega', k'_z) = D[\gamma\omega' - \gamma k'_z v_z, \gamma k'_z - \gamma v_z^2/c^2 \omega'].$$

ACKNOWLEDGMENTS

We are grateful to Tom Antonsen for very informative discussions and useful comments. The work of E. Ott was done as a consultant to Science Applications, Inc., of McLean, Virginia.

This work was supported by the Office of Naval Research.

- ¹O. Buneman, *J. Electron. Control* **3**, 507 (1957); R. L. Kyhl and H. F. Webster, *IRE Trans. Electron Devices* ED-3, 172 (1956); J. R. Pierce, *ibid.* ED-3, 183 (1956); W. Knauer, *J. Appl. Phys.* **37**, 602 (1966); O. Buneman, R. H. Levy, and L. M. Linson, *ibid.* **37**, 3203 (1966); T. M. Antonsen and E. Ott, *Phys. Fluids* **18**, 1197 (1975); E. Ott and J.-M. Wersinger, *ibid.* **23**, 324 (1980); R. C. Davidson, *Theory of Nonneutral Plasmas* (Benjamin, Reading, MA, 1974); A. Nocentini, H. L. Berk, and R. N. Sudan, *J. Plasma Phys.* **2**, 311 (1968); R. C. Davidson, H. Uhm, and S. M. Mahajan, *Phys. Fluids* **19**, 1608 (1976); R. H. Levy, *Phys. Fluids* **8**, 1288 (1965); Y. Carmel and J. A. Nation, *Phys. Rev. Lett.* **31**, 286 (1973); C. Kapetanakis, D. Hammer, C. Striffler, and R. C. Davidson *ibid.* **30**, 1303 (1973).
- ²C. K. Birdsall and J. R. Whinnery, *J. Appl. Phys.* **24**, 314 (1953); C. K. Birdsall, G. R. Brewer, and A. V. Haeff, *Proc. IRE* **41**, 865 (1953); R. J. Briggs, J. D. Daugherty, and R. H. Levy, *Phys. Fluids* **13**, 421 (1970); P. Sprangle and J. L. Vomvoridis, *Naval Research Laboratory Report No. 4688*, 1982; R. C. Davidson and H. Uhm, *Phys. Fluids* **25**, 2089 (1982); R. G. Kleva, E. Ott, and P. Sprangle, *ibid.* **26**, 2689 (1983); W. M. Manheimer, *Part. Accel.* **13**, 209 (1983).
- ³T. M. Antonsen, Jr., and Y. C. Lee, *Phys. Fluids* **25**, 132 (1982).

APPENDIX M

ONE DIMENSIONAL MODELS FOR
RELATIVISTIC ELECTRON BEAM DIODE DESIGN

N-1

One Dimensional Models for Relativistic Electron Beam Diode Design

JOHN M. FINN

*Laboratory for Fusion Energy Studies
University of Maryland
College Park, Maryland*

ARNE FLIFLET AND WALLACE MANHEIMER

*Code 4740
Naval Research Laboratory
Washington, D.C. 20375-5000*

Abstract

Several one dimensional models are derived which approximate the relativistic flow of high current beams in diodes. Using these models as a starting point, a diode for a 1 GW beam for a 35 GHz gyrotron oscillator is easily designed.

1. Introduction

The design of a diode, or electron gun, for a microwave tube is a complicated two dimensional spatial and three dimensional velocity space problem. It involves a calculation of nonlinear particle orbits and self consistent electric and magnetic fields. In virtually all diode design work, the basic tool is the electron trajectory (Herrmannsfeldt) code, which solves for the electron orbits and the self consistent electric and magnetic fields in an arbitrary two dimensional configuration. Since this problem is so complex and the parameter space so vast, a diode design using only this procedure can be very long and expensive. For this reasons, one dimensional approximations to the physics are extremely useful. This is particularly true for space charge limited diodes, which are used for intense pulsed electron beams. Since the electron trajectory code begins with vacuum fields as their first approximations, it is often difficult to converge on a space charge limited flow solution.

The basis of this paper, and many other works in this area, is that there are useful one dimensional approximations to the orbit in infinite media. Then the infinite media approximation is relaxed by taking only a spatially limited part of the infinite flow pattern, and using focusing electrodes to create the fields set up by the remainder of the beam which was excluded. (Harker; Dryden; Kirstein, Kino and Waters; Tsimiring, Manuilov and Fliflet et al.). The shapes of the focusing electrodes are determined by the particle orbit. Along the orbit which is an open curve, both the potential and its normal derivative are known. Laplace's equations must then be solved exterior to this orbit to determine the equipotentials (that is, the shape of the focusing electrodes). However, the solution, subject to this open surface boundary condition, is unstable. To determine the solution, a scheme based on conformal mapping is used. The orbit equation is rewritten as an equation valid in the complex plane. Then the potential is calculated by for real r and imaginary z at some fixed value of real z . This involves the solution of a wave equation, which has stable solutions for *Cauchy* boundary conditions on an open surface. Evaluating the solution at the imaginary part of $z=0$ gives the potential as a function of r at the fixed value of the real part of z chosen. Thus, a stable solution is built up by taking a two dimensional projection of a solution in three dimensions. The equipotentials are then appropriate places for the

location of focusing electrodes.

The only trouble with this method is that once the beam becomes relativistic, and/or self magnetic fields become important, as is the case with intense pulsed beams, there is no one dimensional model which describes the flow. This paper derives a variety of approximate one dimensional models for space charge limited flow in a diode. While no model is exact (the electron flow is inherently two dimensional), they provide important insight and allow for approximate synthesis of the electrodes. The actual electrodes can then be quickly perfected with the Herrmannsfeldt code.

Finally, we note other attempts at one dimensional models. A model similar to one of those in the next section, but with the magnetic field parallel to the cathode plane has been derived by Goldstein. Another approximate model, valid in planar, cylindrical or spherical geometry is the Brillouin model of Creedon. Here the self magnetic fields are assumed so strong that electrons flow on equipotential surfaces, so that the model does not describe the emission from an electrode. Another model (Ott et al) describes the electrostatic field in two dimensions, but the electron flow in one dimension. Finally we note an approximate two dimensional analytic model of focused electron flow in diodes (Goldstein et al).

Section II describes four one dimensional models for electron flow in diodes. The first two are planar, relativistic but either with or without self magnetic fields. The second two are spherical, with no self magnetic fields, and either non-relativistic or superrelativistic. We rely mostly on the planar models since they are valid over the full energy range. However there are still important geometric effects, and the second two models shed light on them. Principally it is shown in Section III that the space charge limited current is larger in realistic geometry than in the analogous planar configuration. Section IV reviews the electrode synthesis technique and derives electrodes for a relativistic beam in a planar configuration. Finally, Section V derives a final electrode configuration using the Herrmannsfeldt code. The goal is to achieve a high quality beam for use in a gyrotron oscillator at 35 GHz and with power in the hundred megawatt range. Accordingly, the diode has a magnetic field of 1.8 - 2.0 kG and produces a 600 kV, 2 kA beam with $\alpha \equiv v_{\perp}/v_{\parallel} = 0.2$. In the diode region and

subsequent drift space, the beam has virtually no variation in α . To achieve the higher values of α , the magnetic field must be compressed to about 25 kG. In doing so, some variation in α across the beam is induced, although the beam quality is more than sufficient for efficient oscillator operation.

Another important consideration is the use of focusing electrodes and emitting regions for high power operation. If the electro field is too high, everything will ultimately emit, including the focusing electrodes. The key is to keep the field sufficiently low and the emissivity of the emitter sufficiently high. For instance, it has been determined (Kirkpatrick et al., 1984) that with focusing electrodes of anodized aluminium and emitting surfaces of reactor/graphite, kilo amp current could be generated for 30 nsec and that the focusing electrodes do not emit for fields as high as 600 kV/cm.

II. One Dimensional Models

In this section we describe three separate one dimensional models which should be of use in the design of a wide class of diodes. These models are, respectively, a relativistic slab model, a conical nonrelativistic model, and a conical superrelativistic model. No fully relativistic one dimensional conical model was found. We have used the slab relativistic model to explore a large area of parameter space for interesting design candidates. This model is used in the electrode synthesis described in Section IV. The conical models were used to estimate geometric corrections to the slab designs, specifically the current required to obtain space charge limited flow.

A. Slab Relativistic Model

The slab diode is completely described by three constants of motion for every particle, namely energy and the conical momenta P_y and P_z . Here, the cathode is the plane $x = 0$ and the anode is at $x = L$. Here x corresponds length along the cathode face in the r, θ plane. The magnetic field B is in the $x - z$ plane, so y corresponds to the azimuthal angle ϕ in the more conventional cylindrically symmetric diode. For any particle which leaves the cathode $x = 0$, these constants of motion are

$$\Delta E = (\gamma - 1)mc^2 + q \Phi(x), \quad (1)$$

$$P_y = \gamma m v_y - \frac{qB_{z0}}{c} (x - x_0) + \frac{qB_{z0}}{c} A_y(x) \quad (2)$$

$$P_z = \gamma m v_z + \frac{qB_{r0}}{c} (y - y_0) + \frac{q}{c} A_z(x). \quad (3)$$

where y_0, z_0 give the initial position of the particle. Constants have been added so that these are zero on the cathode $x = 0$ if Φ, A_y, A_z are also zero there. Because of y, z symmetry only one orbit needs to be considered; without loss of generality it can have $y_0 = z_0 = 0$. From Eqs. (1)-(3) and the definition of γ we find

$$v_x(x, y, z) = c \left[1 - \frac{v_y^2 + v_z^2}{c^2} - \frac{1}{\gamma(x)^2} \right]^{1/2} \quad (4)$$

$$v_y(x, z) = \frac{\Omega_x z}{\gamma(x)} - \frac{q}{mc\gamma(x)} A_y(x), \quad (5)$$

$$v_z(x, y) = - \frac{\Omega_x y}{\gamma(x)} - \frac{q}{mc\gamma(x)} A_z(x), \quad (6)$$

where $\Omega_z = qB_z/mc$ and $\gamma(z) = 1 - q\Phi/mc^2$, from (1). Since v_z is chosen to be positive in (4), these equations will apply only up to the first turning point in z . This is exactly the condition that no orbits cross.

If a steady source of current j_0 is supplied at the cathode, an equilibrium state will be set up with $j_z = j_0$ (by $\nabla \cdot \mathbf{j} = 0$) with density

$$n = \frac{j_0}{qv_z}$$

Thus, Poisson's and Ampere's equations give, respectively,

$$\frac{d^2\Phi}{dx^2} = \frac{4\pi j_0}{v_z} \quad (7)$$

$$\frac{d^2A_z}{dx^2} = \frac{4\pi j_0 v_z}{v_z c} \quad (8)$$

$$\frac{d^2A_y}{dx^2} = \frac{4\pi j_0 v_y}{v_z c} \quad (9)$$

$$dy/dx = v_y/v_z \quad (10)$$

$$dz/dx = v_z/v_z \quad (11)$$

The equations (7)-(11) can be integrated using x as the independent variable as an initial value problem from $x = 0$. The initial conditions imposed are $y = 0, z = 0, \Phi = 0, A_y = A_z = 0$. (all by convention), $\frac{d\Phi}{dx} = 0$ (space charge limited flow), $dA_z/dx = 0$ ($B_y = 0$, corresponding to $B_0 = 0$ in the actual diode) and $dA_y/dx = B_{z0}$. The current j_0 can be adjusted to provide any positive potential at a given anode - cathode gap spacing, $\Phi(L) = V$. For $B_{z0} = 0$, these equations give $y = z = A_y = A_z = 0$, and the Langmuir-Child solution $\Phi \sim j_0^{2/3} x^{4/3}$. A typical numerical solution of the equation for nonzero B_z is shown in Fig. 1. Time does not occur explicitly in the equations we integrate. Nevertheless, the best results are obtained by using a uniform time step, i.e., with $dt = v_z dt$. This gives the best resolution of the gyro-motion in the magnetic field and the singular behavior near the cathode, where the solution approximates Langmuir-Child, even with $B_z \neq 0$.

An equilibrium fully symmetric with respect to y and z is obtained if j_0 is a constant. The synthesis discussed in section IV provides electrode shapes external to the electron beam such that the beam will remain symmetric with respect to y and z if j_0 is uniform in a finite emitting region in

$z, 0 < z < L_e$ (but $-\infty < y < \infty$, corresponding to $0 < \phi < 2\pi$.) However, it is not possible to obtain the correct A_z by such a method, because B_y is proportional to the current I_z within the orbit (see Fig. 1.) For $v_y > 0$ this is zero for the bottom orbit (from the right end of the emitting region) and increases for orbits emitted further to the left, but can never be equal to the value obtained in the pure slab limit, because some current is thrown out. Alternatively, we could note that with a finite emitting region, B_y becomes a function of x and z . In order to bracket the exact solution for a planar diode with a finite emitting region, we integrated the equations (7)-(11) with the full $A_z(z)$ and again with $A_z(z) = 0$. The first model is appropriate when the emitting region of length L_e is very long or for orbits near the top of the beam before they have traveled a distance Δz equal to L_e . The second model is appropriate for $L_e \rightarrow 0$ or for orbits near the bottom of the beam. Results obtained from these models will be discussed in Sec. III. The effect of a finite emitting region on A_y , B_z , and, for that matter, the effect of j_y upon B_z for the $L_e \rightarrow \infty$ case, is negligible for the designs we study because of a strong applied B_z .

B. Conical Nonrelativistic Model

A scaling that reduces the nonrelativistic conical diode problem to one dimension is well known, but we include a brief presentation for completeness. We use spherical coordinates (r, θ, ϕ) to describe a diode with cathode at $\theta = \theta_0$, anode at $\theta = \theta_1$, and ϕ symmetry. The relevant equations for $B_z = B_0 = \text{const.}$ and $B_\phi = 0$ (i.e., ignoring self j_ϕ and j_z) are conservation of energy

$$\frac{1}{2} m v^2 + q \Phi(r, \theta) = 0, \quad (12)$$

conservation of P_ϕ

$$\left(v_r \frac{\partial}{\partial r} + \frac{v_\theta}{r} \frac{\partial}{\partial \theta} \right) \left(m r \sin \theta v_\phi + \frac{q B_0}{2c} r^2 \sin^2 \theta \right) = 0, \quad (13)$$

and the r component of the equation of motion

$$(v \cdot \nabla v)_r = \frac{q}{m} \left(- \frac{\partial \Phi}{\partial r} + \frac{v_\theta B_0 \sin \theta}{c} \right) \quad (14)$$

Poisson's equation and $\nabla \cdot j = 0$ give

$$\frac{\partial^2 \Phi}{\partial r^2} + \frac{2}{r} \frac{\partial \Phi}{\partial r} + \frac{1}{r^2 \sin \theta} \frac{\partial}{\partial \theta} \left(\sin \theta \frac{\partial \Phi}{\partial \theta} \right) = - 4\pi n q, \quad (15)$$

$$\frac{1}{r^2} \frac{\partial}{\partial r} (r^2 n v_r) - \frac{1}{r \sin \theta} \frac{\partial}{\partial \theta} (\sin \theta n v_\theta) = 0. \quad (16)$$

These equations can be reduced to a one-dimensional form, with θ the independent variable, by assuming the scaling

$$\Phi = r^2 \Phi_0(\theta), \quad (17a)$$

$$v = r v_0(\theta), \quad (17b)$$

$$n = n_0(\theta). \quad (17c)$$

Equations (13), (14) then reduce to

$$\frac{1}{2} m v_{\theta 0}^2(\theta) - q \Phi_0(\theta) = 0, \quad (18)$$

$$v_{\theta 0} dQ/d\theta + 2 v_{r 0} Q(\theta) = 0, \quad (19)$$

where

$$Q(\theta) = \sin \theta v_{\theta 0} + \Omega_0 \sin^2 \theta / 2 \quad (20)$$

and $\Omega_0 = q B_0 / mc$. Equation (14) gives

$$\begin{aligned} v_{\theta 0}(\theta) \frac{d v_{r 0}}{d\theta} + v_{r 0}^2 - v_{\theta 0}^2 - v_{\phi 0}^2 \\ = \frac{q}{m} \left[-2\Phi_0(\theta) - \frac{v_{\phi 0}(\theta) B_0 \sin \theta}{c} \right] \end{aligned} \quad (21)$$

From (15) and (16) we obtain

$$\frac{1}{\sin \theta} \frac{d}{d\theta} \left(\sin \theta \frac{d\Phi_0}{d\theta} \right) + 6\Phi_0(\theta) = -4\pi q n_0(\theta), \quad (22)$$

$$\frac{1}{\sin \theta} \frac{d}{d\theta} \left[\sin \theta n_0(\theta) v_{\theta 0}(\theta) \right] + 3 n_0(\theta) v_{r 0}(\theta) = 0. \quad (23)$$

We integrate (19), (21), and (22) with respect to θ to obtain $v_{\phi 0}(\theta)$, $v_{r 0}$, and Φ_0 , respectively, in addition to finding $r(\theta)$, $\phi(\theta)$ by

$$\frac{d}{d\theta} (\ln r) = \frac{v_{r 0}}{v_{\theta 0}}, \quad (24)$$

$$\frac{d\phi}{d\theta} = \frac{v_{\phi 0}}{\sin \theta v_{\theta 0}}. \quad (25)$$

Finally, n_0 and $v_{\theta 0}$ are obtained from (23) and (18).

Note that self magnetic fields cannot be incorporated into these similarity solutions since the dynamical equations (13), (14) require $\mathbf{B} = B_0(\theta)$, $\mathbf{j} = nq \mathbf{v} = r \mathbf{j}_0(\theta)$ [i.e., (17b) and (17c)], which cannot satisfy $\nabla \times \mathbf{B} = 4\pi \mathbf{j}/c$.

C. Conical Superrelativistic Limit

In the limit of superrelativistic electron energies, $\gamma \gg 1$, Eqs. (12)-(14) are replaced by

$$\gamma mc^2 + q \Phi = 0, \quad (26)$$

$$\left(v_r \frac{\partial}{\partial r} + \frac{v_\theta}{r} \frac{\partial}{\partial \theta} \right) \left(r \sin \theta p_\theta + \frac{q}{c} r A_\theta \right) = 0, \quad (27)$$

$$(\mathbf{v} \cdot \nabla p)_r = \frac{q}{m} \left(-\frac{\partial \Phi}{\partial r} - \frac{v_\theta B_\theta - v_r B_r}{c} \right) \quad (28)$$

where $\mathbf{p} = \gamma m \mathbf{v}$ and $\gamma = (1 + p^2/m^2 c^2)^{1/2}$ becomes $\gamma = |\mathbf{p}|/mc$, i.e., $|\mathbf{v}| = c$. Equations (15), (16) are unchanged. One dimensional equations in θ are obtained in this limit by the following scaling

$$\Phi = r \Phi_0(\theta) \quad (29a)$$

$$\mathbf{p} = r \mathbf{p}_0(\theta) \quad (29b)$$

$$\mathbf{v} = \mathbf{v}_0(\theta) \quad (29c)$$

$$\gamma = r \gamma_0(\theta) \quad (29d)$$

$$\mathbf{B} = \mathbf{B}_0(\theta) \quad (29e)$$

$$\mathbf{A} = r \mathbf{A}_0(\theta) \quad (29f)$$

$$n = n_0(\theta)/r. \quad (29g)$$

Note that $n\mathbf{v}$ and $\nabla \times \mathbf{B}$ both scale as $1/r$, so that self fields can be included in these solutions. Equations (26), (27) give

$$\gamma_0(\theta) mc^2 + q \Phi_0(\theta) = 0, \quad (30)$$

$$p_{\theta 0} \frac{dQ}{d\theta} + 2p_{r 0} Q = 0, \quad (31)$$

with

$$Q(\theta) = \sin \theta p_{\theta 0} + q A_{\theta 0}(\theta)/c. \quad (32)$$

Equations (28), (15) and (16) give

$$\begin{aligned} v_{\theta 0} \frac{dp_{r 0}}{d\theta} + v_{r 0} p_{r 0} - v_{\theta 0} p_{\theta 0} - v_{\theta 0} p_{\theta 0} \\ = q \left(-\Phi_0 + \frac{v_{\theta 0} B_{\theta 0} - v_{r 0} B_r}{c} \right) \end{aligned} \quad (33)$$

$$\frac{1}{\sin \theta} \frac{d}{d\theta} \left(\sin \theta \frac{d\Phi_0}{d\theta} \right) + 2\Phi_0 = -4\pi q n_0, \quad (34)$$

$$\frac{1}{\sin \theta} \frac{d}{d\theta} \left(\sin \theta n_0 v_{\theta 0} \right) + n_0 v_{r 0} = 0. \quad (35)$$

The θ component of Ampere's law gives $B_{\theta 0} = -n_0 q v_{\theta 0}$, and the r component

$$\frac{1}{\sin \theta} \frac{\partial}{\partial \theta} (\sin \theta B_{\phi 0}) = n_0 q v_{\phi 0}$$

is consistent by (35). The ϕ component of Ampere's law gives

$$B_{\theta 0} = - 2 A_{\phi 0}, \quad (36a)$$

$$\frac{d}{d\theta} \left[\frac{1}{\sin \theta} \frac{d}{d\theta} (\sin \theta A_{\phi 0}) \right] + 2 A_{\phi 0} = - n_0 q v_{\phi 0}. \quad (36b)$$

Equations (30)-(36), together with (24) and (25) can be integrated as initial value equations from $\theta = \theta_0$ as in the planar and nonrelativistic conical diode cases. When the self magnetic fields are negligible, $B_{\phi 0} = 0$, $B_{\theta 0} = - 2 A_{\phi 0} = - B_0 \sin \theta$ and (36b) is not used.

III. Applications of One Dimensional Models

In this section we describe how the one dimensional models of Sec. II are used in diode design. The slab relativistic model has been used primarily to scan the parameter space for reasonable design candidates. Electrode synthesis has been applied to the promising designs, with further electrode shaping required both for final tuning of the design and for other practical considerations. This model has been used to shed light on certain aspects of the design, for example, the dependence of the results on the self B_z . The conical models have been used to clarify the geometric effects, specifically the variation of the space charge limited current obtained by the Hermansfeldt code from the value predicted by the slab model. Let us assume that we want to produce a beam with $\alpha \equiv |p_z/p_\perp| \approx 1$ in an interaction region of radius $r_f = 1.4$ cm, with a field $B_f = 24$ kg. Assuming that the beam is adiabatic in the drift region between the diode and the interaction region, i.e.,

$$\frac{B_i}{B_f} = \frac{1 - 1/\alpha_f^2}{1 - 1/\alpha_i^2} \quad (37)$$

and

$$r_i = r_f (B_f/B_i)^{1/2}, \quad (38)$$

and taking $\alpha_i = 0.2$, we obtain $B_i = 1.85$ kg, $r_i = 5.05$ cm.

We have used the slab relativistic model to compute α at the anode as a function of the angle χ_0 between the normal to the cathode and the externally imposed magnetic field, i.e., $\chi_0 = \tan^{-1}(B_z/B_r)$. The gap voltage was $\Phi = 600$ kV, and the current density j_0 was 70 A/cm². The results, with and without self $B_y(z)$, are shown in Fig. 3. Without B_y , $\chi_0 = 30^\circ$ gives $\alpha_i = 0.2$, whereas with B_y , $\chi_0 = 40^\circ$ is correct. This indicates that self B_y plays an important role in determining α , although it has little influence on the gap spacing d . Since B_y (or B_z) is zero for the bottom orbit, and since B_y (B_z) can be near its limiting one dimensional value for orbits near the top, this indicates that electrode synthesis may not by itself produce a uniform α across the beam. We will return to this issue in Sec. V. We also show, in Fig. 4, the dependence of α and d upon j_0 , for $\chi_0 = 40^\circ$; $\Phi = 600$ kV, including self $B_y(z)$. It is clear that both of these quantities depend critically upon j_0 .

As we shall discuss further, the Hermansfeldt code in this parameter range shows space charge limited flow at 20-50% higher current than that indicated by the slab model. In order to understand this discrepancy and have more confidence in our results, we have investigated this effect with the nonrelativistic and superrelativistic conical models. We use these models in the following manner: we fix the cathode angle θ_0 (see Fig. 2), a potential Φ , a gap spacing d , a field B_{z0} , and a radius R where a ray is to be limited. We adjust j_0 until the potential equals Φ when the gap spacing is d . Then we vary R . The results for different R values are not obtainable from the scalings (17) or (29) because we do not allow Φ and d to scale appropriately with R ($\Phi \sim R^2, d \sim R$ from (17) or $\Phi \sim R, d \sim R$ from (29)). For a case with $\Phi = 1.07$ MV, $B_{z0} = 2.4$ kg, $d = 3$ cm, $\theta_0 = 158^\circ$, we obtain the results shown in Fig. 5. For both the nonrelativistic and superrelativistic models, the results fit curves of the form $j_0 = j_0(\infty) - A/R$, and the limiting value $j_0(\infty)$ agrees with slab nonrelativistic or slab superrelativistic models. For the cases considered, j_0 for $R = 5$ cm is 20 to 50% higher than for the slab model, in agreement with the results obtained using the Hermansfeldt code.

IV Synthesis Techniques for Determining Electrode Shapes

The electrode synthesis technique is a method of calculating electrode shapes which provide laminar flow for a beam with self electric fields. The method was initially formulated by Harker for planar and axially symmetric cases of space-charge limited non-relativistic flow. The method was extended to temperature-limited MIG type guns by Manuilov and Tsimring. The general approach involves finding a set of ordinary differential equations to represent the beam flow. These equations are used to obtain the boundary conditions for integrating Laplace's equations in the region outside the beam. A difficulty in the direct implementation of this procedure is that the present problem involves Cauchy boundary conditions on an open surface and the solution of Laplace's equation are unstable for these conditions. An elegant method has been developed by Harker which reformulates the mathematical problem in a way which yields stable numerical solutions. This section outlines the synthesis technique for planar geometry and discusses an application for the case of planar relativistic flow.

The synthesis problem consists of finding the electrostatic potential distribution in a region external to a finite laminar flow beam. The potential satisfies Laplace's equation outside the beam or equivalently, the electrostatic field satisfies the Maxwell divergence and curl equation

$$\frac{\partial E_z}{\partial x} + \frac{\partial E_x}{\partial z} = 0 \quad (39)$$

$$\frac{\partial E_z}{\partial z} - \frac{\partial E_x}{\partial x} = 0 \quad (40)$$

with the boundary conditions

$$E_z = E_{zx}, E_x = E_{xz} \quad (41)$$

on the outermost trajectory of the beam.

Equations (39) and (40) form a system of elliptic partial differential equations whose solutions are unstable for the present case of an open surface and Cauchy boundary conditions. However, a stable solution can be obtained by the following approach due to Harker.

First, the beam edge trajectory ($z_e = z_e(t)$, $z_r = z_r(t)$), is converted into the straight line $u = 0$ of the (t, u) plane by means of the conformal transformation

$$z - iz = z_r(t + i\mu) - iz_r(t + i\mu) \quad (42)$$

This can be done because the equations for the beam trajectory can be expressed in the complex plane by analytic continuation. Since coordinates related by a conformal transformation satisfy the Cauchy-Riemann conditions,

$$\frac{\partial z}{\partial u} = \frac{\partial z}{\partial t} \quad (43)$$

$$\frac{\partial z}{\partial u} = - \frac{\partial z}{\partial t} \quad (44)$$

Equations (39) and (40) can be expressed in the form

$$\frac{\partial E_r}{\partial u} = - \frac{\partial E_i}{\partial t} \quad (45)$$

$$\frac{\partial E_i}{\partial u} = \frac{\partial E_r}{\partial t} \quad (46)$$

These equations, together with

$$\frac{\partial \Phi}{\partial u} = - E_r \frac{\partial z}{\partial t} + E_i \frac{\partial z}{\partial t} \quad (47)$$

enable calculation of the potential Φ in the transformed plane (t, u) .

The second step is the transformation of the elliptic system, Eqs. (45) and (46) in the (t, μ) plane, by means of the analytic continuation

$$t \rightarrow p + iq \quad (48)$$

For fixed p this leads to the hyperbolic system in the (q, u) plane:

$$\frac{\partial E_r}{\partial u} = \frac{\partial E_i}{\partial q} \quad (49)$$

$$\frac{\partial E_i}{\partial u} = - \frac{\partial E_r}{\partial q} \quad (50)$$

$$\frac{\partial z}{\partial u} = - \frac{\partial z}{\partial q} \quad (51)$$

$$\frac{\partial z}{\partial u} = \frac{\partial z}{\partial q} \quad (52)$$

Equations (49) and (52) have a stable solution for the present boundary conditions.

The procedure for obtaining the equipotentials is illustrated in Fig. 6. It involves solving the system (49) and (52) in triangular regions such as ABC in Fig. 6. To obtain the solution for this region it is sufficient to specify Cauchy boundary conditions on the line AB. These conditions are the analytic

continuation of Eq. (41) and are formed by integrating the flow equations along the real axis from $t = 0$ to $t = P_D$ and then along the line AB by means of the substitution

$$\frac{d}{dt} \rightarrow i \frac{d}{dq} \quad (53)$$

Solving Eqs. (49)-(52) in the region ABC by a finite difference method allows the potential to be obtained on the line CD, the only region of physical significance. By translating the triangle ABC to other values of p , the potential distribution over the entire single valued region of the plane $(p, u) = (t, u)$ can be found. Applying the transformation (42) yields the equipotential surfaces as a function of x and z .

Electrodes shapes calculated by the synthesis technique are shown in Fig. 7 for the planar relativistic flow model discussed in section II A. The synthesis calculation was based on a current density of 70 A/cm^2 , an angle of 40° between the cathode normal and the external magnetic field, and an external magnetic field by 1.85 kG . The anode-cathode gap voltage is 600 kV . Upper beam edge trajectories are shown with and without the approximation self magnetic field effect included. As shown the effect is quite small for the present parameters and there is negligible effect on the calculated electrodes.

V. Final Diode Design

The final design for the diode, in several configurations, was achieved by means of the electron trajectory (Hermannsfeldt) code. The electrodes found by synthesis generally provide a beam in which α varies by $\pm 50\%$ from top to bottom. This variation, which is not present in the slab model, is due to geometric effects. One of these effects is the fact that the bottom orbit has $B_z = 0$, whereas the top orbit has a value of B_z which can be nearly equal to the one-dimensional value (for fat beams). This effect has been studied in Sec. III and found to provide just such a variation in α .

Our first design is for a 600 kV, 2 kA gun which can use a minimal amount of focussing, depending upon intercepting the outer two thirds of the beam at the anode. This extra charge (and current) takes the place of some of the focussing. A successful design of this type is shown in Fig. 8. The cathode face is at 40° , which we found in Sec. III gives $\alpha = 0.2$ with $B_{z0} = 1.85$ kg. The current density $j_0 = 70 \text{ A/cm}^2$ in the slab model gives, for a cathode surface of radius 5 cm and emitting length 2.1 cm, 4.6 kA. Because of geometric effects as discussed in Sec. III, we used 6.0 kA, corresponding to a perveance $k = 13$ micropervs. This is near the space charge limit; for $k \geq 15$, the results begin to show serious signs of lack of convergence usually associated with approaching the space charge limit at some point on the cathode face. The results show a very flat $\alpha \approx 0.2$, $\pm 10\%$ and very little evidence of orbit crossing. It is possible to reshape the electrodes to have less focussing in order to decrease the electric fields on the parts of the cathode where we wish to inhibit emission. In that case α would not be as flat across the whole 6 kA beam, but that is of no consequence. However, it appears that the electric fields in the design in Fig. 6 are below 300 kV/cm, and the surfaces of anodized aluminium on the focusing electrodes should inhibit emission for at least 50 ns.

In Fig. 9 we show a design with an aperture in the anode allowing roughly the middle third of the beam, and a short drift region bounded by anode surfaces. There is very little orbit crossing still, and α is quite flat in the central third of the beam. (For rays intercepted by the anode, the value shown for α is the value at interception.) However, α is considerably higher now, in the range $0.36 < \alpha < 0.41$. This is apparently due to a combination of effects, including the space charge of the beam and the finite

Larmor radius of the orbits

An alternate design for a 600 kV, 2 kA diode is shown in Fig. 10. Here, uniformity of the beam is achieved by focussing electrodes alone: all of the beam is allowed to pass through the aperture in the anode. The electrode shapes are nearly identical to those of the design in Figs. 8 and 9, except that the emitting region is one third the length, or 7mm; the perveance is, correspondingly, $k = 4.3\mu$ microperus and the magnetic field is a nearly uniform 1.85 kg. Again, the electrode shapes are somewhat different from those obtained by synthesis, for geometric reasons, and the maximum electric field is of order 300 kV/cm. Figure 10 shows essentially no orbit crossing in the diode region and a very uniform $\alpha = 0.19 \pm 5\%$ across the beam at the anode and at the end of the drift region. A combination of coils produce a quite uniform 2.2 kg magnetic field in the diode region that increases to 20 kg at the far end of the compression region. The average value of α at the far end of the compression region agrees well with the adiabatic value $\alpha_f = 1.2$ based on $\alpha_i = 0.22$, $B_i = 2.2$ kg at the beginning of the compression region and $B_f = 28$ kg at the end. However, there is much more variation in α across the beam than adiabatic theory predicts: from (37) one can show

$$\frac{d \ln \alpha_f}{d \ln \alpha_i} = \frac{2}{1 + \alpha_i^2} \quad (39)$$

which shows that the relative variation in α_f should only be twice the relative variation in α_i for $\alpha_i \ll 1$. This is a common effect in this type of simulation and is apparently due to space charge effects that become more pronounced as the beam slows up. The results shown in Fig. 10 are with 25 rays; results with 15 rays give very similar results, including the variation of α across the beam.

Tests have been made to determine the sensitivity of the diode performance to variations in B_z and the potential. For these tests, a 600 kV, 2 kA diode with $B_z = 1.85$ kg was used. These tests are important in order to be able to tune an actual device. In addition, it is important to know whether variation of the voltage during the pulse will have deleterious effects. The nominal diode design here has $\alpha = 0.25$ across the beam. Dropping the potential to 450 kV causes the beam to enter the aperture in the anode less than a centimeter below the point where a 600 kV beam enters, so that it appears that a pulse with $450 \text{ kV} < \phi < 600 \text{ kV}$ will produce a beam that can still fit through the anode aperture.

Furthermore, α is nearly unchanged. These results are not sensitive to the perveance. For B_z ten percent below the nominal value, i.e., 1.67 kg, the beam begins to scrape the top of the drift cavity, and α is larger, in the range $0.32 < \alpha < 0.38$. For B_z twenty percent above, i.e., $B_z = 2.22$ kg has $\alpha \approx .20$. Thus it appears that α scales as $1/B_z$, so that varying B_z may be an effective way to obtain a desired α in this type of diode.

Acknowledgment

This work was supported by the Office of Naval Research, by the Department of Energy through a contract with the Lawrence Livermore Laboratory, and by the Defense Nuclear Agency.

Reference

Creedon J.M. 1975. Relativistic Brillouin Flow in the High v/γ Diode *J. Appl. Phys* **46** 2946

Dryden, V.W. 1962, Exact solutions for space-charge flow in spherical coordinates with application to magnetron injection guns. *J. Appl. Phys.*, **33**, 3118-3124.

Fillet, A.W., A.J. Dudas, M.E. Read and J.M. Baind 1982, Use of Electrode Synthesis Techniques to Design MIG-Type Guns for High Power Gyrotrons. *Int J. Electronics*, **53**, 743

Goldstein, S., R.C. Davidson, J.G. Siambi and R. Lee 1974, Focused Flow Model of Relativistic Diodes. *Phys Rev Lett*, **33**, 1471

Goldstein, S.A. 1976. Magnetic Field Effects on the Emission Law of Electron Current from Cathodes. *J. Appl Phys.*, **47**, 894

Harker, K.J. 1960 a, Determination of electrode shapes for axially symmetric electron guns. *J. Appl. Phys.*, **31**, 2165-2170; 1960 b, Electrode design for analytical design of axially symmetrical ion guns. Internal Memorandum, Microwave Laboratory, Stanford University, Report No. 1013, NASA CR-54052.

Herrmannsfeldt, W.B., 1979, Electron trajectory program. SLAC-Report-226, Stanford Linear Accelerator Center, Stanford, California.

Kirkpatrick, D.A., R.E. Shefer and G. Bekefi, 1984, High Brightness Electrostatically Focused Emission Electron Gun for Free Electron Laser Applications. MIT Plasma Fusion Center preprint PFC/JA-84-40.

Kirstein, P.T., G.S. Kino, W.E. Water 1967 *Space Charge Flow*, McGraw-Hill, New York

Ott, E. T.M. Antonsen, R.V. Lovelace 1977 Theory of Foilless Diode Generation of Intense Relativistic Electron Beams. *Phys. Fluids*, **20**, 1180

Figure Captions

Fig. 1 — Geometry for the slab relativistic diode model. For the bottom orbit, B_y is zero. For the top orbit, B_y is the value obtained by the slab model for electrons to the left of the dashed line. To the right, B_y is less than the slab model value.

Fig. 2 — Geometry of conical diode. For a finite emitting region, the same comments hold for self B_c . The angle α_0 of Fig. 1 corresponds to $\theta_0 - \pi/2$.

Fig. 3 — Dependence of $\alpha = |p_t/p|$ and the gap spacing d upon α_0 for the slab relativistic model.

Fig. 4 — Dependence of α and d upon j_0 for the slab model.

Fig. 5 — Current density j_0 as a function of R for two conical models.

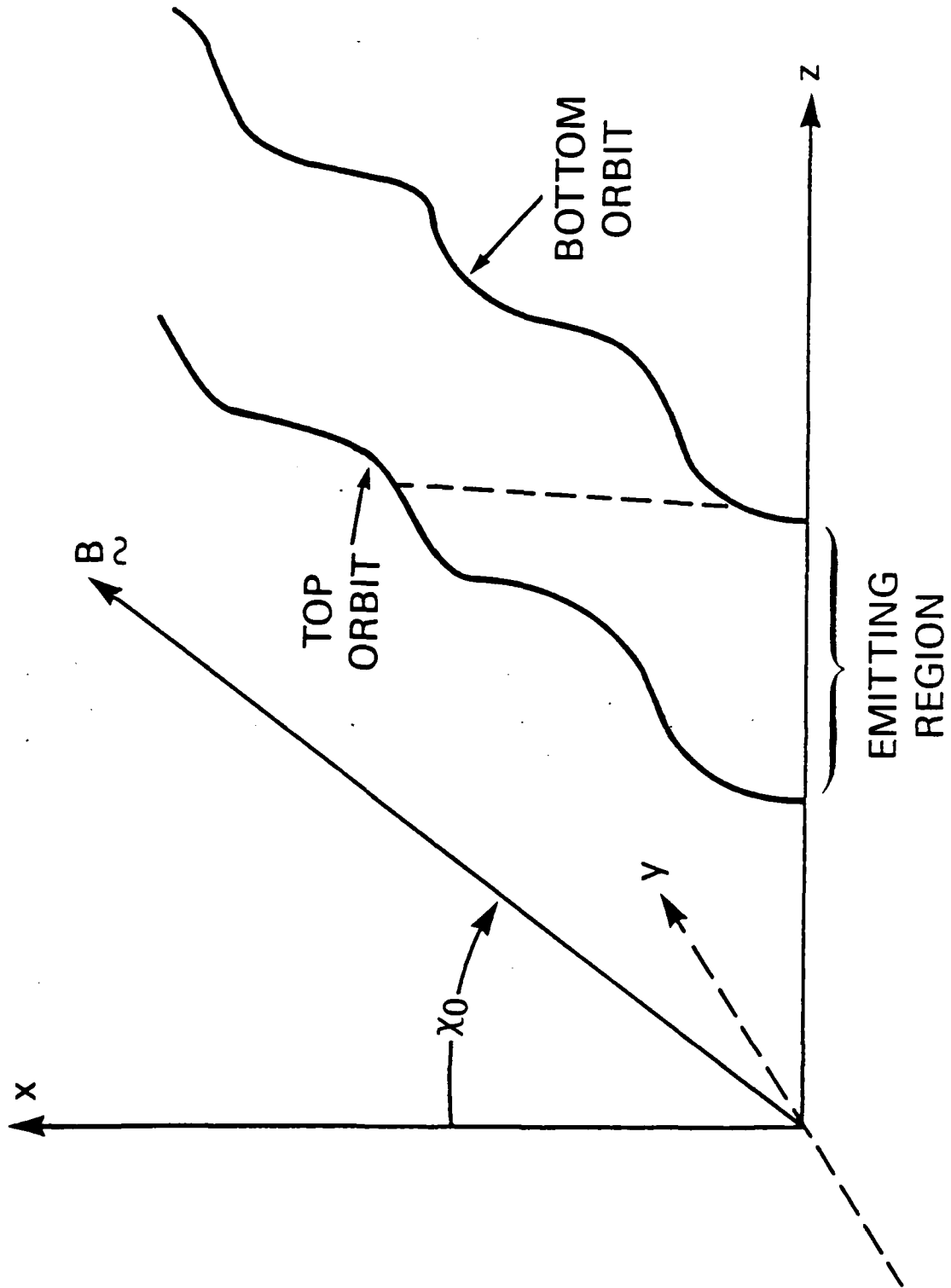
Fig. 6 — Schematic of the solution of Laplace's equation in the complex plane.

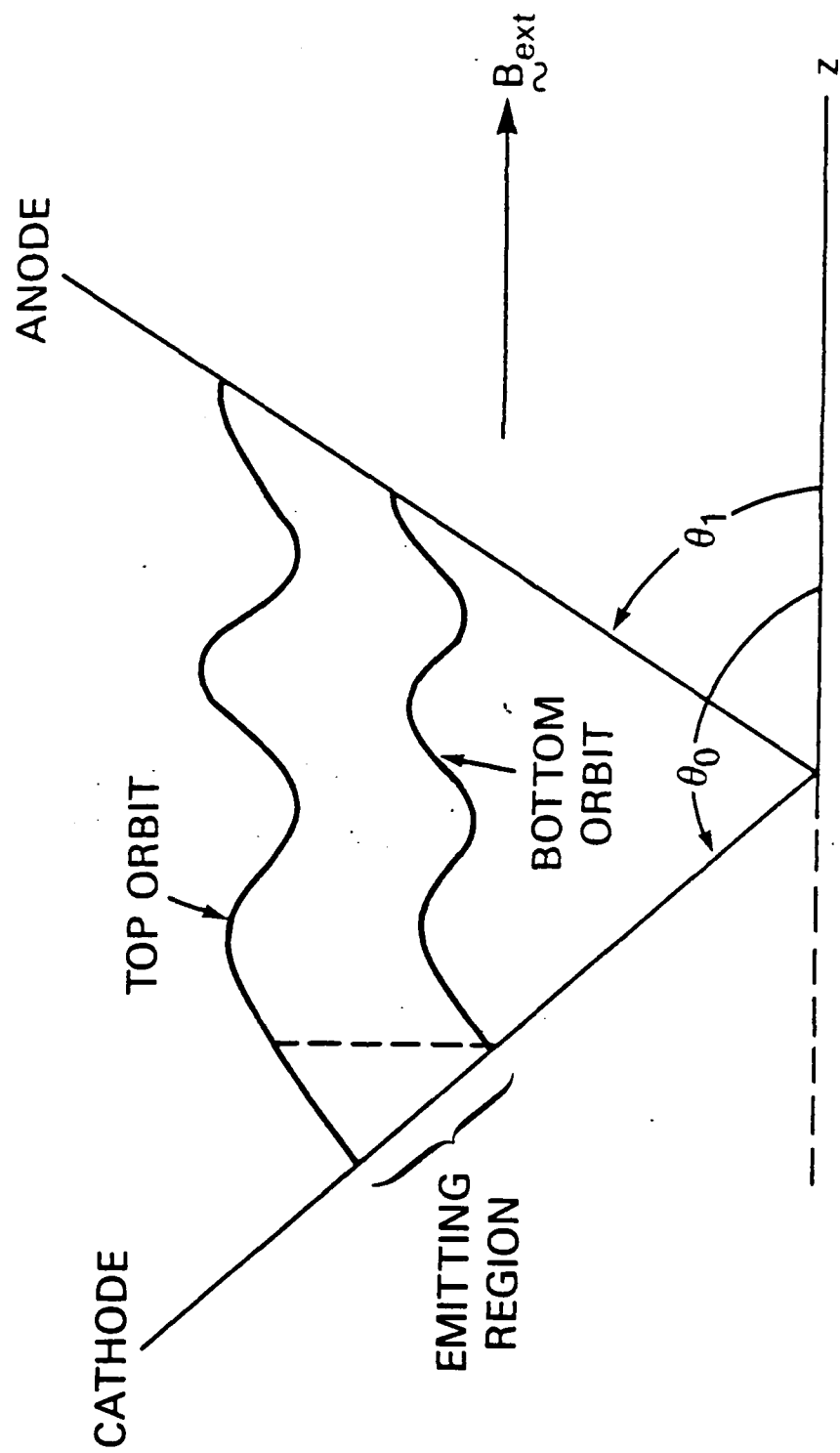
Fig. 7 — Electrode shapes calculated by synthesis technique.

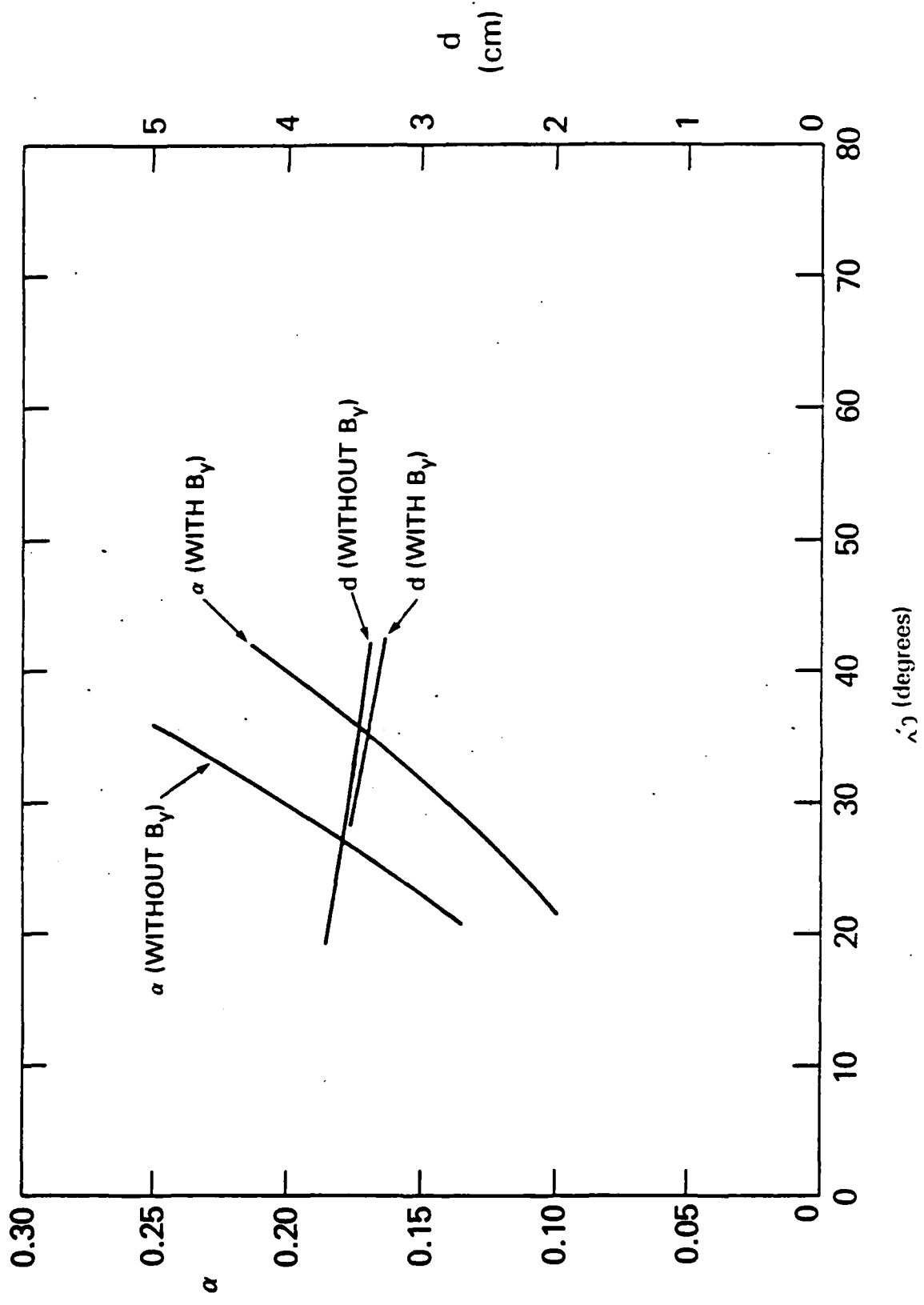
Fig. 8 — A 600 kV, 2 kA diode design with the outer two thirds of a 6 kA beam to be intercepted by the anode. In (a) are equipotentials and actual trajectories integrated by the code; in (b) is shown α vs ray number, from the bottom of the beam to the top, for the electrons when they hit the anode.

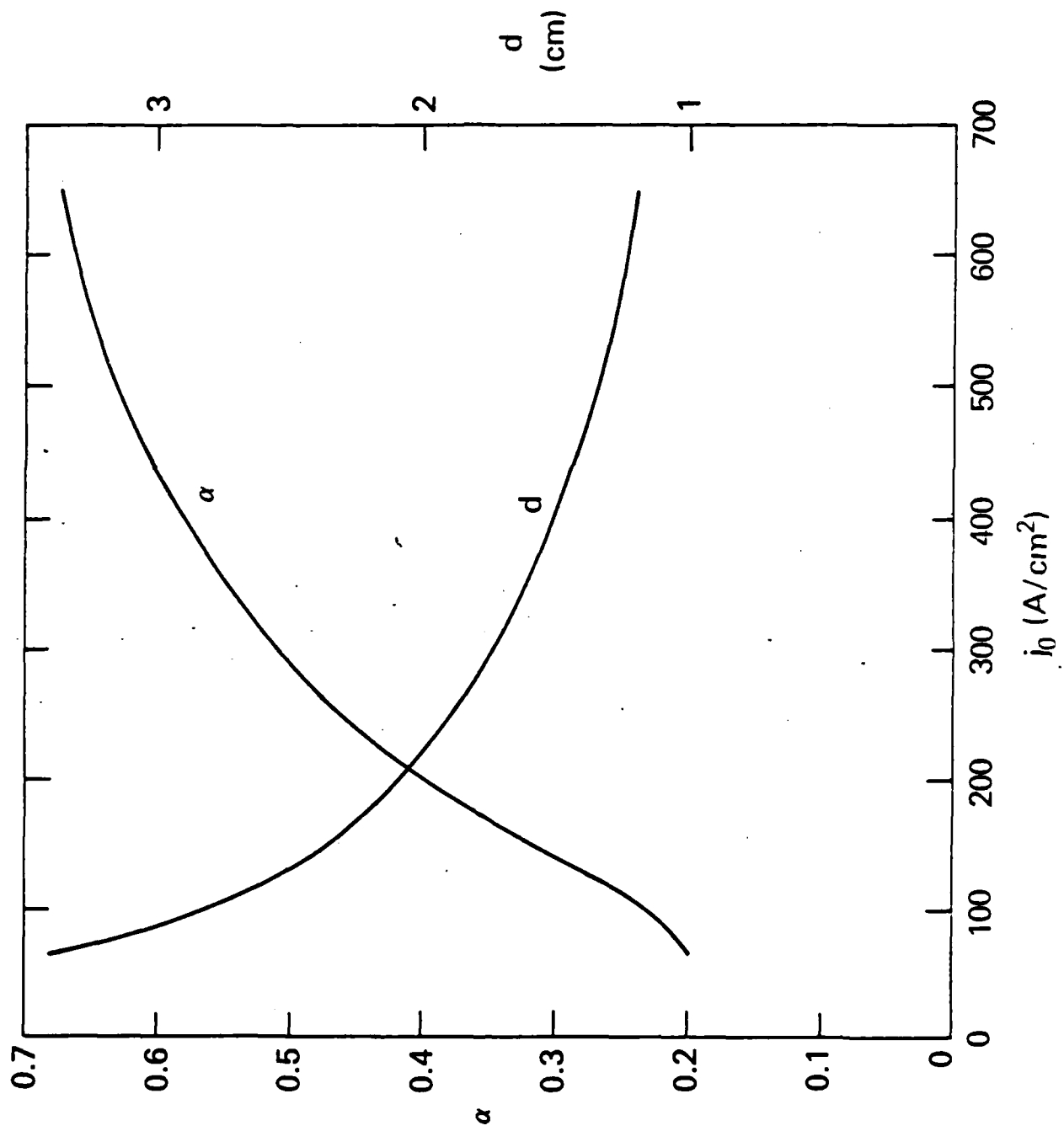
Fig. 9 — Same diode as in Fig. 6 but with an aperture in the anode and a drift region.

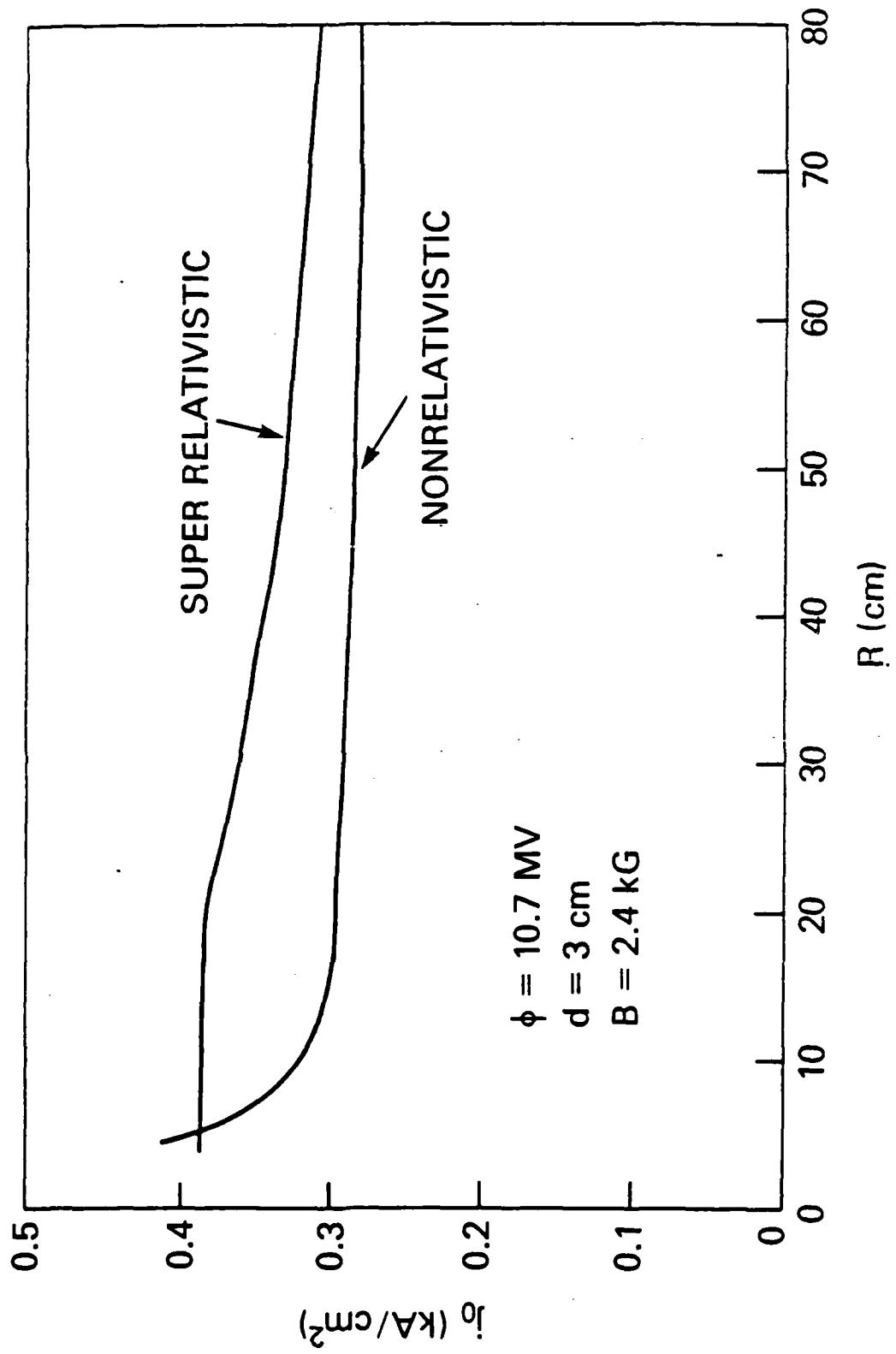
Fig. 10 — (a) Diode design with 600 kV, 2 kA, where the beam uniformity is provided by focussing electrodes alone; (b) α at the aperture in the anode; (c) α at the end of the drift region; (d) orbits in the compression region, (e) α at the end of the compression region.

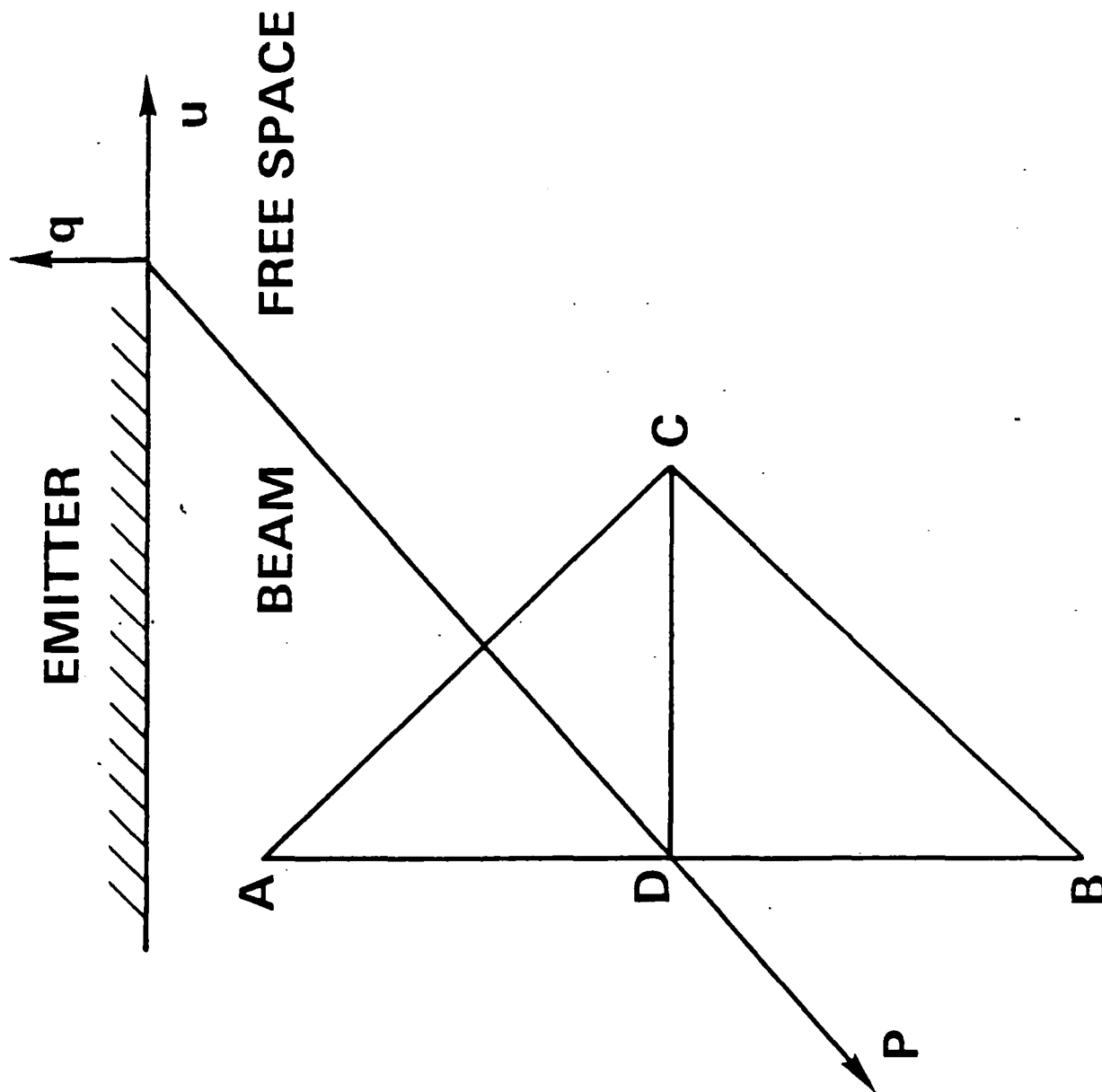


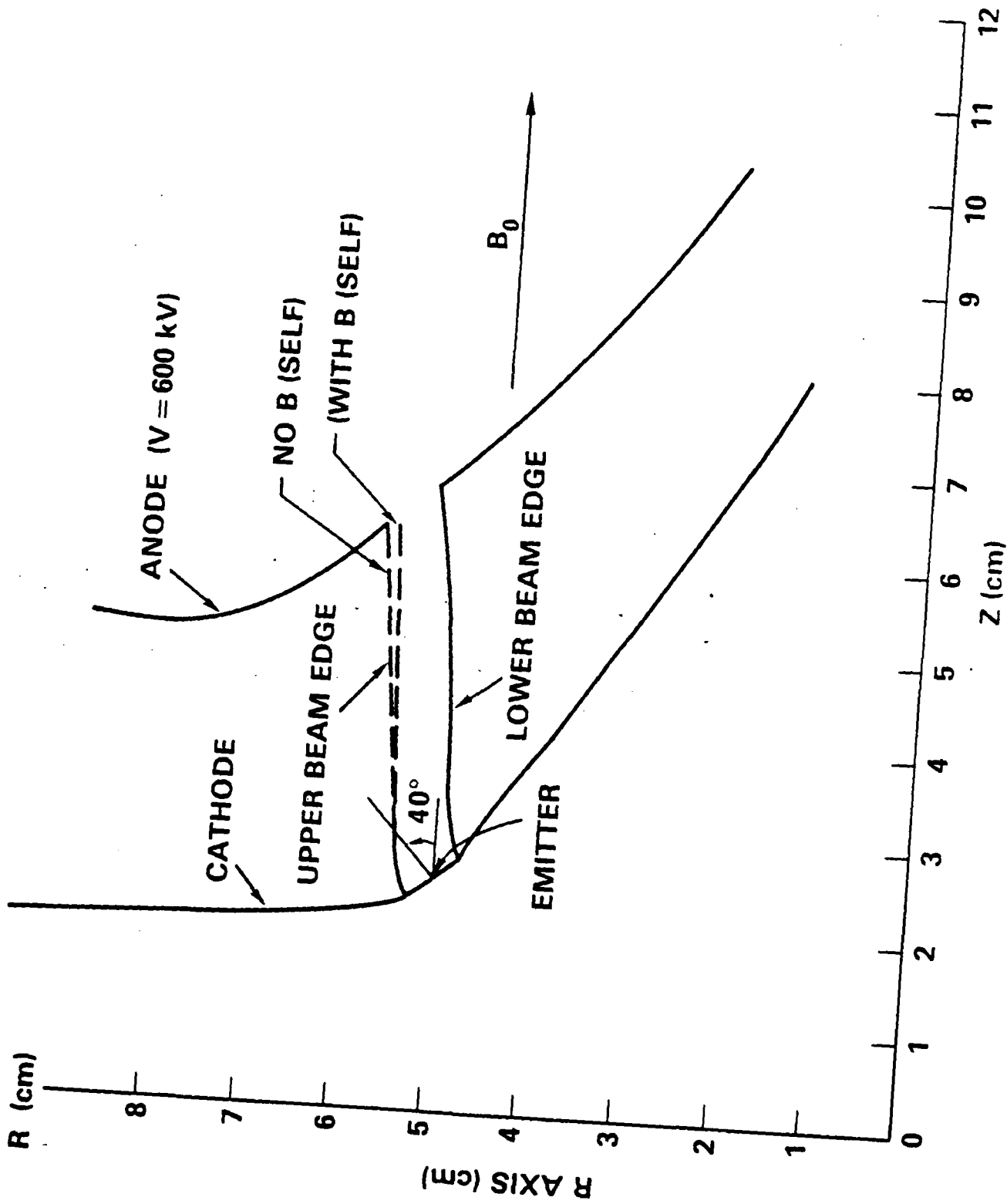


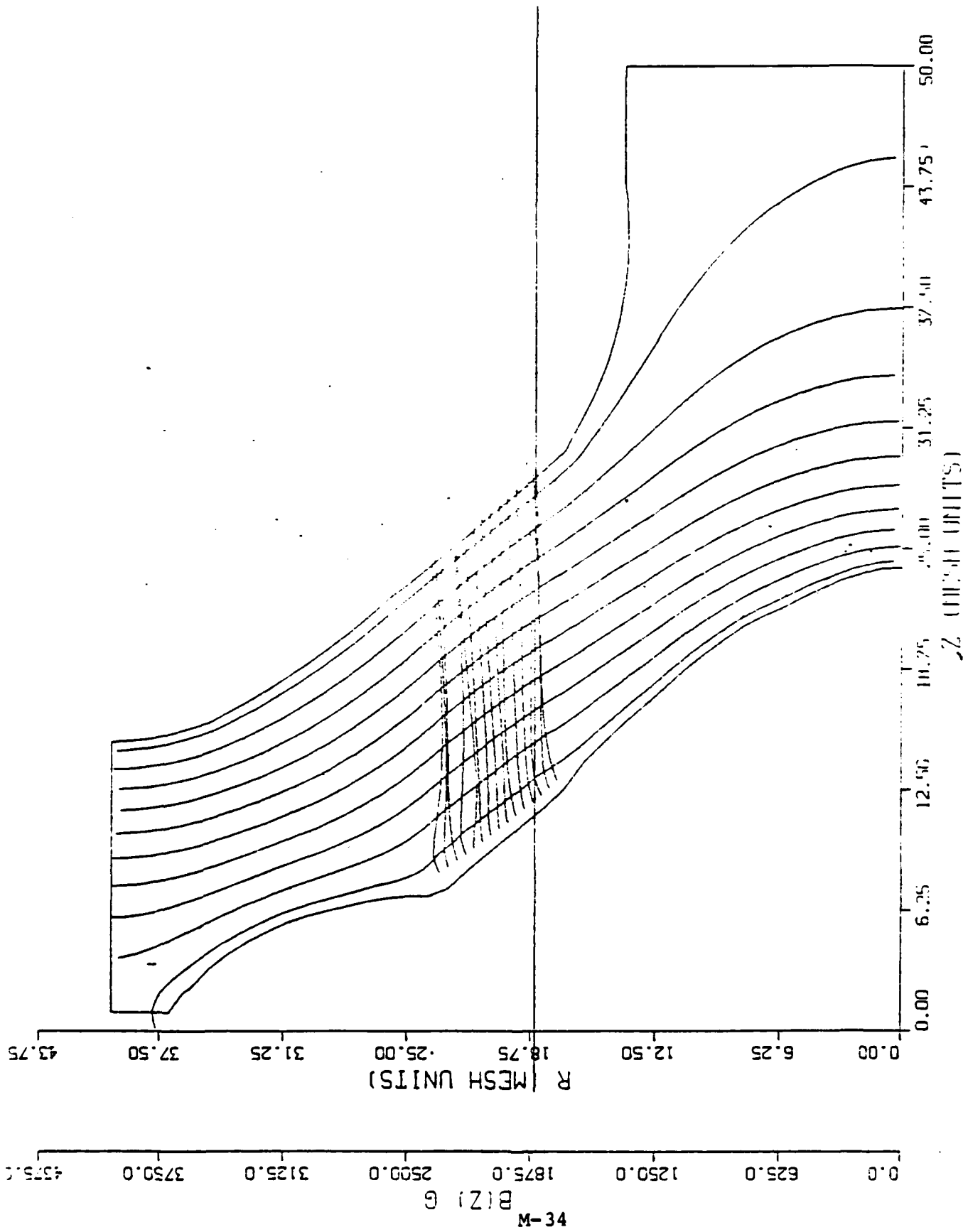










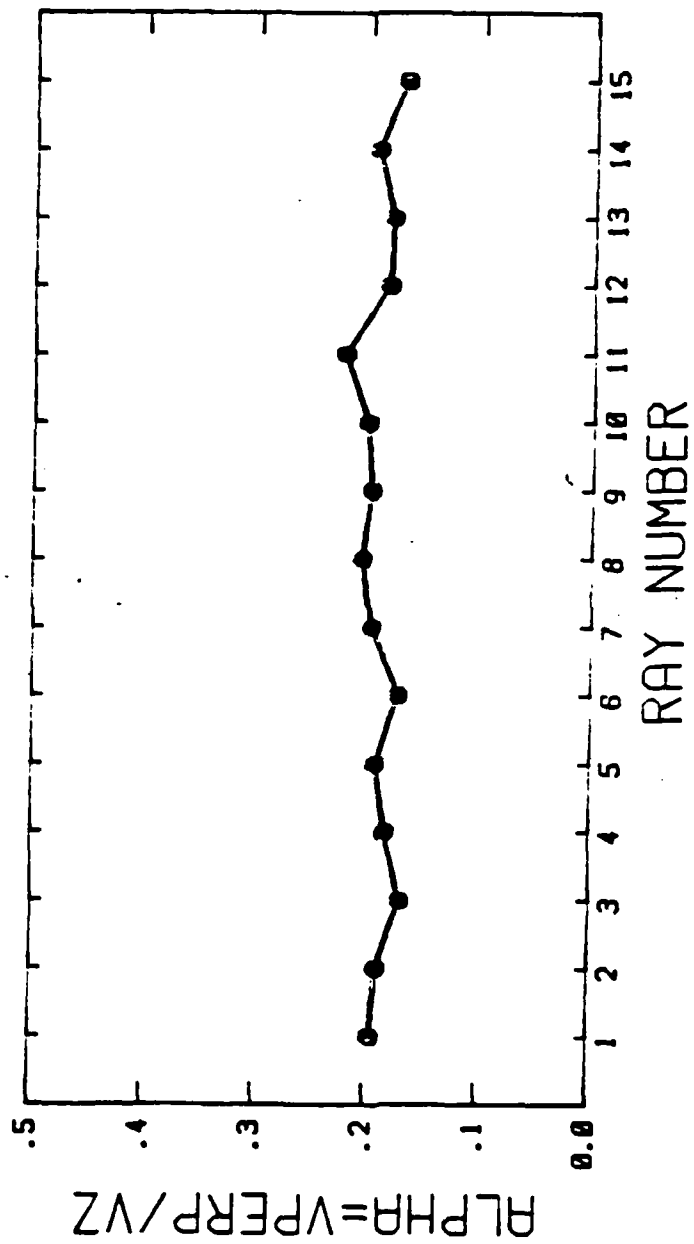


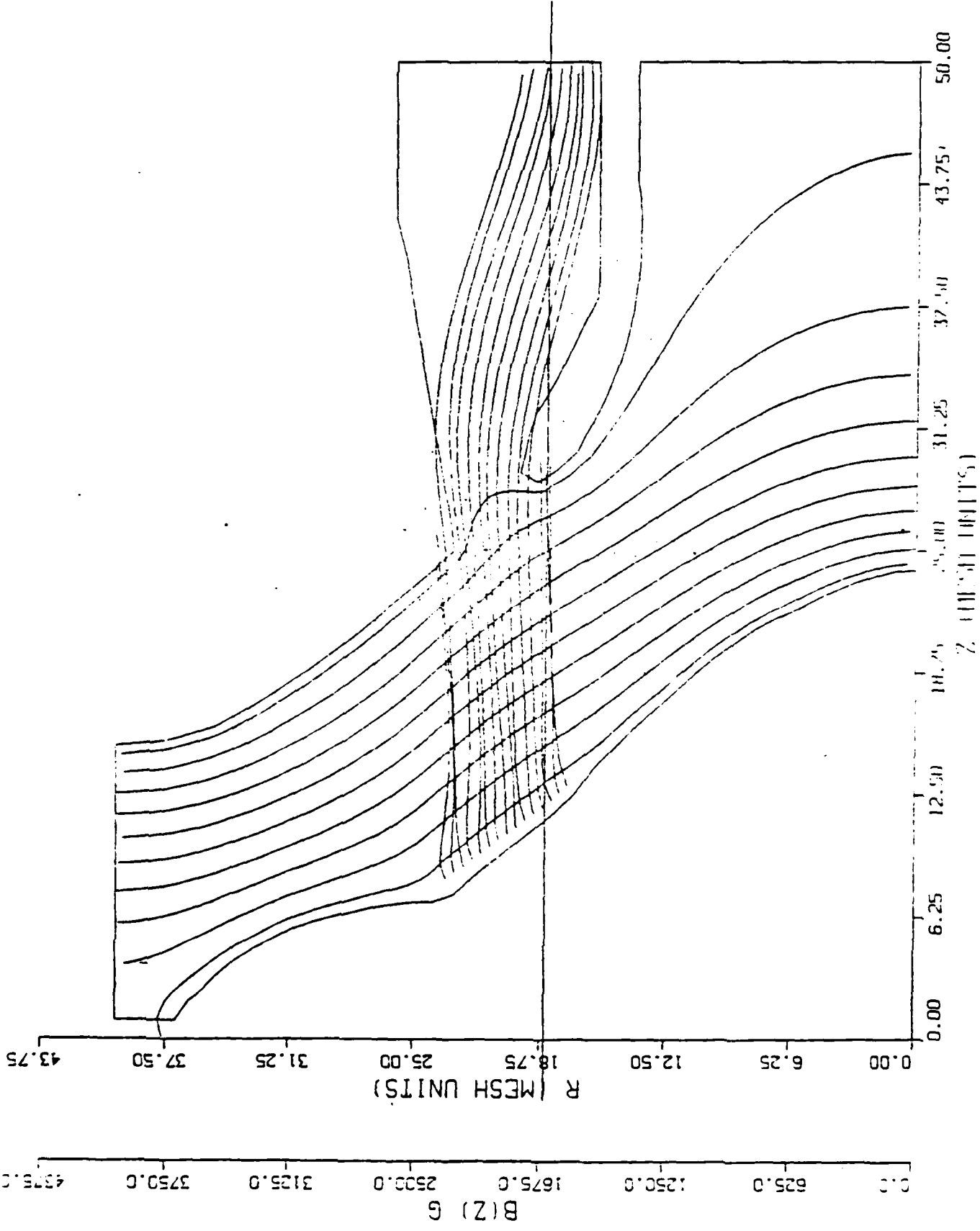
44-M

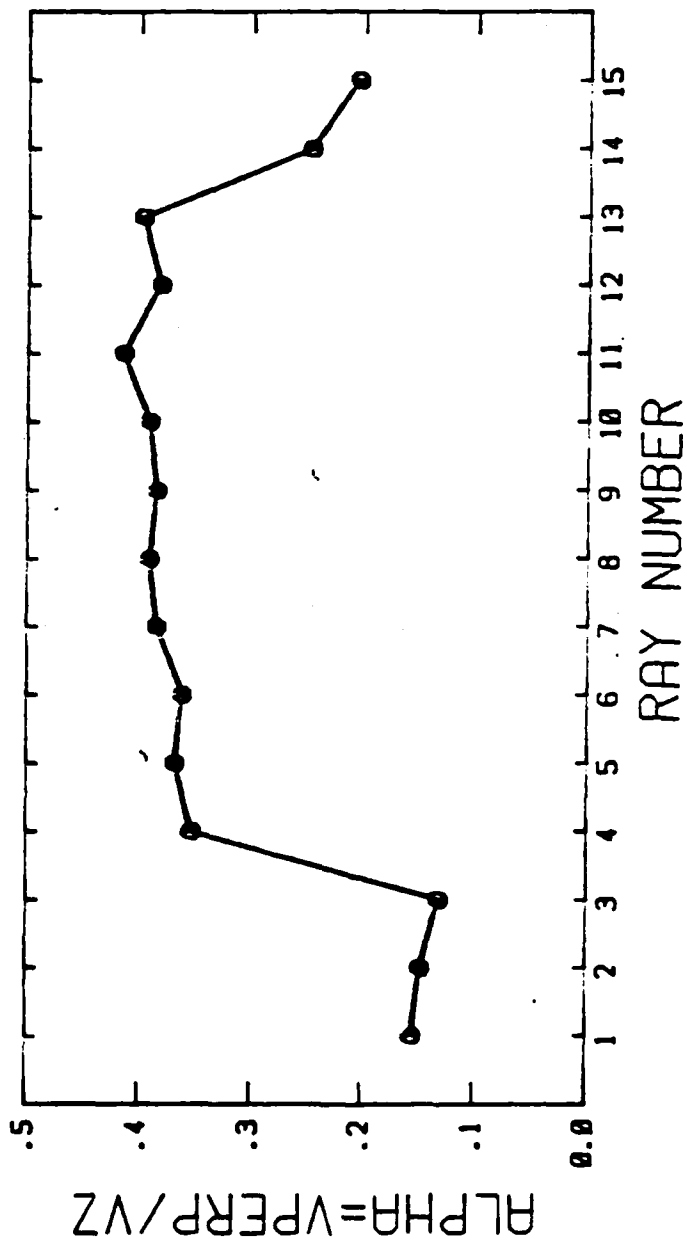
BIZI G

0.0 625.0 1250.0 1875.0 2500.0 3125.0 3750.0 4375.0

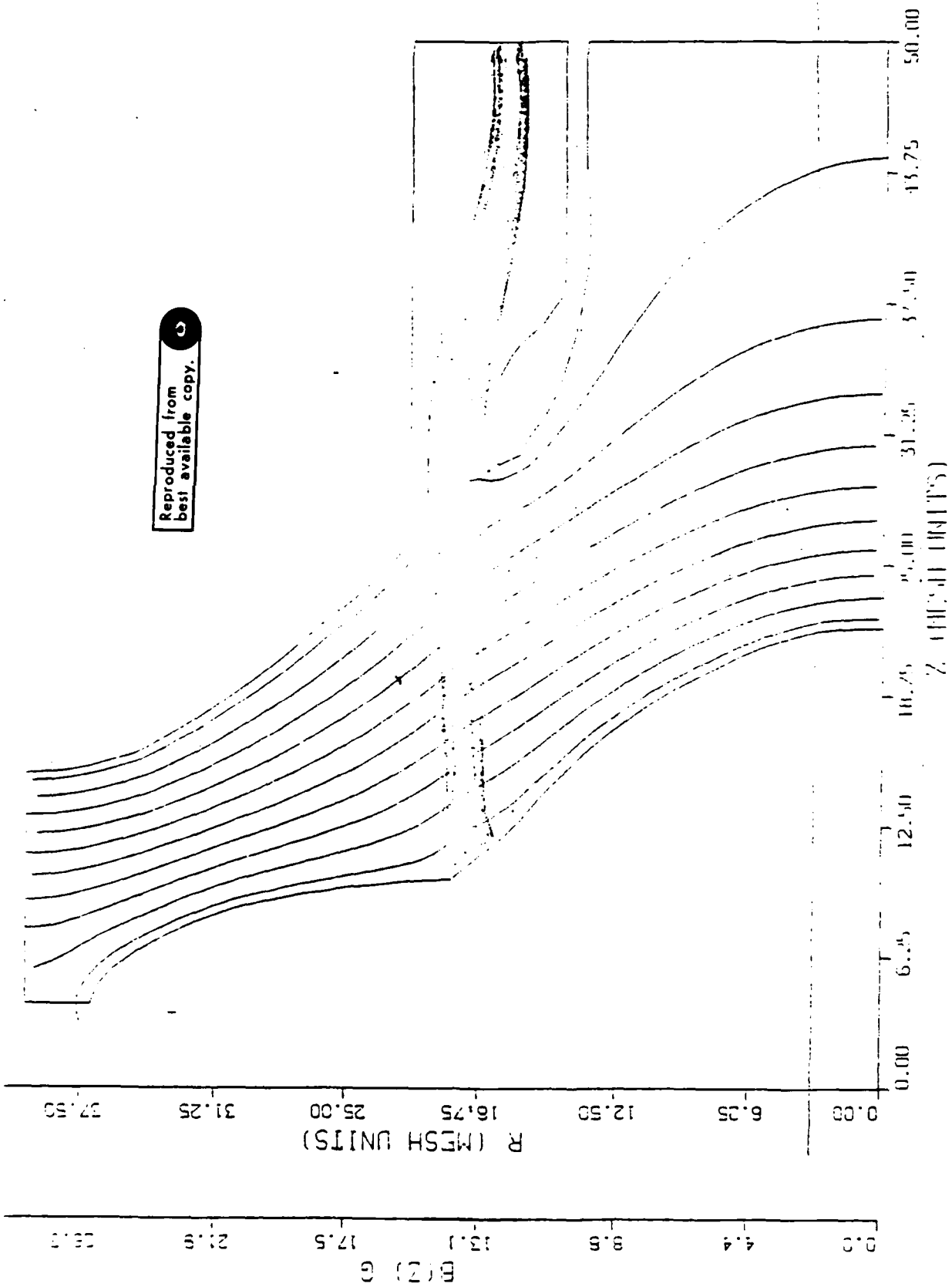
0.00 6.25 12.50 18.75 25.00 31.25 37.50 43.75

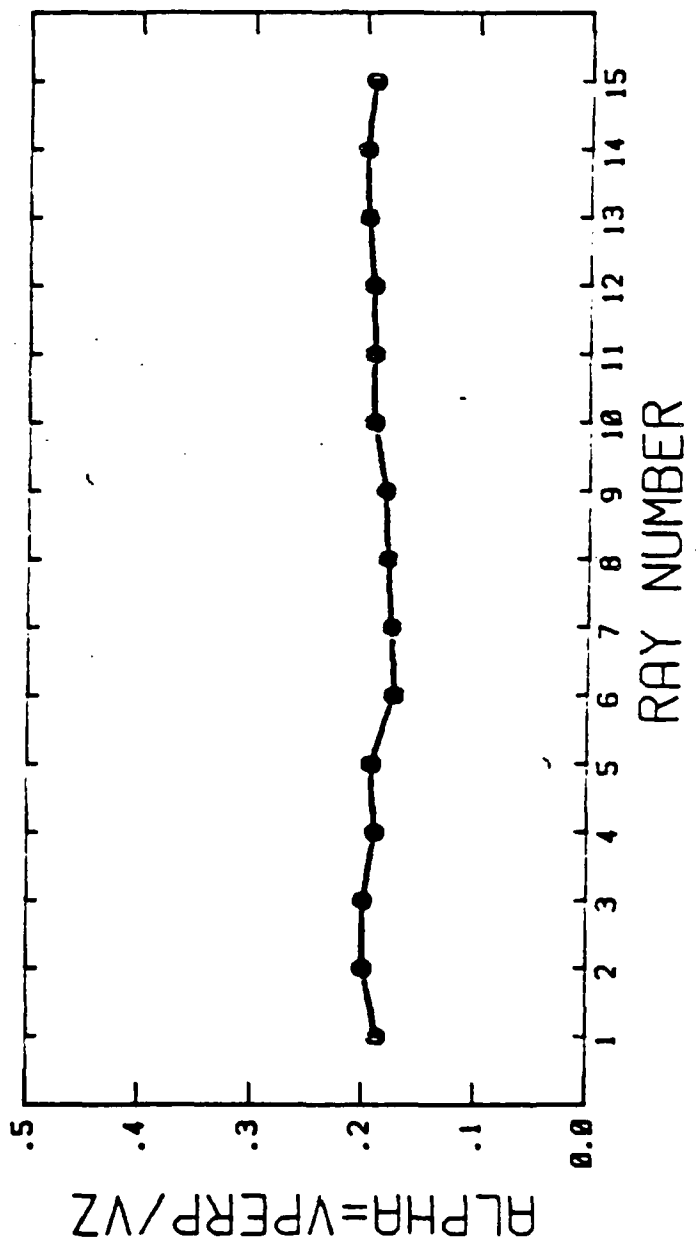


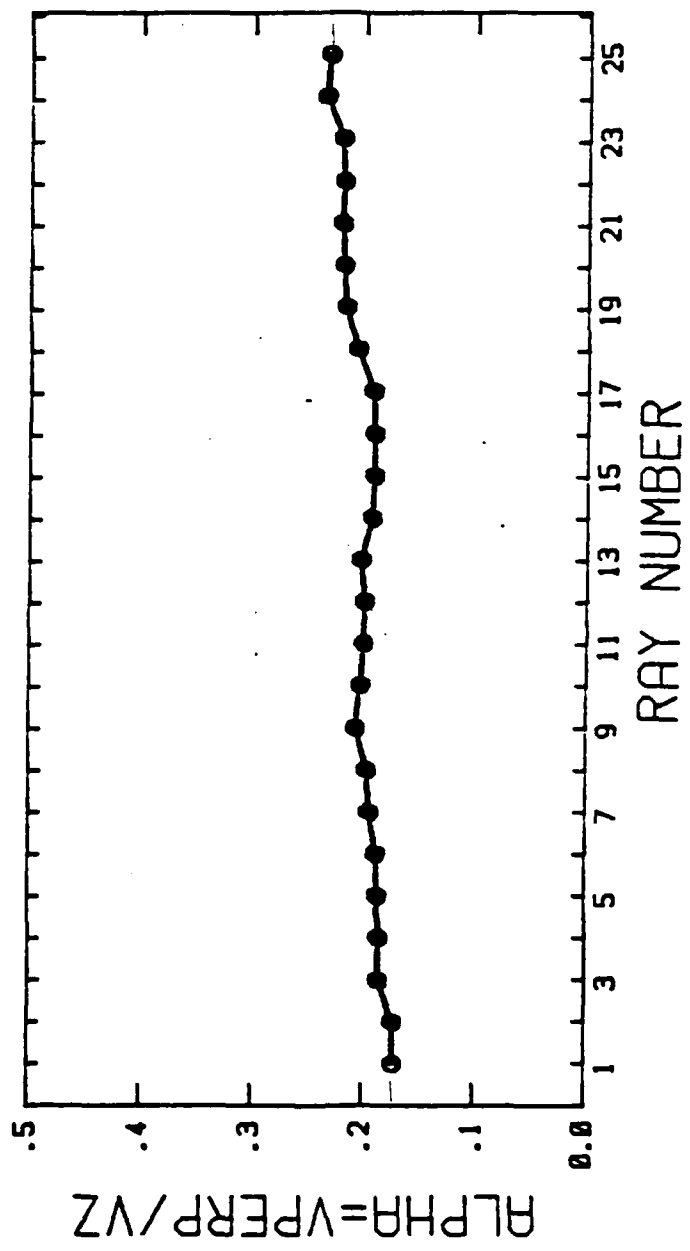




Reproduced from
best available copy.

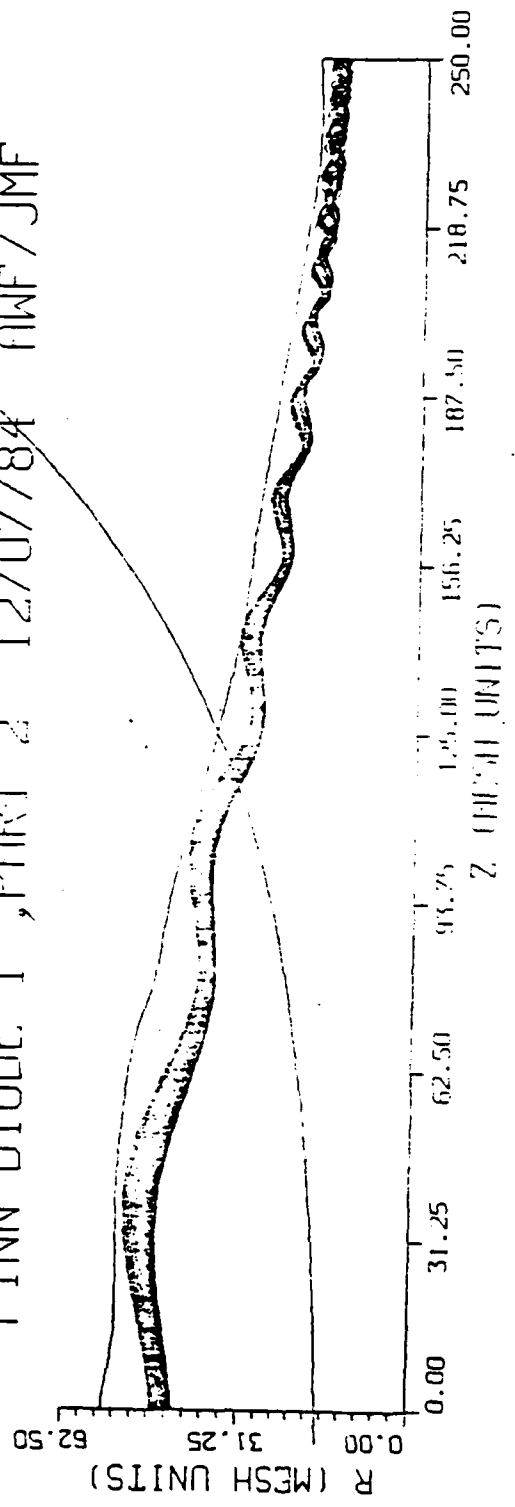




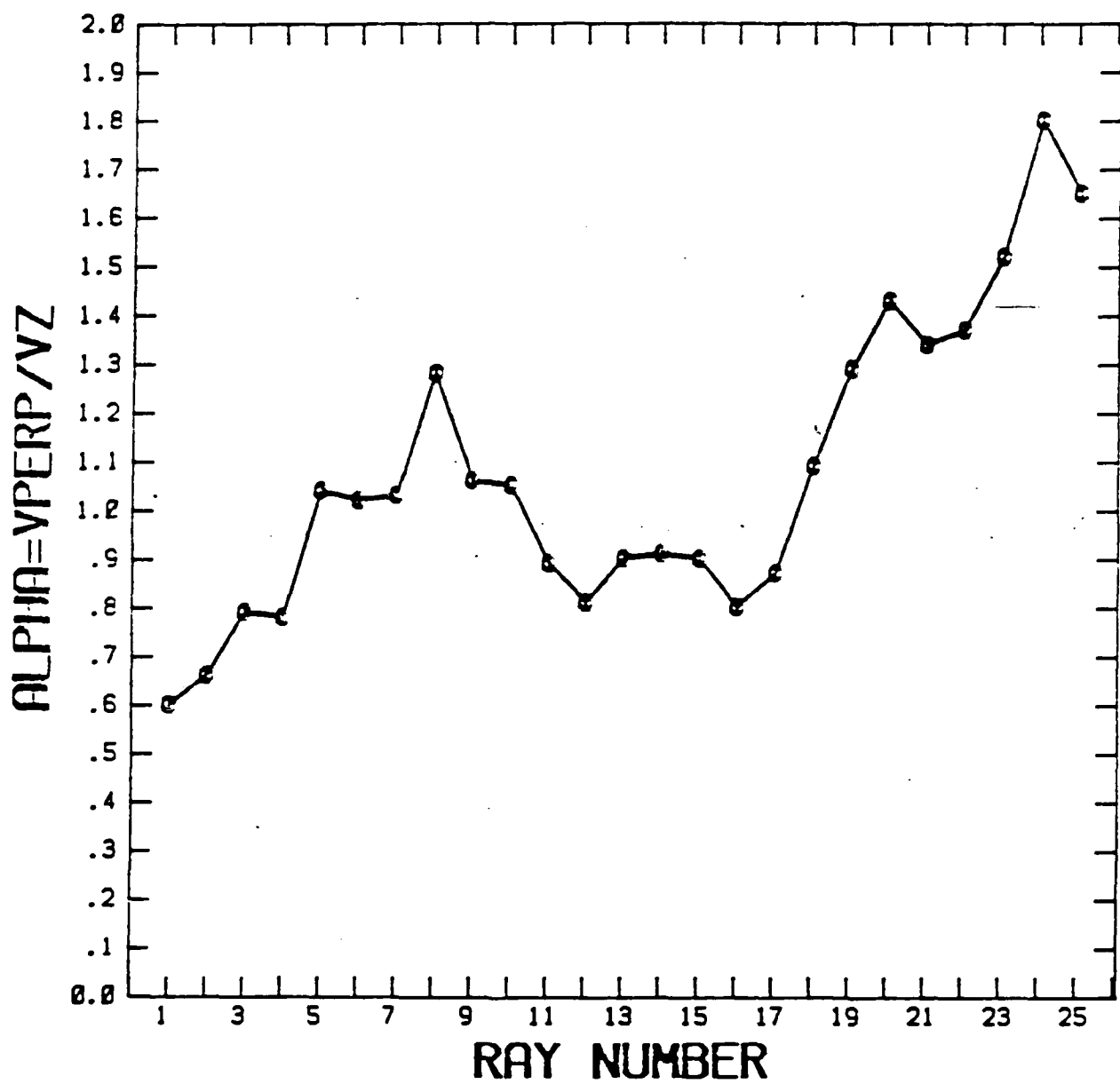


14-M
 0.0 4.4 8.8 13.1 17.5 21.9
 2(Z) G

FINN DIODE 1 , PART 2 12/07/84 FINF/JMF



Reproduced from
 best available copy.



APPENDIX N

COLLECTIVE INSTABILITIES AND HIGH-GAIN

REGIME IN A FREE ELECTRON LASER

COLLECTIVE INSTABILITIES AND HIGH-GAIN REGIME IN A FREE ELECTRON LASER

R. BONIFACIO*, C. PELLEGRINI

National Synchrotron Light Source, Brookhaven National Laboratory, Upton, NY 11973, USA

and

L.M. NARDUCCI

Physics Department, Drexel University, Philadelphia, PA 19104, USA

Received 5 April 1984

We study the behavior of a free electron laser in the high gain regime, and the conditions for the emergence of a collective instability in the electron beam-undulator-field system. Our equations, in the appropriate limit, yield the traditional small gain formula. In the nonlinear regime, numerical solutions of the coupled equations of motion support the correctness of our proposed empirical estimator for the build-up time of the pulses, and indicate the existence of optimum parameters for the production of high peak-power radiation.

Studies of the free electron laser (FEL) in the high gain regime have shown that with an appropriate selection of the electron density, detuning and undulator length, the radiation field and the electron bunching can undergo exponential growth as a result of a collective instability of the electron beam-undulator-radiation field system [1-8]. In this paper, we study the conditions for the onset of this instability using a new secular equation for the characteristic complex frequencies of the FEL system. On the basis of these results, we show how one can re-derive the small-signal gain formula and establish the conditions for its validity. We also consider the problem of the initiation of laser action and of the growth of the radiation field from noise, and propose a formula to evaluate the lethargy (build-up) time of the first pulse. Finally, we study the nonlinear regime of the FEL by numerical methods and obtain results that suggest the existence of an optimum efficiency of the device.

In the derivation of our working equations we select the phase and the energy as the basic electron variables, and assume the slowly varying phase and

* On leave from the University of Milano, via Celoria 16, Milano, Italy.

amplitude approximation for the radiation field as done also in earlier developments [9,10]. In the remainder of the paper we shall adopt the following notations: z represents the direction of propagation of the electron beam and of the electromagnetic wave; it also represents the undulator axis; x and y are the transverse coordinates; B_0 denotes the strength of the helical magnetic field, and λ_0 and N_0 the period length and the number of periods of the undulator, respectively; the undulator parameter is $\kappa = eB_0\lambda_0/(2\pi mc^2)$, where mc^2 is the electron rest energy; λ is the wavelength of the radiation field, γ is the electron energy in units of mc^2 , $\beta_z \approx 1$ is the longitudinal electron velocity and $\beta_p = \kappa/\gamma$ the amplitude of the transverse velocity; the electron phase, ϕ , relative to that of the electromagnetic wave, is connected to z and t by the relation $\phi = 2\pi z/\lambda_0 + 2\pi(z - ct)/\lambda$; the resonant energy γ_R is related to λ_0 , λ and κ by $\gamma_R^2 = \lambda_0(1 + \kappa^2)/2\lambda$, and, finally, the undulator frequency ω_0 is given by $\omega_0 = 2\pi c\beta_z/\lambda_0$.

With these notations, the FEL working equations can be written as [9,10]

$$\dot{\phi}_j = \omega_0(1 - \gamma_R^2/\gamma_j^2), \quad (1)$$

$$\dot{\gamma}_j = -\frac{e c \kappa}{2\pi c^2 \gamma_j} [\alpha \exp(i\phi_j) + \text{c.c.}] , \quad (2)$$

$$\left(\frac{\partial}{\partial z} + \frac{1}{c} \frac{\partial}{\partial t}\right) \alpha = 2\pi n_e \frac{\kappa}{\Sigma} \langle e^{-i\phi/\gamma} \rangle, \quad (3)$$

where j labels the j th electron in the beam ($j = 1, 2, \dots, N_e$, with N_e the total number of electrons); the average $\langle \dots \rangle$ is carried out over all electrons in a beam slice of length λ at the position $z - \langle \beta_z \rangle ct$, where $\langle \beta_z \rangle$ is the average longitudinal velocity. The remaining parameters have the following meaning: n_e is the electron beam longitudinal density at position $z - \langle \beta_z \rangle ct$, Σ is an effective beam transverse cross section describing the overlap of the beam with the radiation field whose amplitude E_0 and phase θ_0 have been combined in the complex amplitude $\alpha = iE_0 \exp(i\theta_0)$. It is important to stress that in this discussion γ is not restricted to be approximately equal to the resonant value γ_R , unlike earlier treatments of this problem. For the purpose of our subsequent analysis, it is convenient to rewrite eqs. (1.3) using the variables

$$z' = z - \langle \beta_z \rangle ct, \quad t' = t, \quad (4)$$

with the result:

$$(\partial/\partial t') \psi_j = \omega_0 (1 - \gamma_R^2/\gamma_j^2), \quad (5)$$

$$(\partial/\partial t') \gamma_j = \frac{e c \kappa}{2 m c^2 \gamma_j} [\alpha \exp(-i\phi_j) + \text{c.c.}], \quad (6)$$

$$\left[(1 - \langle \beta_z \rangle) \frac{\partial}{\partial z'} + \frac{1}{c} \frac{\partial}{\partial t'} \right] \alpha = 2\pi n_e(z') \frac{\kappa}{\Sigma} \langle e^{-i\phi/\gamma} \rangle. \quad (7)$$

The propagation term $(1 - \langle \beta_z \rangle) \partial/\partial z'$ in eq. (7) is important to describe the evolution of the pulse in the FEL, especially when the accumulated path difference $\Delta L \equiv L_{ph} - L_{el} = (c - v)t_{int}$ between the photons and the electrons during an interaction time is comparable to the length of the electron bunch itself. Note that the path difference ΔL can also be expressed in the form $ct_{int}(1 - \langle \beta_z \rangle) = \lambda_0 N_0 (1 - \langle \beta_z \rangle) = N_0 \lambda$. In this paper, we only consider situations where the length of the electron bunch is sufficiently larger than $N_0 \lambda$; thus, we neglect the propagation term and assume the local electron density $n_e(z')$ to be constant.

The linear stability analysis of eqs. (5)–(7) is greatly aided by the introduction of a suitable set of collective variables [8]. For this purpose, we first introduce the relativistic plasma frequency

$$\Omega_p = (4\pi r_e n_0 c^2/\gamma_0^3)^{1/2}, \quad (8)$$

where γ_0 is the initial energy, and r_e the classical electron radius, and the so-called Pierce parameter

$$\rho = (\frac{1}{2} \kappa (\gamma_0/\gamma_R)^2 \Omega_p / \omega_0)^{2/3}. \quad (9)$$

Furthermore, we introduce the quantity

$$\dot{\phi}_0 = \omega_0 (1 - \gamma_R^2/\gamma_0^2), \quad (10)$$

and rescale the time variable as follows:

$$\tau = 2\omega_0 \rho (\gamma_R/\gamma_0)^2 t. \quad (11)$$

In terms of the new scaled variables

$$\psi_j \equiv \phi_j - \dot{\phi}_0 \tau, \quad \Gamma_j \equiv \gamma_j / (\rho \gamma_0), \quad (12)$$

$$A \equiv \alpha \exp(i\dot{\phi}_0 \tau) / (4\pi m c^2 \gamma_0 n_0 \rho^2)^{1/2},$$

the nonlinear equations of motion (5)–(7) take the form

$$(d/d\tau) \psi_j = (1/2\rho)(1 - 1/\rho^2 \Gamma_j^2), \quad (13)$$

$$(d/d\tau) \Gamma_j = -(1/\rho)[(A/\Gamma_j) \exp(i\psi_j) + \text{c.c.}], \quad (14)$$

$$dA/d\tau = i\delta A + (1/\rho) \langle e^{-i\psi} / \Gamma \rangle. \quad (15)$$

Note that in terms of eqs. (13)–(15), the dynamics of the FEL is controlled by only two parameters, the Pierce parameter ρ (eq. (9)) and $\delta = \Delta/\rho$, where Δ is the usual detuning $(\gamma_0^2 - \gamma_R^2)/(2\gamma_R^2)$. Because we neglect space-charge forces, we shall assume in the following that ρ is sufficiently smaller than unity. It is also worth noting that eqs. (13)–(15) are consistent with the conservation law

$$L = |A|^2 + \langle \Gamma \rangle = \text{constant}, \quad (16)$$

or also

$$L = m c^2 n_0 \langle \gamma \rangle + E_0^2 / 4\pi = \text{constant}, \quad (16')$$

which can be readily recognized as the conservation of energy for the electron beam-radiation field system. The method devised to analyze the stability of the system is based on the procedure suggested in ref. [8]. The equations are linearized around the equilibrium state $A_0 = 0$, $\Gamma_{0j} = 1/\rho$, $\langle \exp(-i\psi_0) \rangle = 0$ and perturbed by letting $A = a$, $\Gamma_j = (1/\rho)(1 + \eta_j)$ and $\psi_j = \psi_{0j} + \delta \psi_j$. The linearized equations form the basis for a closed form linear system of equations for the collective variables

$$x = \langle \delta \psi \exp(-i\psi_0) \rangle, \quad (17)$$

$$z = (1/\rho)\langle \eta \exp(-i\psi_0) \rangle, \quad (18)$$

and for the field perturbation a . These take the form

$$dx/dr = y \quad (19)$$

$$dy/dr = -a, \quad (20)$$

$$da/dr = -i\delta a - ix - \rho y. \quad (21)$$

Nontrivial solutions with a time dependence of type $\exp(i\lambda r)$ exist if and only if λ is a solution of the characteristic equation

$$\lambda^3 - \delta\lambda^2 + \rho\lambda + 1 = 0. \quad (22)$$

The results of earlier analyses [1-8] can be recovered by setting formally $\rho = 0$ in eq. (22). Clearly, exponential growths, and thus, unstable behavior, results if the cubic equation (22) has one real and two complex conjugate roots. In this case, the imaginary part of the eigenvalue measured the rate of growth of the unstable solution. The instability condition can be easily derived from eq. (22): in terms of the parameters ρ and δ it takes the form (fig. 1)

$$\rho^2 - \frac{1}{4}\rho^2\delta^2 + \frac{9}{2}\rho\delta - \delta + \frac{27}{4} > 0. \quad (23)$$

The typical behavior of the eigenvalues of eq. (22) as a function of detuning is shown in fig. 2. The eigenvalues are real when δ exceeds a certain threshold value that depends on ρ according to eq. (23), while two of the eigenvalues form a complex conjugate pair when $\delta < \delta_{thr}$.

The small signal gain formula emerges in a natural way from our analysis in the limit $\rho \rightarrow 0$, and for suf-

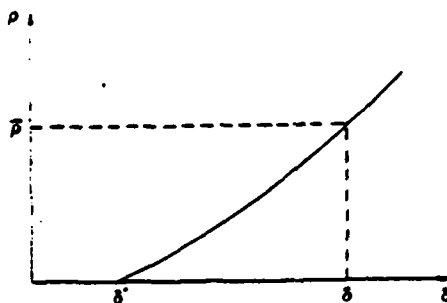


Fig. 1. Instability boundary in the (ρ, δ) plane. For $\delta < \delta_{thr}$, the solutions of eqs. (13)-(15) are unstable for all values of ρ . For selected values of ρ (e.g., $\bar{\rho}$ in the figure) unstable behavior occurs for $\delta < \delta_{thr}$.

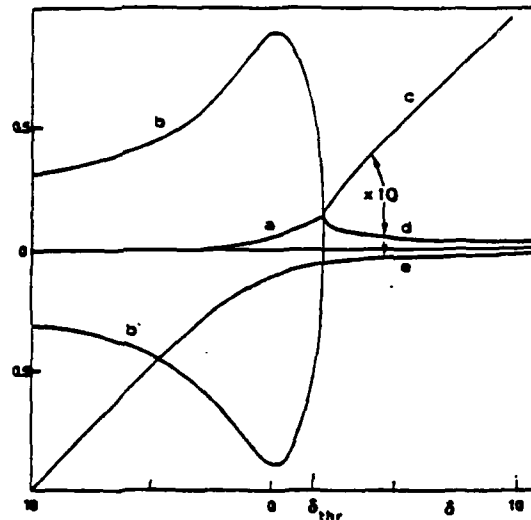


Fig. 2. The behavior of three eigenvalues of the secular equation as a function of the detuning parameter δ and for $\rho = 0.1$. The vertical axis labels both the real and imaginary parts. The real parts have been scaled by a factor of 10 to fit the display. For a sufficiently positive value of δ (i.e., $\delta > \delta_{thr}$) the eigenvalues are real (curves c, d, e). At threshold, two of the real eigenvalues degenerate into one, while, for the same value of δ , the imaginary parts (curves b, b') become different from zero. The real part of the complex conjugate eigenvalues for $\delta < \delta_{thr}$ is labelled by a.

ficiently large values of $|\delta|$. In this limit, the eigenvalues take the approximate form

$$\lambda_1 \approx \delta(1 - 1/\delta), \quad \lambda_{2,3} \approx \pm 1/\delta^{1/2}, \quad \delta > 0,$$

$$\lambda_1 \approx \delta(1 - 1/\delta), \quad \lambda_{2,3} \approx \pm 1/|\delta|^{1/2}, \quad \delta < 0, \quad (24)$$

as one can confirm qualitatively from fig. 2. The output field $A(r)$ in the linear regime can be calculated as a linear superposition of elementary exponential functions whose coefficients are to be fixed from the initial conditions. A lengthy, but straightforward calculation yields the following expressions for the small signal gain:

$$G \equiv [|A(r)|^2 - |A_0|^2] / |A_0|^2$$

$$= (4/\delta^3)(1 - \cos \delta r \cos r/\sqrt{\delta}$$

$$- \frac{1}{2}\delta^{3/2} \sin \delta r \sin r/\sqrt{\delta}), \quad \delta > 0,$$

$$G = (4/\delta^3)(1 - \cos \delta\tau \cosh \tau/\sqrt{|\delta|} - \frac{1}{2}|\delta|^{3/2} \sin \delta\tau \sinh \tau/\sqrt{|\delta|}), \quad \delta < 0. \quad (25)$$

In order to make contact with the usual small-signal gain formula, it is not enough to require that $|\delta|$ be sufficiently larger than unity, but one also must impose the condition $\tau/\sqrt{|\delta|} \ll 1$. In this case, eq. (25) becomes

$$G \approx (4/\delta^3)(1 - \cos \delta\tau - \frac{1}{2}\delta\tau \sin \delta\tau) \quad (26)$$

which, in fact, agrees with the standard expression for G .

In spite of the fact that the equations of motion of the FEL are nonlinear, some aspects of this problem can be handled accurately by analytic means. The evolution below threshold ($\delta > \delta_{\text{thr}}$) is governed by the linear approximation. In this regime, the eigenvalues are real (see fig. 2) and the output field displays small amplitude oscillations when plotted as a function of time. On varying δ , beat patterns or more complicated-looking modulation effects can be observed, whose origin can be understood entirely in terms of the eigenvalues of the linearized problem. A representative example is shown in fig. 3. It may be worth mentioning that while the trace in fig. 3 has been obtained by the appropriate superposition of exponential functions, the exact solution of eqs. (13)–(15) is indistinguishable on the scale of this graph.

The system evolution above threshold ($\delta < \delta_{\text{thr}}$)

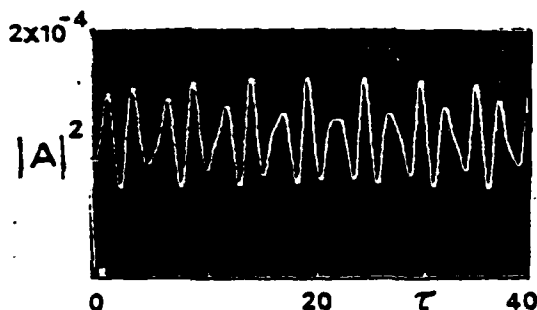


Fig. 3. Output intensity $|A|^2$ for $\rho = 0.01$ and $\delta = 4.0$. The eigenvalues of the linearized equations are -0.519 , 0.628 , 3.066 . The modulation is due to the beat of the different exponential terms in the solution.

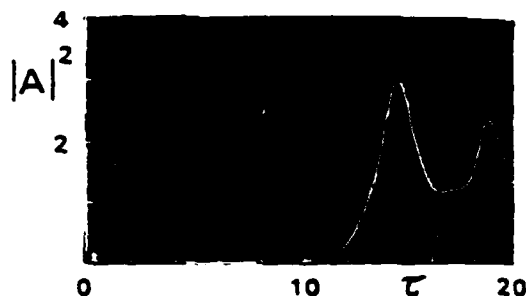


Fig. 4. Output intensity $|A|^2$ versus time above threshold. The parameters used in this simulation are $\rho = 0.0021$, $\delta = 1.86$, $n_0 = 16$.

is entirely different, and is shown in fig. 4 for the case of zero initial field and an initial bunching parameter $(\exp(-i\psi_0))$, small, but different from zero. Under unstable conditions, fluctuations in the electrons injection velocities, or the lack of uniformity in the initial distribution of the electron phase variables, or the presence of an initial field will trigger the growth of a signal. The signal will then grow to a peak value after which it oscillates. This behavior is very general and is independent of the initial triggering mechanism as long as this perturbation is small. This nonlinear regime requires numerical integration of the full equations of motion. This we have done for a number of values of ρ and δ .

Because of the nature of the triggering mechanism, intuitively, one would expect that the time required for the initial pulse to build up (lethargy time) should be a fairly sensitive function of the magnitude of the initial fluctuation. We have examined the dependence of the build up time of the first pulse on the initial value of the bunching parameter, and verified that (a) a significant fraction of the build up process is well described by the linearized equations; and (b) the arrival time of the first peak is well described by the formula:

$$\tau_{\text{peak}} = -(1/\text{Im } \lambda) \ln |\exp(-i\psi_0)| + 1. \quad (27)$$

A test of this equation is provided in fig. 5, where we have plotted the arrival time of the first pulse calculated from the nonlinear equations of motion (13)–(15), as a function of the initial bunching parameter $|\exp(-i\psi_0)|$. One aspect of considerable interest for

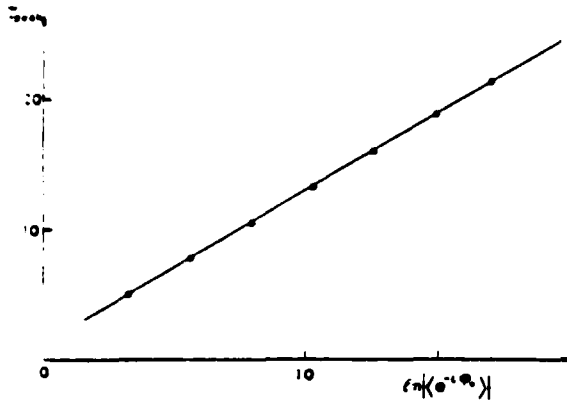


Fig. 5. The arrival time of the first peak (lethargy time) is plotted as a function of the logarithm of the initial bunching parameter (dots). The solid curve corresponds to eq. (26). The parameters used in this scan are $n_0 = 8$, $\rho = 0.4$, $\delta = 1.25$.

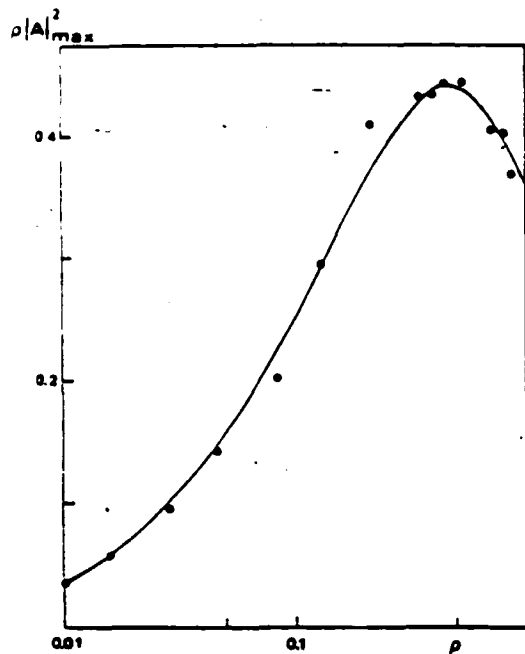


Fig. 6. Dependence of the peak output intensity $\rho|A|_{\max}^2$ on ρ in the neighborhood and just above the instability boundary line of fig. 1. The solid line is only a qualitative average of the points.

the purpose of optimizing the system's parameters is the existence of a maximum peak power output as a function of ρ and δ . We have verified that while the maximum growth rate is obtained for $\delta \approx 0$, the maximum peak amplitude of the first pulse occurs for $\delta \approx \delta_{\text{thr}}$. Thus, we have scanned the (ρ, δ) plane in the neighborhood of, but above, the threshold line and for $A_0 = 0$, and recorded the peak output intensity $\rho|A|_{\max}^2$ as a function of ρ (fig. 6). Notice that it follows from eq. (16) that $\rho|A|^2 = (\gamma_f - \gamma_0)/\gamma_0$, so that $\rho|A|^2$ gives the energy transfer from the electrons to the radiation. The scatter of the points is almost certainly due to the slight variations of the conditions from run to run. The solid line, which is only a qualitative average through the points, suggests the existence of an optimum gain-detuning condition such that the efficiency of the system is maximum for operation just above threshold. It is clear that in the presence of efficiencies as large as, in principle, 40%, the old approximate treatments [1-8] in which the electron momentum is assumed to vary only by small amounts cannot be adequate to describe situations where such large energy exchanges take place between the electron beam and field. On the other hand, it is intuitively obvious that for sufficiently small values of the Pierce parameter, the electron energy will suffer only a limited depletion so that earlier treatments should be sufficiently accurate.

Acknowledgements

One of us (LMN) wishes to acknowledge the support of the Army Research Office and the Research Laboratories of the Martin-Marietta Corporation. We wish to thank Dr. J. Murphy for many useful discussions. The help of H. Sadiky with some of the numerical computations is also gratefully acknowledged. This work has been partially supported by the U.S. Department of Energy.

References

[1] N.M. Kroll and W.A. McMullin, Phys. Rev. A17 (1978) 300.
 [2] A. Gover and Z. Livni, Optics Comm. 26 (1978) 375.
 [3] I.B. Bernstein and J.L. Hirschfeld, Phys. Rev. A20 (1979) 1661.

- [4] C.C. Shi and A. Yariv, *IEEE J. Quantum Electron.* QE17 (1981) 1387.
- [5] P. Sprangle, C.M. Tang and W.M. Manheimer, *Phys. Rev. A* 20 (1980) 302.
- [6] G. Dattoli, A. Marino, A. Renieri and F. Romanelli, *IEEE J. Quantum Electron.* QE17 (1981) 1371.
- [7] A. Gover and P. Sprangle, *IEEE J. Quantum Electron.* QE17 (1981) 1196.
- [8] R. Bonifacio, F. Casagrande and G. Cascati, *Optics Comm.* 40 (1982) 219.
- [9] W.B. Colson and S.K. Ride, in: *Physics of quantum electronics*, Vol. 7, eds. S.F. Jacobs et al. (Addison-Wesley, Reading, MA 1980) p. 377.
- [10] C. Pellegrini, in: *Free electron lasers*, eds. A.N. Chester and S. Martellucci (Plenum Press, NY 1983) p. 91.
- [11] M. Abramowitz and I.A. Stegun, *Handbook of mathematical functions* (Dover Publications, NY, 1970) eq. (3.8.2), p. 17.

APPENDIX O

FREE ELECTRON LASERS FOR THE
XUV SPECTRAL REGION

FREE ELECTRON LASERS FOR THE XUV SPECTRAL REGION *

J.B. MURPHY and C. PELLEGRINI

National Synchrotron Light Source, Brookhaven National Laboratory, Upton, NY 11973, USA

The generation of high intensity coherent radiation in the soft X-ray region from a free electron laser will require the FEL to operate in the high gain or collective instability regime. In this mode of operation, which does not require a cavity resonator, the radiation field grows exponentially along the undulator until nonlinear effects bring on saturation. We discuss the conditions that the electron beam and the undulator must satisfy for the collective instability to develop. We present an example of an electron storage ring with an undulator in a bypass section which satisfies these conditions. We present estimates of the output power that one can expect from such systems.

1. Introduction

The interest sparked by the operation of the first free electron laser (FEL) by Madey and his collaborators in 1975 has led to some exciting results [1-6]. In the last two years remarkable progress has been made toward the realization of the FEL as a source of high power, tunable, coherent radiation. FEL oscillators and amplifiers have been operated at wavelengths varying from the centimeter to the near ultraviolet and at peak power levels up to a hundred megawatts. This wealth of experimental results is due to researchers at numerous laboratories: MSNW, TRW-Stanford, LASL, LBL-LLNL, MIT, NRL, Columbia-NRL, UC-Santa Barbara, Orsay and Frascati.

The theory of FELs has at the same time reached a high level of completeness and is in good agreement with the experimental results. As a result of the experimental and theoretical progress we now have a good understanding of the physics and technology of FELs, which can be used to design systems operating in new wavelength regions, like the XUV spectral region.

The possibility of building a FEL operating at wavelengths shorter than 1000 Å is a result of the progress made in producing high density relativistic electron beams using electron storage rings. Storage rings specially designed for FEL applications and capable of accommodating undulators magnets 5 to 15 m long, should offer the possibility of producing coherent radiation down to a few hundred Angstrom with average powers of the order of watts and peak powers up to hundreds of megawatts. One such ring is being built at Stanford University [7], while similar rings are also being studied at other laboratories [8,9]. In this paper we want to briefly review the different operation modes of an FEL in the XUV region (sects. 2-4), we will then discuss in more detail, the self amplified spontaneous emission mode (sects. 5-9).

2. Principle of operation

In a FEL a relativistic electron beam and an electromagnetic wave traverse an undulator. The coupling of the wave and the transverse electron current, induced by the undulator, can produce an energy transfer between the beam kinetic energy and the radiation field energy if a synchronism condition is satisfied. This condition relates the radiation field wavelength λ , the undulator period λ_u , the undulator field B_u , and strength parameter $K = e\lambda_u B_u / 2\pi mc^2$, and the beam energy γ measured in rest energy units [10]:

$$\lambda = \frac{\lambda_u}{2\gamma^2} (1 + K^2). \quad (1)$$

Notice that this wavelength is also the wavelength at which the spontaneous radiation from an electron traversing an undulator is emitted [11].

An important property of the FEL is that the energy transfer between the beam and the radiation can be enhanced by a collective instability producing an exponential growth of the radiation [12]. When this instability becomes important the FEL is said to operate in the high gain regime. The existence of this regime is very important for FEL operation in the XUV region where we do not have optical components with sufficiently high reflectivity and small absorption [13].

Three modes of operation of an FEL can be considered. In the first mode, self amplified spontaneous emission (SASE), the initial spontaneous radiation emitted by the electrons is amplified; this system does not require any optical components but needs a high density electron beam and a rather long undulator [8,12].

The second mode is the FEL oscillator; an optical cavity is used to reflect back and forth the radiation for further amplification by another electron bunch; this system can get by with a smaller electron beam density and a shorter undulator but needs mirrors for the cav-

ity at wavelengths smaller than 1000 Å these mirrors have yet to be developed and their reflectivity is expected to be on the order of 50%.

In the third mode, or transverse optical klystron [14], an external laser beam at the spontaneous radiation wavelength is used to modulate the beam energy and longitudinal density distribution leading to the emission of coherent radiation at the higher harmonics of the input laser. Of the three modes this is the one requiring the least stringent electron beam parameters. In addition it does not need optical elements but on the other hand it requires an undulator with rather strict magnetic field tolerances and produces the smallest coherent radiation power.

3. FEL growth rate

In all three modes the FEL can be approximately characterized by one parameter, the FEL e-folding length, $4\pi\rho$, measured in number of undulator periods N_u [12]

$$4\pi\rho = 4\pi \left(\frac{K\lambda_0\Omega_p}{8\pi c} \right)^{-2/3} \quad (2)$$

where Ω_p is the electron beam plasma frequency, defined in terms of the electron density n_0 , and energy γ , by

$$\Omega_p = (4\pi r_e c^2 n_0 / \gamma^3)^{1/2} \quad (3)$$

r_e being the classical electron radius.

For an oscillator to operate at short wavelength, where the optical cavity losses can be on the order of 100% per round trip, one needs a value of $4\pi\rho N_u$ on the order of 1, i.e. a number of undulator periods

$$N_u = 1/(4\pi\rho).$$

In the case of SASE [12] the value of $4\pi\rho N_u$ must be on the order of 10.

In the case of SASE and oscillator modes the energy transfer from the beam to the radiation field is on the order of ρ , while in the TOK case the transfer from the input laser to the harmonics is rather small.

The expression (2) for the FEL growth rate applies only if two other conditions on the electron beam are satisfied. One is a condition on the beam energy spread, which must be less than ρ ; the second is a condition on the beam emittance, which must be smaller than the radiation wavelength. If these conditions are not satisfied the radiation growth rate decreases and the output laser power is reduced [8].

For wavelengths in the millimeter region and electron energy of a few MeV the value of ρ can be on the order of 1. In the VUV region with electron energies of several hundred MeV, ρ is on the order of 10^{-3} and one can expect an energy transfer from the beam to the radiation on the order of a few parts in a thousand.

4. The SASE mode

In the wavelength region below 1000 Å, the best accelerators available to produce the high density electrons beams required to operate in the SASE mode are electron storage rings. Existing storage rings, such as the VUV ring of the National Synchrotron Light Source at Brookhaven, can provide an average emittance on the order of 10^{-5} mrad, an energy spread of about 10^{-3} and a peak current of 60 A at an energy of 750 MeV [15]. A ring like this, with straight sections capable of accommodating undulators of 5 to 6 m, would allow us to produce coherent radiation in the 1000 Å region.

We believe that it is now possible to design a storage ring with an energy of 700 to 1000 MeV, the same energy spread and an emittance smaller by an order of magnitude than that of the VUV ring, and peak currents in the range of 100 to 200 A. Such a ring would enable us to produce radiation in the wavelength range of 100 to 500 Å using undulators about 10 m long [7-9].

Using this ring, the peak radiation power that one can obtain in the SASE mode is on the order of 10^{-3} times the beam peak power, or 100 MW. This pulse would have a duration of about 100 ps and a repetition rate of 10 Hz, for an average radiation power of 0.1 W.

With the same system operating in the oscillator mode, one can obtain an average output power of the order of 1 W, a pulse duration of about 100 ps and a repetition rate determined by the ring revolution time to be on the order of a few MHz, and a peak power of about 10 kW. For this oscillator it is also possible, by modulating the system gain, to reduce the repetition rate and increase the peak power.

For the TOK mode one can expect conversion efficiencies on the order of 10^{-6} around the tenth harmonic, so that starting with a 100 MW peak power laser at 2000 Å one should be able to produce about 100 W at around 200 Å.

In all of these cases the angular distribution of the radiation is determined by the electron beam radius, a , and the radiation wavelength; the characteristic angle is on the order of λ/a , i.e. of a few tenth of milliradians. The line width is on the order of the wavelength divided by the electron bunch length, i.e. 10^{-6} - 10^{-5} , for the oscillator and the TOK mode. For the SASE mode it depends on the details of the system and is intermediate between the oscillator limit and the inverse of the number of periods in the undulator, i.e. between 10^{-3} and 10^{-5} .

5. FEL equations

In the remainder of this paper we will discuss the high gain regime and the SASE mode of operation of an FEL. Following the work of other authors [16,17] we

write the FEL equations using the phase and energy as electron variables and use the slowly varying amplitude and phase approximation for the radiation field. These equations can be written in a very general form including the effects of space-charge fields and higher harmonics of the radiation field [13]. To simplify our discussion we neglect these terms and use the results of ref. [13] to evaluate their effects. Our notations are the following: z is the electron beam and electromagnetic wave direction of propagation; x and y are the transverse coordinates; B_0 is the undulator magnetic field (we use a helical undulator for simplicity) and λ_0 , N_u are its period and length in number of periods respectively; λ is the wavelength of the radiation field; γ is the electron energy in units of m_0c^2 ; $\beta_z = 1$ is the longitudinal electron velocity and $\beta_\perp = K/\gamma$ the amplitude of the transverse velocity; the electron phase relative to the electromagnetic wave, ϕ , is related to z and t by $\phi = 2\pi z/\lambda_0 - 2\pi(z - ct)/\lambda$; the resonant energy γ_R is related to λ_0 , λ and K by $\gamma_R^2 = \lambda_0(1 - K^2)/2\lambda$; the undulator frequency ω_0 is $\omega_0 = 2\pi c\beta_z/\lambda_0$; the amplitude, E_0 , and phase, θ_0 , of the radiation field are combined to yield a complex amplitude $\alpha = iE_0e^{i\theta_0}$.

To write the FEL equations it is convenient to use a set of normalized variables and introduce some quantities to characterize the beam properties [12,13]. We will use the relativistic beam plasma frequency already introduced in sect. 3, which for a beam with energy dispersion is given by

$$\Omega_p = \left(\frac{4\pi r_e n_0 c^2}{\langle \gamma_0 \rangle^3} \right)^{1/2} \quad (4)$$

where $\langle \gamma_0 \rangle$ is the average value of the initial electron energy; we introduce also the quantities

$$\rho = \left[\frac{K}{4} \left(\frac{\langle \gamma_0 \rangle}{\gamma_R} \right)^2 \frac{\Omega_p}{\omega_0} \right]^{2/3} \quad (5)$$

and

$$\phi_0 = \omega_0 \left(1 - \frac{\gamma_R^2}{\langle \gamma_0 \rangle^2} \right) \quad (6)$$

and a normalized time

$$\tau = 2\omega_0 \rho \left(\frac{\gamma_R}{\langle \gamma_0 \rangle} \right)^2 t. \quad (7)$$

Using these definitions we can construct a set of dimensionless variables

$$\psi = \phi - \phi_0 t. \quad (8)$$

$$\Gamma = \frac{1}{\rho} \frac{\gamma}{\langle \gamma_0 \rangle}. \quad (9)$$

$$A = \frac{\alpha \exp(i\phi_0 t)}{[4\pi mc^2 \langle \gamma_0 \rangle n_0 \rho]^{1/2}}. \quad (10)$$

and write the FEL equations as [12]

$$\dot{\psi}_i = \frac{1}{2\rho} \left(1 - \frac{1}{\rho^2 \Gamma_i^2} \right), \quad i = 1, 2, \dots, N, \quad (11a)$$

$$\dot{\Gamma}_i = -\frac{1}{\rho} \left(\frac{4e^{i\psi}}{\Gamma_i} - \text{c.c.} \right), \quad (11b)$$

$$\dot{A} = i\delta A + \frac{1}{\rho} \left\langle \frac{e^{-i\psi}}{\Gamma_i} \right\rangle, \quad (11c)$$

with

$$\delta = \Delta/\rho, \quad (11d)$$

and Δ the detuning parameter

$$\Delta = (\gamma_0^2 - \gamma_R^2)/2\gamma_R^2. \quad (11e)$$

The dot indicates differentiation with respect to τ . The angular brackets indicate an average over the particle initial phases, i.e. $\langle \cdot \rangle = (1/N)\sum$, where N is the number of particles.

From these equations we can show that the quantity:

$$H = \langle \Gamma \rangle + |A|^2 \quad (12)$$

is an invariant. In terms of laboratory variables this can be written as

$$\bar{H} = mc^2 n_0 \langle \gamma \rangle + \frac{E_0^2}{4\pi} = \text{constant}, \quad (13)$$

which is seen to be the conservation of energy relation for the electron beam-radiation field system. It is also convenient, using eq. (9), to rewrite eq. (12) as

$$\left\langle \frac{\gamma - \langle \gamma_0 \rangle}{\langle \gamma_0 \rangle} \right\rangle = \rho (|A|^2 - |A_0|^2), \quad (14)$$

which relates directly the change in the field amplitude A to the average change in electron energy. One can see from eq. (14) that, assuming $|A_0| \ll |A|$, the quantity $\rho |A|^2$ measures the efficiency of energy transfer from the electron beam to the radiation field.

In integrating the FEL equations the maximum time is defined by the undulator length $t_{\text{max}} = N_u \lambda_0/c$. In terms of the scaled time τ this becomes

$$\tau_{\text{max}} = 4\pi\rho \left(\frac{\gamma_R}{\langle \gamma_0 \rangle} \right)^2 N_u. \quad (15)$$

6. The FEL collective instability and coherent radiation generation

The system of eqs. (11a)-(11c) has been discussed in ref. [12] where it has been shown that for $\delta < \delta_{\text{th}} = 1.9$ the system is unstable and the field amplitude A grows exponentially. Both the radiation field and the beam bunching grow exponentially. We can characterize the bunching by the parameter $b = |\langle e^{-i\psi} \rangle|$. The nonlinear

I. THEORY

regime and saturation that follow the initial exponential growth have also been studied in these papers.

In this paper we want to discuss a collectively unstable system using the parameters that apply to an electron beam obtained from a storage ring.

We assume that the initial field amplitude is zero and we introduce an initial noise in the electron phase distribution so that the initial value of $b = \langle |e^{i\phi}| \rangle$ is $1/\sqrt{N_0}$, N_0 being the number of electrons in one radiation wavelength. In fig. 1 we show the evolution of the field amplitude $|A|$ versus τ , for different values of the initial electron beam rms energy spread, σ_{e0} , and for $\delta = 0$. One can see that for $\sigma_{e0} \ll \rho$ the field amplitude $|A|$ reaches a value of the order of unity, so that, from eq. (14), we have an energy transfer efficiency of the order of ρ , i.e., at the peak of $|A|$ we have transferred a fraction ρ of the beam energy to the radiation field.

Fig. 2 shows the evolution of the rms beam energy spread for the same values of σ_{e0} as in fig. 1. One can see that when the field peaks the energy spread becomes on the order of ρ provided $\sigma_{e0} \leq \rho$.

The time needed to reach the peak can be seen from figs. 1 and 2 to be $\tau = 10$. Assuming $\gamma_s = \gamma_R$ we can see from eq. (15) that to reach the peak we need an undulator with a number of periods $N_u = 1/\rho$.

Let us summarize the results of this section:

1) the electron beam, undulator magnet, radiation field system is unstable, if $\delta < \delta_{th}$, and both the field amplitude, $|A|$, and the beam bunching, b , will grow exponentially up to a saturation level where $|A| = 1$ and $b = 1$;

2) if the system initial conditions are $|A_0| = 0$, b_0 , determined by noise, $\sigma_{e0} < \rho$, the electron beam will transfer a fraction ρ of its energy in a number of undulator periods of the order of $1/\rho$.

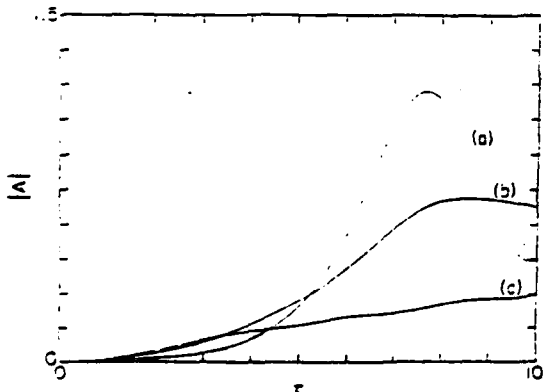


Fig. 1. Plot of $|A|$ versus τ for $b = 9.1 \times 10^{-3}$, $\rho = 3 \times 10^{-3}$ and several values of the initial rms energy spread, $\sigma_{e0} = 0.1 \rho$, 0.75ρ and ρ , labeled a, b and c, respectively.

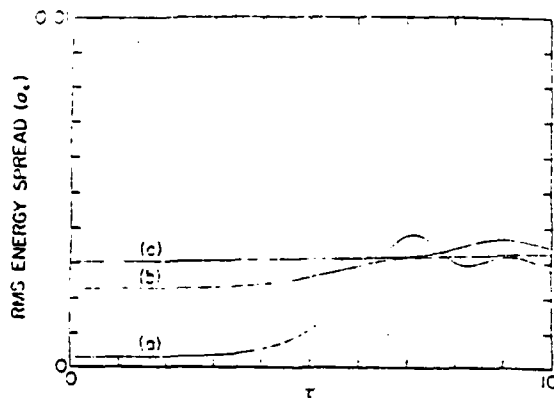


Fig. 2. Plot of σ_e versus τ for $b = 9.1 \times 10^{-3}$, $\rho = 3 \times 10^{-3}$ and several values of the initial rms energy spread, $\sigma_{e0} = 0.1 \rho$, 0.75ρ and ρ , labeled a, b and c, respectively.

3) after traversing the undulator we have $|A| = 1$, $b = 1$ and $\sigma_e = \rho$.

7. The electron beam-undulator system

As we wish to discuss the operation of an FEL over a large wavelength range (30–2000 Å) we will consider operating the storage ring at energies ranging from 300–500 MeV. In addition we will consider 3 undulator designs, a 5 mm period undulator for λ in the range of 30–100 Å, a 1 cm period undulator for λ in the range of 100–250 Å and one with $\lambda_u = 2.5$ cm for λ in the range of 500–2000 Å.

To calculate the undulator properties we assume it to be of the hybrid (permanent magnet and iron) type and calculate the magnetic field from [19]

$$B_0 = 3.33 \exp\left(-5.47 \frac{g}{\lambda_0} + 1.3 \frac{g^2}{\lambda_0^2}\right) \text{ T.} \quad (16)$$

where λ_0 and g are the period and the gap, respectively. A complete listing of the undulator data can be found in table 1. The output radiation wavelengths for the 3 undulators are signified by \square 's in figs. 5a–5c.

The electron beam described in table 2 can be obtained in a storage ring, as we discussed in sect. 5. However, if we tried to install the undulators described

Table 1
Undulator magnets

Period, λ_0 (cm)	0.5	1.0	2.5
Gap, g (cm)	0.1	0.2	0.5
Pump strength, B_0 (T)	1.2	1.2	1.2
Undulator parameter, K	0.56	1.12	2.80

Table 2
Electron beam parameters in the bypass section

Energy E (MeV)	500.00	400	300.00
Beta horizontal, β_x (m)	3.00	3.00	3.00
Beta vertical, β_y (m)	1.00	1.00	1.00
Coupling, χ	0.01	0.01	0.01
rms horizontal beam radius, σ_x (m)	1.01E-04	8.10E-05	6.07E-05
rms horizontal angular spread, σ'_x (rad)	3.37E-05	2.70E-05	2.02E-05
rms vertical angular spread, σ'_y (rad)	5.81E-06	4.65E-06	3.49E-06
rms vertical beam radius, σ_y (m)	5.81E-06	4.65E-06	3.49E-06

in table 1 directly in the ring such that the electron beam would pass through the small aperture of the undulator on each revolution, it would become impossible to operate the ring. The small aperture (gap) of the undulator would result in vanishing small beam lifetimes due to collisions with undulator walls. The minimum allowable gap depends on both the ring and undulator parameters and must be determined experimentally.

For this reason we propose to install the undulator in a ring bypass, as shown in fig. 3. The electron beam would normally circulate in the ring, where the effect of synchrotron radiation damping would produce the beam properties of table 2. About once per damping time, of the order of 50 ms for the storage ring illustrated in table 3, the beam is taken into the bypass and focused in the undulator by a special quadrupole triplet. In going through the undulator the electron beam produces the radiation, its energy is decreased by ρE_T and its energy spread increases from its initial value to about ρ . The beam is then taken back into the storage ring and

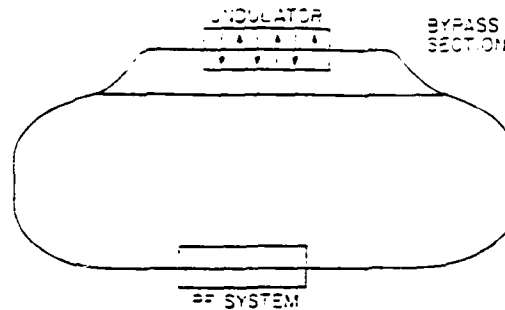


Fig. 3. Sketch of storage ring and bypass section

left there for a time long enough for synchrotron radiation damping to bring its characteristics back to their starting value. A more detailed discussion of the storage ring and bypass system is given in the next section.

As the electron beam circulates in the ring it performs both vertical and horizontal oscillations, the so-

Table 3
Storage ring parameters

Energy, E (MeV)	500	400	300
Gamma, γ	978	752	587
Bending radius, R_b (m)	4	4	4
Average radius, R_{av} (m)	15	15	15
Number of achromatic bends, M	6	6	6
RF voltage, V (MV)	1	1	1
Harmonic number, h	100	100	100
Number of bunches	1	1	1
Average current, I_0 (A)	0.10	0.10	0.10
Electron number, N	1.97+11	1.97E-11	1.97E+11
Synchronous phase, α_s	1.38E-03	5.67E-04	1.79E-04
Momentum compaction, α	1.22E-02	1.22E-02	1.22E-02
Horizontal emittance, ϵ_x (mrad)	3.41E-09	2.18E-09	1.23E-09
Vertical emittance, ϵ_y (mrad)	3.38E-11	2.15E-11	1.22E-11
Zero current bunch length, σ_{p_0} (m)	1.99E-03	1.42E-03	9.24E-04
Zero current energy spread, σ_{e_0}	2.14E-04	1.71E-04	1.29E-04
Synchrotron tune, ν_s	1.97E-02	2.23E-02	2.54E-02
Synchrotron radiation loss, L_s (MeV)	1.38E-03	5.67E-04	1.79E-04
RF acceptance, ϵ_{RF}	3.23E-02	3.61E-02	4.17E-02

I. THEORY

called betatron oscillations. The betatron functions, β_H and β_V , which characterize the amplitude and period of the betatron oscillations, are a measure of the focusing properties of the magnetic lattice. Together with the emittance, ϵ , which is the area in the position-angular deviation phase space in which the beam is contained, the beta functions determine the beam size, i.e., the rms beam height, $\sigma_H = \sqrt{\epsilon_H \beta_H}$. The choice of the beta functions in the bypass is determined by the requirement of keeping ρ as large as possible, which requires small β_H, β_V , without violating the energy spread condition $\sigma_e < \rho$. In effect for a beam with nonzero transverse emittances ϵ_H, ϵ_V , it is necessary to add to the real energy spread an effective spread given by [20]

$$\sigma_{eff} = \frac{1}{2} \left(\frac{2\pi}{\lambda_u} \right)^2 \frac{K^2}{1-K^2} \epsilon_V \beta_V - \frac{\gamma^2}{1-K^2} \left(\frac{\epsilon_H}{\beta_H} - \frac{\epsilon_V}{\beta_V} \right) \quad (17)$$

In what follows we will make sure that the condition $\sigma_{eff} < \sigma_e$ is always satisfied.

In the cases that we will consider in the next section the undulator length varies between two and three meters and is determined by the condition $N_u = 1/\rho$. This length is also consistent with our assumption on the beta-functions.

8. The electron storage ring and bypass section

The storage ring that we consider is similar to those used as synchrotron radiation sources, for instance the National Synchrotron Light Source VUV ring [15]. Its main characteristics are given in table 3.

Since we want to maximize the electron density to obtain a large value of ρ in the undulator, we have chosen a ring design which minimizes the beam emittance and the bunch length. When the beam enters the bypass section it undergoes additional focusing to increase ρ , as shown in table 2.

The ring has two 10 m long straight sections, one used for the radiofrequency system and one for the bypass switching magnets. The arcs joining the two long straights each have three equal periods. Each period has 2 dipole magnets with a focusing quadrupole between them and two quadrupole doublets on the external sides. The ring energy dispersion is controlled by the central quadrupole and is nonzero only in the dipoles and in the region between them.

The momentum compaction, $\alpha = (dE/E)'(dl/l)$, relates the change in orbit length to the relative energy deviation from the design energy E_0 of the ring. For a ring with this magnetic structure the momentum compaction α , and the horizontal emittance, ϵ_H , are ap-

proximately given by [21]

$$\alpha = \frac{1}{6} \left(\frac{\pi}{M} \right)^2 \frac{R_B}{R_{av}} \quad (18)$$

$$\epsilon_H = 7.7 \times 10^{-11} \frac{\gamma^2}{M^3} \text{ (mrad)} \quad (19)$$

where R_B, R_{av} are the bending and average ring radii and M is the number of achromatic bends. An achromatic bend, typically consists of two dipole magnets with a horizontally focusing quadrupole in between, and is designed to focus all the entering electrons, regardless of energy, to the same point on exiting the bend. The vertical emittance is determined by the coupling between horizontal and vertical oscillation due to magnet misalignment, $\epsilon_V = \chi \epsilon_H$.

At zero or small current the rms energy spread and the bunch length are determined by synchrotron radiation and are given by [22]

$$\sigma_{e0} = 4.38 \times 10^{-7} \frac{\gamma}{R_B^{1/2}} \quad (20)$$

$$\sigma_{p0} = \frac{\alpha R_{av}}{\nu_s} \sigma_{e0} \quad (21)$$

where $\nu_s = \omega_s/\omega_0$ is the ring synchrotron oscillation tune. At large currents the microwave instability [23], caused by the beam interaction with the broad-band high frequency storage ring impedance can increase the energy spread, σ_e , and the bunch length, σ_p . An increase of σ_p reduces the value of ρ while at the same time σ_e increases and the condition $\sigma_e \geq \rho$ can be violated.

To evaluate this effect we use the approximate condition [23]

$$eI_p \left| \frac{Z(n)}{n} \right| \leq 2\pi E_0 \alpha \sigma_e^2 \quad \text{for } n \geq \frac{R_{av}}{\sigma_p} \quad (22)$$

where I_p is the peak current, related to the average bunch current, I_b , by

$$I_p = (2\pi)^{1/2} \frac{R_{av}}{\sigma_p} I_b \quad (23)$$

and $|Z(n)/n|$ is the effective longitudinal coupling impedance of the ring.

From eqs. (21)–(23) an expression for the microwave instability limited bunch length and energy spread can be obtained

$$\sigma_p = R_{av} \left(\frac{\alpha I_b \epsilon}{\sqrt{2\pi} E_0 \nu_s^2} \left| \frac{Z(n)}{n} \right| \right)^{1/3} \quad (24)$$

$$\sigma_e = \frac{\nu_s}{\alpha R_{av}} \sigma_p \quad (25)$$

The storage ring coupling impedance is determined by the vacuum chamber geometry and by the bending radius in the curved section [23,24] and is a quantity difficult to calculate "a priori...". However in modern

Table 4
Bunch length and peak current

Effective coupling impedance (Ω)	0.1	1.0	10
Bunch length, σ_p (μ -wave limit) (cm)	0.95	2.0	4.3
Peak current, I_p (A)	397	184	86

storage rings values of the order of 1Ω have been obtained. Since this quantity is very important in determining the performance of our system we have chosen to use in our calculations three values of $Z(n)/n$, i.e. 0.1, 1 and 10Ω . Let us notice that a 10Ω coupling impedance is large, and is a pessimistic assumption, while a 1Ω value is realistic and has been already obtained. On the other hand, a 0.1Ω value would require a breakthrough in storage ring design.

The microwave instability limited bunch lengths and peak currents, which depend on the value of the coupling impedance but not the energy, are given in table 4. The bunch lengths are typically a few centimeters and the peak currents are in the 100-400 A range.

To test the beam for stability against transverse coherent oscillations we have used the conditions that

the coherent betatron tune shift be smaller than the synchrotron tune [23]

$$\delta\nu_{\beta} = \frac{eI_p}{\pi r E} Z_{T,eff} < \nu_s \quad (26)$$

with the transverse coupling impedance $Z_{T,eff}$ evaluated from the longitudinal impedance as [23]

$$Z_{T,eff} = 2 \left(\frac{R}{b} \right)^2 \frac{Z(n)}{n} \quad (27)$$

The ring described in table 3 will be free from transverse instability problems provided the effective impedance can be kept on the order 1Ω or less.

As a final measure of the ring's feasibility we compute the Touschek lifetime [25] τ_t . The Touschek lifetime is the time in which losses due to Coulomb collisions between electrons in the same bunch have reduced the beam current to half of its initial value. For the range of ring parameters given in table 3 $\tau_t > 1$ h.

9. Results

In figs. 4a-4c we plot the FEL parameter, ρ , and the microwave instability limited energy spread, σ_p , versus

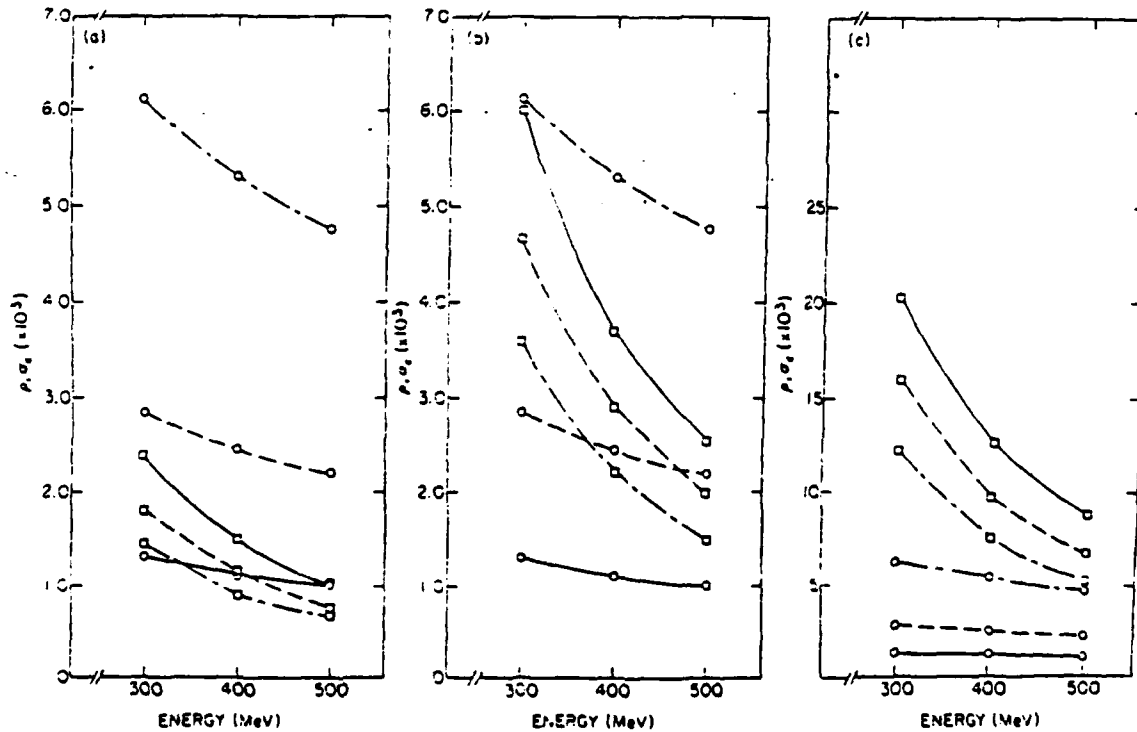


Fig. 4 Plots of the FEL parameter, ρ , and the microwave instability limited rms energy spread, σ_p , versus energy for (a) $\lambda_n = 5$ mm, (b) $\lambda_n = 1$ cm and (c) $\lambda_n = 2.5$ cm. The ρ values are signified by a \square and the σ_p values are given by a \circ . Each figure displays the ρ and σ_p values for 3 values of $Z_{eff} = 0.1, 1.0$ and 10Ω . A solid line corresponds to $Z = 0.1 \Omega$, a dashed line to $Z = 1 \Omega$ and (- - -) to $Z = 10 \Omega$. The lines are not fitted to the points, they are drawn simply to indicate trends.

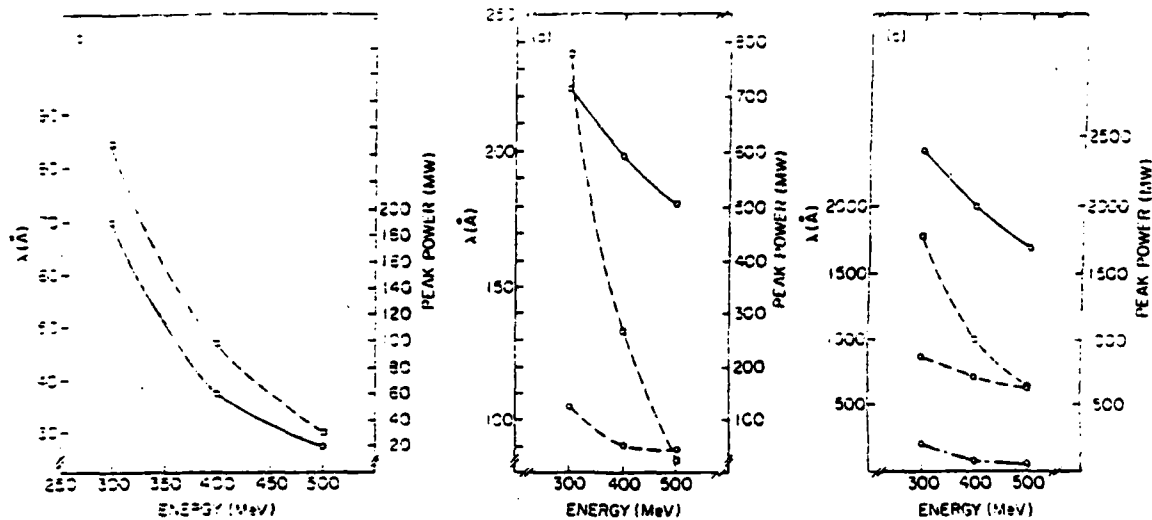


Fig. 5. Plot of the output wavelength λ and the estimated peak power output versus energy for (a) $\lambda_0 = 5$ mm, (b) $\lambda_0 = 1$ cm and (c) $\lambda_0 = 2.5$ cm. The λ values are signified by a \square and the power values are given by a \circ . For the power curves, a solid line corresponds to $Z = 0.01 \Omega$, a dashed line to $Z = 1 \Omega$ and (-.-) to $Z = 10 \Omega$.

the beam energy for the 5 mm, 1 cm and 2.5 cm undulators, respectively. Recalling that the limit on the allowable energy spread is $\sigma_e \leq \rho$ it can be seen from fig. 4a that if the ring impedance can be kept at or below 0.1Ω one can expect to obtain high intensity coherent soft-X-rays in the range of 30–85 Å. From figs. 4b and 4c it can be seen that the energy spread in the ring will not pose any problems for the generation of intense radiation in the range of 85–2000 Å.

Figs. 5a–5c are plots of the peak power versus energy for the three undulator designs. The peak power is calculated assuming that the radiation pulse length is equal to the electron bunch length.

10. Conclusions

Using the system described, an electron storage ring with an undulator in a special bypass section, we can obtain high intensity coherent radiation by sending the beam through the undulator and using the FEL collective instability to produce radiation. Compared to other systems, such as an FEL oscillator or a transverse optical klystron, this system has the advantage that it does not require mirrors to form an optical cavity or an input high power laser to bunch the electron beam. On the other hand, by its very nature, this system can only produce high intensity, short radiation pulses with a repetition rate of the order of 10 Hz.

The storage ring needed to operate the system is characterized by a small transverse emittance. The other important ring parameter is the longitudinal coupling

impedance. For a value of the order of 1Ω one can obtain peak powers on the order of 500 MW down to wavelengths of about 500 Å and 50 MW to 80 Å; the power decreases sharply at lower wavelength. If it should become possible to reduce $|Z(\pi)/\pi|$ to 0.1Ω one could get peak powers on the order of 20 MW down to 30 Å.

One should also remember that in this paper we have concentrated our attention on the first harmonic production only; however, from the results of ref. [18], we know that the system will also produce higher harmonics and this can shift down the lower limit for soft X-ray production.

We want to emphasize that the results presented here are preliminary, and that one might improve the system performance by optimizing other ring parameters such as the momentum compaction or the radiofrequency voltage and frequency. To obtain a more complete understanding of the system one should investigate diffraction effects on the radiation due to the finite beam radius and consider a three dimensional calculation taking into account the electron density variation in both the transverse and longitudinal direction.

This work is supported by the US Department of Energy.

References

- [1] A presentation of many of these results appear in these Proceedings (1984 FEL Conf., Italy) Nucl. Instr. and Meth. A237 (1,2) (1985).
- [2] L.R. Elias et al., Phys. Rev. Lett. 36 (1976) 717.

- [3] M. Billardon et al., Phys. Rev. Lett. 51 (1983) 1652.
- [4] B.E. Newman et al., Int. Quant. Elec. Conf. Paper WHH1, San Diego, California (1984).
- [5] T.J. Orzechowski et al., *ibid.*, post-deadline paper.
- [6] J.A. Pasour, R.F. Lucey and C.A. Kapetanios, Phys. Rev. Lett. 53 (1984) 1728.
- [7] J.M.J. Madey, in: Free Electron Generation of Extreme Ultraviolet Coherent Radiation, eds., J.M.J. Madey and C. Pellegrini, American Institute of Physics, Conf. Proc. Vol. 113 (1984), p. 12.
- [8] J. Murphy and C. Pellegrini, Int. Quant. Elec. Conf., paper WQ02, San Diego, California (1984); in course of publication in J. Optic. Soc. Amer. B.
- [9] K.-J. Kim et al., OSA Annual Meeting, San Diego, California (1984).
- [10] J.M.J. Madey, J. Appl. Phys. 42 (1971) 1906.
- [11] B.M. Kincaid, J. Appl. Phys. 48 (1977) 2664.
- [12] R. Bonifacio, C. Pellegrini and L.M. Narducci, Optics Comm. (1984) 373.
- [13] D.T. Attwood et al., in ref. [7], p. 294.
- [14] B.M. Kincaid et al., in ref. [7], p. 110.
- [15] L. Blumberg et al., IEEE Trans. Nucl. Sci. NS-26 (1979) 3842.
- [16] W.B. Colson and S.K. Ride, in: Physics of Quantum Electronics, vol. 7, eds., S.F. Jacobs et al. (Addison-Wesley, Reading, MA., 1980) p. 377.
- [17] C. Pellegrini, in: Free Electron Lasers, eds. S. Martellucci and A.N. Chester (Plenum, New York, 1983) p. 91.
- [18] J.B. Murphy, C. Pellegrini and R. Bonifacio, Brookhaven National Laboratory Report, BNL-34156 (1984).
- [19] K. Halbach, Proc. Bendor Free Electron Laser Conf., J. de Physique 44 (1982) 211.
- [20] A. Lucio and C. Pellegrini, in: Free Electron Lasers, eds., S. Martellucci and A.N. Chester (Plenum, New York, 1983) p. 28.
- [21] S. Krinsky, ref. [7], p. 44.
- [22] M. Sands, in: Physics with Intersecting Storage Rings, ed. B. Touschek (Academic Press, New York, 1971) p. 257.
- [23] D. Boussard, CERN Lab II/RF/INT 75-2 (1975); J.M. Wang and C. Pellegrini, in: Proc. 11th Int. Conf. on High Energy Accelerators, Geneva (1980) ed., W.S. Newman, p. 554; A. Chao, in: Physics of High Energy Particle Accelerators, ed., M. Month, AIP Conf. Series, no. 105 (1983) p. 353; C. Pellegrini, in: Physics of High Energy Particle Accelerators, eds., R.A. Carrigan, F.R. Huson and M. Month, AIP Conf. series no. 87 (1982) p. 77.
- [24] A. Faltens and L.J. Laslett, Particle Accel. 4 (1973) 151; V. Brady, A. Faltens and L.J. Laslett, Lawrence Berkeley Laboratory, Report LBID-536 (1981).
- [25] H. Bruck, Circular Particle Accelerators (Presses Universitaires de France, Paris, 1966).

END

FILMED

1-86

DTIC